Dipartimento di Matematica e Fisica
PhD Course in Physics
XXXV cycle

Title of Thesis

Estimating the Attenuation from Sounding Radar Data in Terrestrial and Planetary Investigation

PhD Candidate
Jamaledin Baniamerian

Tutor
Prof. Elena Pettinelli
Co-Tutor
Dr. Sebastian Emanuel Lauro
Coordinator
Prof. Guiseppe Degrassi

Rome, March 2023
Academic Year 2023/2024

Summary

Ground Penetrating Radar (GPR) or Georadar is a geophysical technique, based on electromagnetic (EM) pulse reflection, that probes the subsurface in a wide range of frequencies, from a few megahertz (MHz) to gigahertz (GHz). GPR has been extensively used for applications in shallow investigation on Earth, and more recently, in planetary exploration. Propagating electromagnetic waves in a lossy medium are subject to attenuation that depends on the electromagnetic properties of the composing materials, medium structure, and the nominal operating frequency of the transmitted signal. Therefore, evaluating the attenuation of propagating EM wave provides insights to the material's constitutive parameters. In particular, estimation of attenuation from georadar data has important implications in planetary investigations since the attenuation of radar waves can vary significantly between materials. Therefore, the estimation of radar wave attenuation may help discriminate between regolith and ice, especially at high frequencies. This thesis is devoted to estimating attenuation using radar data collected on earth and by orbiting or rover radar on the Mars and the Moon.

The centroid-frequency downshift of the traveling pulse is an effective method for estimating the attenuation of propagating electromagnetic wave. Assuming the transmitted pulse is a Ricker wavelet, two novel forward formula, using the amplitude and power spectrum of the recorded reflections, are developed to estimate the absorption attenuation in term of loss tangent (ratio of energy loss to energy storage) of the medium. The retrieval of loss tangent from data is performed through a probabilistic inversion approach. The new methods are validated by implementing to datasets generated by two types of synthetic models simulated by gprMax, a well-established FDTD based open-source software. In addition, the total energy loss (the sum of scattering and intrinsic loss) is deduced from least square fit to the amplitude of records, as well, and consequently, contribution of scattering and intrinsic loss can be separated. The developed strategies are applied to GPR data collected on a volcanic ash deposit, to estimate the attenuation components of subsurface deposit.

These methods could be particularly suitable for dry and cold environment, typical of the Moon and Mars, whose shallow subsurface is dominated by fine materials (regolith) mixed with rocky inclusions. In this aspect, the same methods are used to estimate the loss tangent of lunar regolith - stratigraphy on the far side of the Moon from the observations (500 MHz channel) made by the Lunar Penetrating Radar (LPR) onboard the Yutu-2 rover of the Chang'E-4 mission. An attenuation analysis is then conducted on data acquired by Mars Advanced Radar for Subsurface and Ionosphere Sounding (MARSIS) radar sounder over the South Polar Layer Deposits (SPLD) at Ultimi Scopuli at 3, 4 and 5MHz frequencies. A different strategy is used in this case, and loss tangent is estimated using a linear relation between basal-surface echo intensities.

To the Memory of

Mahsa (Jina) Amini *whose violent death by the Iran's regime led to "Women, life, freedom" protest (September, 2022) in Iran.*

Kian Pirfalak, *a nine-year-old child, killed by mercenaries of the Iran's regime.*

Khodanour Lojei, *a young man, killed by a gunshot in his kidney. He was tied to a flagpole with a bottle of water in front of him, but he could not reach it.*

And hundreds of children, women, and men who were victims in the Mahsa Amini protests.

Donna, Vita, Libertà

Acknowledgments

I would like to express my sincere gratitude to my supervisors Prof. Elena Pettinelli and Dr. Sebastian Emanuel Lauro for their continuous support and guidance during my PhD. It was invaluable to have their coherent knowledge of the subject, their passion for research, and their optimism. It was Dr. Lauro who introduced me to the real world of research. I would also like to thank Dr. Elisabetta Mattei and Dr. Barbara Cosciotti for their assistance and help.
I would especially like to thank the PhD coordinator, Prof. Guiseppe Degrassi.
Without my wife, Sahar Nazeri, I would not have been able to complete this work. I would like to thank her.

Contents

Chapter 1

Principle of Electromagnetism

Geophysical methods are based on studying the propagation of the different physical fields within the earth's interior. One of the most widely used fields in geophysics is the electromagnetic (EM) field generated by natural or controlled sources. Electromagnetism is the study of the effects of moving or stationary electric charges. Moving charges produce a current, which gives rise to a magnetic field. A time-varying electric field produces a magnetic field, and vice versa. In other words, time varying electric and magnetic fields are coupled, resulting in an electromagnetic field. Electromagnetic waves may propagate in both lossless (e.g., air and perfect dielectrics) and lossy media (material with nonzero conductivity, such as pure water). Waves propagating in a lossless medium do not attenuate, but when EM wave propagates in a lossy medium, part of the power carried by the EM wave is converted into heat. For most earth problems, we assume isotropy, homogeneity, linearity, and temperature-time-pressure independence of the electrical parameters of local regions of the earth.

This chapter summarizes the fundamentals of electromagnetic wave theory; their properties and propagation particularly in lossy media; material electromagnetic properties with the emphasis made on water, ice and rocks; and wave reflection and transmission at planar boundaries.

1.1 Maxwell's Equations

The theory of electromagnetic is described by a set of basic physical laws formulated through the Maxwell's equation which relate the variations of electric and magnetic fields, charges, and currents associated with electromagnetic waves. Maxwell's equations are uncoupled first-order linear differential equations that can be coupled by the empirical constitutive relations which reduce the number of basic vector field functions from five to two.

1.1.1 Maxwell's Equations in Time Domain

The differential forms of time-varying Maxwell's equations are given by:

$$\nabla \times \mathbf{e}(\mathbf{r},t) = -\partial \mathbf{b}(\mathbf{r},t)/\partial t \tag{1.1}$$

$$\nabla \times \mathbf{h}(\mathbf{r},t) = \mathbf{j}_t(\mathbf{r},t) = \mathbf{j}_i(\mathbf{r},t) + \mathbf{j}_c(\mathbf{r},t) + \mathbf{j}_d(\mathbf{r},t) \tag{1.2}$$

$$\nabla . \mathbf{d}(\mathbf{r},t) = \rho_q(\mathbf{r},t) \tag{1.3}$$

$$\nabla . \mathbf{b}(\mathbf{r},t) = 0 \tag{1.4}$$

where the definition and units of quantities are:
$\mathbf{e}$ = electric field intensity (volt/m)
$\mathbf{b}$ = magnetic flux density (weber/m^2)
$\mathbf{h}$ = magnetic field intensity (ampere/m)
$\mathbf{j}_t$ = total electric current density (ampere /m^2)

$\mathbf{j}_i$ = source electric current density (ampere $/m^2$); $\mathbf{j}_c(\mathbf{r},t) = \sigma\ \mathbf{e}(\mathbf{r},t)$
$\mathbf{j}_c$ = conduction electric current density (ampere $/m^2$)
$\mathbf{j}_d(\mathbf{r},t)$ = displacement electric current density (ampere $/m^2$); $\mathbf{j}_d = \partial\mathbf{d}(\mathbf{r},t)/\partial t$
$\mathbf{d}$ = electric flux density (coulomb$/m^2$)
ρ_q = electric charge density (coulomb$/m^3$)

All field quantities ($\mathbf{e}$, $\mathbf{b}$, $\mathbf{h}$, $\mathbf{j}$, $\mathbf{d}$) are assumed to be time-varying and each is a function of space coordinate $\mathbf{r}$. In preceding sections these quantities are described in detail. Equations (1.1) through (1.4) present the conventional forms of Maxwell's equations that are based on the experiments, of Faraday (equation (1.1)), Ampere (equation (1.2)) and Gauss (equation (1.4)). Thus they are empirical but they can describe most macroscopic electromagnetic phenomena. Equations (1.1) through (1.4), are uncoupled differential equations of the five vector functions, that are coupled through constitutive relations (section 1.2).

1.1.2 Maxwell's Equations in Frequency Domain

To obtain equations in the frequency domain, a Fourier transformation pair, as expressed below for a function f, is performed:

$$\mathbf{F}(\mathbf{r},\omega) = \int_{-\infty}^{\infty} \mathbf{f}(\mathbf{r},t)\ e^{-j\omega t} dt; \qquad \mathbf{f}(\mathbf{r},t) = \frac{1}{2\pi}\int_{-\infty}^{\infty} \mathbf{F}(\mathbf{r},\omega)\ e^{j\omega t} d\omega \tag{1.5}$$

which amounts to assuming $e^{j\omega t}$ time dependence; ω is angular frequency and $j = \sqrt{-1}$. These fields are referred to time-harmonic fields with a time dependency of the form $e^{j\omega t}$:

$$\nabla \times \mathbf{E}(\mathbf{r},\omega) = -j\omega\mathbf{B}(\mathbf{r},\omega) = -j\omega\mu\mathbf{H}(\mathbf{r},\omega) \tag{1.6}$$

$$\begin{aligned} \nabla \times \mathbf{H}(\mathbf{r},\omega) &= \mathbf{J}_i(\mathbf{r},\omega) + \mathbf{J}_c(\mathbf{r},\omega) + j\omega\mathbf{D}(\mathbf{r},\omega) \\ &= \mathbf{J}_i(\mathbf{r},\omega) + \sigma\mathbf{E}(\mathbf{r},\omega) + j\omega\varepsilon\mathbf{E}(\mathbf{r},\omega) \\ &= \mathbf{J}_i(\mathbf{r},\omega) + (\sigma + j\omega\varepsilon)\,\mathbf{E}(\mathbf{r},\omega) \end{aligned} \tag{1.7}$$

$$\nabla.\mathbf{D}(\mathbf{r},\omega) = \rho_q(\mathbf{r},\omega) \tag{1.8}$$

$$\nabla.\mathbf{B}(\mathbf{r},\omega) = 0 \tag{1.9}$$

These expressions in effect are obtained by replacing $\partial/\partial t = j\omega$ and considering the constitutive relations:

$$\begin{aligned} \mathbf{D} &= \varepsilon\ \mathbf{E} \\ \mathbf{B} &= \mu\ \mathbf{H} \\ \mathbf{J}_c &= \sigma\ \mathbf{E} \end{aligned} \tag{1.10}$$

Once the time-harmonic fields (fields in frequency domain) are obtained, the general transient fields as a function of time can be computed by inverse Fourier transform:

$$\begin{aligned} \mathbf{e}(\mathbf{r},t) &= \frac{1}{2\pi}\int_{-\infty}^{\infty} \mathbf{E}(\mathbf{r},\omega)\ e^{j\omega t} d\omega \\ \mathbf{b}(\mathbf{r},t) &= \frac{1}{2\pi}\int_{-\infty}^{\infty} \mathbf{H}(\mathbf{r},\omega)\ e^{j\omega t} d\omega \end{aligned} \tag{1.11}$$

1.1.3 Maxwell's Equations in Wavenumber Domain

Sometimes it can be useful to express in algebraic form the spatial dependence of Maxwell's equations, rather than the temporal one. In this case triple Fourier transform is used [35]:

$$\begin{aligned} \mathbf{e}(\mathbf{r},t) &= \int_{-\infty}^{\infty} \hat{\mathbf{E}}(\mathbf{k},t)\, e^{-j\mathbf{k}.\mathbf{r}}\ d\mathbf{k} \\ \mathbf{b}(\mathbf{r},t) &= \int_{-\infty}^{\infty} \hat{\mathbf{H}}(\mathbf{k},t)\, e^{-j\mathbf{k}.\mathbf{r}}\ d\mathbf{k} \end{aligned} \tag{1.12}$$

where $\mathbf{k}$ presents the wavenumber. Substitution of these integrals in equations (1.1) through (1.4) yields:

$$-j\mathbf{k}\times\hat{\mathbf{E}}\left(\mathbf{k},t\right)=-\frac{\partial\hat{\mathbf{B}}\left(\mathbf{k},t\right)}{\partial t} \tag{1.13}$$

$$-j\mathbf{k}\times\hat{\mathbf{H}}\left(\mathbf{k},t\right)=-\frac{\partial\hat{\mathbf{D}}\left(\mathbf{k},t\right)}{\partial t} \tag{1.14}$$

$$-j\mathbf{k}.\hat{\mathbf{D}}\left(\mathbf{k},t\right)=\hat{\rho}\left(\mathbf{k},t\right) \tag{1.15}$$

$$-j\mathbf{k}.\hat{\mathbf{B}}\left(\mathbf{k},t\right)=0 \tag{1.16}$$

1.2 Constitutive Relations

The constitutive relations, in frequency-domain are generally defined as:

$$\begin{aligned}\mathbf{D}&=\tilde{\boldsymbol{\varepsilon}}\left(\omega,\mathbf{E},\mathbf{r},t,T,P,...\right)\mathbf{.}\ \mathbf{E}\\ \mathbf{B}&=\tilde{\boldsymbol{\mu}}\left(\omega,\mathbf{E},\mathbf{r},t,T,P,...\right)\mathbf{.}\ \mathbf{H}\\ \mathbf{J}_c&=\tilde{\boldsymbol{\sigma}}\left(\omega,\mathbf{E},\mathbf{r},t,T,P,...\right)\mathbf{.}\ \mathbf{E}\end{aligned} \tag{1.17}$$

in which the tensors $\tilde{\boldsymbol{\varepsilon}}$, $\tilde{\boldsymbol{\mu}}$, $\tilde{\boldsymbol{\sigma}}$, describe the dielectric permittivity, magnetic permeability, and the electric conductivity as functions of angular frequency ω, electric field strength $\mathbf{E}$ or magnetic induction $\mathbf{B}$, position $\mathbf{r}$, time t, temperature T, and pressure P, [148]. Each of these three tensors is complex in the general case, permitting the phases of $\mathbf{D}$ - $\mathbf{E}$, of $\mathbf{H}$ - $\mathbf{B}$, and of $\mathbf{J}_c$ - $\mathbf{E}$ to be different.

Materials are classified as *linear* versus nonlinear, *homogeneous* versus non-homogeneous (inhomogeneous), *isotropic* versus nonisotropic (anisotropic), and *dispersive* versus nondispersive, according to their lattice structure and behavior. Following is a brief description of the constitutive relations of these mediums.

Non-linearity
Materials whose constitutive parameters are not functions of the applied field are usually known as linear, otherwise they are nonlinear. In practice, many materials exhibit almost linear characteristics as long as the applied field is within certain ranges. In *non-linear* materials

$$\begin{aligned}\mathbf{d}\left(\mathbf{r},t\right)&=\varepsilon\left(\mathbf{e}\right)*\mathbf{e}\left(\mathbf{r},t\right)\\ \mathbf{b}\left(\mathbf{r},t\right)&=\mu\left(\mathbf{e}\right)*\mathbf{h}\left(\mathbf{r},t\right)\\ \mathbf{j}_c\left(\mathbf{r},t\right)&=\sigma\left(\mathbf{e}\right)*\mathbf{e}\left(\mathbf{r},t\right)\end{aligned} \tag{1.18}$$

where $*$ indicates convolution that become simple producte in frequency domain

$$\begin{aligned}\mathbf{D}\left(\mathbf{r},\omega\right)&=\varepsilon\left(\mathbf{E}\right)\mathbf{E}\left(\mathbf{r},\omega\right)\\ \mathbf{B}\left(\mathbf{r},\omega\right)&=\mu\left(\mathbf{H}\right)\mathbf{H}\left(\mathbf{r},\omega\right)\\ \mathbf{J}_c\left(\mathbf{r},\omega\right)&=\sigma\left(\mathbf{E}\right)\mathbf{E}\left(\mathbf{r},\omega\right)\end{aligned} \tag{1.19}$$

Inhomogeneity
When the constitutive parameters of media are not functions of position, the materials are referred to as homogeneous; otherwise, they are inhomogeneous. Almost all materials exhibit some degree of non-homogeneity. However, for most materials used in practice the non-homogeneity is so small that the materials are considered as homogeneous. In *inhomogeneous materials*, the constitutive relations in time domain are:

$$\begin{aligned}\mathbf{d}\left(\mathbf{r},t\right)&=\varepsilon\left(\mathbf{r}\right)*\mathbf{e}\left(\mathbf{r},t\right)\\ \mathbf{b}\left(\mathbf{r},t\right)&=\mu\left(\mathbf{r}\right)*\mathbf{h}\left(\mathbf{r},t\right)\\ \mathbf{j}_c\left(\mathbf{r},t\right)&=\sigma\left(\mathbf{r}\right)*\mathbf{e}\left(\mathbf{r},t\right)\end{aligned} \tag{1.20}$$

In frequency domain they are given by simple products:

$$\begin{aligned}\mathbf{D}(\mathbf{r},\omega) &= \varepsilon(\mathbf{r})\,\mathbf{E}(\mathbf{r},\omega)\\ \mathbf{B}(\mathbf{r},\omega) &= \mu(\mathbf{r})\,\mathbf{H}(\mathbf{r},\omega)\\ \mathbf{J}_c(\mathbf{r},t) &= \sigma(\mathbf{r})\,\mathbf{E}(\mathbf{r},\omega)\end{aligned} \tag{1.21}$$

Anisotropy
If the constitutive parameters depend on the direction of applied field, the materials are *anisotropic*; otherwise, they are known as isotropic. In anisotropic materials, the constitutive relations may be written in tensor form:

$$\begin{aligned}\mathbf{D}(\mathbf{r},\omega) &= \tilde{\boldsymbol{\varepsilon}}\mathbf{.}\ \mathbf{E}(\mathbf{r},\omega)\\ \mathbf{B}(\mathbf{r},\omega) &= \tilde{\boldsymbol{\mu}}\mathbf{.}\ \mathbf{H}(\mathbf{r},\omega)\\ \mathbf{J}_c(\mathbf{r},\omega) &= \tilde{\boldsymbol{\sigma}}\mathbf{.}\ \mathbf{E}(\mathbf{r},\omega)\end{aligned} \tag{1.22}$$

For example, for displacement current in Cartesian coordinate

$$\begin{bmatrix}D_x\\ D_y\\ D_z\end{bmatrix} = \begin{bmatrix}\varepsilon_{xx} & \varepsilon_{xy} & \varepsilon_{xz}\\ \varepsilon_{yx} & \varepsilon_{yy} & \varepsilon_{yz}\\ \varepsilon_{zx} & \varepsilon_{zy} & \varepsilon_{zz}\end{bmatrix}\begin{bmatrix}E_x\\ E_y\\ E_z\end{bmatrix} \tag{1.23}$$

Dispersion
Dispersion implies that a given physical property is frequency-dependent. All materials used in practice display some degree of dispersion. The permittivity and conductivity, especially of dielectric material, and the permeability of ferromagnetic material and ferrites exhibit dispersive characteristics. The frequency dependence comes about because when a time-varying electric field is applied, the polarization response of the material cannot be instantaneous. Such response in time domain can be described by convolution:

$$\begin{aligned}\mathbf{d}(\mathbf{r},t) &= \varepsilon(t) * \mathbf{e}(\mathbf{r},t)\\ \mathbf{b}(\mathbf{r},t) &= \mu(t) * \mathbf{h}(\mathbf{r},t)\\ \mathbf{j}_c(\mathbf{r},t) &= \sigma(t) * \mathbf{e}(\mathbf{r},t)\end{aligned} \tag{1.24}$$

where $*$ indicates convolution. In integral form, for example:

$$\mathbf{d}(\mathbf{r},t) = \int_{-\infty}^{t} \boldsymbol{\varepsilon}(t-t')\mathbf{e}(\mathbf{r},t')\ dt' \tag{1.25}$$

Substituting (1.11) in (1.25) yields

$$\mathbf{d}(\mathbf{r},t) = \frac{1}{2\pi}\int_{-\infty}^{\infty}\int_{-\infty}^{t} \boldsymbol{\varepsilon}(t-t')\mathbf{E}(\mathbf{r},\omega)\ e^{j\omega t'}\ dt'd\omega \tag{1.26}$$

In the frequency domain relations (1.24), reduce to simple products:

$$\begin{aligned}\mathbf{D}(\mathbf{r},\omega) &= \varepsilon(\omega)\mathbf{E}(\mathbf{r},\omega)\\ \mathbf{B}(\mathbf{r},\omega) &= \mu(\omega)\mathbf{H}(\mathbf{r},\omega)\\ \mathbf{J}_c(\mathbf{r},\omega) &= \sigma(\omega)\mathbf{E}(\mathbf{r},\omega)\end{aligned} \tag{1.27}$$

The GPR wavelet often undergoes a significant change in shape as it travels through the subsurface, and echoes received at later times are noticeably broader than those received at earlier times. This phenomenon is known as *wavelet dispersion*. If the polarity of applied fields alternates, the polarization vectors the permittivity and permeability will be alternating as well, with the same frequency of the applied fields.

General linear relationship
In fact, the more general relationship between $\mathbf{d}(\mathbf{r},t)$ and $\mathbf{e}(\mathbf{r},t)$ is:

$$\begin{aligned}\mathbf{d}(\mathbf{r},t) &= \int_{-\infty}^{\infty} \tilde{\boldsymbol{\varepsilon}}(\mathbf{r}-\mathbf{r}',t-t').\ \mathbf{e}(\mathbf{r}',t')\ dt'd\mathbf{r}' \\ \mathbf{b}(\mathbf{r},t) &= \int_{-\infty}^{\infty} \tilde{\boldsymbol{\mu}}(\mathbf{r}-\mathbf{r}',t-t').\ \mathbf{h}(\mathbf{r}',t')\ dt'd\mathbf{r}'\end{aligned} \tag{1.28}$$

where

$$\begin{aligned}\tilde{\boldsymbol{\varepsilon}}(\mathbf{k},\omega) &= \int_{-\infty}^{\infty} \tilde{\boldsymbol{\varepsilon}}(\mathbf{r},t)\ e^{j\mathbf{k}.\mathbf{r}-j\omega t}d\mathbf{r}dt \\ \tilde{\boldsymbol{\mu}}(\mathbf{k},\omega) &= \int_{-\infty}^{\infty} \tilde{\boldsymbol{\mu}}(\mathbf{r},t)\ e^{j\mathbf{k}.\mathbf{r}-j\omega t}d\mathbf{r}dt\end{aligned} \tag{1.29}$$

In the Fourier space, equation (1.28) becomes

$$\begin{aligned}\mathbf{D}(\mathbf{k},\omega) &= \tilde{\boldsymbol{\varepsilon}}(\mathbf{k},\omega)\,.\,\mathbf{E}(\mathbf{k},\omega) \\ \mathbf{B}(\mathbf{k},\omega) &= \tilde{\boldsymbol{\mu}}(\mathbf{k},\omega)\,.\,\mathbf{H}(\mathbf{k},\omega)\end{aligned} \tag{1.30}$$

Simple Forms
In vacuum the constitutive relations take their simplest form as:

$$\mathbf{D}(\mathbf{r},\omega) = \varepsilon_0\mathbf{E}(\mathbf{r},\omega), \quad \mathbf{B}(\mathbf{r},\omega) = \mu_0\mathbf{H}(\mathbf{r},\omega) \tag{1.31}$$

where ε_0 and μ_0 are permittivity and permeability of vacuum, with numerical values

$$\varepsilon_0 = 8.854\times10^{-12}\ \ (farad/m); \quad \mu_0 = 4\pi\times10^{-7}\ \ (henry/m) \tag{1.32}$$

and the next simple form occurs for linear, homogeneous, isotropic and non-dispersive materials that is expressed in frequency domain as:

$$\mathbf{D}(\mathbf{r},\omega) = \varepsilon\mathbf{E}(\mathbf{r},\omega), \quad \mathbf{B}(\mathbf{r},\omega) = \mu\mathbf{H}(\mathbf{r},\omega), \quad \mathbf{J}_c(\mathbf{r},\omega) = \sigma\mathbf{E}(\mathbf{r},\omega) \tag{1.33}$$

In most elementary electromagnetic earth problems the following assumptions are made in order to simplify analysis [148]:
1. All media are linear, isotropic, homogeneous, and possess electrical properties which are independent of time, temperature, or pressure.
2. Magnetic permeability is assumed to be that of free space, i.e., $\mu \approx \mu_0$.

However, there are some exceptions that above assumptions cannot be made, for example:
1. Anisotropic media are included in some simple electromagnetic boundary-value problems to aid in interpretation of data.
2. In deep crustal studies the effects of temperature and pressure must be considered.
3. The time dependence of electric conductivity due to varying moisture content in surface soils cannot be ignored in some shallow geotechnical investigations.
4. Inhomogeneous media entering into electromagnetic boundary-value problems are treated as 1-D inhomogeneous (plane-layered), 2-D inhomogeneous (infinite cylinders of arbitrary cross-section), 3-D inhomogeneous.

1.3 Wave Equation and Its Solutions

Taking the curl of equations (1.1) and (1.2) yields the wave equation in time domain:

$$\nabla^2\mathbf{e} - \mu\varepsilon\ \partial^2\mathbf{e}/\partial t^2 - \mu\sigma\ \partial\mathbf{e}/\partial t = 0 \tag{1.34}$$

$$\nabla^2\mathbf{h} - \mu\varepsilon\ \partial^2\mathbf{h}/\partial t^2 - \mu\sigma\ \partial\mathbf{h}/\partial t = 0 \tag{1.35}$$

while μ, ε and σ are assumed constant with respect to time in obtaining equations (1.34) and (1.35), however, they can be function of frequency. Fourier transformation of equations (1.34) and (1.35) with respect to time leads to the wave equations in frequency

$$\nabla^2\mathbf{E} + \left(\mu\varepsilon\omega^2 - j\mu\sigma\omega\right)\mathbf{E} = 0 \tag{1.36}$$

$$\nabla^2\mathbf{H} + \left(\mu\varepsilon\omega^2 - j\mu\sigma\omega\right)\mathbf{H} = 0 \tag{1.37}$$

the complex propagation constant is defined as:

$$\gamma = \sqrt{\mu\varepsilon\omega^2 - j\mu\sigma\omega} \tag{1.38}$$

In effect these equations are obtained replacing $\partial/\partial t \equiv j\omega$ and $\partial^2/\partial t^2 \equiv -\omega^2$ in (1.34) and (1.35). Equations (1.36) and (1.37) are valid in frequency domain even if the permittivity, permeability and conductivity are frequency dependent.

In equations (1.36) and (1.37) if $\mu\varepsilon\omega^2 << \mu\sigma\omega$, that is the case for earth material at frequencies less than 10^5 and corresponds to the displacement current much smaller than conduction current, the second derivatives in time in equations (1.34) and (1.35) are eliminated, yielding *diffusion equations*:

$$\nabla^2\mathbf{e} - \mu\sigma\ \partial\mathbf{e}/\partial t = 0 \tag{1.39}$$

$$\nabla^2\mathbf{h} - \mu\sigma\ \partial\mathbf{h}/\partial t = 0 \tag{1.40}$$

that in frequency domain (time-harmonic fields) are given by:

$$\nabla^2\mathbf{E} - j\omega\mu\sigma\ \mathbf{E} = 0 \tag{1.41}$$

$$\nabla^2\mathbf{H} - j\omega\mu\sigma\ \mathbf{H} = 0 \tag{1.42}$$

Under this circumstance, the propagation constant (wave number) is given by

$$\gamma \approx \sqrt{-j\mu\sigma\omega} \tag{1.43}$$

For most of earth materials $\mu \approx \mu_0$, and conductivity, σ, can varies order of magnitude. Therefore, the diffusive properties of electromagnetic signals are primarily dependent on the conductivity. The diffusive behavior of EM signals is a very important aspect of time-domain electromagnetic (TDEM) methods.

If $\mu\varepsilon\omega^2 >> \mu\sigma\omega$ that corresponds to displacement currents much larger than conduction currents in large frequencies ($> 10^6$ Hz), the wave equations are:

$$\nabla^2\mathbf{e} - \mu\varepsilon\ \partial^2\mathbf{e}/\partial t^2 = 0 \tag{1.44}$$

$$\nabla^2\mathbf{h} - \mu\varepsilon\ \partial^2\mathbf{h}/\partial t^2 = 0 \tag{1.45}$$

and in frequency domain (time-harmonic fields) are given by:

$$\nabla^2\mathbf{E} + \mu\varepsilon\omega^2\mathbf{E} = 0 \tag{1.46}$$

$$\nabla^2\mathbf{H} + \mu\varepsilon\omega^2\mathbf{H} = 0 \tag{1.47}$$

the complex propagation constant is defined as:

$$\gamma \approx \sqrt{\mu\varepsilon\omega^2} \tag{1.48}$$

Here, energy is conserved and propagate as waves. The properties of the waves (wavelength, propagation velocity, etc) depend on the product of $\mu\varepsilon$. For most materials $\mu \approx \mu_0$ and ε varies over several orders of magnitude, consequently, the wave properties are primarily dependent on the dielectric permittivity. Wave properties are an important aspect of ground-penetrating radar (GPR) surveys.

Return to equation (1.38), since γ in general is a complex value, it can be expressed as:

$$\gamma = \alpha + j\beta \tag{1.49}$$

where α (Np/m) is the medium's attenuation constant, and β (rad/m) is phase constant. The combination of equations (1.49) and (1.38) leads to (e.g., [5], [114], [146]):

$$\alpha = -\frac{\omega}{c}\mathcal{I}\left\{\sqrt{\varepsilon_{er}}\right\} \tag{1.50}$$

$$\beta = \frac{\omega}{c}\mathcal{R}\left\{\sqrt{\varepsilon_{er}}\right\} \tag{1.51}$$

where $\varepsilon_{er} = \varepsilon'_r - j\varepsilon''_r$ is effective complex-relative permittivity [see equation (1.77)], and $c = 1/\sqrt{\varepsilon_0\mu_0}$ is light velocity in vacuum. Assuming, for example, the electric field of a plane wave with only $\hat{x}$ component that is uniform in x and y directions, the solution of wave equation gives a traveling wave in $+z$ direction at a single frequency (time-harmonic or monochromatic wave):

$$\mathbf{E}(z,t) = \mathcal{R}\left\{\mathbf{E}(z)\, e^{j\omega t}\right\} = \widehat{\boldsymbol{x}}\,\mathcal{R}\left\{E_0\; e^{j(\omega t-\beta z)}\right\} e^{-\alpha z} \tag{1.52}$$

and using

$$\mathbf{H}(z,t) = -\frac{1}{j\omega\mu}\nabla\times\mathbf{E}(z,t) \tag{1.53}$$

the time varying magnetic field is obtained:

$$\mathbf{H}(z,t) = \mathcal{R}\left\{\mathbf{H}(z)\, e^{j\omega t}\right\} = \widehat{\boldsymbol{y}}\,\frac{1}{\eta}\mathcal{R}\left\{E_{\mathbf{0}}e^{j(\omega t-\beta z)}\right\} e^{-\alpha z} \tag{1.54}$$

where E_0 is the amplitude of electric field, $\mathbf{E}(z)$, at $z = 0$, and the intrinsic impedance is defined as:

$$\eta = \sqrt{\mu/\varepsilon_e} \tag{1.55}$$

where ε_e is effective dielectric permittivity defined by equation (1.75). The carried power density of the wave is a quantity of great interest which its average value is defined by (e.g., [5], [114], [146]):

$$\bar{\mathbf{S}} = \frac{1}{2}\Re\left[\mathbf{E}\times\mathbf{H}^{\dagger}\right] = \hat{\boldsymbol{z}}\;|E_0|^2\, e^{-2\alpha z}\;\Re\left(\frac{1}{2\eta^{\dagger}}\right) \tag{1.56}$$

where $\dagger$ indicates the conjugate operator. The equations (1.52) and (1.54) show the fields $\mathbf{E}(z,t)$ and $\mathbf{H}(z,t)$ decay with distance, z, exponentially as $e^{-\alpha z}$, and consequently, the power density decreases as $e^{-2\alpha z}$. It is worth mentioning that in many engineering problems the ratio of two power level e.g., the received and transmitted powers of a radar system are of main interest that is conveniently represented in dB scale. The key properties of an EM wavefield are phase velocity, V, attenuation, α, and electromagnetic impedance, η which will be discussed in proceeding sections.

1.4 Attenuation of Electromagnetic Waves in Lossy Media

The propagating electromagnetic waves in lossy media undergo energy attenuation. The attenuation describes the energy loss in the material as a cost of moving charges and consequent transfer of electromagnetic field energy to mechanical and eventually thermal energy. Assuming a uniform plane wave traveling in the $+z$ direction in a lossy medium, the attenuation constant and phase constant are obtained by combination of equation (1.38) and (1.49) (e.g., [5], [114]):

$$\alpha = \omega\sqrt{\mu\varepsilon'}\left\{\frac{1}{2}\left[\sqrt{1+\left(\frac{\sigma_e}{\omega\varepsilon'}\right)^2}-1\right]\right\}^2 = \omega\sqrt{\mu\varepsilon'}\left\{\frac{1}{2}\left[\sqrt{1+tan\delta^2}-1\right]\right\}^{1/2}\quad(Np/m) \tag{1.57}$$

$$\beta = \omega\sqrt{\mu\varepsilon'}\left\{\frac{1}{2}\left[\sqrt{1+\left(\frac{\sigma_e}{\omega\varepsilon'}\right)^2}+1\right]\right\}^2 = \omega\sqrt{\mu\varepsilon'}\left\{\frac{1}{2}\left[\sqrt{1+tan\delta^2}+1\right]\right\}^{1/2}\quad(rad/m) \tag{1.58}$$

where σ_e is effective conductivity that is equivalent to $\sigma_e = \sigma + \omega\varepsilon''$, and ε' refers to the real part of complex permittivity presented by $\varepsilon = \varepsilon' - j\varepsilon''$. It is critical to note that α and β must be always real values, even though the propagation constant γ is complex. In other words, although the material properties such as dielectric permittivity and conductivity can be expressed as complex quantities equations (1.57) and (1.58) require real values of all three material parameters, applicable at a specific angular frequency. The phase velocity, assuming $\mu \approx \mu_0$, is given by:

$$V = \frac{\omega}{\beta} = \frac{c}{\mathcal{R}\left\{\sqrt{\varepsilon_{er}}\right\}} \quad (m/s) \tag{1.59}$$

In lossless medium where $\alpha = 0$ and $\gamma = j\beta = j2\pi/\lambda$ the phase velocity is

$$V = \omega/\beta = 1/\sqrt{\varepsilon'} = c/\sqrt{\varepsilon'_r} \tag{1.60}$$

The attenuation coefficient, α, includes all loss information, and β collects all phase information in a single parameter. Figure (1.1) schematically presents the attenuation of an electric field by distance.

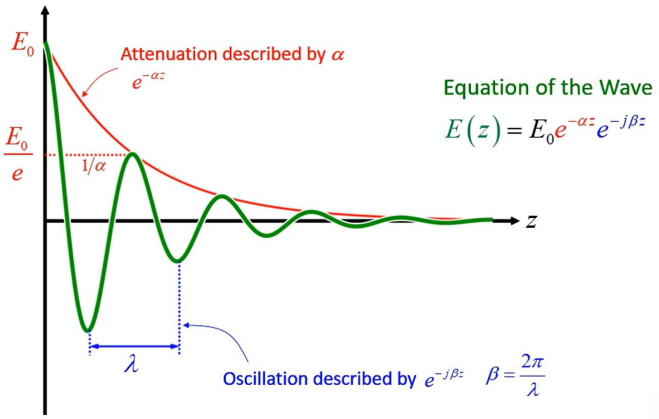

Figure 1.1: Attenuation of an electric field by distance.

The intrinsic impedance is a real value for lossless medium, given by $\eta = \sqrt{\mu/\varepsilon'}$. In the low loss media ($\sigma_e/\omega\varepsilon' \ll 1$) the attenuation is approximated as:

$$\alpha \approx \frac{\sigma_e}{2}\sqrt{\mu/\varepsilon'} = \frac{\omega}{2V} tan\delta \tag{1.61}$$

The low loss assumption is reasonable for glacier ice. However, it cannot be necessarily assumed to generally hold for sub-glacial materials such as saturated bedrock and sediments or for marine-accreted ice of ice shelves. Most common minerals have by themselves negligibly small electrical conductivity at pressures and temperatures prevailing near the surface of the Earth, except for metallic minerals and minerals exhibiting semi-conductive behavior, like sulfides, oxides, and graphite. The low-loss assumption is questionable for a wide range of materials, including shales, sandstones, coal, metamorphic rocks, igneous rocks, and graphite and sulfides ([143]). Overall, the low-loss assumption is less likely to be applicable in three general types of geologic materials:
(1) materials containing sufficient concentration of conductive minerals
(2) sediments and rocks saturated with high-conductivity fluids
(3) saturated clay-bearing rocks and sediments.

The attenuation coefficient, α, phase constant, β, intrinsic impedance η, wavelength λ, velocity V and skin depth δ_s for lossy medium are summarized in Table (1.1). Absorption coefficient, α_p describes how power decays as a function of distance. The difference of absorption α_p and attenuation coefficient is that α describes the decay of amplitude while α_p talk about the power decay of wave.

$$P(z) = P_0 e^{-\alpha_p z} \tag{1.62}$$

The Absorption coefficient and attenuation coefficient are related through:

$$\alpha_p = 2\alpha \tag{1.63}$$

The skin depth (penetration depth) is defined as the distance which wave amplitude decays by an amount e^{-1} and is expressed as:

$$\delta_s = 1/\alpha \ (m) \tag{1.64}$$

Note that as the imaginary part of the complex relative permittivity tends to zero, the skin depth tends to infinity. Figure (1.2) depicts penetration depth variation as a function of frequency for different types of earth's surface components including pure water, sea water, dry soil, wet soil, and dry ice. The penetration depths for pure water and sea water are calculated at 20 ^oC, and the salinity of sea water is 35 g/kg. The penetration depths for dry soil and wet soil assume the volumetric water content is 0.07 and 0.5, respectively. The penetration depth of dry ice is calculated at 0 ^oC.

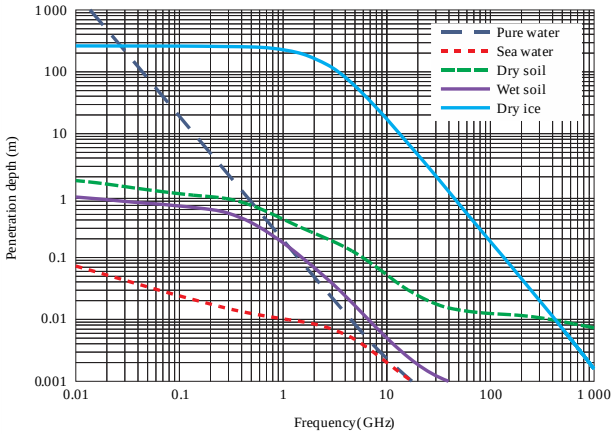

Figure 1.2: Penetration depth of surface materials as a function of frequency [122].

Table 1.1: Propagation constant, wavelength, velocity, and skin depth of EM wave in lossy media [5]. Notes: $\sigma_e = \sigma + \omega\varepsilon''$ and $\varepsilon = \varepsilon' - j\varepsilon''$, $tan\delta = \sigma_e/\omega\varepsilon'$.

Quantity	Exact Relation	Low loss $\frac{\sigma_e}{\omega\varepsilon'} \ll 1$	high loss $\frac{\sigma_e}{\omega\varepsilon'} \gg 1$
Attenuation coefficient	$\alpha = \omega\sqrt{\mu\varepsilon'}\left\{\frac{1}{2}\left[\sqrt{1+\left(\frac{\sigma_e}{\omega\varepsilon'}\right)^2}-1\right]\right\}^{\frac{1}{2}}$	$\alpha \approx \frac{\sigma_e}{2}\sqrt{\mu/\varepsilon'}$ $= \frac{\omega}{2V}\tan\delta$	$\alpha \approx \sqrt{\frac{\omega\mu\sigma_e}{2}}$
Phase constant	$\beta = \omega\sqrt{\mu\varepsilon'}\left\{\frac{1}{2}\left[\sqrt{1+\left(\frac{\sigma_e}{\omega\varepsilon'}\right)^2}+1\right]\right\}^{\frac{1}{2}}$	$\beta \approx \omega\sqrt{\mu\varepsilon'}$	$\beta \approx \sqrt{\frac{\omega\mu\sigma_e}{2}}$
Wavelength	$\lambda = \frac{2\pi}{\beta}$	$\lambda \approx \frac{2\pi}{\omega\sqrt{\mu\varepsilon'}}$	$\lambda \approx 2\pi\sqrt{\frac{2}{\omega\mu\sigma_e}}$
Intrinsic impedance	$\eta = \frac{j\omega\mu}{\gamma} = \sqrt{\frac{j\omega\mu}{\sigma_e + j\varepsilon'\omega}}$	$\eta \approx \frac{\omega\mu}{\beta} = \sqrt{\frac{\mu}{\varepsilon'}}$	$\eta \approx \sqrt{\frac{\omega\mu}{2\sigma_e}}(1+j)$
Velocity	$V = \frac{\omega}{\beta}$	$V \approx \frac{1}{\sqrt{\mu\varepsilon'}}$	$V \approx \sqrt{\frac{2\omega}{\mu\sigma_e}}$
Skin depth	$\delta = \frac{1}{\alpha}$	$\delta \approx \frac{2}{\sigma_e}\sqrt{\varepsilon'/\mu}$	$\delta \approx \sqrt{\frac{2}{\omega\mu\sigma_e}}$

1.5 Electromagnetic Characteristic of Material

1.5.1 Dielectrics, Polarization, and Permittivity

Dielectrics (insulators) are material whose atoms do not contain any free charge, and negative and positive charges are bounded by atomic or molecular forces. Thus dielectrics are not able to provide free conduction electrons as in metals. A particular dielectric material may be characterized by limited movement of charged particles or orientation of polar molecules when an external electric field is applied. This motion of charged particles or rotation of polar molecules is referred to dielectric polarization. Figure (1.3) schematically displays the polarization of a body which is placed in an external field.

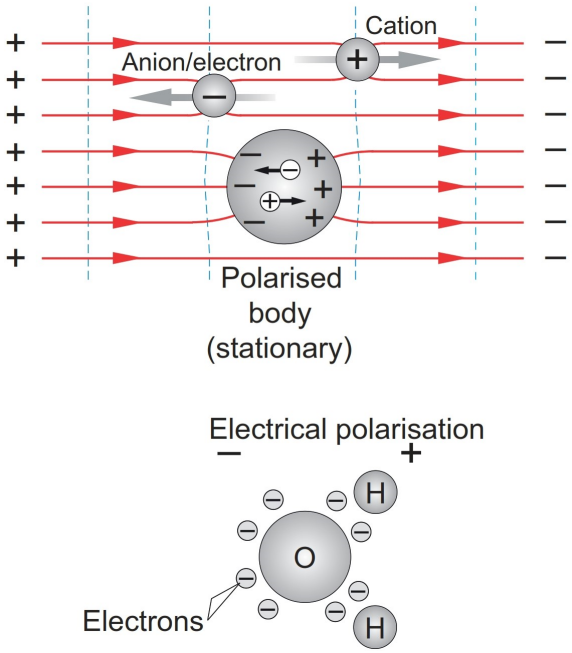

Figure 1.3: (upper panel) Polarization of a body in an external electric field due to movement of electrical charges within the body, and (lower panel) a polarized H_2O molecule.

The total dipole moment of a material is obtained by summing the dipole moments of all the orientational polarization dipole. The electric polarization vector, $\mathbf{P}$, is defined as the total dipole moment per unit volume. The units of $\mathbf{P}$ are coulomb-meters per cubic meter or coulombs per square meter, which is representative of a surface charge density. The vector representing the intensity of polarization inside a material is directed from negative to positive charge. Polarization of dielectric materials allows the material to store electric energy by shifting its bound charges against external forces when external forces are applied. The structure of some materials allows their dipole moments to persist even in the absence of an applied field. These type of materials have permanent dipole moments that are randomly oriented, and when an electric field is applied, the dipoles are aligned with the applied field. Water is a good example of such materials (Figure 1.3, lower panel).

When an external electric field, $\mathbf{E}$, is applied to a dielectric material the electric flux density inside the material is given by:

$$\mathbf{D} = \varepsilon_0 \mathbf{E} + \mathbf{P} \tag{1.65}$$

the electric field, $\mathbf{E}$, and polarization, $\mathbf{P}$, are related as:

$$\mathbf{P} = \varepsilon_0 \chi_e \mathbf{E} \tag{1.66}$$

where χ_e is electric susceptibility that is in general a dimensionless-complex quantity, and can be constant or a varying function of frequency, time, position, temperature, etc. Substituting equation (1.66) into (1.65) and equating the result to (1.10) yields:

$$\mathbf{D} = \varepsilon_0 \mathbf{E} + \mathbf{P} = \varepsilon_0 \left(1 + \chi_e\right) \mathbf{E} = \varepsilon \ \mathbf{E} \tag{1.67}$$

consequently

$$\varepsilon = \varepsilon_0 \left(1 + \chi_e\right) \tag{1.68}$$

By definition, the relative permittivity of a dielectric material is the ratio of permittivity of material to permittivity of free space:

$$\varepsilon_r = \frac{\varepsilon}{\varepsilon_0} = (1 + \chi_e) \tag{1.69}$$

In general, the permittivity is a frequency-dependent complex-quantity, whose real and imaginary parts in turn account for the energy storage and dissipation. The ability of materials to store energy increases as the real component of permittivity value increases. Once the complex permittivity is known, the attenuation of propagating electromagnetic waves in materials can be calculated. While the main constituents of the rocks are the solid minerals, presence of water content dramatically affects the dielectric permeability and electrical conductivity of subsurface materials. The permittivity of water, water ice and rocks is discussed in the proceeding sections.

Types of Electric Polarization

Electric polarization is caused by applying an external electric field, and comprehensively refers to a phenomenon of relative displacement of the negative and positive charges of atoms or molecules, orientation of existing dipoles toward the direction of the field, or the separation of mobile charge carriers at the interfaces of impurities or other defect boundaries. A dielectric material is made up of atoms or molecules that possess one or more of five basic types of electric polarization as listed below. Each type of polarization requires time to perform, therefore, the degree of overall polarization depends on the time variation of the electric field [55].

1. **Electronic polarization**: The applied electric field can cause deformation or translation of the originally symmetrical distribution of the electron clouds of atoms or molecules. This is essentially the displacement of the outer electron clouds with respect to the inner positive atomic cores. The polarization amplitude that is created by the electric field depends strongly on the time-variation of the field. For a certain frequency, especially around the resonant frequency of the oscillator, the induced dipole moment may be very large.

2. **Ionic or molecular polarization**: The electric field causes the atoms or ions of a polyatomic molecule to be displaced relative to each other. This polarization is evident in materials, such as sodium chloride (NaCl) that possess positive and negative ions, tending to displace themselves when an electric field is applied.

3. **Dipolar polarization** (orientational polarization): Dipolar polarization can occur in material which contain polar molecules or molecules that have asymmetric structures and possess a permanent dipole moment. The most important example is water that its molecular structure is shown in Figure (1.3). When an electric field is applied, the atoms in water molecules will rotate to align themselves with the direction of applied field. In liquid water there is not resistance to rotation and polarization occur at high frequencies as well. In ice polarization occurs more slowly.

4. **Spontaneous or hopping polarization**: Spontaneous polarization occurs in materials whose crystalline structure exhibits electrical order. This implies that spontaneous polarization occurs only in single crystals or crystallites in polycrystalline materials with a noncentrosymmetic structure, because only in a noncentrosymmetic structure the centroid of the negative charges does not coincide with that of the positive charges.

5. **Interface or space charge polarization**: The orientational, and spontaneous polarization are due to the bound positive and negative charges within the atom or molecule itself, which are linked intimately to each other and normally cannot be separated. However, electric polarization may also be associated with mobile and trapped charges. This polarization is generally referred to as space charge polarization. This occurs mainly in amorphous or poly-crystalline solids or in materials

consisting of traps. Charge carriers (electrons, holes, or ions), which may be injected from electrical contacts, can be trapped in the bulk or at the interfaces, or may be impeded to be discharged or replaced at the electrical contacts. In this case, space charges will be formed, field distribution will be distorted, and hence, the average relative permittivity will be affected.

Figure (1.4) qualitatively illustrates the time response of the various polarization processes (in a generic dielectric) when a step-function external electric field is applied. In general, the time required for electronic and molecular polarization and depolarization is very short. The time required for orientational, hopping, or space charge polarization and depolarization is relatively long and depending on the dielectric system varies over a wide range. Such polarization phenomena are sometimes referred to as relaxation processes. A relaxation phenomenon occurs when a restoring action tends to bring the excited system back to its original equilibrium state.

Electronic polarization is always present in atoms or molecules in all kinds of materials, and ionic polarization is present only in materials made of two or more different kinds of atoms that form ions due to the sharing of the valence electrons of one or more atoms with the others. For both electronic and ionic polarization, the dipole moments are induced by applied electric field, so they are a kind of induced dipole moments. In short, both electronic and ionic polarizations are due to the translation or deformation of the valence electron clouds from their original thermal equilibrium state to a new equilibrium state. These types of polarization only slightly depend on temperature because they are intra-molecular phenomena. In orientational polarization that directions of permanent dipole moments are randomly distributed in the material, an applied electric field will reorient them toward the direction of the field, resulting in orientational polarization. The net polarization will return to zero after the removal of the external field because thermal perturbation tends to randomize the alignment. This is why polarization decreases with increasing temperature. In rocks, which are multiphase systems made up of minerals with different compositions, most of these types of polarization take place, with the result that dielectric permeability is a complicated function of frequency, temperature, pressure, and other factors [99].

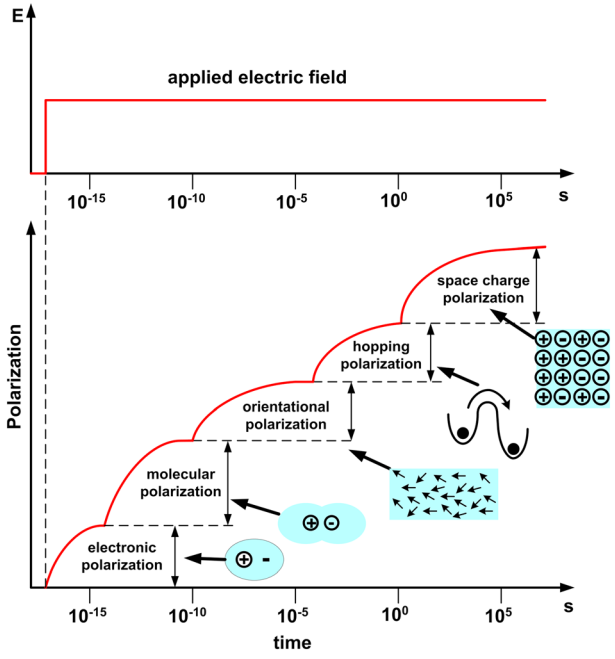

Figure 1.4: Total polarization time response of a generic material to a step function electric field [104].

1.5.2 Magnetics, Magnetization, and Permeability

Magnetic materials are those that exhibit magnetic polarization (magnetization) when they are placed in an external magnetic field. The applied magnetic field can align magnetic dipole moments of material and produces a magnetization vector defined by:

$$\mathbf{M} = \chi_m \mathbf{H} \tag{1.70}$$

where χ_m is called the magnetic susceptibility which in general is a dimensionless-complex quantity. The magnetic flux density is related to the magnetic field intensity, $\mathbf{H}$, and magnetization, $\mathbf{M}$, by:

$$\mathbf{B} = \mu_0 (\mathbf{H} + \mathbf{M}) = \mu_0 (1 + \chi_m) \mathbf{H} = \mu \mathbf{H} \tag{1.71}$$

then magnetic permeability is written by:

$$\mu = \mu_0 (1 + \chi_m) \tag{1.72}$$

The relative magnetic permeability is defined as:

$$\mu_r = \frac{\mu}{\mu_0} = (1 + \chi_m) \tag{1.73}$$

We consider permeability as a real value quantity in this thesis. For the natural materials (that are nonmagnetic) encountered in remote sensing, including water, ice, soil, and vegetation μ equals to that of free space i.e., $\mu_0 = 4\pi \times 10^{-7}$ (H/m).

1.5.3 Conductors and Conductivity

Conductors are the materials that allow charges to pass fairly freely through them. A good example is copper. Nonconductors or insulators, such as plastic and pure water, are materials through which charge cannot move freely. The properties of conductors and insulators depend on the structure and electrical nature of their atoms. In conductors, atomic outer shell contains free electrons. In the absence of external field, these free electrons move with different velocities in random directions and produce zero net current. When a conductor is subjected to an electric field, the electrons start to move in direction opposite the applied electric field, and a conduction current is produced in the conductor. The current density, $\mathbf{J}$, is related to the applied electric field, $\mathbf{E}$.

The conductivity, σ, characterizes the free-electron properties of materials. The reciprocal of conductivity describes resistivity. In general, conductivity varies as a function of frequency. At low frequencies, the charge response is effectively instantaneous, and the conduction current is in phase with the electric field, and the conductivity will be represented by a real value. At higher frequencies, the conduction current is out of phase with the electric field variations, therefore, the conductivity is a complex value quantity where the imaginary component represents the out-of-phase component of the current. The out-of-phase component of conductivity is usually small at most radar frequencies.

The conductivity is directly proportional to (1) the number of charge carriers per unit volume, (2) the charge that each one carries, and (3) the mobility of the charge carriers. This basic statement is true for electronic conduction in solids; ionic conduction in solids, aqueous fluids, and melts; and for ionic conduction within the electrical double layer at the mineral/fluid interface. In following the different mechanisms of conduction, electronic conduction and ionic conduction are described briefly [39].

Effect of Temperature on Conductivity

In conductors as temperature increases, the increased thermal energy of the conductor causes the increase of free-moving electrons colliding, hence the conductivity decreases whereas the electrical conductivity of semiconductors increases as temperature increases. This difference is related to the structural differences between metals and semiconductors on an atomic level.

Electronic Conduction

All materials contain electrons. However, not all electrons are mobile. In solids, electrons have well-defined energy states that form bands. These bands are separated by disallowed energy states. Electrons may be mobile if they occupy a partially filled band of energy states. Then, externally applied energy, for example, from the ambient temperature or an externally applied electric field, can promote an electron to a higher energy, which is reflected in its kinetic energy *i.e.*, its motion. A good conductor, such as

metal, has a partially filled energy band, and applying external energy causes electrons to move within this band. In contrast, insulators have full energy bands, so electrons cannot gain energy from external sources, and therefore aree unable to move. The electronic conductivity of a solid depends very much on the temperature. By increasing temperature electron mobility diminishes and conductivity decreases.

Ionic Conduction

There are fewer ions available for carrying charges than electrons in a metal or semiconductor, and since ions of different charges impede each other and even bond together, their mobility is smaller than that of electrons. Charged ions mediate conduction in pore fluids. In an aqueous solution of $NaCl$, for example, there are finite nonzero concentrations of the charged ions H^+, H_3O^+, OH^-, Na^+, and Cl^-, all of which transfer charge when an electric potential difference is applied to the fluid.

1.5.4 Complex Effective Permittivity and Loss Tangent

Recalling the Maxwell-Ampere differential equation (equation (1.7)) considering the complex permittivity, $\varepsilon = \varepsilon' - j\varepsilon''$:

$$\begin{aligned}\nabla \times \mathbf{H} &= \mathbf{J}_i + \mathbf{J}_c + \mathbf{J}_d = \mathbf{J}_i + \mathbf{J}_c + j\omega\mathbf{D} = \mathbf{J}_i + \sigma_s\mathbf{E} + j\omega\varepsilon\mathbf{E} \\ &= \mathbf{J}_i + \sigma_s\mathbf{E} + j\omega\left(\varepsilon' - j\varepsilon''\right)\mathbf{E} = \mathbf{J}_i + \left(\sigma_s + \omega\varepsilon''\right)\mathbf{E} + j\varepsilon'\omega\mathbf{E} \\ &= \mathbf{J}_i + j\omega\left(\varepsilon' - j\varepsilon'' - j\frac{\sigma_s}{\omega}\right)\mathbf{E} = \mathbf{J}_i + j\omega\varepsilon_e\ \mathbf{E}\end{aligned} \tag{1.74}$$

where σ_s is static conductivity and

$$\varepsilon_e = \varepsilon' - j\left(\varepsilon'' + \frac{\sigma_s}{\omega}\right) = \varepsilon'_e - j\varepsilon''_e \tag{1.75}$$

presents the complex effective permittivity. Consequently, the relative complex permittivity, ε_r, and the relative complex effective permittivity, ε_{er}, in turn are defined as:

$$\varepsilon_r = \frac{\varepsilon}{\varepsilon_0} = \frac{\varepsilon'}{\varepsilon_0} - j\frac{\varepsilon''}{\varepsilon_0} = \varepsilon'_r - j\varepsilon''_r \tag{1.76}$$

$$\varepsilon_{er} = \frac{\varepsilon_e}{\varepsilon_0} = \frac{\varepsilon'}{\varepsilon_0} - j\left(\frac{\varepsilon''}{\varepsilon_0} + \frac{\sigma_s}{\omega\varepsilon_0}\right) = \varepsilon'_{er} - j\varepsilon''_{er} \tag{1.77}$$

and the effective conductivity is given by:

$$\sigma_e = \sigma_s + \omega\varepsilon'' \tag{1.78}$$

Note that real part of permittivity is associated with the stored energy when the materiel is exposed to electromagnetic field, and the imaginary part is associated with the energy loss in material. The absorption attenuation of materials commonly is described by the loss tangent quantity which is defined as the ratio between imaginary and real part of effective complex permittivity:

$$tan\delta = \frac{\varepsilon''_e}{\varepsilon'_e} = \frac{\varepsilon'' + \frac{\sigma_s}{\omega}}{\varepsilon'} = \frac{\varepsilon''}{\varepsilon'} + \frac{\sigma_s}{\omega\varepsilon'} = tan\delta_p + tan\delta_c \tag{1.79}$$

where $tan\delta_p$ and $tan\delta_c$ specify polarization and conductivity contribution in loss tangent, respectively. Materials are classified as low loss (good dielectrics) and high loss (good conductors) according to the values of $tan\delta = \sigma_e/\omega\varepsilon'$. In practice, a material can be considered low loss if $tan\delta << 1$ and high loss if $tan\delta >> 1$ (e,g., [146]).

1.5.5 Debye Relaxation and Cole-Cole Model

Relaxation is the phenomenon associated with non-instantaneous polarization response of a material to the applied electric field, and relaxation time is the time delay between the dielectric polarization of a material and the applied electric field . In real world, no material is free of dielectric losses, and therefore,

no material is free of absorption and dispersion [1]. In other words, there is no material having frequency-independent permittivity $\varepsilon(\omega) = \varepsilon'(\omega) - j\varepsilon''(\omega)$. The dispersion is intrinsic property of permittivity of all dielectric material. There are several relations that compute the real and imaginary parts of the complex permittivity for many materials as a function of frequency. Among many, the well-known Debye model can be used to describe the spectral behavior of a wide range of geomaterials (up to GHz frequencies). Debye equation with only one relaxation time is expressed by (e.g., [55]):

$$\varepsilon_e(\omega) = \varepsilon'_e(\omega) - j\varepsilon''_e(\omega) \tag{1.80}$$

$$\varepsilon'_e(\omega) = \varepsilon'(\omega) = \varepsilon_\infty + \frac{\varepsilon_s - \varepsilon_\infty}{1 + (\omega\tau_0)^2} \tag{1.81}$$

$$\varepsilon''_e(\omega) = \varepsilon''(\omega) + \frac{\sigma_s}{\omega} = \frac{(\varepsilon_s - \varepsilon_\infty)\ \omega\tau_0}{1 + (\omega\tau_0)^2} + \frac{\sigma_s}{\omega} \tag{1.82}$$

and the effective conductivity is given as:

$$\sigma_e = \sigma_s + \frac{(\sigma_\infty - \sigma_s)\,\omega^2}{\omega^2 + \omega_{rel}^2} \tag{1.83}$$

where ε_s and ε_∞ are the permittivity value at zero frequency (static permittivity) and infinity (very large) frequencies, respectively, and $\tau_0 = 1/\omega_{rel}$ is relaxation time, and σ_∞ is conductivity at very high frequency and is expressed as:

$$\sigma_\infty = \sigma_s + (\varepsilon_s - \varepsilon_\infty)\,\omega_{rel} \tag{1.84}$$

Debye equations are satisfactory only if $\varepsilon_s - \varepsilon_\infty < 1$. The relations of (1.81) and (1.82) can be used to estimate the real and imaginary parts of the complex permittivity for many materials including gases, liquids, and solids. Assuming that the static conductivity is negligible, $\sigma_s \approx 0$, the maximum of ε''_e is given by:

$$\frac{d\varepsilon''_e(\omega)}{d\omega} = 0 \Rightarrow \omega_0\tau_0 = 1 \tag{1.85}$$

at this frequency the components of permittivity is obtained as:

$$\varepsilon'_e\ |_{\omega=\omega_0} = \frac{\varepsilon_s + \varepsilon_\infty}{2} \tag{1.86}$$

$$\varepsilon''_{e_{max}} = \varepsilon''_e\ |_{\omega=\omega_0} = \frac{\varepsilon_s - \varepsilon_\infty}{2} \tag{1.87}$$

Similarly, the maximum value of loss tangent, $\tan\delta = \frac{\varepsilon''_e(\omega)}{\varepsilon'_e(\omega)}$, occurs at

$$\omega_\delta\tau_0 = (\frac{\varepsilon_s}{\varepsilon_\infty})^{1/2} > 1 \tag{1.88}$$

and

$$\tan\delta_{max} = \tan\delta\ |_{\omega=\omega_\delta} = \frac{\varepsilon_s - \varepsilon_\infty}{(\varepsilon_s\varepsilon_\infty)^{1/2}} \tag{1.89}$$

Figure (1.5) qualitatively presents the $\varepsilon'_e(\omega)$, $\varepsilon''_e(\omega)$ and $tan\delta(\omega)$ as functions of frequency, assuming that $\sigma_s \approx 0$. At high frequencies (i.e., $\omega \gg \omega_{rel}$) the effective conductivity approaches σ_∞. The combination of equations (1.81) and (1.82) yields a circle that is expressed as:

$$\left(\varepsilon' - \frac{\varepsilon_s + \varepsilon_\infty}{2}\right)^2 + \varepsilon''^2 = \left(\frac{\varepsilon_s - \varepsilon_\infty}{2}\right)^2 \tag{1.90}$$

Note that, only the positive part of the circle has physical meaning, as displayed in Figure (1.6).

[1] Dispersion is dependence of complex permittivity and permeability and thus the wave velocity on frequency.

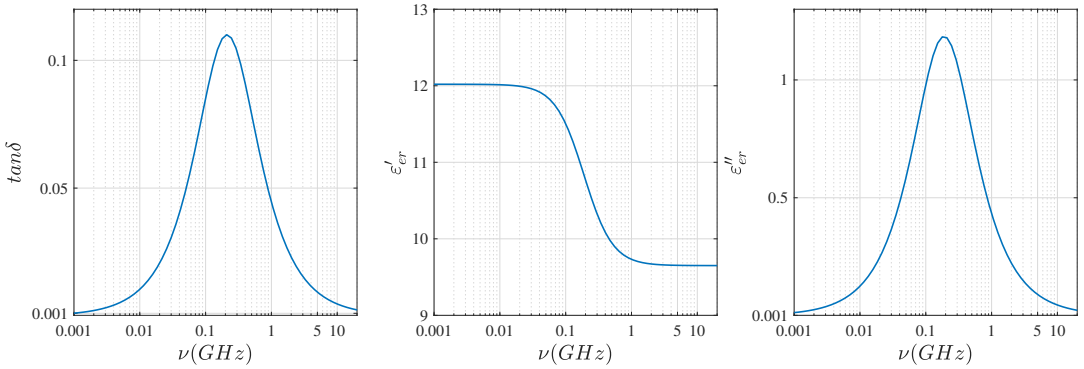

Figure 1.5: Variation of $\varepsilon_e'(\omega)$, $\varepsilon_e''(\omega)$ and $tan\delta$ as functions of frequency with negligible contribution of static conductivity, σ_s [55].

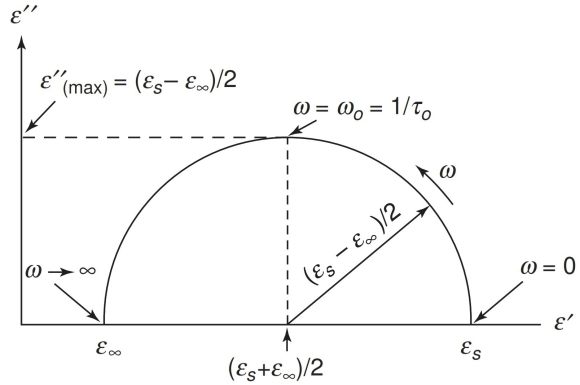

Figure 1.6: Argand diagram for cases with only one relaxation time. σ_s, is negligible.

If the effect of static conductivity, σ_s, is not negligible:
Case I: $\omega\tau_0 \ll 1$

$$\varepsilon_e'' = \frac{\sigma_s}{\omega}, \quad tan\delta = \frac{\sigma_s}{\omega\varepsilon_s} \tag{1.91}$$

Case II: $\omega\tau_0 \approx 1$

$$\begin{aligned} \varepsilon_e'' &= \frac{\varepsilon_s - \varepsilon_\infty}{2} + \sigma_s\tau_0 \\ tan\delta &= \frac{\varepsilon_s - \varepsilon_\infty + 2\sigma_s\tau_0}{\varepsilon_s + \varepsilon_\infty} \end{aligned} \tag{1.92}$$

Case III: $\omega\tau_0 \gg 1$

$$\begin{aligned} \varepsilon_e'' &= \frac{\varepsilon_s - \varepsilon_\infty}{\omega\tau_0} \\ tan\delta &= \frac{\varepsilon_s - \varepsilon_\infty + \sigma_s\tau_0}{\omega\tau_0\varepsilon_\infty} \end{aligned} \tag{1.93}$$

The variations of ε_e'' and $tan\delta$ with ω considering the contribution of non negligible σ_s are shown in Figure (1.7), (also see Chapter 4). In geophysics, knowledge of the relationship between loss tangent, frequency, and temperature is important and are briefly discussed in the following sections.

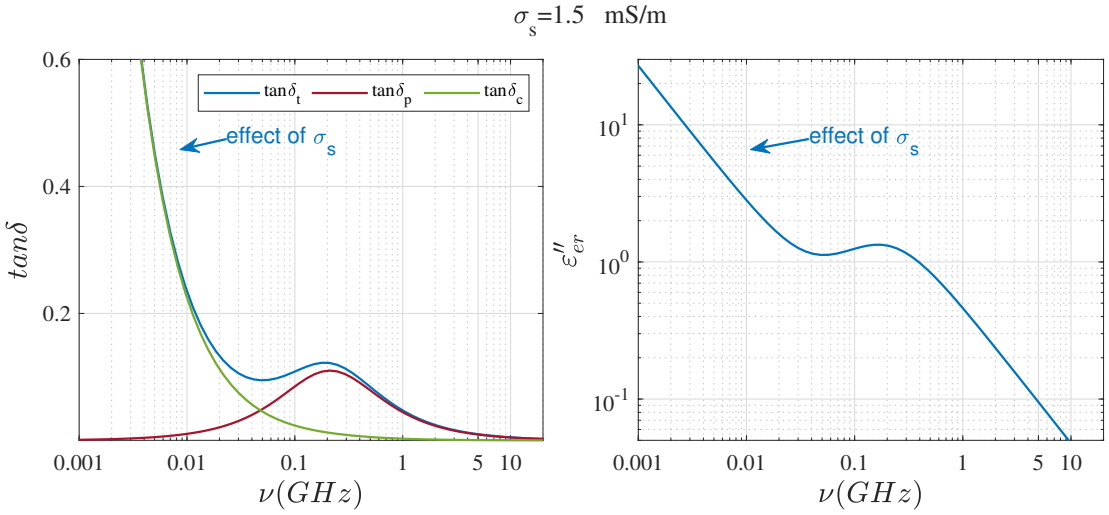

Figure 1.7: Variation of $\varepsilon''(\omega)$ and $tan\delta$ as functions of frequency with contribution of non-negligible σ_s.

Discussion: Dielectric loss and Frequency Dependence

The nature of intrinsic loss dependence on frequency is primarily determined by the fact that dielectric loss is caused by conduction currents or polarization processes.

For dielectric loss due to relaxation phenomena $tan\delta$ has the following characteristics (see Figure 1.5): at low frequencies, the value of ε' remains constant so long as there is time during a half-cycle of the applied field for the polarization process to be completed. At frequencies near $1/\tau_0$ the relative permittivity exhibits dispersion because a phase shift between polarization and the driving field, which is frequency dependent, is found. At very high frequencies, when slow polarization processes do not have time to develop significantly during a half-cycle, the value of ε' is constant.

In cases in which there is little conductivity in dielectric material, and in addition, a relaxation process is well developed, the behavior of $tan\delta$ as a function of frequency is as follows (see Figure 1.7): at low frequencies, conduction dominates over relaxation processes, and $tan\delta$ decreases with increasing frequency. As frequency increases further, relaxation processes become relatively more important and $tan\delta$ increases until the period of the driving field becomes equal to the relaxation time for the process.

Dielectric Properties and Temperature Dependence

Complex permittivity is a complex function of both frequency and temperature, apart from the dependence on other parameters such as pressure, etc. Temperature dependence of ε' and ε'' is mainly through the temperature dependence of the relaxation time which for a single relaxation time is expressed as (e.g., [55]):

$$\tau_{rel}(T) = \tau_h \, e^{\frac{H}{kT}} \Rightarrow \omega_{rel}(T) = \omega_h \, e^{-\frac{H}{kT}} \tag{1.94}$$

where τ_h is pre-exponential factor, and H is the activation energy, k is Boltzmann constant, and T is temperature in Kelvin. The activation energy, H, represents an energy barrier that must be overcome in order for the charges to fully separate or for the dipole moments alignment. As temperature increases, the charges have more energy, thus making it easier to overcome this energy barrier. Therefore, as temperature increases, the time constant of relaxation shifts to a smaller period and relaxation frequency increases. As shown in Figure (1.8), for increasing temperatures, $\varepsilon'(\omega, T)$ decreases and the peak of $\varepsilon''(\omega, T)$ shifts toward higher frequencies.

By replacing τ_0 with $\tau_{rel}(T)$ in Debye equations the complex permittivity will be written as:

$$\varepsilon'(\omega, T) = \varepsilon_\infty^T + \frac{\varepsilon_s^T - \varepsilon_\infty^T}{1 + \omega^2 \tau_h^2 e^{\frac{2H}{kT}}} \tag{1.95}$$

$$\varepsilon''(\omega, T) = \frac{\left(\varepsilon_s^T - \varepsilon_\infty^T\right) \omega \tau_h e^{\frac{H}{kT}}}{1 + \omega^2 \tau_h^2 e^{\frac{2H}{kT}}} \tag{1.96}$$

where ε_s^T and ε_∞^T are the values of ε_s and ε_∞ at temperature T. The difference between low and high frequency limit permittivity is also temperature dependent and is given by:

$$\varepsilon_s - \varepsilon_\infty = \frac{A}{T} \tag{1.97}$$

where A is a constant. Consequently, dielectric loss is affected significantly by changes in temperature. The manner of change depends on the nature of loss mechanism. If relaxation processes is weak, the relationship between $tan\delta$ and temperature is exponential because conduction loss plays the primary role in such materials. Considering

$$\varepsilon'' \approx 0; \qquad \sigma(T) = \sigma_0 \; e^{-H/kT} \tag{1.98}$$

we obtain:

$$tan\delta = \frac{\sigma_0}{\omega\varepsilon'} \; e^{-H/kT} \tag{1.99}$$

that shows the $tan\delta$ increases by temperature. If the free conduction in a material is slight and relaxation polarization is present, a maximum loss tangent as a function of temperature is observed at that temperature (T_{max} in Figure 1.9) at which the relaxation time is close to a half-period of the applied electric field. For temperatures which cause the relaxation time to be greater than or less than the half-period of the applied field, the loss is less.

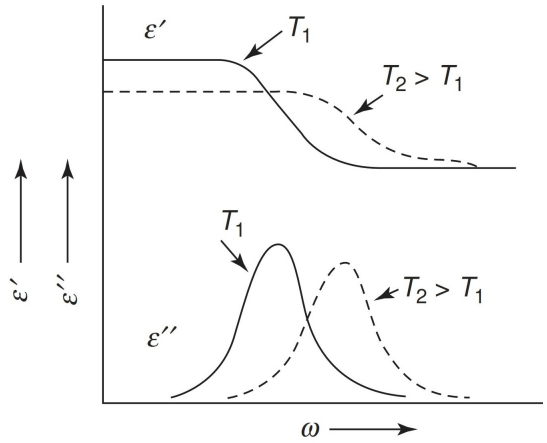

Figure 1.8: Effect of the temperature on the dielectric behavior of a generic material. For increasing temperatures the real part of permittivity decreases, and the peak of imaginary part shifts toward higher frequencies [55].

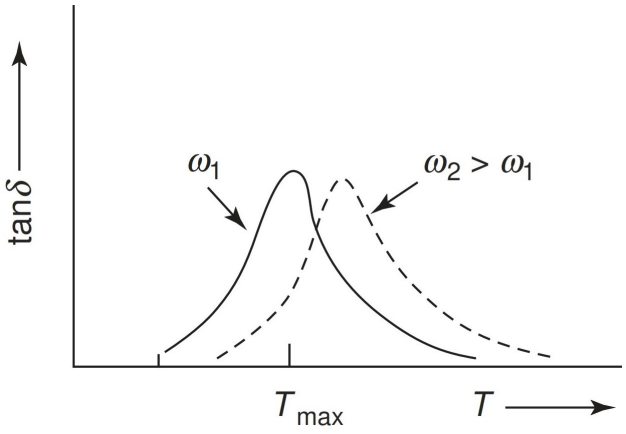

Figure 1.9: $\tan\delta$ as a function of temperature for fixed frequencies ω_1 and ω_2 where $\omega_2 > \omega_1$ [55].

Cole-Cole Model

Debye equation based on a single relaxation time is a good approximation for pure polar liquids, however, it is inappropriate for most of dielectric materials, e.g., polymers and hydrocarbons. In this case, a distribution of relaxation time is necessary to describe the permittivity. Cole and Cole [20] proposed an empirical formula that often successfully describes the permittivity behavior of natural liquids, solids and heterogeneous mixtures. The Cole-Cole complex permittivity is given by:

$$\varepsilon_e(\omega) = \varepsilon_\infty + \frac{\varepsilon_s - \varepsilon_\infty}{1 + (j\omega\tau_0)^{1-\alpha}} - j\frac{\sigma_s}{\omega} \tag{1.100}$$

where α is broadening factor with $0 < \alpha < 1$. All equations are still valid if τ_0 is replaced with τ, expressed by:

$$\tau = \tau_0 \frac{\varepsilon_s + 2}{\varepsilon_\infty + 2} \tag{1.101}$$

1.6 Mixing Formula

The mixing formula are used to obtain the effective permittivity of a mixture of two or more materials with different permittivity. Figure (1.10) presents a simple example of a dielectric environment with the permittivity of ε_e in which many spheres of radius a and the permittivity of ε_i are embedded. If the dimension a is comparable to or greater than a wavelength, substantial scattering can take place. Also, if the occupied fraction of the volume by the spheres, f, is a few percent or higher, a correlation between the spheres needs to be considered. Assuming that dimensions of the spheres are much smaller than a wavelength, and the spheres are sparsely distributed, the Maxwell–Garnett mixing to compute the effective permittivity is expressed by *e.g.*, [127], [128]:

$$\varepsilon_{eff} = \varepsilon_{en} + 3f\ \varepsilon_{en} \frac{\varepsilon_i - \varepsilon_{en}}{\varepsilon_i + 2\varepsilon_{en} - f(\varepsilon_i - \varepsilon_{en})} \tag{1.102}$$

where f is a dimensionless quantity, the volume fraction of inclusions in mixture. This formula is in wide use in very diverse fields of application.

Polder–Van Santen formula is the other important mixing formula. The basic form of this formula for spherical scatterers is:

$$(1-f)\frac{\varepsilon_{en} - \varepsilon_{eff}}{\varepsilon_{en} + 2\varepsilon_{eff}} + f\frac{\varepsilon_i - \varepsilon_{eff}}{\varepsilon_i + 2\varepsilon_{eff}} = 0 \tag{1.103}$$

Polder-van Santen mixing formula is symmetric and Maxwell–Garnett formula is asymmetric. The Polder–van Santen formula can be extended to many species each with ε_i and fi:

$$\sum_{i=1}^{N} \frac{\varepsilon_i - 1}{\varepsilon_i + 2\varepsilon_{en}} f_i = \frac{\varepsilon_i - 1}{3\varepsilon_{en}} \tag{1.104}$$

where $\sum_{i=1}^{N} f_i = 1$. Note that these mixing formulas above are for low-frequency cases where the scattering is negligible. More exact formulas, including scattering and correlations between particles, must be obtained by considering the propagation constant of the coherent wave [52].

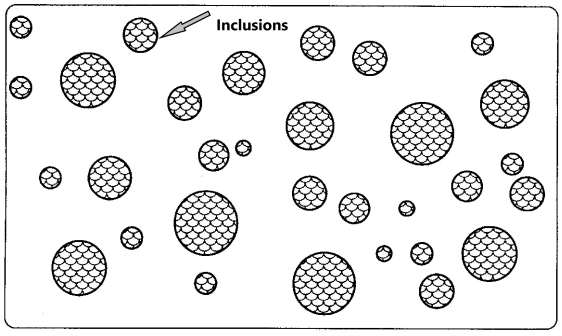

Figure 1.10: A mixture of two materials.

1.7 Electrical Property of Water, Ice and Rocks

This section provides forward formulas for computing the complex relative permittivity of pure water, pure water ice, and wet and dust ice.

1.7.1 Electrical Property of Water

Subsurface environments are commonly mixture of various materials *e.g.*, water, ice, soil grain, ions, vacuum (hence porosity), etc, each with different properties and percentage. Among them, water is the most natural polarizable material with high relative permittivity of ~ 80. In addition, water content contains ions, causing electrical conductivity associated with ions movement. Since, the pore space of natural occurring soils and rock can be filled by water, the water absence or presence is a dominant factor determining the electrical properties of investigated medium. In the absence of liquid water, the real part of the permittivity is approximately constant for the most geological materials over the radar frequency range (e.g., [2].)

Pure Water

Pure water is a poor electrical conductor and behaves as a polarizable material until frequencies exceed 10 GHz. Typically, in this range of frequency the water-molecule dipole-moment cannot instantly rotate to align with the applied electric field. This phenomenon which is referred to as a natural relaxation process causes energy dissipation in the material. If water is subjected to an alternating electric field, as the frequency increases into the relaxation frequency range, the water molecule dipole moment cannot instantly rotate to align with the applied electric field. This phenomenon causes energy dissipation in the form of heat, through reduction of real component of permittivity and increase of its imaginary part (see, Figure 1.5) [1]. The complex relative permittivity of pure water ice can be described by [74]:

$$\begin{aligned}
\varepsilon_{r_{pw}} &= \varepsilon'_{r_{pw}} - j\varepsilon''_{r_{pw}} \\
\varepsilon'_{r_{pw}} &= \varepsilon_\infty + \frac{\varepsilon_s - \varepsilon_1}{1 + \left(\frac{\nu_{GHz}}{\nu_1}\right)^2} + \frac{\varepsilon_1 - \varepsilon_\infty}{1 + \left(\frac{\nu_{GHz}}{\nu_2}\right)^2} \\
\varepsilon''_{r_{pw}} &= \frac{\left(\frac{\nu_{GHz}}{\nu_1}\right)(\varepsilon_s - \varepsilon_1)}{1 + \left(\frac{\nu_{GHz}}{\nu_1}\right)^2} + \frac{\left(\frac{\nu_{GHz}}{\nu_2}\right)(\varepsilon_1 - \varepsilon_\infty)}{1 + \left(\frac{\nu_{GHz}}{\nu_2}\right)^2}
\end{aligned} \tag{1.105}$$

where

$$\begin{aligned}
\varepsilon_s &= 77.66 + 103.3\Theta \\
\varepsilon_1 &= 0.0671\varepsilon_s \\
\varepsilon_\infty &= 3.52 - 7.52\Theta \\
\nu_1 &= 20.20 - 146.4\Theta + 316\Theta^2 \\
\nu_2 &= 39.8\nu_1 \\
\Theta &= \frac{1}{T} - 1
\end{aligned} \tag{1.106}$$

Note that ν_{GHz} is frequency in gigahertz and, T is temperature in Kelvin. Variation of real and imaginary parts of pure water relative permittivity versus frequency at $T = 280,\ 340\ ^oK$ is depicted in Figure (1.11). Losses start to have a significant effect for the frequencies higher than $500MHz$. Figure (1.12) presents complex relative permittivity of pure water as a function of temperature at $\nu = 5,\ 500\ MHz$. Temperature increase lead to decrease of loss, and the real part of permititvity behaves independent of frequency by variation of temperature .

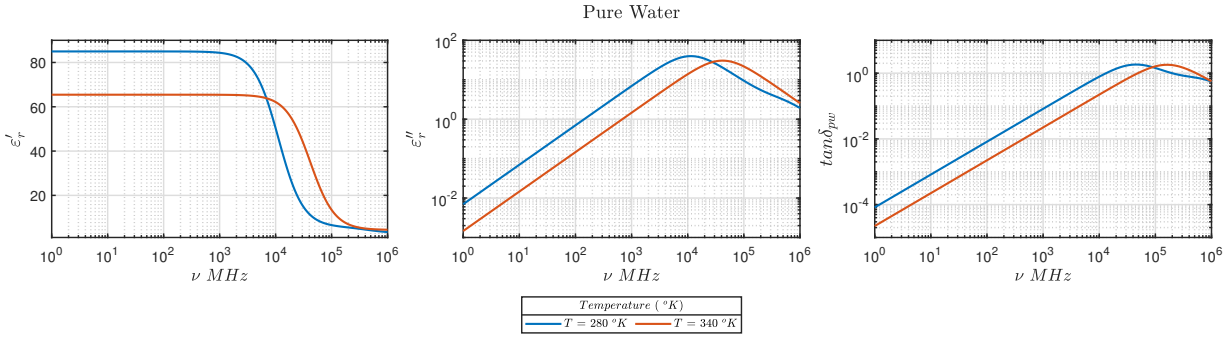

Figure 1.11: Pure water properties. Complex relative permittivity of pure water as a function of frequency at $T = 280,\ 340\ ^oK$.

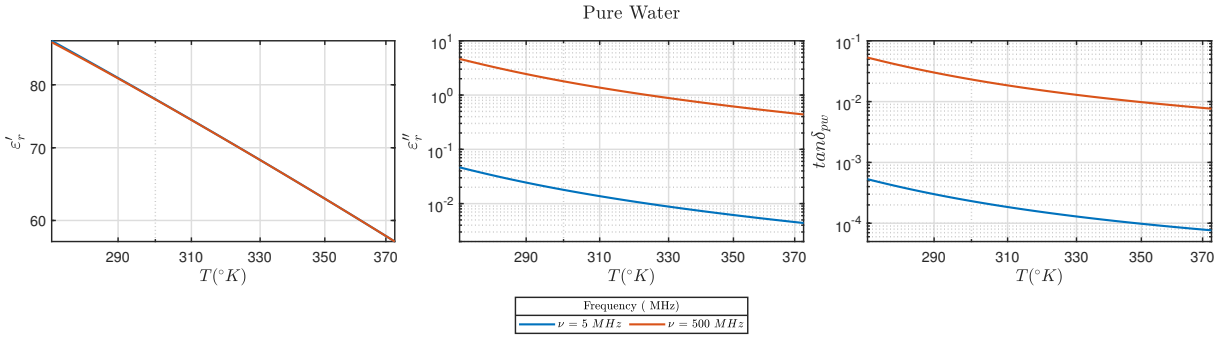

Figure 1.12: Pure water properties. Complex relative permittivity of pure water as a function of temperature at $\nu = 5,\ 500\ MHz$.

Saline Water

The complex relative permittivity of saline water, $\varepsilon_{r_{sw}}$, is a function of frequency, temperature and salinity, $S\ (g/kg)$, [85]:

$$\begin{aligned}
\varepsilon_{r_{sw}} &= \varepsilon'_{r_{sw}} - j\varepsilon''_{r_{sw}} \\
\varepsilon'_{r_{sw}} &= \varepsilon_\infty + \frac{\varepsilon_{ss} - \varepsilon_{1s}}{1 + \left(\frac{\nu_{GHz}}{\nu_{1s}}\right)^2} + \frac{\varepsilon_{1s} - \varepsilon_{\infty s}}{1 + \left(\frac{\nu_{GHz}}{\nu_{2s}}\right)^2} \\
\varepsilon''_{r_{sw}} &= \frac{\left(\frac{\nu_{GHz}}{\nu_{1s}}\right)(\varepsilon_{ss} - \varepsilon_{1s})}{1 + \left(\frac{\nu_{GHz}}{\nu_{1s}}\right)^2} + \frac{\left(\frac{\nu_{GHz}}{\nu_{2s}}\right)(\varepsilon_{1s} - \varepsilon_{\infty s})}{1 + \left(\frac{\nu_{GHz}}{\nu_{2s}}\right)^2} + \frac{18\sigma_{sw}}{\nu_{GHz}}
\end{aligned} \tag{1.107}$$

where

$$\begin{aligned}
\varepsilon_{ss} &= \varepsilon_s\ \exp\left(-3.56417 \times 10^{-3} S + 4.74868 \times 10^{-6} S^2 + 1.15574 \times 10^{-5} TS\right) \\
\nu_{1s} &= \nu_1 \left[1 + S\left(2.39357 \times 10^{-3} - 3.13530 \times 10^{-5} T + 2.52477 \times 10^{-7} T^2\right)\right] s \\
\varepsilon_{1s} &= \varepsilon_1\ \exp\left(-6.28908 \times 10^{-3} S + 1.76032 \times 10^{-4} S^2 + -9.22144 \times 10^{-5} TS\right) \\
\nu_{2s} &= \nu_2 \left[1 + S\left(-1.99723 \times 10^{-2} + 1.81176 \times 10^{-4} T\right)\right] \\
\varepsilon_{\infty s} &= \varepsilon_\infty \left[1 + S\left(-2.04265 \times 10^{-3} + 1.57883 \times 10^{-4} T\right)\right]
\end{aligned} \tag{1.108}$$

the parameters ε_∞, ε_1, ε_s, ν_1 and ν_2 are obtained from equation (1.106). Note that in equation (1.108) T indicates temperature in ^oC with the modification of $\Theta = \frac{1}{T+273.15} - 1$.

$$
\begin{aligned}
&\sigma_{sw} = \sigma_{35} R_{15} R_{T15} \\
&\sigma_{35} = 2.903602 + 8.607 \times 10^{-2} T + 4.738817 \times 10^{-4} T^2 - 2.991 \times 10^{-6} T^3 + 4.30747 \times 10^{-9} T^4 \\
&R_{15} = S \frac{37.5109 + 5.45216 S + 1.4409 \times 10^{-2}\ S^2}{1004.75 + 182.283\ S + S^2} \\
&R_{T15} = 1 + \frac{\alpha_0\,(T-15)}{\alpha_1 + T} \\
&\alpha_0 = \frac{6.9431 + 3.2841\ S - 9.9486 \times 10^{-2}\ S^2}{84.850 + 69.024\ S + S^2} \\
&\alpha_1 = 49.843 - 0.2276\ S + 0.198 \times 10^{-2}\ S^2
\end{aligned}
\tag{1.109}
$$

Figure (1.13) presents real and imaginary part of the relative permittivity and loss tangent for saline water as a function of frequency for various values of salinity S at the temperature 240 and 300 ^oK, and Figure (1.14) presents real and imaginary part of the relative permittivity and loss tangent for saline water as a function of temperature for various values of salinity S at frequency $\nu = 5\ MHz$ and $\nu = 5\ GHz$. In addition, Figure (1.15) shows the variation of static conductivity of saline water, σ_{sw}, versus temperature for various salinity. Both quantities have prominent effect on conductivity. By increasing salinity and temperature, conductivity increases.

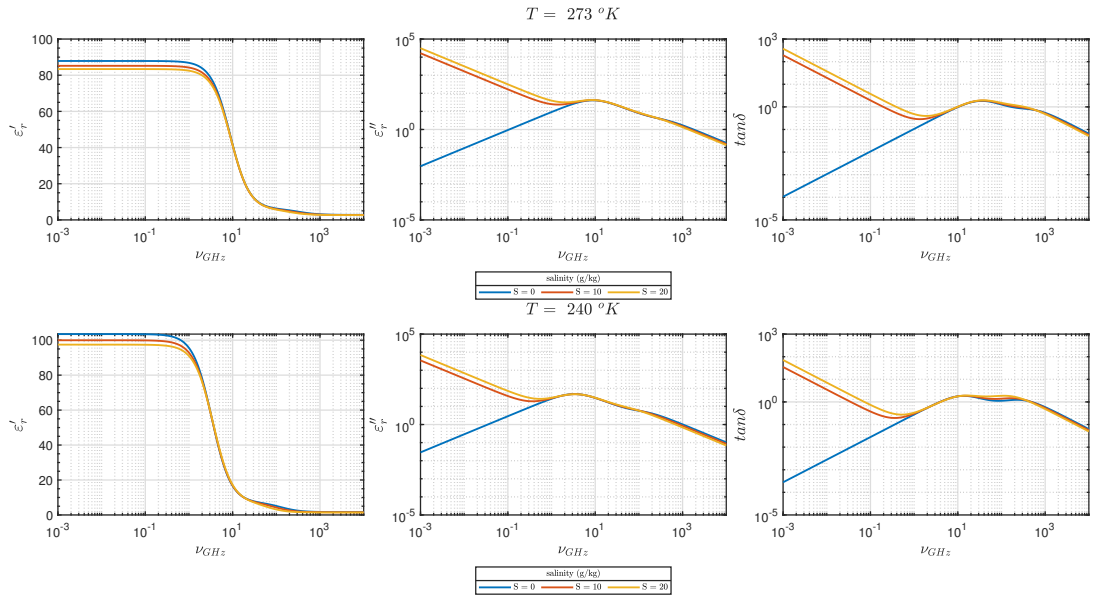

Figure 1.13: Complex relative permittivity of saline water as a function of frequency at $T = 273$ and $T = 240$ ^oK.

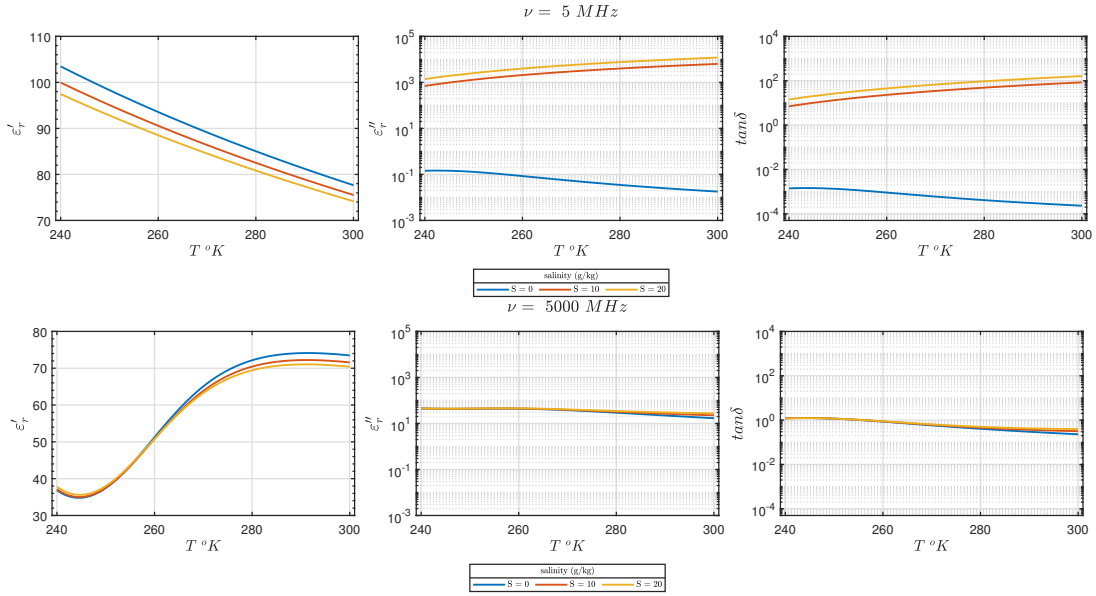

Figure 1.14: Complex relative permittivity of saline water as a function of temperature at $\nu = 5\ MHz$ and $\nu = 5\ GHz$.

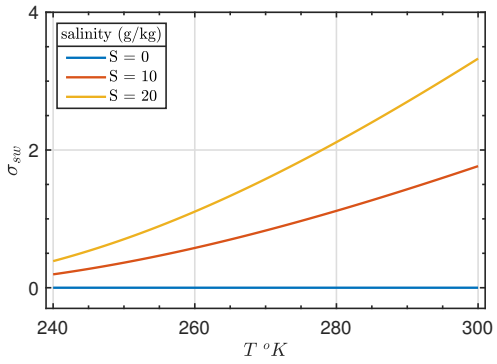

Figure 1.15: Variation of saline water conductivity by temperature for various values of salinity.

1.7.2 Electrical Property of Ice

The polar ice sheets and glacier ice contain the majority of the terrestrial water ice mass. These icy bodies possess spectral and polarimetric signatures in the microwave range which are suitable for both active (radar) and passive (radiometric) remote sensing. The signatures are related to the special dielectric properties and characteristic structural behavior, as well, ranging from microscopic to macroscopic scale.

Pure Water Ice

pure water ice is composed of frozen pure water. In literature, pure water ice has been studied in the laboratory over a wide range of temperatures and frequencies, even though not all frequency bands have been uniformly explored [104]. In general, measurements confirm that the dielectric behavior of pure water ice follows the Debye model at relatively high temperatures (above 230 K), as displayed in Figure (1.16).

In particular, the different experimental procedures employed to form and grow ice, including sample history and aging, can introduce microscopic and macroscopic differences, such as specific crystal orientations, dislocations, cracks and fractures, gas bubbles and inclusions, chemical impurities, and vacancies and other lattice imperfections. Moreover, the ice growth process and the cooling procedure can affect, often in a non-controllable way, the ice/electrode contact (introducing gaps of air or cracks), as

the materials have different thermal expansion coefficients. All these aspects can significantly modify the characteristic Debye behavior expected for pure water ice, as they can introduce additional relaxations, shorten the relaxation time and widen the characteristic bell-shaped curve ([104] and the references therein).

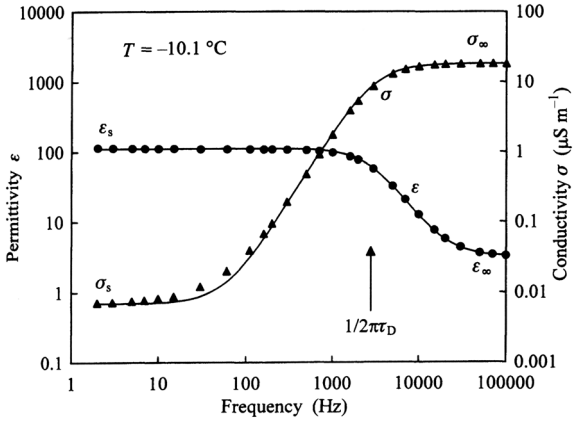

Figure 1.16: Real part of permittivity and conductivity as a function of frequency (2 Hz–100 kHz) for a single crystal of pure water ice measured at 263 K ([137] modified by [102].

Considering that relative complex permittivity of pure water ice is expressed by:

$$\varepsilon_{r_{ice}} = \varepsilon'_{r_{ice}} - j\varepsilon''_{r_{ice}} \tag{1.110}$$

where the real part $\varepsilon'_{r_{ice}}$ describes the dispersion or phase delay during propagation of an electromagnetic wave in the medium, and in addition, it is responsible for refraction and impedance variation at the transition between free space and the medium. Therefore, spatial variations of $\varepsilon'_{r_{ice}}$ produce distortions in wave propagation, and thus all types of scattering. The $\varepsilon'_{r_{ice}}$ is independent of frequency from 1 MHz to about 1000 GHz and only slightly depends on temperature [see Figure (1.17), (1.18)], the maximum of 3.19 being found at 273 K with the following linear dependence on $T > 240$ K, [83]:

$$\varepsilon'_{r_{ice}} = 3.1884 + 0.00091\,(T - 273) \tag{1.111}$$

where T is temperature in Kelvin. In principle $\varepsilon'_{r_{ice}}$ depends on ionic and other impurities present in the ice. Contrarily, the measurement of imaginary part of pure water ice, that is responsible for wave absorption, in this frequency range is challenging due to the sensitivity limit of the instruments, especially at low temperatures. Several authors have attempted to estimate the dissipative behavior of pure water ice in the MHz – GHz range by interpolating low-frequency and microwave data (e.g.,[49], [83], [36]): The imaginary part in the frequency range from 10 KHz up to 1 GHz is governed by the high-frequency tail of the Debye relaxation. The low-frequency tail is a term proportional to frequency, ν. Hufford, 1991, [49] from a critical analysis of published data explains $\varepsilon''_{r_{ice}}$ from 100 KHz to 1 THz by the two terms as:

$$\varepsilon''_{r_{ice}} = \frac{A_1}{\nu_{GHz}} + A_2\ \nu_{GHz} \tag{1.112}$$

where the first term accounts for the right-tail of Debye relaxation and the second term is due to the lattice vibration resonance in the far-infrared region, ν_{GHz} is frequency in GHz and the parameters A_1 and A_2 are defined by[82]:

$$\begin{aligned}
A_1 &= (0.00504 + 0.0062\ \Theta)\exp(-22.1\ \Theta) \quad (GHz)\\
A_2 &= \frac{0.0207}{T}\frac{\exp(335/T)}{[\exp(335/T)-1]^2} + 1.16\times10^{-11}\ \nu^2_{GHz} + \exp\left[-10.02 + 0.0364\ (T-273)\right] \quad (GHz^{-1})\\
\Theta &= \frac{300}{T} - 1
\end{aligned} \tag{1.113}$$

The real and imaginary parts of complex relative permittivity, and loss tangent of dry ice versus frequency for $T = 170,\ 200\ ^oK$ are shown in Figure (1.17). In addition variation of complex relative permittivity of dry ice versus temperature at frequencies 5 and 500 MHz is presented in Figure (1.18). The loss tangent of water ice increases by orders of magnitude with temperature, exponentially affecting the attenuation of the radar wave. Figure (1.18) indicates that cold, pure water ice has a loss tangent that is orders of magnitude below that of other substances, resulting in very little attenuation, and it is thus extremely transparent to radar waves. As ice temperature approaches the melting point, its loss tangent becomes higher than that of rock, thus strongly limiting the penetration of the radar signal.

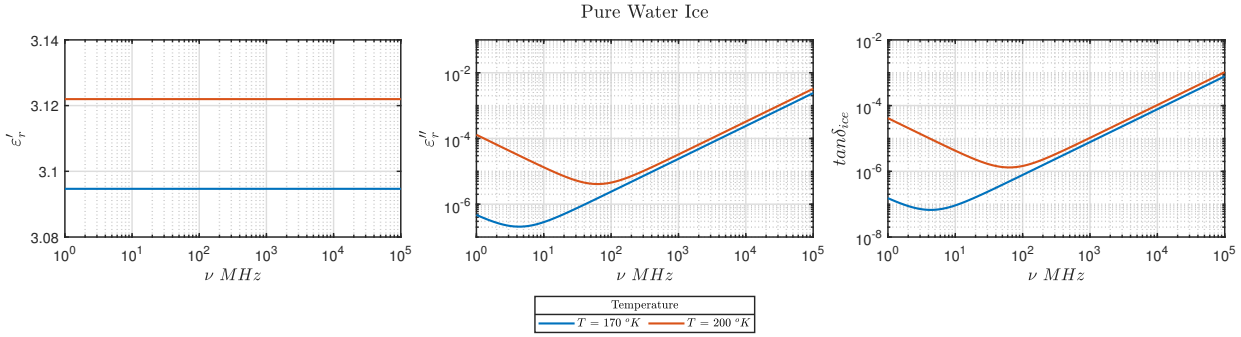

Figure 1.17: Pure water ice properties versus frequency. Real and imaginary part of pure water ice relative complex permittivity as a function of frequency at $T = 170,\ 200\ ^oK$. In very low frequency, $\nu < 10\ MHz$, the ε_{im} and $tan\delta_{ice}$ are almost constant.

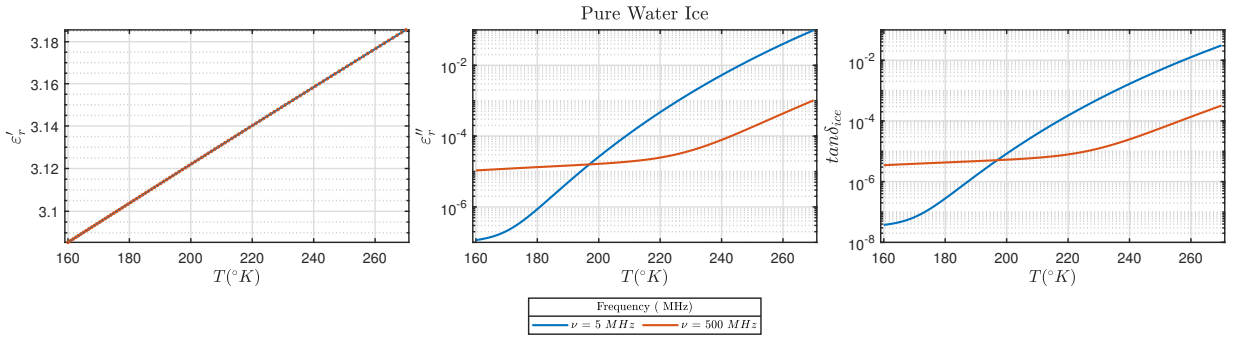

Figure 1.18: Pure water ice properties versus temperature. Real and imaginary part of pure water ice relative complex permittivity as a function of temperature at $\nu = 5,\ 500\ MHz$.

Wet Ice

When the ice is wet (at 273 K), its grains are surrounded by liquid water. Considering ice grains as spherical inclusions within a liquid water background, the Maxwell Garnett dielectric mixing formula is applied to express the complex relative permittivity of wet ice as a combination of the complex relative permittivity of dry ice $\varepsilon_{r_{ice}}$ and pure water ε_{pw}:

$$\varepsilon_{wet_{ice}} = \left[\frac{(\varepsilon_{r_{ice}} + 2\varepsilon_{pw}) + 2\,(\varepsilon_{r_{ice}} - \varepsilon_{pw})\,(1 - fw)}{(\varepsilon_{r_{ice}} + 2\varepsilon_{pw}) - (\varepsilon_{r_{ice}} - \varepsilon_{pw})\,(1 - fw)}\right]\varepsilon_{pw} \tag{1.114}$$

where fw is liquid water volume fraction. The variation of real and imaginary parts of wet ice, and the loss tangent as a function of liquid water content at $\nu = 20\ MHz$ and $T = 273\ K$ is depicted in Figure (1.19). In addition, Figure (1.21) present the same parameters as functions of frequency at $T = 170, 270\ K$ for $f_w = 0.2$.

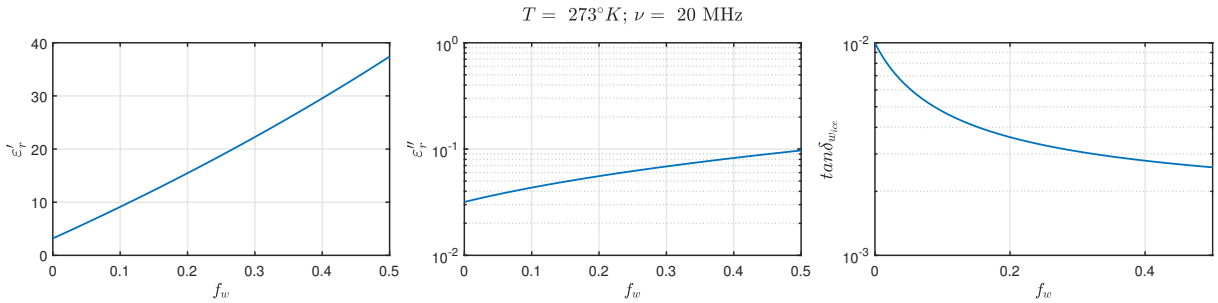

Figure 1.19: Wet ice properties versus water volume fraction. Real and imaginary part of wet ice relative complex permittivity as a function of water volume fraction.

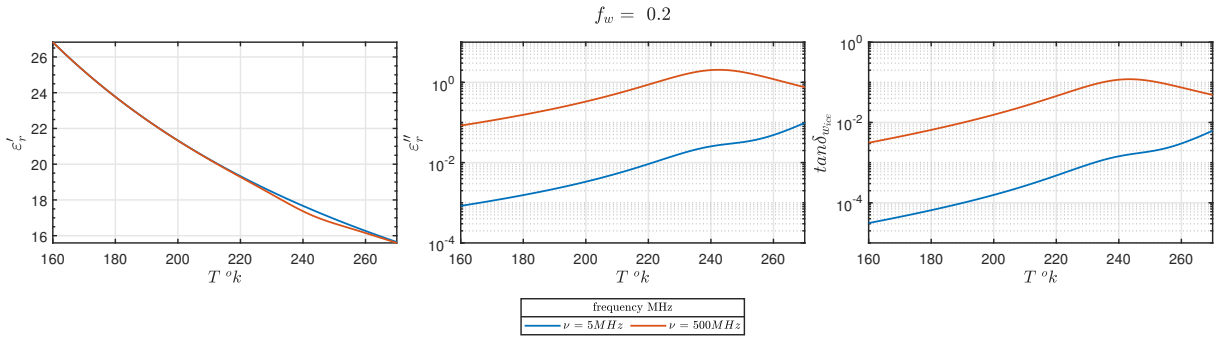

Figure 1.20: Wet ice properties versus temperature. Real and imaginary part of wet ice relative complex permittivity as a function of temperature.

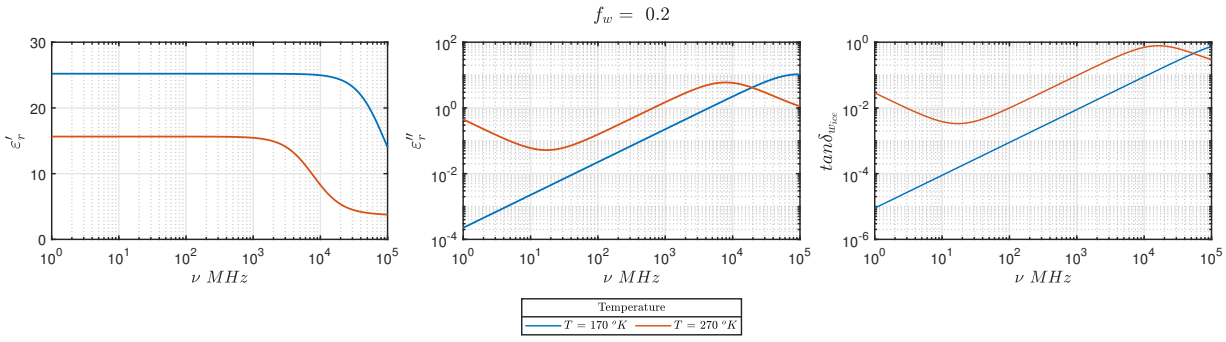

Figure 1.21: Wet ice properties versus frequency. Real and imaginary part of wet ice relative complex permittivity as a function of frequency.

Dusty Ice

The ground ice and ice on the planetary surface can consist of mixture of ice and different inclusions. The effective relative permittivity can be described by various models. For example here the Maxwell Garnett mixing formula (equation (1.102)) is used to investigate the effect of dust on the dielectric properties of the ice-dust mixture. The host medium is considered as pure water ice and the inclusions have a relative complex permittivity of $\varepsilon_{dust} = 8.8 - j0.017$. Figure (1.22) presents the real and imaginary component of effective relative permittivity and loss tangent as functions of temperature for different fractions of dust. The behavior of dusty ice is intermediate between the trends of water ice and dust. The inclusions result in increase of attenuation. It is worth noting that the presence of dust in the water ice also introduces a small variation in the real part of the dielectric permittivity. Variation of dusty ice permittivity with frequency is presented in Figure (1.23). Impurities modify this behavior so that the loss tangent increases and becomes independent of frequency. The temperature effect is prominent.

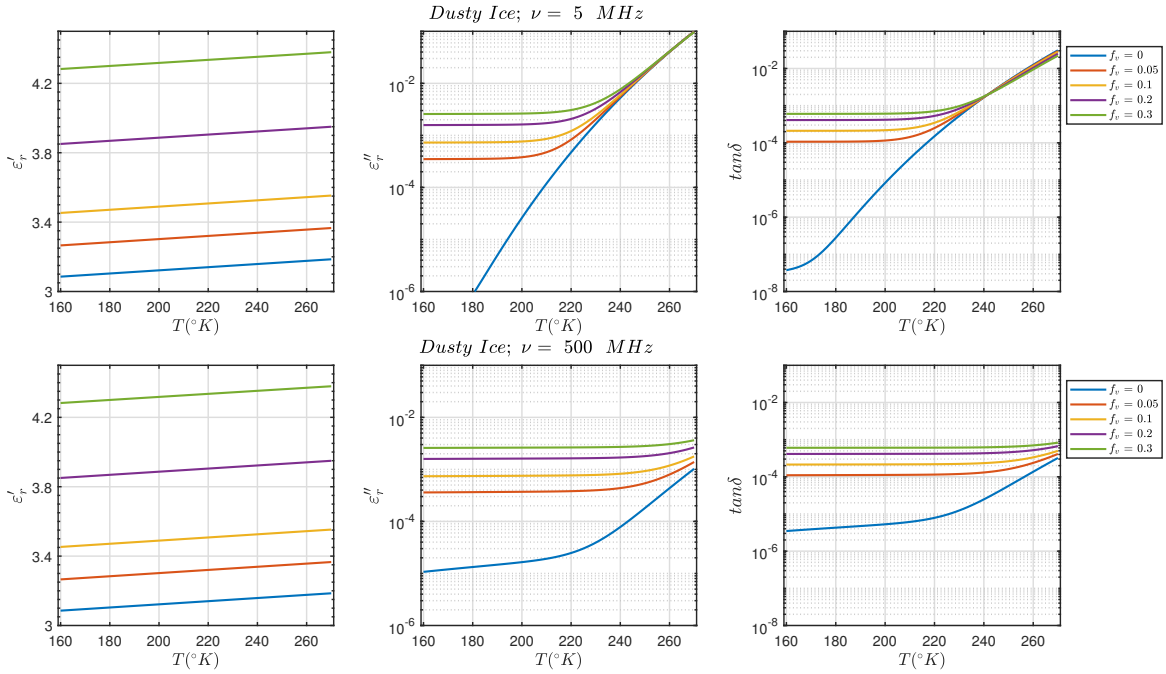

Figure 1.22: Dusty ice properties. Real and imaginary part of dusty ice relative complex permittivity as a function of temperature at $\nu = 5$ and 500 MHz; as a function of frequency at $T = 170,\ 230\ ^oK$. In legend f_v indicates the dust volume fraction and $f_v = 0$ accounts for pure water ice. The attenuation in pure water ice is temperature dependent, however, presence of dust modifies such behavior, so that attenuation of the ice-dust mixture increases and at low temperatures becomes temperature independent. The attenuation in pure water ice at low temperature is negligible. Impurities modify this behavior so that the loss tangent increases and becomes independent of frequency. The temperature effect is prominent.

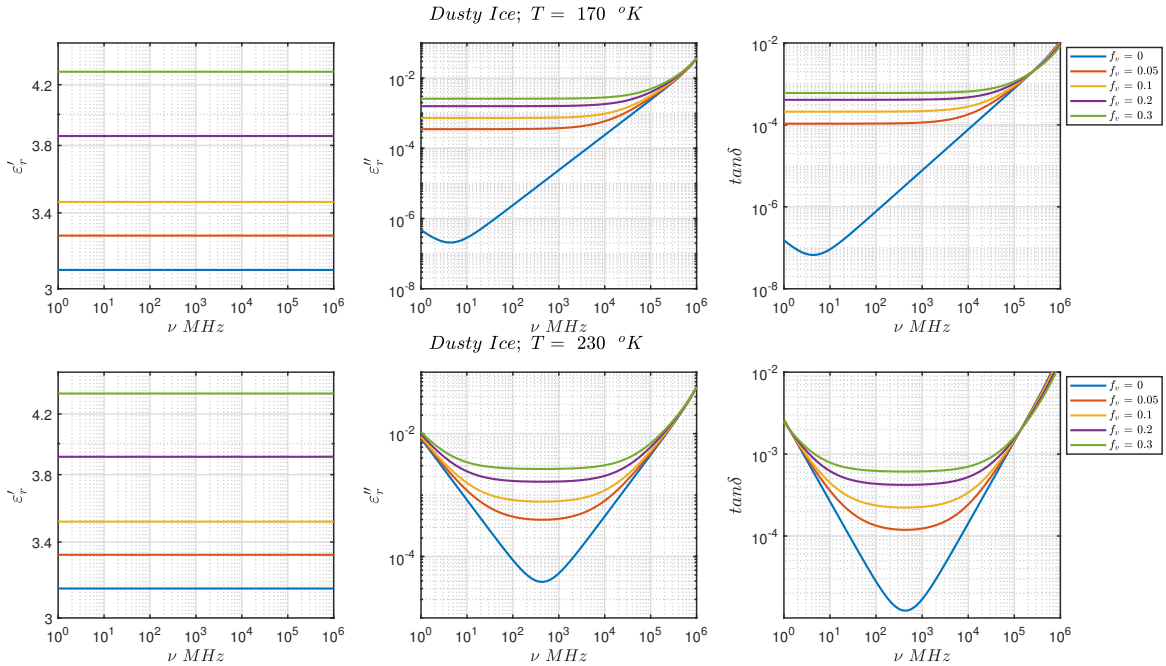

Figure 1.23: Dusty ice properties. Real and imaginary part of dusty ice relative complex permittivity as a function of frequency at $T = 170,\ 230\ ^oK$. In legend f_v indicates the dust volume fraction and $f_v = 0$ accounts for pure water ice. The attenuation in pure water ice at low temperature is negligible (upper panel, blue line). Impurities modify this behavior so that the loss tangent increases and becomes independent of frequency. The temperature effect is prominent.

1.7.3 Electrical Property of Rocks

A rock is a composite of one or more types of mineral grains, however, because of the possible presence of non-mineral substances, in particular water, the properties of a rock might not be a simple combination of the constituting minerals properties. For a petrophysical characterization of rocks, two electrical parameters are relevant, specific electrical resistivity (or its inverse, conductivity) and dielectric permittivity.In the following, the resistivity and permittivity of rocks are discussed.

Rock Components (Minerals and Pore Fluids)

Most rock-forming minerals, particularly silicates and carbonates, have very high specific resistivity ($> 10^9\ \Omega\ m \equiv \sigma_s < 10^{-9}\ S/m$) and practically are insulators. Sulfides and some oxides are conductive minerals. They are rare in the earth's crust. An important member of the conductive group is graphite. The relative permittivity of most abundant rock-forming minerals are in the range $4-10$. Some minerals have higher values, such as the sulfide and oxide groups [121]. The variations of magnitude of the electrical properties within one type or group are attributed to impurities and crystalline structures, which also produce electrical anisotropy. Table (1.2) shows values of specific electrical resistivity and relative permittivity of some minerals.

Among the pore fluids, water is the only effective conductor. In many cases, the ionic conduction of the pore water is the dominant conduction mechanism in a porous or fractured rock, and the specific electrical resistivity is controlled mainly by: (1) the chemical composition, concentration, and temperature of the brine or electrolyte; (2) the volume fraction (porosity, saturation) and distribution of the electrolyte in the rock. With respect to the electrical properties, there are two main types of pore fluids: (1) Water: conducting with high permittivity $\varepsilon_r \approx 80$ (2). Oil, gas: nonconducting with low permittivity $\varepsilon_r \approx 1-3$. Gases and oil are essentially nonconductors with the specific electrical resistivity in the order of $> 10^9\ \Omega\ m$. There also exists a distinct difference of the relative permittivity between water and other fluids as shown in Table (1.3).

Table 1.2: Specific electrical resistivity and relative permittivity ε_r at radio frequencies of selected minerals (taken from [121]).

Mineral		Special resistivity in Ωm	Relative permittivity ε_r	Mineral		Special resistivity $\Omega\ m$	Relative permittivity ε_r
Silicates	Quartz	2.0×10^{14}	4.5	Sulfates	Anhydrite	1.0×10^{9}	6.5
	Amphibole	4.8×10^{10}	8.0		Gypsum	1.05×10^{11}	6.4
	Microcline	1.8×10^{11}	5.48		Apatite	8.3×10^{11}	11.7
	Orthoclase	1.4×10^{12}	5.6		Barite	1.2×10^{7}	10.0
	Albite	4.8×10^{8}	6.95		Halides		
	Anorthite	7.7×10^{9}	6.9		Halite	5.0×10^{13}	5.9
	Labradorite	6.3×10^{8}	5.87		Sylvite		
	Muscovite	2.2×10^{12}	7.6		Fluorite	7.7×10^{13}	6.76
	Biotite	8.3×10^{10}	6.3	Oxides, sulfides	Hematite	1.0×10^{2}	25.0
	Chlorite	1.6×10^{9}	9.0		Magnetite	1.0×10^{-4}	
	Kaolinite	3.2×10^{7}	11.8		Pyrite	1.0×10^{-3}	$33.7 - 81.0$
Carbonates	Calcite	9.0×10^{13}	6.35		Galena	1.0×10^{-3}	17.9
	Dolomite	4.3×10^{13}	7.46		Sphalerite	2.6×10^{11}	7.5
	Aragonite	3.4×10^{12}	8.67		Graphite	1.4×10^{-5}	
	Siderite	8.3×10^{9}	9.3				

Table 1.3: Relative dielectric permittivity of some pore fluids, including contaminants (taken from [121]).

Fluid	$\boldsymbol{\varepsilon_r}$	**Fluid**	$\boldsymbol{\varepsilon_r}$
Air	1.0	Diesel	2.0-2.4
Water	80-81	Trichloethane	7.5
Natural oil	2.0-2.4	Benzene, toluene	2.3-2.4

Specific Electrical Resistivity of Rocks

The electrical resistivity of rocks varies over many orders of magnitude. It is controlled mainly by factors such as rock type, porosity, connectivity of pores, nature of the fluid, clay content, and metallic (or graphite) content. The most of common rock-forming minerals are characterized by very high resistivity (low conductivity). Comparable behavior is expected for dry rocks. In porous or fractured water-bearing rock, the electrolytic conductivity of the water and interactions between solid and fluid components create an enhanced electrical conductivity. Figure (1.24) gives an overview of the mean ranges of the specific resistivity and relative permittivity of some common rock types. The dominant influence of the pore water on the electrical properties produces a broad range of rock properties for each type, which usually overlaps different types. If the pores or fractures contain water, two tendencies are observed: (1) Resistivity decreases with increasing porosity and fracturing (2) Relative permittivity increases with increasing porosity and fracturing.

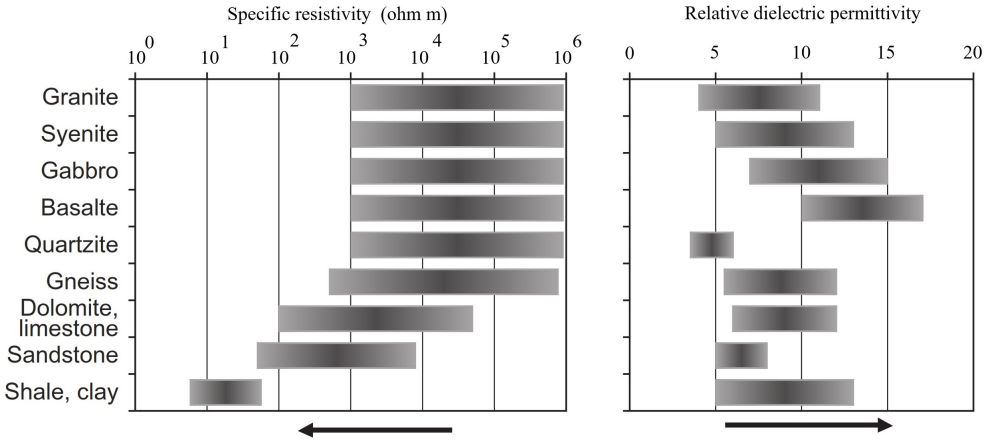

Figure 1.24: Mean value ranges and tendencies for specific electrical resistivity and dielectric permittivity. The arrow indicates the effect of water-filled pores and fractures (taken from [121]).

Dielectric Properties of Rock Constituents

Most rock-forming minerals have a relative permittivity in the order of $\varepsilon_r = 3 - 10$; higher values show, for example, sulfides and some oxides. The dielectric permittivity of water is about 80 and is temperature dependent. This results in a strong correlation between permittivity and the water content of a rock. Table (1.4) gives some relative permittivity for rock-forming components.

Figure (1.25) schematically shows the relative permittivity of rock components. Permittivity of rocks and soils is of particular interest for interpretation of GPR and borehole electromagnetic propagation measurements. Table (1.5) shows some characteristic values. It includes the propagation velocity of electromagnetic wave and the attenuation coefficient. We note the strong influence of water content and water conductivity upon attenuation; this originates limitations for radar penetration depth.

Table 1.4: Relative permittivity at radio frequencies for rock-forming components (taken from [121]).

Substance	ε_r	Substance	ε_r
Quartz	4.5-4.7	Gas	1
Calcite	6.4-8.5	Oil	2.2
Dolomite	6.1-7.3	Water	80
Anhydrite	5.7-6.5		
Halite	5.7-6.2	Shale (dry)	13-16

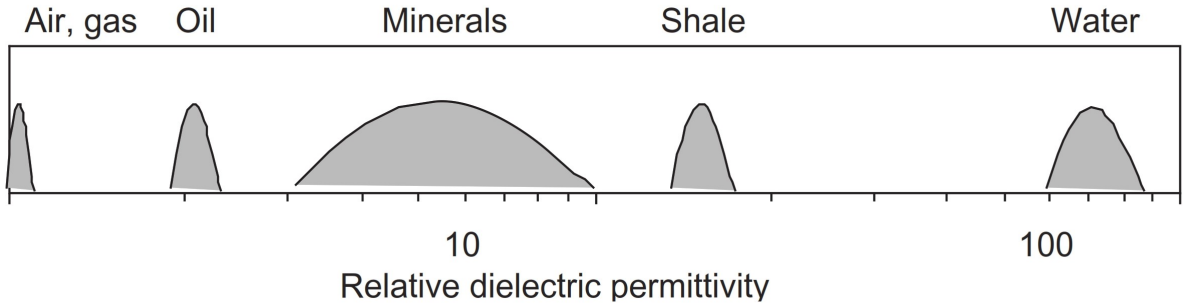

Figure 1.25: Relative permittivity of rock components (taken from [121]). The minerals and shale are assumed to be exposed to water.

Table 1.5: Dielectric permittivity and properties of electromagnetic wave propagation in some materials (taken from [121]).

Substance	ε_r	Velocity cm/ns	*Attenuation* dB/m
air	1	30	0
Dry sand	4	15	0.01
Water-saturated sand	25	6	0.03-0.3
clay	5-40	4.7-13	1-300
Peat	60-80	3.4-3.9	0.3
Water (fresh)	80	3.4	0.1
Water (saline)	80	3.4	1000

Electrical Conductivity of Rocks

The electrical conductivity of rocks depends critically upon how current is carried through the rock. Deep in the Earth at high temperatures, conduction occurs through the solid minerals by electronic conduction, with minerals acting as semiconductors. In the upper crust, there are a number of ways in which conduction occurs. The most common is through the movement of charged ions in the pore fluid which either fully or partially saturates the pores of the rock. If the rock is composed of insulating minerals such as silicates, mineral conduction is negligible ($10^{-14} - 10^{-10}$ S/m). Contrarily, the conductivity of the pore fluids, which they contain, is much larger ($10^{-3} - 10^{-1}$ S/m). Hence, conduction takes place exclusively through the pore fluid by the movement of charged ions. Consequently, the conductivity of rocks is controlled by the way the pore fluids are connected throughout the rock, and this depends on the rock's micro-structure. In summary, the conductivity of rocks depends on: (1) Conductivity of the fluid that occupies the pores; (2) porosity of the rock; (3) degree of the porosity saturation with fluid; (4) connectedness of pathways available for electrical conduction. The most satisfactory expression for conductivity of water-bearing rock is given by Archie formula [56]:

$$\sigma_b = a\ \sigma_w W^m \tag{1.115}$$

where σ_b is bulk conductivity of rock, σ_w is conductivity of electrolyte filling the pore structure, W is volume fraction of present water in the rock, and a, m are parameters to force equation to fit the behavior of given rock. Note that, the pore structures are complicated in general and hence difficult to describe geometrically. Figure (1.26) shows the conductivity of several types of earth material.

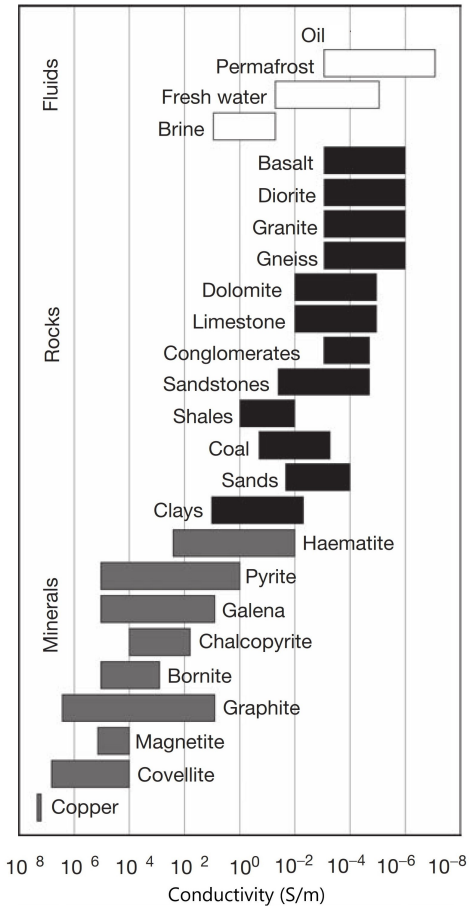

Figure 1.26: Conductivity of several geomaterials (taken from [39]).

1.8 Wave Reflection and Transmission at Normal Incidence

In real-world problems, the electromagnetic fields encounter boundaries, scatterers, and other objects. When an incident wave encounters a reflecting interface separating two half spaces, a fraction of the wave intensity will be reflected into the first medium and remaining part will be transmitted into the second one (Figure (1.27)). For a normal incident plane wave with the electric field of the form [see equation (1.52)]:

$$\mathbf{E}^i = \hat{\boldsymbol{x}}\ E_0 e^{-\alpha_1 z} e^{-j\beta_1} \tag{1.116}$$

the reflected and transmitted electric fields are expressed as:

$$\mathbf{E}^r = \hat{\boldsymbol{x}} \rho E_0 e^{\alpha_1 z} e^{j\beta_1} \tag{1.117}$$

$$\mathbf{E}^t = \hat{\boldsymbol{x}} \tau E_0 e^{-\alpha_2 z} e^{-j\beta_2} \tag{1.118}$$

and those of magnetic field by:

$$\mathbf{H}^i = \hat{\boldsymbol{y}} \frac{E_0}{\eta_1} e^{-\alpha_1 z} e^{-j\beta_1} \tag{1.119}$$

$$\mathbf{H}^r = -\hat{\boldsymbol{y}} \frac{\rho E_0}{\eta_1} e^{\alpha_1 z} e^{j\beta_1} \tag{1.120}$$

$$\mathbf{H}^t = \hat{\boldsymbol{y}} \frac{\tau E_0}{\eta_2} e^{-\alpha_2 z} e^{-j\beta_2} \tag{1.121}$$

where ρ and τ are reflection and transmission coefficients. Magnitudes of average power carried by the incident, reflected and transmitted waves, for a cross section of area A are expressed by:

$$\bar{P}_i = \frac{\left|\mathbf{E}^i\right|^2}{2\eta_1} A \tag{1.122}$$

$$\bar{P}_r = \frac{\left|\mathbf{E}^r\right|^2}{2\eta_1} A \tag{1.123}$$

$$\bar{P}_t = \frac{\left|\mathbf{E}^t\right|^2}{2\eta_2} A \tag{1.124}$$

The reflectivity (or reflectance or power reflection coefficient) is defined as the ratio of the reflected power to the incident power:

$$\Gamma = \frac{\bar{P}_r}{\bar{P}_i} = |\rho|^2 \tag{1.125}$$

and, transmittivity (or transmittance or power transmission coefficient) is defined as the ratio of the transmitted power to incident power:

$$\mathbb{T} = \frac{\bar{\bar{P}}_t}{\bar{P}_i} = |\tau|^2 \left(\frac{\eta_1}{\eta_2}\right) \tag{1.126}$$

Conservation of power requires that the incident power equals the sum of the reflected and transmitted powers:

$$\bar{P}_i = \bar{P}_r + \bar{P}_t \tag{1.127}$$

that results in

$$\Gamma + \mathbb{T} = 1 \tag{1.128}$$

It is apparent that the ratio of the reflected to the incident power densities is equal to the square of reflection coefficient magnitude. However, the ratio of the transmitted to the incident power density is not equal to the square of the magnitude of the transmission coefficient. The transmitted field can be greater than the incident field, meaning a transmission coefficient greater than unity. However, by the conservation of power, the transmitted power density cannot exceed the incident power density.

1.8.1 Reflection and Transmission Coefficients

Reflection and transmission coefficients are in general complex quantities that depend on the constitutive parameters of the two media *i.e.*, dielectric permittivity, magnetic permeability, and electrical conductivity, the direction of wave travel (angle of incidence), and the direction of electric and magnetic fields (wave polarization). The reflection and transmission coefficients which account for the reflected and transmitted field can be determined by applying boundary conditions on the fields along the interface, through enforcing continuity of the tangential components of the electric and magnetic fields across the interface. Fallowing the expressions derived by Stratton [133], the reflection, ρ, and transmission, τ, coefficients for a normal incidence are of the form:

$$\rho = \frac{\eta_2 - \eta_1}{\eta_2 + \eta_1} = \frac{\mu_2\gamma_1 - \mu_1\gamma_2}{\mu_2\gamma_1 + \mu_1\gamma_2} = \frac{\sqrt{\frac{\mu_2}{\varepsilon_{e2}}} - \sqrt{\frac{\mu_1}{\varepsilon_{e1}}}}{\sqrt{\frac{\mu_1}{\varepsilon_{e2}}} + \sqrt{\frac{\mu_1}{\varepsilon_{e1}}}} \tag{1.129}$$

$$\tau = \frac{2\eta_2}{\eta_2 + \eta_1} = \frac{2\mu_2\gamma_1}{\mu_2\gamma_1 + \mu_1\gamma_2} \tag{1.130}$$

that are interrelated by:

$$\tau = 1 + \rho \tag{1.131}$$

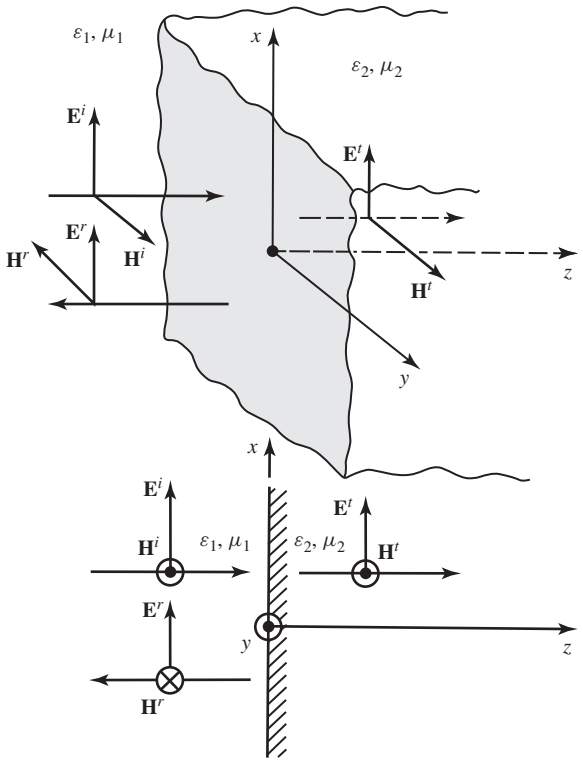

Figure 1.27: Wave reflection and transmission at normal incidence by a planar interface [5].

Note that according to equation (1.55), the intrinsic impedance of mediums is defined by $\eta = \sqrt{\mu/\varepsilon_e}$ which is in turn a real or complex value for lossless and lossy medium. The most materials on and near the Earth's surface, including most common minerals, rocks, ice, and water, have magnetic permeability approximately equals to that of free space, $\mu \approx \mu_0$, except for a small subset of minerals that are not very abundant. Hence, magnetic permeability can be eliminated from these equations, giving rise to:

$$\rho = \frac{\eta_2 - \eta_1}{\eta_2 + \eta_1} = \frac{\gamma_1 - \gamma_2}{\gamma_1 + \gamma_2} = \frac{\alpha_1 + j\beta_1 - \alpha_2 - j\beta_2}{\alpha_1 + j\beta_1 + \alpha_2 + j\beta_2} = \frac{(\alpha_1 - \alpha_2) + j\,(\beta_1 - \beta_2)}{(\alpha_1 + \alpha_2) + j\,(\beta_1 + \beta_2)} \tag{1.132}$$

and

$$\tau = \frac{2\eta_2}{\eta_2 + \eta_1} = \frac{\gamma_1}{\gamma_1 + \gamma_2} \tag{1.133}$$

The amplitude of reflection coefficient is expressed by:

$$\mid \rho \mid = \sqrt{\frac{(\alpha_1 - \alpha_2)^2 + (\beta_1 - \beta_2)^2}{(\alpha_1 + \alpha_2)^2 + (\beta_1 + \beta_2)^2}} \tag{1.134}$$

and power reflection coefficient, Γ, is the square of equation (1.134), $\Gamma = \mid \rho \mid^2$. In addition the reflection coefficient can be written as:

$$\rho = \mid \rho \mid e^{j\phi} \tag{1.135}$$

where ϕ is the phase shift given by:

$$tan\phi = \frac{2\,(\alpha_2\beta_1 - \alpha_1\beta_2)}{(\alpha_1^2 + \beta_1^2) - (\alpha_2^2 + \beta_2^2)} \tag{1.136}$$

In both low-loss and high-loss cases the tangent of the phase shift angle is small. It is worth noting that if the medium underlying the reflecting interface is a non-conductive dielectric, it needs to have a thickness of at least $\lambda/2$ for its properties to fully determine the reflection strength. So, a radar wave reflecting from an interface between two perfect dielectric materials is sensitive to the properties of the sub-interface material to within about $\lambda/2$ below the interface ([143]).

1.8.2 Radar Wave Reflection from Glacier Beds

Ice-penetrating radar represents the most successful geophysical technique in glaciology, which efficiently yields observational constraints on fundamental properties of land ice masses on Earth and ice masses on Mars, such as thickness, internal structures, and bed properties. Much of the success of radar imaging in glaciology is due to the fact that glacier ice is a polycrystalline solid with either no or little liquid water and low concentration of impurities from atmospheric deposition, e.g., sea salts and acidic impurities. Hence, glacier ice is a poor electrical conductor and is quite transparent to electromagnetic waves over a broad range of frequencies.

In general in nonmagnetic mediums, including glaciers, radar reflections can be caused by contrasts in either real permittivity or conductivity of medium or both. The radar waves can typically transmit much energy through weak englacial reflectors and provide information on deep structure. The radar reflectivity of the ice bed offers basically the only insight from radar surveys into the nature of geologic materials underlying ice masses. The ice-ice subsurface conditions, e.g., the presence or absence of subglacial liquid water, can be deduced from the lateral and temporal variations in radar bed reflectivity. In particular, two limiting cases of reflection coefficient in equation (1.134), assuming that the first medium is ice (i.e., medium 1 is low loss), are examined here.

Case 1: When the medium 2 is low loss as well, *i.e.*, $\sigma_e/\varepsilon_2'\omega \ll 1$, attenuation coefficient is negligible and the reflection coefficient will be:

$$\mid \rho \mid = \frac{\sqrt{\varepsilon_1'} - \sqrt{\varepsilon_2'}}{\sqrt{\varepsilon_1'} + \sqrt{\varepsilon_2'}} \tag{1.137}$$

The reflection coefficient simplifies to a function of only permittivity of ice, ε_1', and the sub-ice geologic material, ε_2'. This is a very practical result because it agrees with a widely used form of radar reflection coefficient in the case of an interface between two perfect dielectrics. The tangent of the phase shift angle is always zero for the low-loss case but the phase shift angle is either zero or 180^o. Accordingly the real permittivity of subglacial can be estimated as:

$$\varepsilon_2' \approx \varepsilon_1' \left(\frac{1- \mid \rho \mid^2}{1+ \mid \rho \mid^2} \right)^2 \tag{1.138}$$

Case 2: When the medium 2 is high loss *i.e.*, $\sigma_e/\varepsilon_2'\omega \gg 1$, attenuation coefficient of the sub-ice cannot be ignored and the reflection coefficient will be:

$$\mid \rho \mid = \sqrt{\frac{(\alpha_1 - \alpha_2)^2 + \beta_2^2}{(\alpha_1 + \alpha_2)^2 + \beta_2^2}} = \sqrt{\frac{\varepsilon_1'\omega - \sqrt{2\varepsilon_1'\omega\sigma_{e2}} + \sigma_{e2}}{\varepsilon_1'\omega + \sqrt{2\varepsilon_1'\omega\sigma_{e2}} + \sigma_{e2}}} \approx \sqrt{\frac{\sigma_{e2} - \sqrt{2\varepsilon_1'\omega\sigma_{e2}}}{\sigma_{e2} + \sqrt{2\varepsilon_1'\omega\sigma_{e2}}}} \tag{1.139}$$

equation (1.139) shows that the reflection coefficient depends on angular frequency, ω, the real permittivity of ice, ε_1', and effective conductivity of sub-ice material, $\sigma_{e2} = \sigma_{s2} + \omega\varepsilon_2''$. Given the radar frequency and real permittivity of ice (medium 1) the subglacial effective conductivity can be obtained from equation (1.139):

$$\sigma_{e2} \approx 2\varepsilon_1'\omega \left(\frac{1+ \mid \rho \mid^2}{1- \mid \rho \mid^2} \right)^2 \tag{1.140}$$

Note that transmission coefficient can be estimated through equation (1.131).

Figure (1.28) shows the full version of the amplitude reflection coefficient (equation 1.134) plotted for the case of 5 and 500 MHz linear frequency as functions of relative permittivity and electrical conductivity of the sub-ice material. The relative permittivity and conductivity of first medium (water ice) are respectivelly considered 3.2 and 10^{-5} S/m. In $\rho - \sigma_{e2}$ plots, the horizontal line segments on the left corresponds to the case which the sub-ice medium is a composition of lossless dielectric materials. These line segments can be approximated by equation (1.137), which is commonly used in glaciology and GPR studies to make inferences about the nature of geologic materials. Due to the fact that common minerals have relatively low relative permittivity, approximately 4-10, and liquid water has very high relative permittivity, the strength of the basal reflection coefficient is often interpreted solely as the function of water content. This is also a common practice in GPR investigations of interfaces between sediment layers.

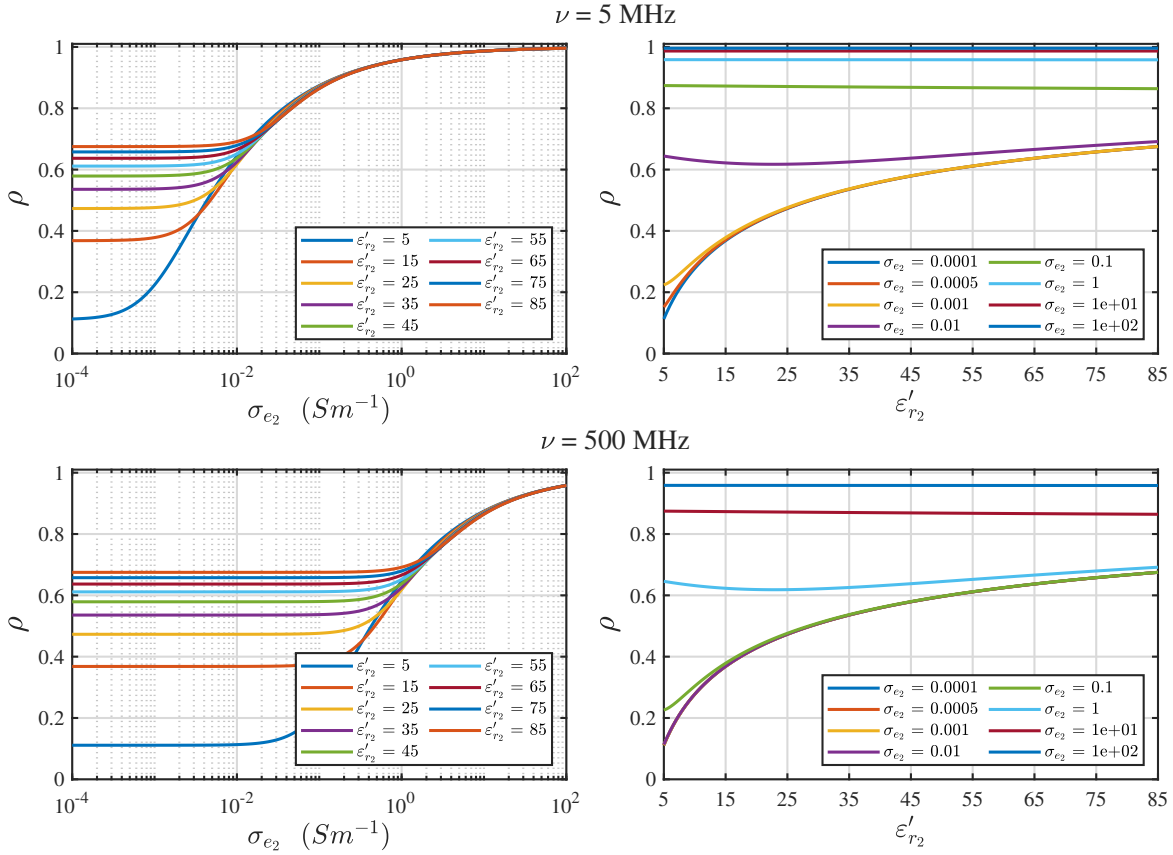

Figure 1.28: The amplitude reflection coefficient variation as a function of (left) effective conductivity and (right) relative real-permittivity of sub-ice medium. The operating frequency is 5 MHz. For ice, the relative permittivity and electrical conductivity of ice are assumed 3.2 and 10^{-5} S/m, respectively. The full version of the amplitude of reflection coefficient, equation (1.134), has been used (modified after [143]).

In glaciology and planetary science, for instance, bright radar reflectors have been used in the search for subglacial lakes since open water bodies beneath ice should be the most reflective subglacial materials, at least in the low-loss regime described by equation (1.137). The plots in left panel show that starting at electrical conductivity of about $10^{-3} - 10^{-2}$ S/m, for 5 MHZ and $0.1 - 1$ S/m for 500 MHz the reflection coefficient becomes increasingly more dependent on the conductivity than on the permittivity of the sub-ice material. However, by increasing the conductivity, the reflection coefficient will be independent of relative permittivity of subglacial materials and reaches high values. This means that high-conductivity subglacial materials can appear at least as bright as subglacial lakes filled with fresh melt-water. Such high-conductivity materials can include seawater or brine-saturated sediments and bedrock as well as clay-bearing sediments or bedrock saturated with natural waters of any reasonably high conductivity [143]. The plots in right panel show that for conductivity higher than 0.001 S/m and 0.1 S/m for 5 and 500 MHz, respectively, the reflection coefficient is high, independently of relative permittivity values.

1.8.3 Transverse Electric and Magnetic Field Modes

Electromagnetic (EM) waves are transverse vector wave fields, and can be separated into two independent components defined by field orientation with respect to the boundary. For planar interfaces, it is common to decompose the incident wave into components whose vector components have a compatible orientation with respect to the boundary. These two wave fields are referred to the transverse electric field (TE) and transverse magnetic field (TM) waves as depicted in Figure (1.29). The TE (also called *Perpendicular Polarization*) wave always has its electric field perpendicular to the plane of incidence . The transverse magnetic field (also called *Parallel Polarization*) has its electric field parallel to the plane of incidence. Note that, in TM mode the magnetic field vector is perpendicular to the plane of interface. The plane of incidence is defined as the plane containing the normal to the boundary and the direction of propagation

of the incident wave.

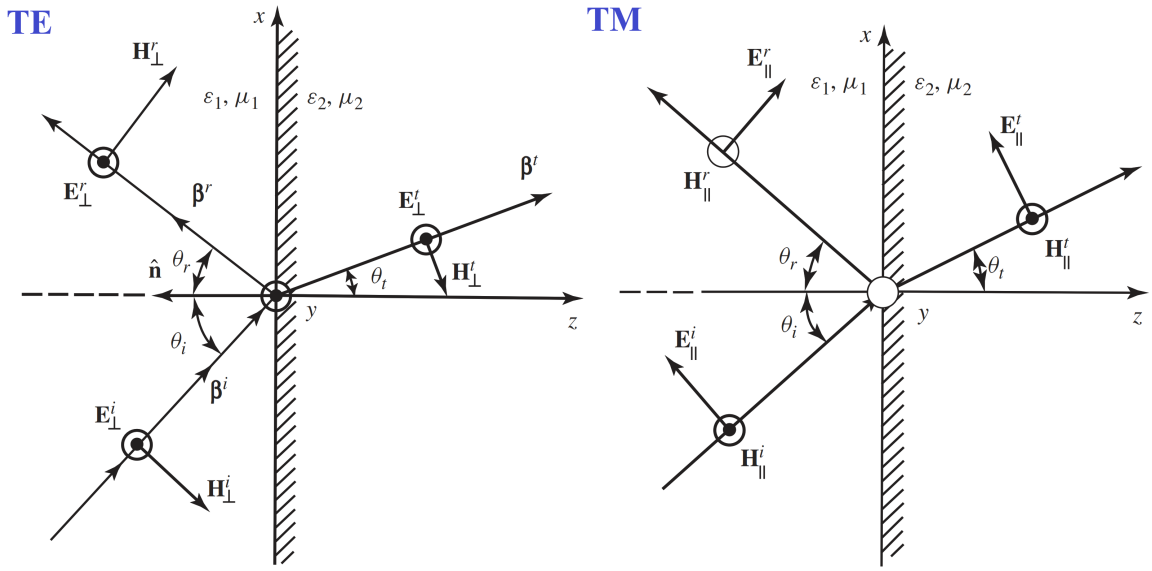

Figure 1.29: EM waves are transverse vector wave fields. For any given propagation direction, two independent fields exist: (left) one with the electric field perpendicular to plane of incidence that is called traverse electric (**TE**) or perpendicular polarization; and (right) one with electric field parallel to plane of incidence that is called traverse magnetic (**TM**) or parallel polarization. Note that, in TM the magnetic field vector is perpendicular to the plane of interface (Taken from [5]).

1.9 Reflection and Transmission of Multiple Interfaces

1.9.1 Reflection Coefficient of Single Slab Layers

To compute the reflectivity of such medium, the problem is modeled as a three-layer configuration. Figure (1.30) depicts a uniform plane wave incident at a normal angle on a surface in medium 1. Part of the incident wave is reflected at the boundary between media 1 and 2, and the remaining part crosses the boundary and propagates down to the medium 2. The propagating wave in medium 2 is partly reflected back up at the boundary 2-3 and partly transmitted to the medium 3. The upward propagating wave in medium 2 will be partly reflected at the boundary 2-1 and partly transmitted into the medium 1. This reflection process continues infinitely (multiple bounces), and each reflection causes energy loss. The total reflection coefficient in medium 1 is equal to the amplitude sum of upward reflected electric field in medium 1 divided by the amplitude of the incident electric field. Using the foregoing procedure for normal wave incidence, the effective reflection coefficient of the two-layer structure (media 2 and 3) is given by [5]:

$$\rho = \frac{\rho_{12} + \rho_{23} e^{-2\gamma_2 d}}{1 + \rho_{12}\ \rho_{23} e^{-2\gamma_2 d}} \tag{1.141}$$

that is derived by using the relations:

$$\rho_{12} = -\rho_{21} \tag{1.142}$$

$$\tau_{12} = 1 + \rho_{12} = 1 - \rho_{21} \tag{1.143}$$

$$\tau_{21} = 1 + \rho_{21} = 1 - \rho_{12} \tag{1.144}$$

with following definition of the terms:
ρ_{12}: reflection coefficient at boundary 1 and 2
ρ_{21}: reflection coefficient at boundary between medium 2 and 1
τ_{12}: transmission coefficient from medium 1 to 2
τ_{21}: transmission coefficient from medium 2 to 1
ρ_{23}: reflection coefficient at boundary between medium 2 and 3
γ_2: propagation constant in medium 2

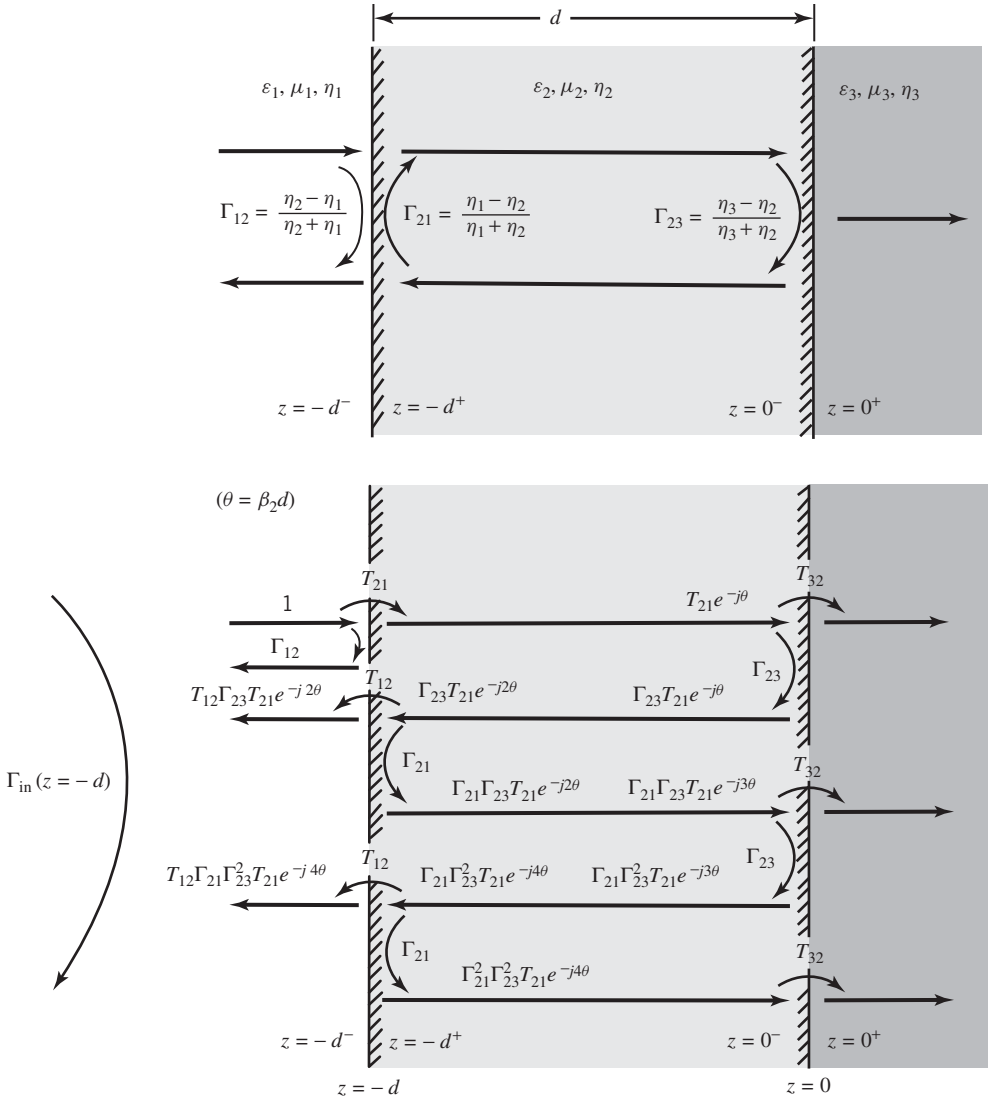

Figure 1.30: Reflection and transmission coefficients for wave propagation in dielectric slab. In the figure, the Γ presents reflection coefficient, and T presents transmission coefficient. The lower panel illustrates the multiple reflections (Taken from [5]) .

If the magnitude of reflection coefficients are low compared to unity *i.e.,* $|\rho_{12}| \ll 1$ and $|\rho_{23}| \ll 1$, equation (1.141) can be approximated by the numerator:

$$\rho \approx \rho_{12} + \rho_{23} e^{-2\gamma_2 d} \tag{1.145}$$

The equation (1.145) will be very convenient for representing the reflection coefficient of multiple interfaces when the individual intrinsic reflection coefficients at each interface are low compared to unity (*i.e.,* the multiple reflections is negligible). A specific scenario of interest is a lake or ocean water surface covered by a uniform layer of ice. In this case, Medium 1 is air, medium 2 is the intervening uniform layer of thickness d (ice, oil, or snow), and medium 3 represents water body.

1.9.2 Reflection Coefficient of Multiple Layers

For a structure composed of N layers (Figure 1.31) each with its own thickness and constitutive parameters which are in addition confined between two semi-infinite media, the reflection coefficient for the entire system under normal wave incidence is approximated as [5]:

$$\rho \approx \rho_0 + \rho_1 e^{-2\gamma_1 d_1} + \rho_2 e^{-2(\gamma_1 d_1 + \gamma_2 d_2)} + \ldots + \rho_N e^{-2(\gamma_1 d_1 + \gamma_2 d_2 + \ldots + \gamma_{2N} d_N)} \tag{1.146}$$

where the individual reflection coefficients are computed by:

$$\rho_i = \frac{\eta_{i+1} - \eta_i}{\eta_{i+1} + \eta_i} \ , \qquad i = \ 0, 1, 2, \ldots N \tag{1.147}$$

where indexes 0 and *N+1* refers to the confining semi-infinite media. The expression (1.147) is accurate enough provided that $\rho_i \ll 1$.

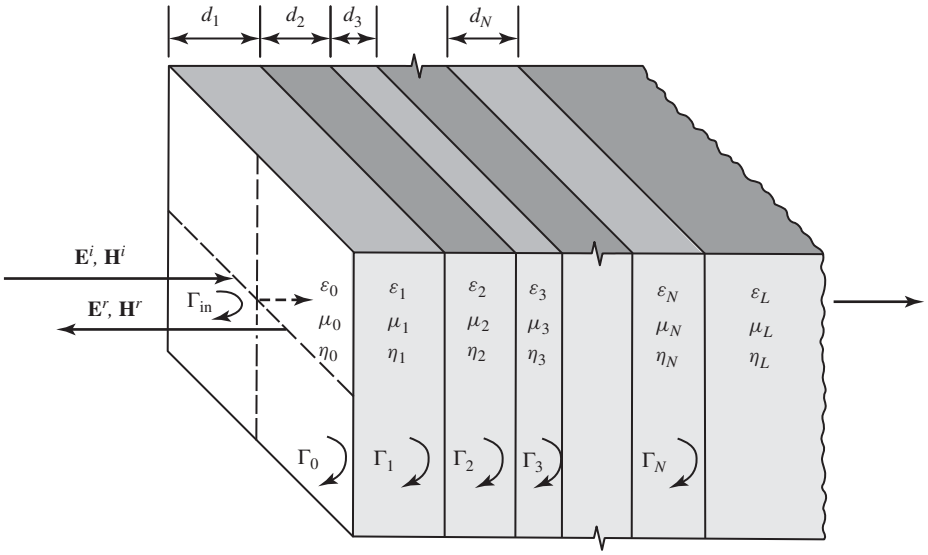

Figure 1.31: Normal wave propagation through N layers sandwiched between two media [5].

Chapter 2

Ground Penetrating Radar in Exploration

2.1 Introduction

There are a wide variety of geophysical methods based on electromagnetic (EM) phenomena that respond to electrical properties of the subsurface medium (Figure (2.1)). Among them are those which use high frequency electromagnetic waves (Radio and Radar). Ground penetrating radar (GPR) or Georadar is a non-invasive geophysical method widely used in sedimentology, glaciology, and archaeology for high resolution investigation of subsurface and has undergone a rapid development during the recent decades. Particularly GPR is a very effective method to investigate the structure of snow, ice sheets and glaciers since ice is one of the most transparent natural material in the range of radar frequencies.

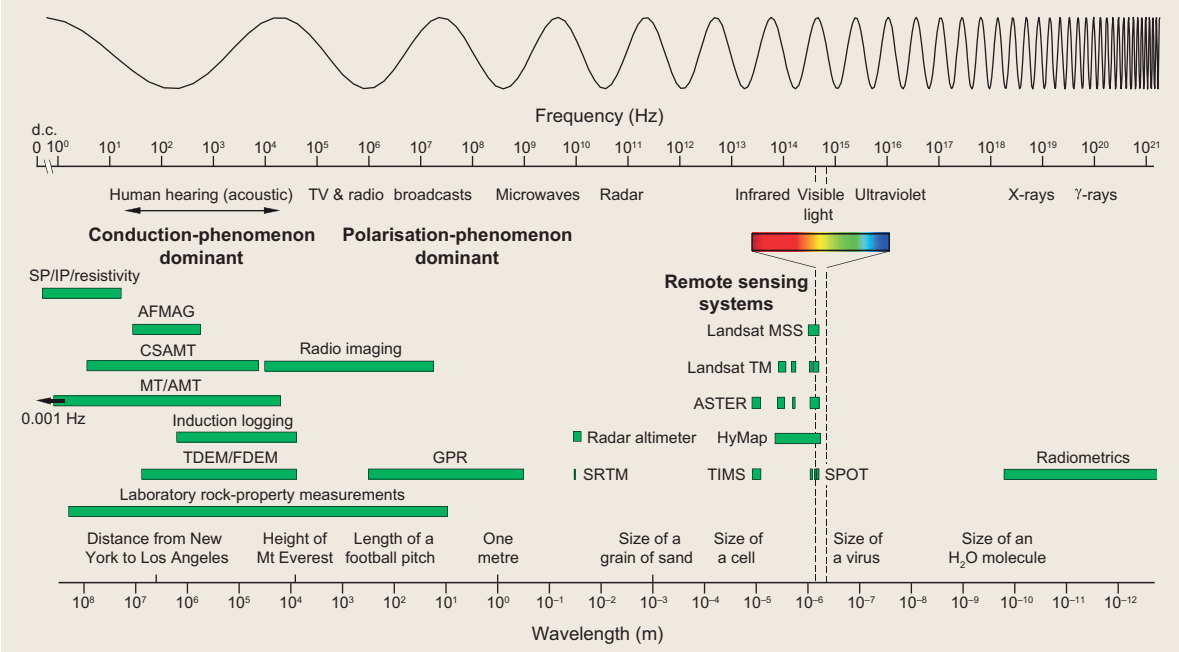

Figure 2.1: The electromagnetic spectrum and the frequency bands used by the various geophysical methods [22].

GPR is based on electromagnetic pulse reflection method, so that a pulse of EM energy radiates from the transmitter, propagates through the medium, and then, is reflected by physical property contrasts (electrical interfaces) in the subsurface and finally arrives at the receiver. A reflection profiling mode of the radar on soil over bedrock is illustrated in Figure (2.2). The recorded reflected pulse by the subsurface creates a time-depth image (radargram) which contains information about the buried geological

structures. In addition to reflection at the dielectric discontinuity, the propagating electromagnetic pulse can be scattered by the irregularity of surface and volume inhomogeneities at the pulse wavelength scale, as well, and will be attenuated (absorption and scattering) in medium before reaching a subsurface interfaces. The basic constituents of a radar system are shown in Figure (2.3). The capability of subsurface sounding radar to detect an underground dielectric discontinuity is thus strongly dependent on the medium through which the radar pulse propagates.

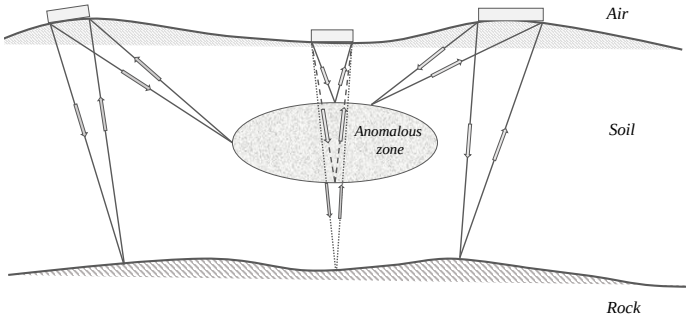

Figure 2.2: Conceptual illustration of the radar being used in the reflection profiling mode on soil over bedrock (modified after [21]).

The properties of materials underlying superficial deposits can be inferred by applying inversion algorithms to the acquired GPR data. For this purpose, a knowledge of the electromagnetic properties of the shallow deposits and an accurate evaluation of the signal attenuation are required to improve the reliability of radar investigation particularly in the planetary crusts to support the interpretation of georadar data.

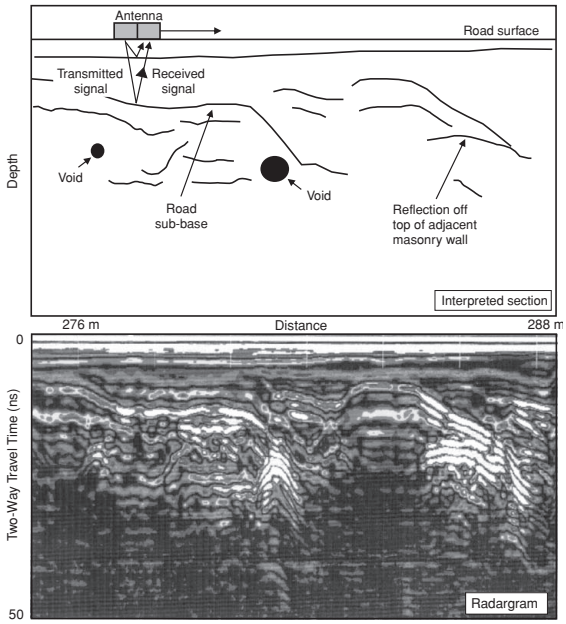

Figure 2.3: Constituents of a radar system. (upper panel) A moving antenna along a profile over a subsurface structure and (lower panel) recorded returned-signals [117].

Maxwell's equations mathematically describe the physics of EM fields, while constitutive relationships quantify material properties. Combining the two sets of equation builds the foundations to interpret GPR signals quantitatively. The permittivity and conductivity are of the main interest in GPR investigation. GPR has its most efficiency in media with low conductivity where the signal can penetrate to larger depth. Georadar signals are commonly characterized by the bandwidth, B, to center frequency, ν_c, ratio

[2]:

$$R = B/\nu_c \tag{2.1}$$

and every effort is made to make R as large as possible. In most GPR systems this ratio is approximately equal to 1, and hence, GPR can be characterized by its center frequency. The GPR pulse width at half amplitude, W, in time is directly related to the bandwidth , B, and centroid operating frequency by [2]:

$$W = 1/B = 1/\nu_c \tag{2.2}$$

The centroid operating frequency for a radar survey is selected based on the required spatial resolution and depth of penetration. Depending on the objectives, if the target is small and shallow, it is better to maximize resolution. In reality, maximizing the resolution while ensuring adequate penetration is always an optimization problem. The center frequency of the radar system has a major impact on the depth of penetration of the radar system. As frequency decreases, the signal attenuation in the medium decreases, the emitted power increases, and the impact of clutter and masking the desired signals by responses from smaller scale features are reduced [2].

2.2 Applications of GPR in Exploration

The areas of application for ground-penetrating radar are diverse [117]; (1) **geological application**: Detection of natural cavities and fissures, subsidence mapping, sapping sand body geometry, sapping the superficial deposits, soil stratigraphy mapping, slacial geological investigations, sineral exploration and resource evaluation, fracture mapping in rock salt, location of faults and dykes; (2) **Environmental application**: Mapping and monitoring pollutants within groundwater, landfill investigations including capping effectiveness, location of buried fuel tanks and oil drums, lapping animal burrows and tree roots, lroundwater investigations, letection of UXO; (3) **Glaciological application**: Ice thickness mapping, determination of internal glacier structures, ice movement studies, detection of concealed surface and basal glacier crevasses, mapping water conduits within glaciers, determination of thickness and type of sea and lake ice, subglacial mass balance determination, snow stratigraphy mapping, subglacial landform mapping, glacial hazard assessment; (4) **Archaeology application**: Location of buried structures, graves, post-holes, etc., detection and mapping of Roman roads, foundations, etc., detection of voids (crypts, burial mounds, etc.), investigation of ancient monuments and statues; (5) **Planetary exploration**: Detecting dielectric discontinuities associated with compositional and/or structural discontinuities of planets' subsurface allows mapping the stratigraphy, *i.e.,* characteristic of ice or rocks distribution vs. depth, which can be of fundamental importance to better understand the dynamics and history of the first meters to kilometers of the subsurface.

Note that, in the conversion of radargram into a geological stratigraphy *i.e.*, the transformation of two way travel time in depth, the wave velocity, and hence, dielectric permittivity is the key parameter.

2.3 Medium Properties in GPR Context

Velocity, attenuation, wavelength, polarization, scattering, relaxation, and resonance are the important properties and processes to electromagnetic wave propagation in ground penetrating radar. These properties can be extracted from the recorded responses to ground penetrating radar to describe the subsurface and targets buried within.

Space and time distributions of material's electromagnetic properties are mainly described in terms of complex dielectric permittivity and complex magnetic permeability whose real and imaginary parts account for energy storage and dissipation, respectively. In all materials, the real part is greater than that of free space resulting in a slower velocity of propagation than free space, and the imaginary part is non-zero that results in frequency dependence of properties.

The electrical properties of geological materials are primarily controlled by the water content. Variations in the electrical properties of soils are usually associated with changes in volumetric water content which, in turn, give rise to radar reflections. In rocks, the radar is sensitive to changes in rock type and water-filled or dry fractures [21]. Magnetic properties are dominated by the distribution of iron in the ground. However, in most geological applications of GPR, electrical properties are the dominant factor controlling GPR response, and the effect of magnetic property is negligible, and magnetic permeability,

μ, can be assumed equal to that of free space μ_0. Field polarization and scattering processes are dominantly controlled by the geometric orientation and spatial distribution of contrasts in material properties at scales of propagating pulse wavelength. Total energy, including the part converted from electrical or magnetic to some other type *e.g.,* thermal, chemical or mechanical energy is conserved, but the converted energy is described in terms of electromagnetic loss (attenuation).

Antenna position across the ground can be used to accurately locate horizontal position of the targets. Velocity of traveling wave propagation can be determined from geometry of scattering that creates hyperbola patterns in the data. Thus, distance can be calculated from the two-way travel time, and it is often assumed that the distance is equivalent to depth. However, this is not correct for off-track reflectors. Other physical properties such as density, porosity, and water content may be inferred through an appropriate mixing model. The geometry of targets can be inferred from measurements for various orientation of antenna and transmitter-receiver relative to antenna.

2.4 Responses to GPR

Without heterogeneity (*i.e.*, variation of material properties in space and time) there will be nothing for GPR to respond. Contrasts in material properties at the boundary between two different mediums on the spatial scale of the wavelength of propagating electromagnetic wave cause scattering. Scattering is a mechanism by which some of the GPR emitted energy is returned to the receiver. In general, scattering consists of: reflection, refraction and diffraction, that in physics are defined as [91]:

1. **Reflection**: abrupt change in the direction of a propagating wave that strikes the boundary between adjacent media with different electromagnetic properties (permittivity, conductivity and permeability). The greater the contrast, the greater will be the amount of energy reflected.

2. **Refraction**: change in direction of a wave as it passes from one medium to another medium with different electrical properties.

3. **Diffraction**: spreading of waves around obstacles. One consequence of diffraction, for example, for light is that sharp shadows are not produced. The phenomenon is the result of interference of spreading waves and is most pronounced when the wavelength of the radiation is comparable to the linear dimensions of the obstacle.

Contrast at an interface or across a boundary, in terms of reflection and refraction, are often described by Fresnel reflection and transmission coefficients as discussed in Chapter 1. This assumes sharp boundaries between thick layers of two different materials. Sharp and thick terms are defined in the context of a wavelength in the material. Note that, if there are no contrasts in the medium, there will be nothing scattered to be arrive at the receiver. The objects smaller than the wavelength causes '*clutter*' noise on the radar section. If there are many small objects the noise content may be dominant, and no useful information can be extracted.

When the interface or boundary between two materials is rough at EM wavelength scales, or when roughness at wavelength scale occurs throughout the volume of a material as well, the rough surface and volume scattering may blur the scattered antenna pattern and blur the images. Such scattering is very frequency-dependent and causes the loss of energy. The scattered wave at an interface behaves as if it was radiated from another antenna at the interface. The fraction of the propagating energy that is returned in the direction of the receiver by the scattering processes is similarly followed back to the receiver and described in terms of the geometric spreading losses, exponential material losses, interface scattering losses, coupling to the antenna, and antenna properties. Note that, scattering is a function of the contrast in material properties at a boundary, the spatial scale of the contrast, angle of propagating wave to the interface, polarization of the wave, and the wavelength of the propagating wave.

Resonance may also occur when the electromagnetic energy excites a normal mode in a metallic object or a dielectric cavity, causing the energy to bounce back and forth along a path, re-radiating "ringing" in the direction of the receiver. Certain distribution of properties may also create wave-guides in the subsurface which guide electromagnetic waves.

2.5 GPR Antenna and Signal Paths

Ground penetrating radar antennas are a metallic structure that create and detect key EM fields. The transmit antenna translates the excitation voltage into a temporal and spatial distributed field, and the receiving antenna detects the temporal variation of a vector component of the transmitted EM field plus the responses, and translates it into a recordable signal [2].

The movement of charges in response to the electric field (voltage/distance) creates a current flow in the antenna which this current flow induces a magnetic field. As the electric field varies in time, current varies in time, as well, and consequently, the magnetic field varies in time. The time varying magnetic field induces secondary current flow which generates secondary magnetic field. This coupling of electric currents and magnetic fields back and forth and results in acceleration and deceleration of charges and propagation of an electromagnetic field in medium [91]. As the electromagnetic energy propagates away from the antenna, for the surface spreading wave the field intensity declines as the inverse of distance, and the field intensity of propagating wave through the medium declines as the exponential of distance and attenuation in material, as well.

The geometry of the metallic conductor in the antenna controls the current flow and thus the geometry of the radiated electromagnetic fields. These are described as antenna properties in terms of gain, efficiency, directivity, aperture and impedance. In the immediate vicinity of the antenna, the field pattern and propagation behavior are different than those far away from the antenna. These are called near field and far field zones. The approximate boundary between near field and far field zones at a distance is related to the size and geometry of the antenna and wavelength of electromagnetic field [91]. Efficient field generation and detection requires finite size of antennas. In frequency-domain terminology, the antenna dimension must be commensurate with the wavelength of the signals. The preferred antennas for GPR have short electric dipoles (or small magnetic dipoles). By making these antennas as small as possible, without totally eliminating efficiency, a fair degree of accuracy and invariant behavior can be achieved [2]. A shield is a container which encloses the antenna. The purpose of shielding is to selectively enhance some signals and suppress others. The main objectives of the shield are:

1. maximize the energy to/and from the subsurface target
2. minimize the direct transmitter to receiver energy
3. minimize the coupling with the signals in the air
4. minimize environmental EM noise as indicated by signals

Shielded antennas are most common for higher-frequency GPR systems (typically above 100 MHz) where antennas are smaller. Shielding is never perfect, and even with the most ideal shield, spurious signal leakage can occur. Antenna shielding may have some disadvantageous, for example, shielding can generate repeated large signals [2].

On the ground, GPR signals can travel along several paths from transmitter to receiver as shown in Figure (2.4). The relative importance of each path depends on the target depth, the separation between the transmitter and receiver, and elevation of the transmitter-receiver. In most GPR cases, the transmitter-receiver separation is small and the predominant paths are **a**, **b**, and **c** in Figure (2.4). Paths **d** and **e** are also important if both the transmitter and receiver are far from the target, even if the transmitter and receiver are close together.

2.6 Energy Loss

Several factors result in a decrease of EM pulse energy as it propagates through the subsurface media. A main cause of energy loss is the *absorption* that is a complex function of the electromagnetic properties of the media through which the radar signal is traveling. Absorption transfers the electromagnetic energy into heat. *Scattering* results in energy loss as well. The emitted signals in a medium encounter heterogeneous electrical and magnetic properties on many scales. The objects with dimensions of the same order as the wavelength of radar signal will scatter energy randomly. Scattering by the objects with a dimension smaller than the pulse wavelength is called Rayleigh scattering that causes clutter noise on the radar section. Where the objects are large enough relative to the radar wavelength, they may give rise

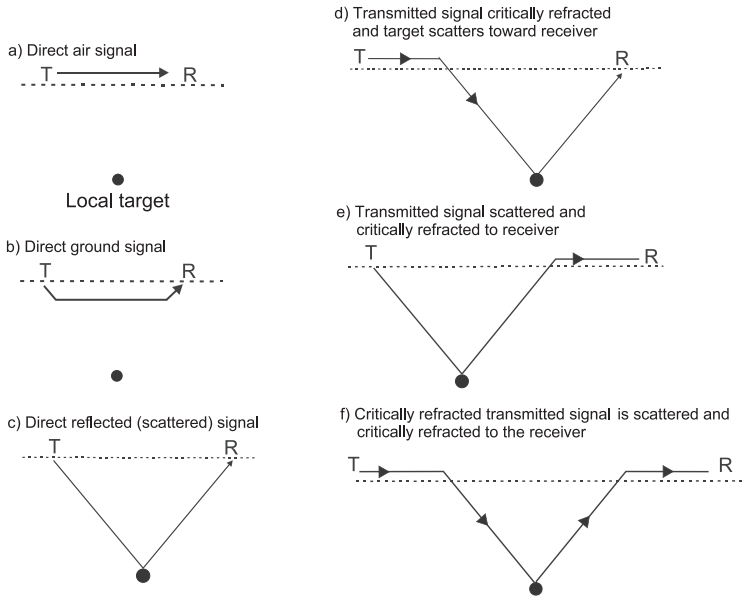

Figure 2.4: The possible paths from transmitter to receiver. The dominant paths are those presented in a, b and c [2].

to point diffraction. These phenomena disperse the signal energy but also provide evidence of presence such objects. In addition, the reflection and transmission from each interface causes energy loss, and the loss occurs each time when radiowaves pass through a boundary. Further, the signal energy is lost by the *geometric spreading* of the energy. As the radar signals travel away from the transmitter, the geometric spreading, approximately at a rate of $1/r^2$, causes a reduction in energy per unit area, where r is the traveled distance.

In summary, as presented in Figure (2.5), the total loss includes five terms [117]: (1) antenna losses; (2) transmission losses between the interfaces including air-ground; (3) losses caused by the geometric spreading of the radar signal; (4) absorption within the medium that depends on the medium's electromagnetic properties, and (5) scattering of the propagating signal by the targets. A more detailed explanation of absorption (intrinsic) and scattering attenuation follows.

2.6.1 Absorption (Intrinsic) Attenuation

In alternating electric fields, a dielectric material is often characterized by its dielectric loss that leads to conversion of a fraction of electrical energy to heat. The absorption attenuation occurs as the result of two processes (assuming nonmagnetic materials): (1) conduction current that depends on the electric field itself and (2) polarization or displacement current that depends on the rate of electric field changes.

Because dielectric materials always possess some degree of conductivity, absorption loss is observed both in direct current flow and in alternating fields. For direct current flow, intrinsic loss depends only on the conductivity, but in alternating fields loss takes place with displacement currents and depends on the relaxation time for the polarization and the frequency range. Polarization by electron and ion displacement takes place in a very short time, $10^{-14} - 10^{-15}$ and $10^{-12} - 10^{-13}$ s, respectively. Thus, loss from this type of polarization does not occur at radio frequencies. The time required for relaxation polarization to take place is considerably longer [99].

The displacement currents [$\omega\varepsilon'\mathbf{E}$ in equation (1.74)], which are what attributing the imaginary aspect of displacement component of total current, are out of phase with the applied electric field and consequently with conduction currents [$(\sigma_s + \omega\varepsilon'')\,\mathbf{E}$ in equation (1.74)] by $\pi/2$ *rad*. The intrinsic attenuation is commonly described by loss tangent, $tan\delta$, that is defined as the ratio of conduction to displacement currents in a material. The phase angle, ϕ, between total current density and the electric field is determined through $\phi = \delta - \pi/2$ (Figure (2.6)).

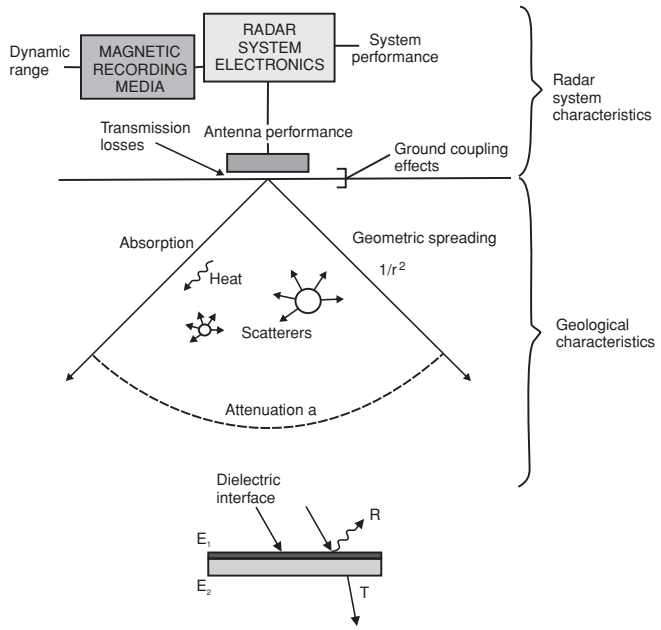

Figure 2.5: The factors that lead to reduction in propagating signal strength [117].

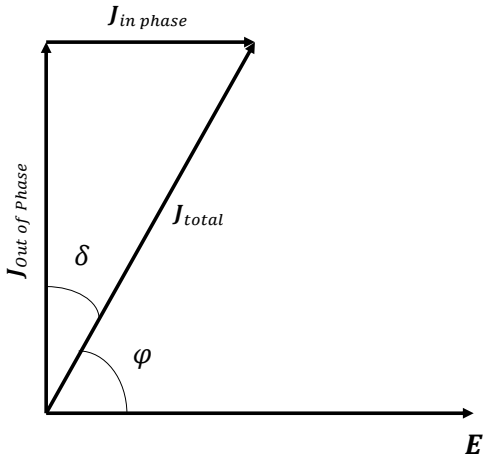

Figure 2.6: Vector diagrams for current density and electric field intensity in a dielectric. The quantity $tan\delta$ describes the intrinsic attenuation (absorption).

2.6.2 Scattering Attenuation

The presence of small heterogeneities (scatters) in medium properties generates weak or undetectable responses. However, such scatters can have a prominent impact on the propagating wave. In effect, the heterogeneities dissipate the wave energy by scattering it in all directions. The scattered energy depends on the heterogeneity of the medium and the roughness of targets or reflectors in the medium. Each heterogeneities can become a transmitter of a part of the incident energy. By increasing the frequency, scattering from small-scale heterogeneity increases. The scattering attenuation coefficient depends on the number of scatters per unit of volume, N, and cross section of scatters, C_s [1]:

$$\alpha_s = \frac{NC_s}{2} \tag{2.3}$$

Due to cross section frequency-despondency, the scattering attenuation coefficient is very frequency-dependent and can significantly attenuates propagating electromagnetic waves. The Rayleigh scattering

cross section of a pulse is expressed as:

$$C_s = ca^6\nu^4 \tag{2.4}$$

where c is a constant with units of $1/(m^4Hz^4)$, a indicates the sphere radius, and ν is the pulse frequency. Volume scattering becomes prominent in ice because the absorption attenuation is too small in cold ice medium. In the medium with a large number of small scatters (in comparison with wavelength), the scattering is described as the reflection of the wave in random and not expected directions. Contrarily, the large size targets can be considered as planar reflectors. Figure (2.7) schematically presents the incident pulse scattering by heterogeneity.

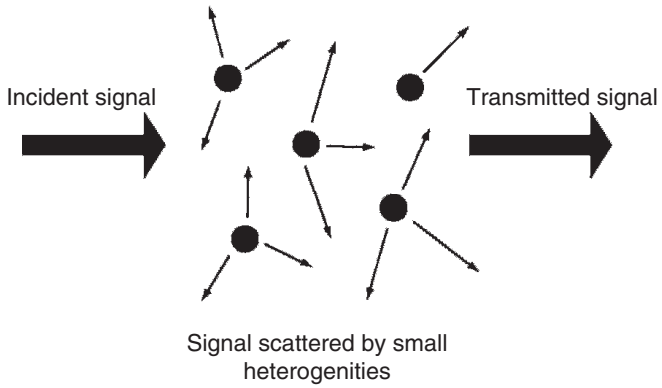

Figure 2.7: Scattering of GPR incident pulse by heterogeneity in material properties.

Radar Scattering from Surface

Electromagnetically, the roughness of a surface is measured relative to the EM wave wavelength λ . For a surface with *rms* height s, the electromagnetic roughness k_s is defined by [145]:

$$k_s = \frac{2\pi}{\lambda}s \tag{2.5}$$

The Rayleigh roughness criterion describes the condition that a surface electromagnetically can be considered smooth. Figure (2.8) geometrically shows two rays incident normally upon a surface. If the surface was perfectly flat, the electric field of the two reflected rays would have been in-phase. However, since the rough surface is higher at point B than at point A by a height h, the field of the ray reflected from point B travels a shorter distance by $2h$ with the phase difference of $\Delta\phi = 2kh$ where $k = 2\pi/\lambda$ is the wavenumber and λ is the wavelength of incident wave. For oblique incidence at angle θ as shown in Figure (2.8) the phase difference will be given by $\Delta\phi = 2kh\cos\theta$. According to the Rayleigh roughness criterion the surface is smooth if:

$$\Delta\phi < \pi/2 \tag{2.6}$$

or equivalently

$$h < \frac{\lambda}{8\cos\theta} \tag{2.7}$$

For a random surface with the *rms* surface-height s, the Rayleigh criterion can be written as:

$$s < \frac{\lambda}{8\cos\theta} \tag{2.8}$$

and $k_s < 0.8$ if $\theta = 0$.

Figure (2.9) depicts the scattering patterns for three surfaces with varying degrees of electromagnetic roughness. The pattern for the perfectly smooth surface is essentially a delta function, as shown in Figure (2.9, left). The component of the scattering pattern along the specular direction is called the coherent component because the reflected wave has a uniform phase front. The scattering pattern of the perfectly smooth surface consists of only a coherent component. If the surface is slightly rough with k_s on the order of 0.1, the scattering pattern will be dominated by the coherent component along the specular

direction, as shown in Figure (2.9, right), but the pattern also includes non-coherent components along all other directions. If the surface roughness is increased to $k_s > 2$, the coherent component becomes negligibly small and the non-coherent component becomes dominant along all directions, including the specular direction (Figure 2.9, lower panel).

The back-scattered signal arrived at the receiver is a result of either *surface scattering*, *volume scattering* or some *combination of both*. Figure (2.10, left) schematically presents surface scattering by an air-soil interface which may be the result of (1) single-scattering by facets oriented such that their surface normal points towards the radar, (2) multiple scattering involving reflections by multiple facets, or (3) resonant effects with particular sinusoidal components of the surface shape [145]. A vegetation canopy in Figure (2.10, middle) is considered as a volume-scattering medium because the layer between the soil surface and top of the canopy contains many individual scatters in the form of leaves, needles, and branches. The back scattering from vegetation often includes a component due to scattering by the soil surface as well as multiple scattering involving both the soil surface and the canopy constituents. Figure (2.10, right) displays a three layer configuration which snow layer covers a soil surface. In this case, the back-scatter generally includes: scattering by the upper surface (air-snow interface), volume scattering by the ice crystals within the snow background; surface scattering by the snow-soil interface; and multiple scattering due to two interfaces and the snow volume between them.

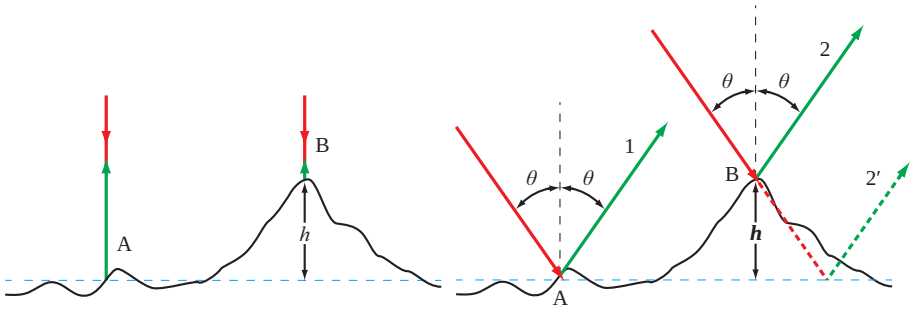

Figure 2.8: (a) normal incidence,(b) oblique incidence [145].

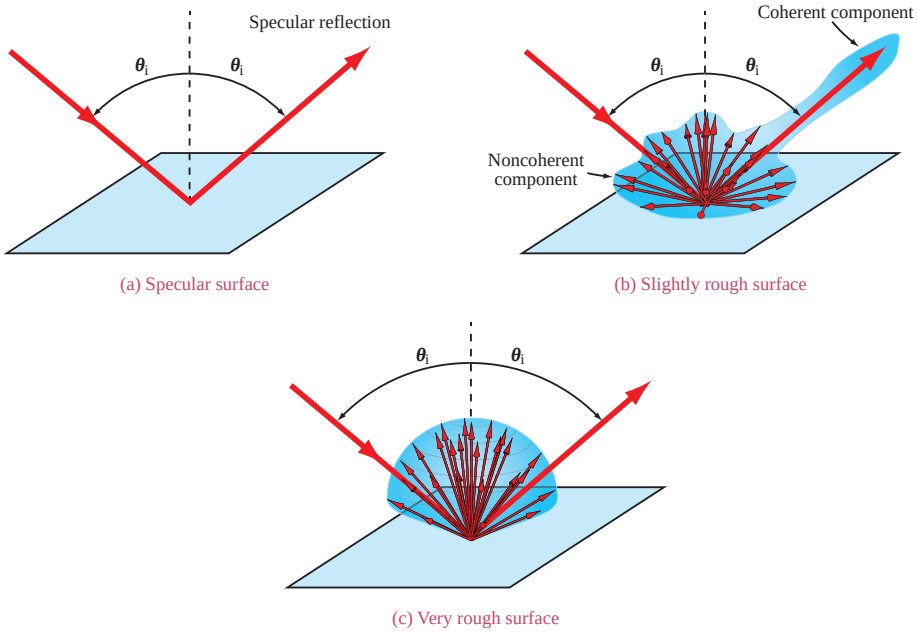

Figure 2.9: The bistatic-scattering pattern consists of a coherent component along the specular direction and a non-coherent component along all directions. For a perfectly smooth surface, only the coherent component exists, and at the opposite extreme, for a very rough surface the coherent component becomes negligibly small in comparison with the non-coherent component [145].

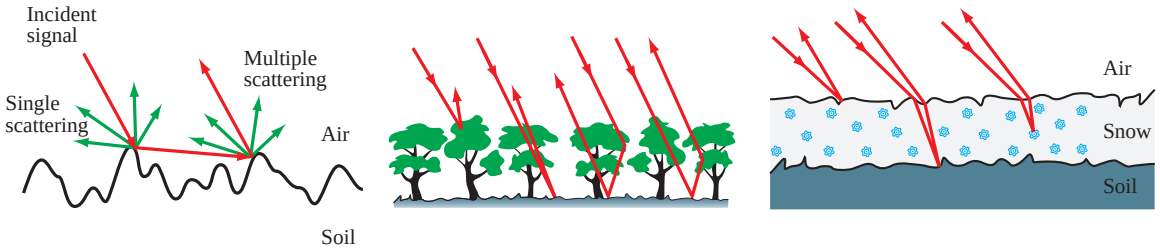

Figure 2.10: Scattering from (left) random surface, (middle) vegetation canopy, (right) snow-covered soil [145].

2.7 Resolution and Radar Range Equation

2.7.1 Radial and Lateral Resolution

Resolution indicates how precisely the position and geometrical attributes of a target such as size, shape, and thickness can be extracted. Resolution for GPR has two components: (1) depth or range resolution and (2) lateral or angular resolution. For GPR, maximum penetration depth corresponds to the maximum depth at which a buried target can be detected, and depth resolution is the minimum detectable separation in depth between two buried targets [21] [Figure (2.11)]. The spatial resolution can be dealt with in term of transmitted pulse separation that gives rise to the radial resolution of [2]:

$$\Delta r \geq \frac{WV}{4} \tag{2.9}$$

and the lateral resolution:

$$\Delta l \geq \sqrt{\frac{rWV}{2}} \tag{2.10}$$

where r is the distance to the source, and W is the pulse width at half amplitude, and V is velocity of pulse. The depth resolution length is independent of distance from the source, however, at larger distances, it is affected by pulse dispersion and attenuation. The resolution is increased as the bandwidth is increased, and this usually requires that the center frequency of the radar increases. There must be a compromise between range and resolution for GPR systems.

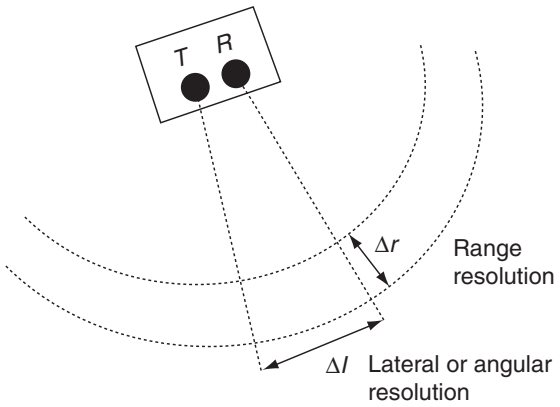

Figure 2.11: Resolution for GPR divides into two parts; namely, range resolution and lateral (or angular) resolution [2].

2.7.2 Radar Range Equation

The radar range equation (RRE) is used to estimate the maximum range at which targets can be detected for the given geologic material properties, attenuation characteristics and system parameters. The choice of radar equation for radar sounding analysis, and radar in general, has important implications for

scientific interpretation of radar echoes. Radar signal range in the ground is affected by a number of factors, including: radar system performance, attenuation, and the reflection properties at a boundary where the electrical properties vary. Therefore, even though there is one fundamental radar equation, it will take different forms depending on the properties of the target and source geometry. These forms explain different aspects of the problem and highlight sensitivity to certain parameters, such as the exponent of geometric power fall-off or the origin of certain multiplying constants. Haynes [47] presents a comprehensive treatment of radar equations for low-frequency radar sounding and radar in general that emphasizes different targets and sources geometries.

One such equation that relates the received-signal power, P_r, to transmitted signal power, P_s, is mathematically expressed as [3]:

$$P_r = \xi_t \xi_r G_t G_r \; g C_s \frac{V^2}{4\pi\nu^2} \frac{e^{-4\alpha L}}{16\pi^2 L^4} P_s \tag{2.11}$$

where the parameters are:

P_r: Received signal power
ξ_t: Transmitter antenna efficiency
ξ_r: Receiver antenna efficiency
G_t: Transmitter antenna gain
G_r: Receiver antenna gain
g: Back-scatter gain of target
C_s: Target scattering cross section area
ν: Frequency
α: Attenuation coefficient of medium (absorption and scattering)
V: Propagation velocity in medium
L: Target distance; and L^4 presents spherical spreading loss
P_s: Source signal power

The system performance is defined as the ratio of the minimum received-signal power, $P_{r_{min}}$, to the transmitted signal power, P_s, given by $Q = P_{r_{min}}/P_s$.

Smooth, plane specular reflector: The power returned by a smooth specular reflector [Figure (2.12), left] is reduced by power reflection coefficient, Γ, (equation (1.125)) of the interface radiating upwards from a distance twice as far away as the boundary. Thus, the back-scatter gain and scattering cross-section product is:

$$g C_s = \pi L^2 \Gamma \tag{2.12}$$

therefore, the received power is:

$$P_r = \xi_t \xi_r G_t G_r \Gamma \frac{V^2}{64\pi^2\nu^2} \frac{e^{-4\alpha L}}{L^2} P_s \tag{2.13}$$

Rough, plane specular reflector: For a rough, specular reflector the return power is not simply calculated. The cross-sectional area of the target is estimated by the area of the first Fresnel zone [Figure (2.12), right]. The first Fresnel zone is an area of the surface for which reflected signals travel a path with the length less than $L + \frac{\lambda}{4}$ where L is the normal distance to the plane, and λ is the wavelength of signal in the medium. The effective radius of the circular area on the target is:

$$r = \sqrt{\left(L + \frac{\lambda}{4}\right)^2 - L^2} \tag{2.14}$$

and the area of the first Fresnel zone is:

$$C_s = \pi r^2 = \pi \left(\frac{\lambda^2}{16} + \frac{\lambda L}{2}\right) \tag{2.15}$$

for $L \gg \lambda$

$$C_s \simeq \frac{\pi \lambda L}{2} \tag{2.16}$$

and

$$gC_s \simeq \frac{\pi \lambda L \Gamma}{2} = \frac{\pi L \Gamma V}{2\nu} \tag{2.17}$$

then, the received power will be:

$$P_r = \xi_t \xi_r G_t G_r \Gamma \frac{V^3}{128\pi^2 \nu^3} \frac{e^{-4\alpha L}}{L^3} P_s \tag{2.18}$$

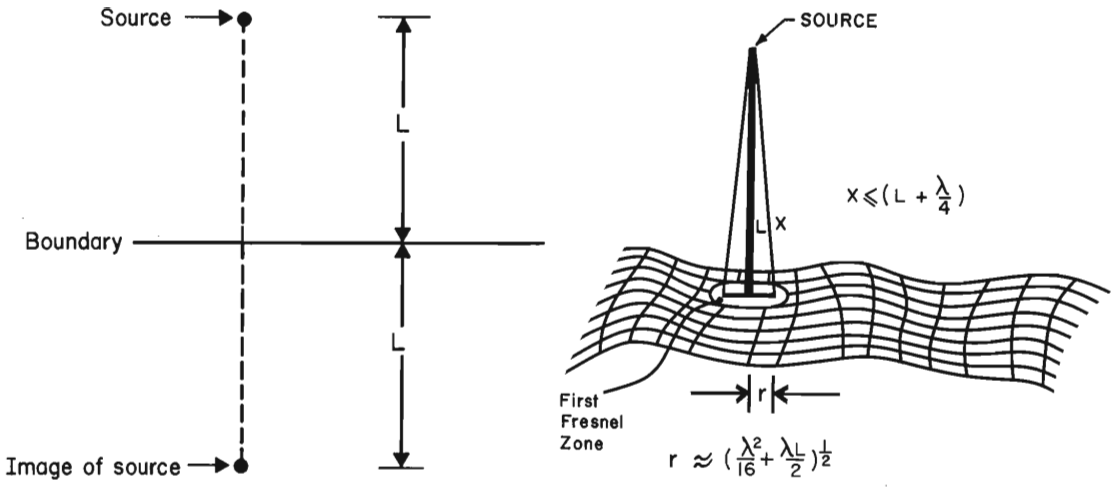

Figure 2.12: Reflection from planar boundary. (left) a smooth planar boundary and (right) a rough planar boundary [3].

Point target: In general gC_s is a complicated function of frequency and angle of illumination. For most computational purposes, it is necessary to specify gC_s from detailed knowledge of the specific point target under consideration. For some special applications, the Rayleigh law of scattering is useful [see equation (2.4)]. A conducting sphere with radius, a, which is much less than the wavelength of the exciting signal has an effective cross-sectional area and backscatter gain:

$$gC_s = \frac{64\pi^5 a^6 \nu^4}{V^4} \tag{2.19}$$

The Rayleigh scattering law demonstrates the strong frequency dependence of the gC_s. Finally, the received power is expressed by:

$$P_r = \xi_t \xi_r G_t G_r \frac{\pi^2 a^6 \nu^2}{V^2} \frac{e^{-4\alpha L}}{L^4} P_s \tag{2.20}$$

2.8 Glacier Radar Sounding

Radio-echo sounding (RES) is a proven tool for characterizing the geometry, internal structure and environment of ice sheets and glaciers. A deep ice sounding usually uses frequencies between 1 and 300 MHz. Radar sounding of glacier characteristics can be measured from aircraft and from moving surface vehicles. Radar sounding has the following physical basis: a short electromagnetic pulse is emitted by an antenna mounted on a platform moving over the glacier surface. The pulse penetrates the glacier and is reflected by inhomogeneities in the ice and by the bedrock, and finally an echo returns to the antenna. The ice thickness, depths of reflecting interfaces, and mean glacier temperatures and velocities can be determined by the analysis of the pulse travel time in the ice [9].

Glaciers, as geophysical objects, have a very complex structure that depends on the physical conditions of their formation, such as precipitation cycles, climate and weather changes, and snow and firn

metamorphism. As glaciers move over bedrock, they may entrap rocks, resulting in moraines layer formation. Further, irregular glacier movement disturbs the continuity of the ice, resulting in the formation of deep cracks, fractures, and voids. Thus, the inhomogeneity of glacial ice is caused not only by variations in the ice itself, but also by moraine intrusions, air bubbles, and sometimes liquid water. Ambient air temperatures, solar radiation, and the thermodynamic interaction with the underlying bedrock determine the temperature distribution in the glacier [9].

Glacial ice is a nonmagnetic ($\mu_{ice} \approx \mu_0$) dielectric, and its electrical properties can be described by only a complex permittivity. For glacial ice $\tan\delta \ll 1$, thus it is a low loss medium. By measuring the two-way travel time of propagating electromagnetic wave, $\Delta\tau$, it is possible to calculate the ice thickness:

$$h = \frac{1}{2} V_{ice}\ \Delta\tau \tag{2.21}$$

where V_{ice} is speed of the electromagnetic wave in ice, that is obtained from permittivity of ice. The electromagnetic wave loses energy as it travels through the ice, so the returning echo is smaller than the transmitted pulse. The total change in power of the signal during its travel to the bedrock and back to the receiver is described by [9]:

$$N_T = N_G + N_R + N_\phi + N_S + N_A + N_P \tag{2.22}$$

where: N_G is geometrical spreading loss, N_R losses due to reflection from interfaces, N_ϕ changes in signal strength due to focusing effects, N_S losses due to scattering, N_A losses due to signal absorption in ice and N_P apparent losses due to rotation in polarization of the received signal relative to the orientation of the receiving antenna.

The spatial variation in glacial ice's physical properties is considerable, and the largest changes of wave amplitude occur within the body of the glacier that are caused by changes in ice density, temperature and liquid water content. The variation of electrical parameters between different layers and the boundary geometry of those layers are the most important features for radar sounding of glaciers. Generally, an ice sheet or glacier can be described using a model consists of multiple homogeneous layers having flat interfaces with varying thickness and permittivity. The pulse duration to be used is determined by the system resolution required, *i.e.*, it depends on the distance between the interfaces to be measured. For example, if the thickness resolution is 10 m, the duration of sounding pulse should not exceed 0.1 μs. The choice of operating frequency for a particular purpose is determined by: the conditions of wave propagation in the ice, the desired rise time of the sounding pulse, and limitations of the platform upon which the system is mounted.

2.9 Planetary Radar Sounding: General Aspects

The platforms for planetary studies by radar system can be stationary on the earth surface or transmitter and/or the receiver onboard a spacecraft orbiting or passing on a planetary object. The spaceborne radar systems are classified in two categories: (1) imaging radar (also known as Synthetic Aperture Radar (SAR)); and (2) sounding radar. One or both have been utilized to observe planetary surfaces and subsurface with great success, at the Moon, Venus, Mars, and Titan. The two techniques use the same basic principle of monostatic (colocated transmitter and receiver) radar, but differ in geometry of observation, choice of frequency and bandwidth, and data processing algorithms. In this study we only consider sounding radar [110].

Planetary radar exploration (*e.g.*, Moon, Mars, Venus, Galilean satellites of Jupiter) is based on transmitting a radio signal toward the target and then receiving and analyzing the echos. Radar has been widely used in planetary studies for decades ([110] and the reference there in). In planetary exploration the application of radar data can be of a priority interest since: (1) planetary shallow crusts are generally dry and cold which minimizes the attenuation and dispersion of the electromagnetic waves, and (2) radar measurements do not require a physical contact between antenna and soil. These critical properties enable radar application to investigate much deeper subsurface of bodies in the solar system.
The planetary crusts that are aimed to be explored by radar sounders can be divided in two groups: (1) rocky materials such as those found on the Moon, Mars, Venus, and asteroids. Regolith, basalt, hydrated salts, dry clay, and meteorites are studied to simulate this type of materials. (2) icy materials such as those in lunar cold traps and on Martian polar caps, Europa, Ganymede, and comets. Water

ice, CO_2 ice, ice-dust mixtures, and saline ice are usually considered good analogues for the this group. As in terrestrial samples, dielectric properties of planetary materials depend on density (porosity), water content and salinity, mineral composition (oxides content), temperature, and frequency.
To maximize the penetrating depth, longer wavelengths are used in sounding radar. Sounding radar frequency are typically in the range of 3 to 100 MHz. Antennas operating at such frequencies are quite large with a simple design, such as a dipole, to have a reasonably low mass to be installed on a spacecraft. Note that, on Earth, deep penetration of high-frequency radio waves, *i.e.*, on the order of a few kilometers, has been extensively reported only through the Greenland and Antarctic ice sheets (e.g., [126], [25]). Similarly, dry and cold geological materials forming the outer shells of rocky and icy planets and satellites are also favorable environments for deep radio wave propagation.

The resulting data of radar sounding of planetary bodies is a two-dimensional image known as a *radargram* with the dimensions of along-track and time-delay which depends on the penetrating depth. Bright returns in a radargram indicate strong contrasts in the dielectric properties of materials at geologic interfaces and can provide geometric information that reveals subsurface structure. Sounding radar receives the back scattered echoes from the nadir direction, which includes the surface of terrain directly beneath the sensor. The first arrival echoes are attributed to the surface, and the later echoes may result from the signal encountering interfaces between subsurface layers of contrasting permittivity.

Echoes arising from cross-track surface topography may overprint echoes from the nadir subsurface that arrive with the same time delay, so making interpretation more challenging. In some cases, the cross-track clutter obscures subsurface echoes so that separating them is impossible. A common solution is to use digital elevation data, if available, to generate a synthetic radargram that could simulate the apparent position and intensity of echoes from cross-track clutter [110].

Six orbiting radar sounders and five GPRs mounted on rovers/landers have been employed so far to explore the Moon, Mars, and comet 67P/GC. Planned missions to the icy moons of Jupiter will also depend heavily on radar sounders to detect evidence of an internal ocean on Europa and to understand the habitability conditions on Europa, Ganymede, and Callisto. In the next sections, radar sounding of the Moon and Mars and Jupiter icy moons is over viewed. In particular, in Chapter 6 some acquired radar data sets on Moon and Mars are analyzed in detail to estimate the attenuation of the explored subsurface.

2.9.1 Overview of Mars Radar-Missions

Radar sounding of the Mars subsurface provided evidence for the presence of ice and potentially liquid water near the surface. One particular focus of investigations, since 2005, has been the search for basal liquid water in the south polar layered deposits (SPLD).

Mars Advanced Radar for Subsurface and Ionospheric Sounding (MARSIS)

The Polar Layer Deposit (PLD) have proven to be ideal targets for radar sounding. The European Space Agency (ESA) selected a multifrequency coherent orbiting radar, known as Mars Advanced Radar for Subsurface and Ionospheric Sounding (MARSIS) ([108], [109], [54]), to fly on the Mars Express mission in 2005. MARSIS uses a complex multi-frequency sounder, with modes for subsurface and ionospheric sounding. In the subsurface mode, MARSIS transmits a series of radar pulses, that is, a chirp with duration 250 μs and is linearly modulated in frequency over a bandwidth $B = 1\ MHz$. The central frequency of the chirp is selected among 4 different values, 1.8, 3, 4 and 5 MHz. The choice of the central frequency is made according to the predicted Solar Zenith Angle (SZA), in order to ensure that the working chirp frequency is above the cut off plasma frequency characterizing the local Mars ionosphere. The antenna system consists of a main two-element dipole that was 40 m in length, and a secondary receiver-only monopole antenna for identifying off-nadir clutter in the subsurface modes (Figure (2.13)).

MARSIS was able to penetrate almost 4 km of the Martian surface in the south polar region, detecting the interface between bottom of the polar deposits and the bedrock [111]. Because of the surface smoothness in the investigated area, topographic roughness is well below the MARSIS wavelength and scattering is almost fully coherent. Under these conditions, the size of the MARSIS footprint is well approximated by the first Fresnel zone. The radius of this zone ranges between 3 and 5 km, depending on satellite altitude and frequency.

The objectives of MARSIS subsurface mission were: (1) to detect, map, and characterize interfaces related to water, both liquid and solid, in the subsurface of Martian crust; (2) to detect geologic interfaces and characterize the surface for roughness and radar properties ([97], [69], [96], [68]). The ionospheric mode was intended to measure ionospheric properties that might affect the subsurface signals, and to study the characteristics of the ionosphere itself.

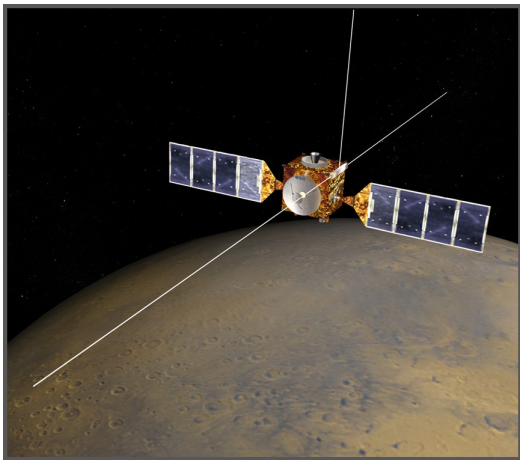

Figure 2.13: MARSIS antenna configuration on Mars Express.

SHAllow RADar (SHARAD)

SHAllow RADar (SHARAD) is a subsurface sounding radar provided by ASI (Agenzia Spaziale Italiana, the Italian Space Agency) as a Facility Instrument to the NASA's 2005 Mars Reconnaissance Orbiter (MRO) mission (launched in 2005) for the characterization of the upper kilometers of the Martian surface [123], [124]. The SHARAD was carried on NASA's Mars Reconnaissance Orbiter, which arrived at Mars in 2006. SHARAD operates at a central frequency of 20 MHz, with a 10 MHz bandwidth that provides a range resolution of 15 m in free space. SHARAD was intended to obtain higher resolution sounding data, using a higher frequency, at the expense of deep penetration capability. The higher vertical resolution of SHARAD allowed the delineation of fine structure of PLD, and provided evidence for the sequence of events responsible for the evolution of the PLD. The primary objective of the SHARAD is to map, in selected locales, dielectric interfaces to several hundred meters depth in the Martian subsurface and to produce a detailed picture of the shallow stratigraphy [124].

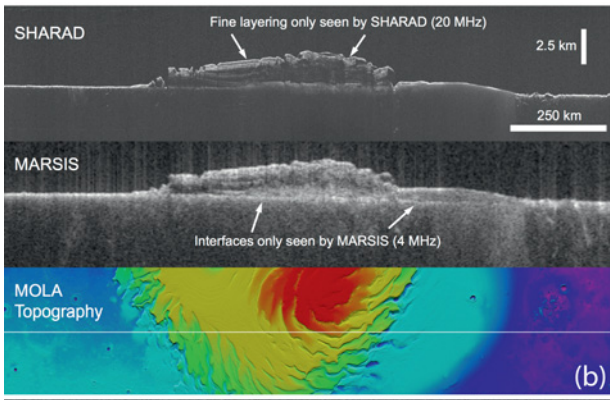

Figure 2.14: SHARAD (top) and MARSIS (middle) radargrams and ground track are shown on shaded relief topography (bottom) of the north polar plateau of Mars. The radargrams have been corrected for the speed of radio waves in ice for all points below the nadir ground track surface echo (taken from [110]).

Independent of any ability to directly detect water or ice, SHARAD was expected to collect significant new scientific data available toward addressing critical scientific problems on Mars, including the

existence and distribution of buried paleo-channels, subsurface layering, an improved understanding of the electromagnetic properties of the "stealth" region, insights into the nature of patterned ground, and other morphologies that suggest the presence of water at present or in the past. Thus MARSIS and SHARAD provide a complementary view into the subsurface of Mars (Figure (2.14)).

MOSIR and RoPeR

Tianwen-1 is China's first Mars mission that was launched on 23 July 2020. There are 13 scientific payloads on Tianwen-1, 7 payloads on the orbiter, and 6 payloads on the rover. The rover that is called *Zhurong* has landed in Utopia Planitia in Mars's northern Hemisphere, a topographically transitional region between the southern and northern highlands. It is expected that Tianwen-1 will contribute significantly to advance our scientific knowledge of Mars.

Mars Orbiter Scientific Investigation Radar (MOSIR) is a payload on the orbiter. The MOSIR uses two frequency channels, $10-20$ MHz and $30-50$, MHz and has wide-band dipole antennas. The detection depth, depending on the dielectric properties of the subsurface material is $\sim 100-1000\ m$. The instrument can work in HH (horizontal transmission–horizontal reception) and HV (horizontal transmission–vertical reception) polarization modes. MOSIR uses linear frequency modulation techniques for pulse compression. The scientific objective of MOSIR is to survey the characteristics and distribution of soil and structures of Martian subsurface, survey the subsurface in search for ice and liquid water, and estimate the ionospheric total electron content.

Mars Rover Penetrating Radar (RoPeR) payload on the Zhurong rover, is equipped with a high and a low frequency channel with the central frequency of 1300 MHz and 55 MHz, and bandwidth $450-2150$ MHz and $15-95$ MHz, respectively. The detection depth, depending on the dielectric properties of subsurface material, is approximately $3-10$ m and $10-100$ m with a vertical resolution of 1 cm and 1 m, respectively. The scientific objective of RoPeR is to explore the soil structure of the Mars in roving area and to search for water ice. The radar transmitting signal is a kind of linear frequency modulation. Figure (2.15) illustrates the position of payloads on the orbiter and rover of Tianwen-1.

Radar Imager for Mars' Subsurface Experiment (RIMFAX)

Radar Imager for Mars' Subsurface Experiment (RIMFAX) is a part of the payload for NASA's Mars' 2020 Perseverance Rover, which landed at in Jezero crater in February [45], [32]. RIMFAX is a Frequency Modulated Continuous Wave (FMCW) radar, which transmits a signal in a range of frequencies, rather than a single wide-band pulse. The operating frequency range of 150–1200 MHz covers the typical frequencies of GPR used in geology. In general, the full bandwidth (with effective center frequency of 675 MHz) will be used for shallow imaging down to several meters, and a reduced bandwidth of the lower frequencies (center frequency 375 MHz) will be used for imaging deeper structures. RIMFAX provides the capability for the rover investigations of Mars to image the shallow subsurface under the rover. The principal goals of the RIMFAX is to investigate the subsurface structure, and to provide information regarding subsurface composition and dielectric properties of Jezero crater, given that the river delta to be studied at this site is a prime target to look for signs of past life/habitable environments. Figure (2.16) schematically presents the sites where the rovers of various mission landed on the Mars.

The performance of RIMFAX, in terms of depth resolution and depth of penetration, depends mainly on the complex permittivity and density of the material through which the radar signal propagates. RIMFAX can do time lapse stationary soundings over the diurnal cycle detecting changes in the surface reflection coefficient and the amplitude and phase from reflectors in the shallow subsurface. These measurements can possibly reveal interaction between the water in the atmosphere and surface of Mars. Figure (2.17) presents an illustration of RIMFAX mounted on the Mars 2020 rover traversing the Martian surface.

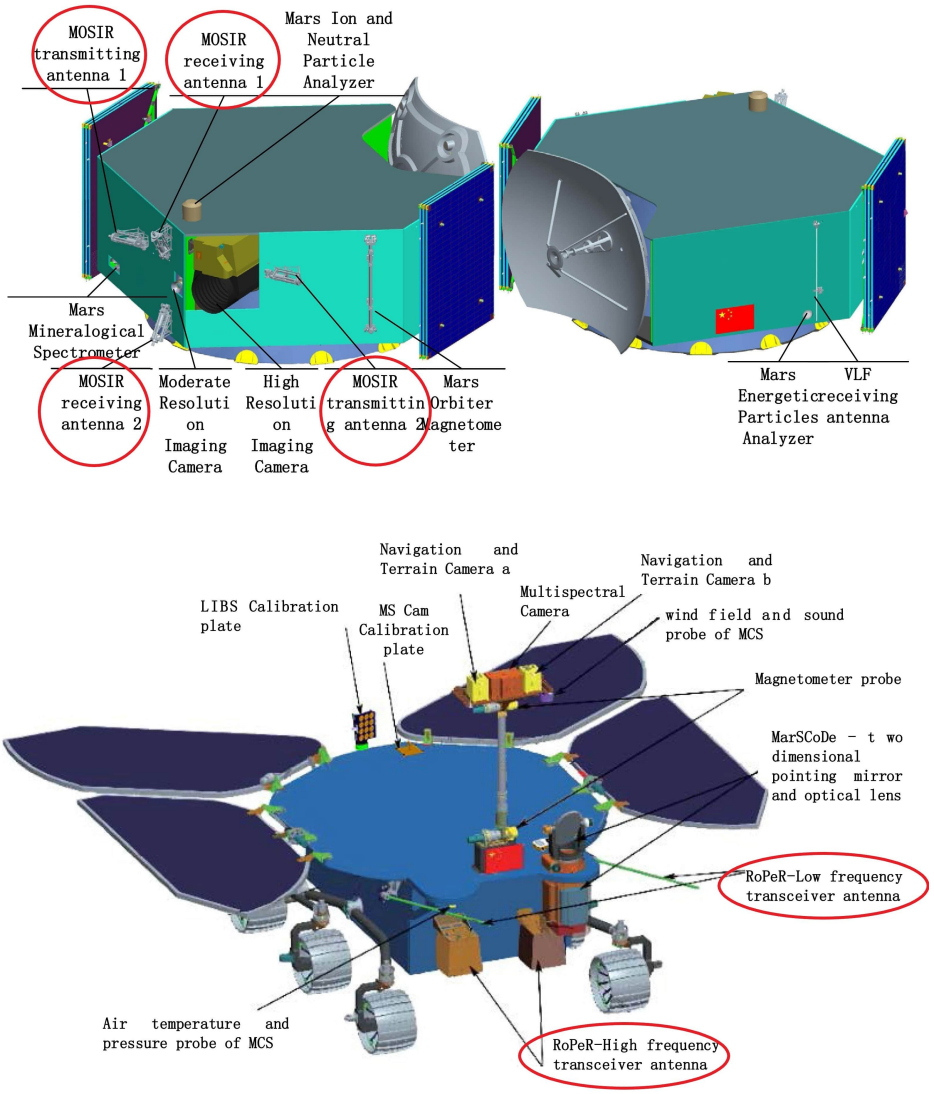

Figure 2.15: The position of payloads on the orbiter (upper panel) and rover (lower panel) of Tianwen-1 [154].

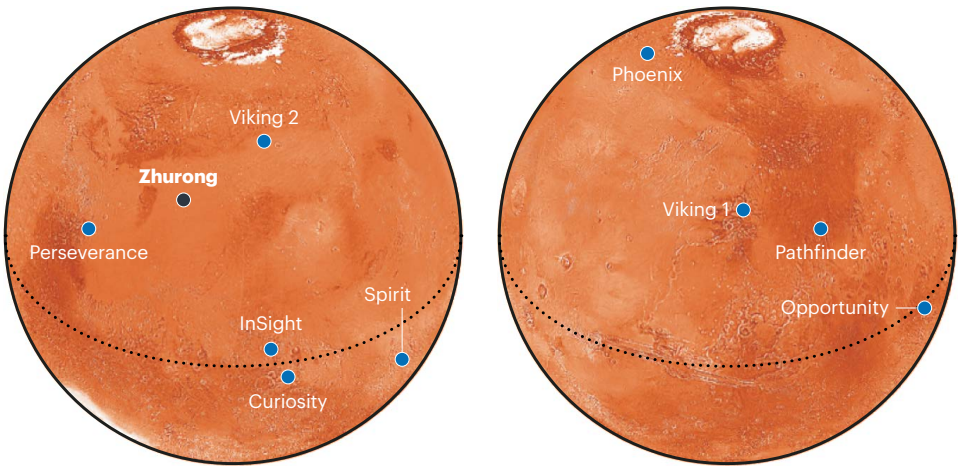

Figure 2.16: The landing sites of the rovers on the Mars [78].

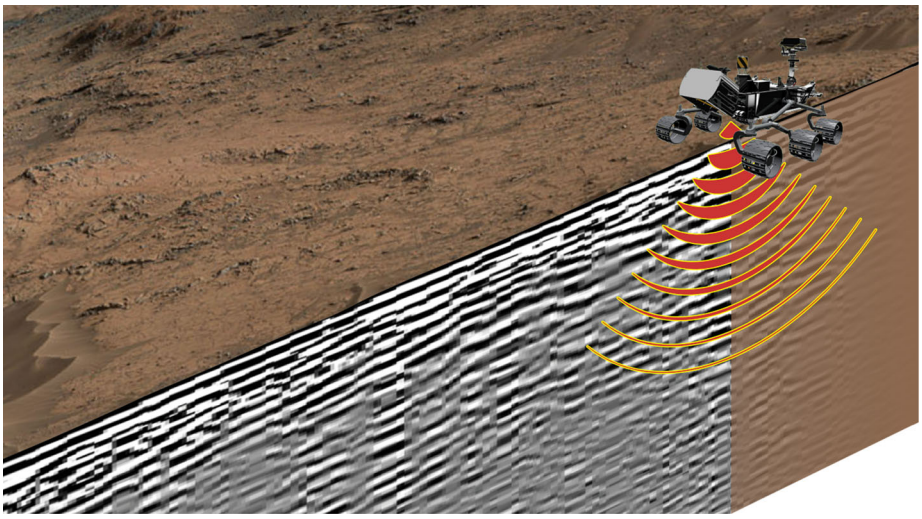

Figure 2.17: Illustration of the Mars 2020 Perseverance rover traversing the surface of Mars, including RIMFAX transmission of radar waves into the subsurface and visualization of subsurface geomorphology and layering in collected data [45].

2.9.2 Overview of Moon Radar-Missions

In the last decades, space-borne and rover-deployed ground penetrating radar has progressively become the most suitable geophysical technique to investigate lunar subsurface stratigraphy. Two different experiments involving subsurface radio wave propagation were tested during the Apollo 17 mission: (1) Surface Electrical Properties (SEP) experiment onboard the Lunar Roving Vehicle [129] and (2) Apollo Lunar Sounder Experiment (ALSE) onboard the Apollo spacecraft [112]. SEP was devoted to examine the electrical properties of the upper portion of the lunar subsurface (about 2 km) and showed that the investigated layer behaves like a dielectric insulator. ALSE, instead, was a chirp radar equiepped with two antennas, a 20 m long high fequency antenna and a 2.7 m very high frequency Yagi antenna. ALSE operated at three central frequencies 5.3, 15.8, and 160 MHz that imaged the bottom of various buried craters and detected several subsurface geological units, like those in Mare Crisium, up to a depth of about 1000–1400 m [84]. The main goals of ALSE were: (1) sounding the structure of the lunar subsurface, (2) creating a topographic map of the surface, and (3) measuring galactic noise around the moon.

In 2007, Japan Aerospace Exploration Agency launched the Kaguya missions. The orbiting spacecraft (SELENE) was equipped with a GPR, Lunar Radar Sounder (LRS) for exploration of lunar crust down to a depth of 1 to 2 km. The LRS operated at the central frequency of 5 MHz with a 2 MHz bandwidth which provided a free space range resolution of 75 m. LRS was designed primarily to investigate subsurface stratification and tectonic features. The deepest reflector was found in the northeastern Mare Imbrium at an apparent depth of 1050 m [92]. The mission is now concluded.

The first attempt to survey the Moon's subsurface using a GPR onboard a rover was made during the Chang'E-3 (CE-3) mission by China in 2013 which was equipped with low and high frequency antennas [50]. The rover carrying the GPR is called Yutu. The Lunar Penetrating Radar (LPR) operated at 60 and 500 MHz frequencies. The high-frequency GPR observations revealed a detailed subsurface structure up to a depth of about 10 m. The rover collected some data but got stuck in the lunar regolith after about 100 m of navigation. On 3 January 2019, the Chang'E-4 (CE-4) lander touched down on the eastern floor of Von Kármán crater, becoming the first spacecraft to land safely on the Moon's farside ([71], [150]). The mission was planned to last three months. However, after more than three years, the Yutu-2 rover is still operating and has acquired about 1000 m of radar data. The CE-4 LPR is a dual-frequency GPR system same as Chang'E-3, operating at 60 MHz (low frequency) and 500 MHz (high frequency), with a frequency bandwidth of 40 to 80 MHz and 250 to 750 MHz, respectively. The goals of the two missions are to estimate the depth of the lunar regolith and determine the structure of the lunar subsurface along the rover path. However, interpretation of the low frequency data is still challenging due to antenna coupling with the rover and lunar surface, in addition to limited length of the radar profile, $\sim$ 100 m ([50],[31]). The low-frequency signals acquired by both rovers are strongly affected by very large electromagnetic disturbances due to antenna coupling with the rover and lunar surface that

interfere with the radar returns from the subsurface. Thus, these data cannot be considered reliable and should not be used to assess lunar geology at landing sites [106].

A different type of GPR was tested during the first sample return mission operated by CNSA on the moon. The rover landed on Oceanus Procellarum and consisted of a lander focused on extracting lunar soil samples and sending them back to Earth via a modular system (ascender–orbiter–returner). The Lunar Regolith Penetrating Radar (LRPR) on board Chang'E-5 mission consisted of a static array of 12 fixed high-frequency antennas located at the base of the lander around the drill at a height of about 90 cm above the ground. Each antenna could transmit and receive signals, meaning that when one antenna transmitted, the other 11 were set to receiving mode. The goal was to reconstruct the structure of the regolith in the drilling area before sample extraction by using a multiview/multistatic configuration. The radar imaged the hyperfine structure of about 2 m of regolith and the distribution of lunar fines and rock fragments. Two kilograms of lunar soil was returned to Earth on 16 December 2020, and some samples were measured to estimate their dielectric properties e.g., [135].

2.9.3 Overview of Jupiter Icy Moons-Missions

Two radar systems are expected to explore the icy Jovian moons:

(1) Radar for Icy Moon Exploration (RIME), a 9 MHz radar of the ESA mission JUICE which is planned to be launched in 2023 and expected to reach Jupiter in 2031 [16]. RIME has been chosen as the main geophysical instrument to sound Ganymede, Europa, and Callisto down to a depth of 9 km. RIME is equipped with a 16 m dipolar antenna. The goal of this radar is investigations of Jupiter and its system with particular emphasis on Ganymede as a planetary body and potential habitability [40].

(2) Radar for Europa Assessment and Sounding Ocean to Near-surface (REASON), which will be mounted on the NASA Europa Clipper spacecraft and launched in 2024 to arrive at Jupiter in 2030. This radar is equipped with two sets of antennas: a single 16 m low-frequency dipolar antenna, like that designed for RIME, and two 2.6 m high frequency dipolar antennas. REASON will be devoted to investigating Europa.

2.9.4 ESA Mission to Venus

The European Space Agency (ESA) mission to Venus, EnVision, will carry the low-frequency Subsurface Radar Sounder (SRS), which will be equipped with a single dipolar antenna similar to that designed for RIME. It is expected that SRS will be able to probe buried craters and layers of lava flows and investigate the structure of the tesserae, a highly deformed terrain that may move like Earth's continents. This mission will be the most challenging performed thus far by a radar sounder because Venus is likely to have a hot subsurface that will not allow the signal penetration. The mission is planned for the beginning of the decade 2030–2031 after a 15 month voyage to reach the planet.

The EnVision mission aims to address three fundamental questions about the science of Venus: (1) How geologically active is Venus today? (2) How have the surface and interior of Venus evolved? (3) How has Venus' climate become so hostile? SRS will focus on the second question and contribute to providing direct evidence of the geological history of the Venusian crust by imaging the shallow subsurface profile ([139]).

The characteristics of orbiter and payload radar sounders and their main goals are summarized in Tables (2.1), (2.2) and (2.3).

Table 2.1: Some characteristics of the orbiter radar sounders (taken from [105]).

Radar instrument	**Type of signal**	**Cent. freq** (MHz)	**BW** (MHz)	**Vertical Res. In free space** (m)	**Altitude** (km)	**Mission**	**Target**	**Year of launch**
ALSE	chirp	5,16,160	0.5, 1.6, 16	150, 50, 5	110	Apollo 17	Moon	1972
MARSIS	chirp	1.8, 3, 4, 5	1	150	400-800	Mars Express	Mars	2003
SHARAD	chirp	20	10	15	300	Mars Reconnaissance Orbiter	Mars	2007
LRS	chirp	5	2	75	100	Kaguya	Moon	2007
CONSERT	impulse	90	10	30	10-100	Rosetta (orbiter/ lander)	67P/ Churyumov Gerasimenko comet	2004
MOSIR	chirp	2.5, 17.5, 40	5-20	30-7.5	265-800	Tianwen-1	Mars	2020
RIME	chirp	9	1, 3	50, 150		JUICE	Jupiter icy moons	2023
REASON	chirp	9, 60	1, 10	150, 15		Europa Clipper	Europa	2024
SRS	chirp	9	6	20		EnVision	Venus	2031

Table 2.2: Some characteristics of GPR on rover (taken from [105]).

Radar instrument	**Type of signal**	**Cent. freq** (MHz)	**BW** (MHz)	**Vertical Res. In free space (m)**	**Step size** (m)	**Mission**	**Target**	**Year of launch**
LPR	impulse	60 500	40 500	~ 6 ~ 0.5	~0.08 0.04	Chang'e-3	Moon: Mare Imbrium	2013
LPR	impulse	60 500	40 500	~ 6 ~ 0.5	~0.08 0.04	Chang'e-4	Moon: Von Karman crater	2018
LRPR	impulse	2000	2000	~ 0.1	-	Chang'e-5	Moon: Oceanus Procellarum	2020
RIMFAX	FMCW	375 675	150-600 150-1200	~ 0.3 ~ 0.15	0.05,0.1	Mars2020	Mars: Jezero crater	2020
RoPeR	chirp	55 1300	15-95 450-2150	~ 2 ~ 0.1	0.5	Tianwen-1	Mars: Utopia Planitia	2020
WISDOM	Step frequency	500 3000	2500	0.11	0.1	ExoMars	Mars	2022

Table 2.3: Main goals of the radars or planetary exploration.

Radar instrument	Main goals
ALSE	(1) sounding the structure of the lunar subsurface (2) creating a topographic map of the surface (3) measuring galactic noise around the moon
MARSIS	(1) detect, map, and characterize interfaces related to water, both liquid and solid, in the subsurface of Martian crust (2) detect geologic interfaces and characterize the surface for roughness and radar properties.
SHARAD	(1) In selected locales, mapping dielectric interfaces to several hundred meters depth in the Martian subsurface (2) produce a detailed picture of the shallow stratigraphy
LRS	Investigation of lunar subsurface stratification and tectonic features
CONSERT	Survey the internal structure of 67P/CG comet
MOSIR	(1) survey the characteristics and distribution of soil and structures of Martian subsurface (2) survey the subsurface in search for ice and liquid water (3) estimate the ionospheric total electron content
RIME	Investigations of Jupiter and its system with particular emphasis on Ganymede as a planetary body and potential habitability
REASON	Investigating the Europa
SRS	Investigation of buried craters and layers of lava flows subsurface the Venus and investigating the structure of the tesserae
LPR	Estimate the depth of the lunar regolith and determine the structure of the lunar subsurface along the rover path
LRPR	Reconstruct the structure of the regolith in the drilling area before sample extraction
RIMFAX	Investigate the subsurface structure to provide information regarding subsurface composition and dielectric properties of Jezero crater om Mars, to look for signs of past life-habitable environments
RoPeR	Exploration of the soil structure of the Mars in roving area and search for water ice

Chapter 3

General Discrete Inverse Problems: Probabilistic Approach

3.1 Introduction

Geophysical methods are based on the study of different physical fields being propagated through the earth's interior like electromagnetic field and seismic wave. The responses to these fields mainly depends on the physical properties of the explored medium. The conventional approach to geophysical data analysis consists of constructing different geological models and comparing the theoretical geophysical data computed for these models with the observed data. Numerical modeling of geophysical data for given model parameters is called a *forward problem*. The forward problem solution can predict geophysical data for specific geological structures. The final goal of geophysical observation is determining the geological structures from the geophysical data. It is a very difficult problem due to the complex structure of the Earth's interior. Usually the real geology is approximated by simple models, and then, the model parameters are retrieved from the data. This problem is called an *inverse problem*. The success of geophysical interpretation depends on effectively solving the corresponding inverse problems to approximate real geological structures by reasonable models.

In this Chapter, the general framework of probabilistic approach to inverse problems ([86], [138]) is outlined and then will be used in the following chapters.

3.2 Probability

Considering that the probability distribution P is defined over a subset A of the space S. For a random variable x, the probability that A will be in S is characterized by probability density function (*pdf*), $f(x)$, that is always a positive function:

$$P(A) = \int_A f(x)\, dx \tag{3.1}$$

with the property that

$$\int_{-\infty}^{+\infty} f(x)\, dx = 1 \tag{3.2}$$

The simplest *pdf* is the uniform distribution. This distribution states that all values within a given range are equally likely. Formally the uniform distribution on the interval $[x_1, x_2]$ has the probability density function of the form:

$$f(x) = \begin{cases} \frac{1}{x_1 - x_2} & \text{if } x_1 \leq x \leq x_2 \\ 0 & \text{otherwise} \end{cases} \tag{3.3}$$

The most commonly used *pdf* is the normal or Gaussian probability density function. A Gaussian distribution with mean of μ and standard deviation of σ_x is defined by:

$$f\left(x, \mu, \sigma_x^2\right) = \frac{1}{\sqrt{2\pi\sigma_x^2}} \exp\left(-\frac{(x-\mu)^2}{2\sigma_x^2}\right) \tag{3.4}$$

The mean value specifies the center of distribution, and the variance determines the spread of *pdf*. Theoretically it is elegant, and arises naturally in a number of situations. Importantly, the analytical properties of the Gaussian function make it very common. The Gaussian function is easy to manipulate, and its form is so well understood that we often assume quantities are distributed normally, even though they are not entirely Gaussian. Figure (3.1) for example presents a Gaussian distribution with mean of μ and standard deviation of σ.

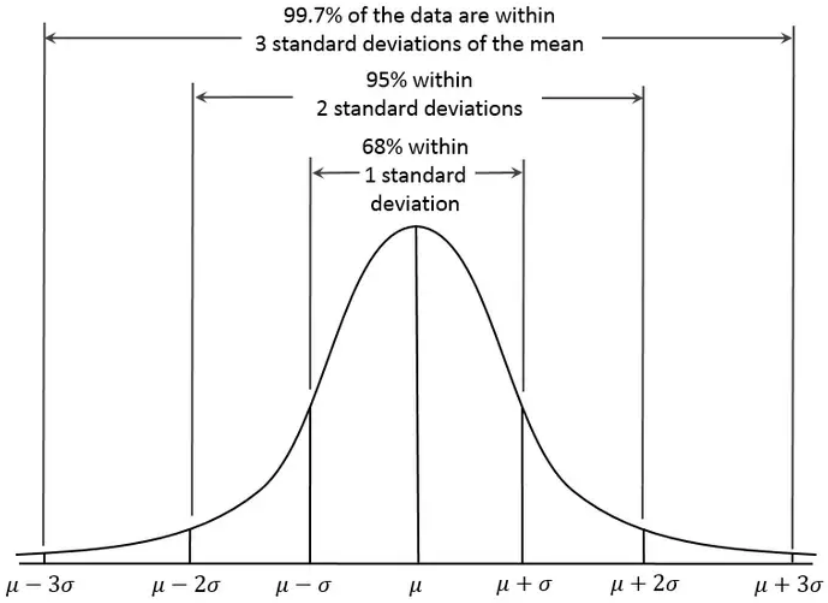

Figure 3.1: Normal (Gaussian) distribution with mean and standard deviation μ and σ, respectively. Areas under the curve that lie between 1, 2 and 3 standard deviations on each side of the mean are indicated.

The cumulative distribution function (*cdf*) of a one-dimensional random variable is given by the definite integral of the associated *pdf*:

$$F\left(a\right) = P\left(x \leq a\right) = \int_{-\infty}^{a} f(x)\, dx \tag{3.5}$$

Note that $F\left(a\right)$ must lie in the interval $[0, 1]$ for all a. The median of a continuous probability distribution is a value that splits the probability distribution into two portions with areas equal to $1/2$.

$$\int_{-\infty}^{median} f(x)\, dx = \frac{1}{2} \tag{3.6}$$

The mean or expected value of the random variable x is defined by:

$$\mu = \int_{-\infty}^{+\infty} x\ f(x)\, dx \tag{3.7}$$

with the variance as

$$\sigma_x^2 = \int_{-\infty}^{+\infty} (x-\mu)^2\, f(x)\, dx \tag{3.8}$$

the square root of variance *i.e.*, σ_x gives the standard deviation. The variance and standard deviation are measures of spread of the random variable around its expected value. Figure (3.2) presents a geometric visualization of the mode, median and mean of an arbitrary probability density function.

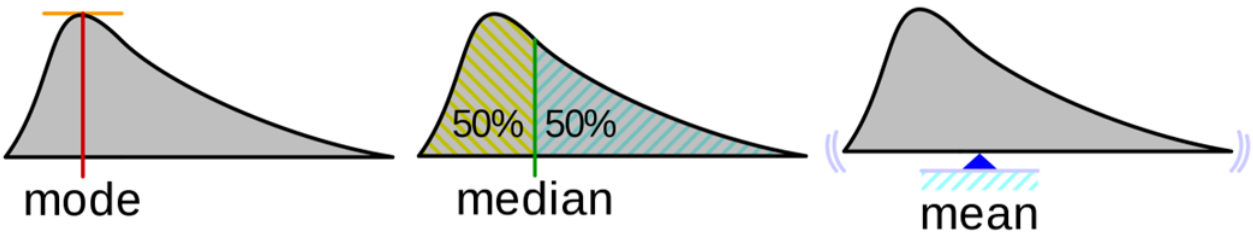

Figure 3.2: The mode, median and mean of an arbitrary probability density function.

For the multi-random variables, $\boldsymbol{x} = \{x_1, x_2, ...x_N\}$, that are normally distributed, the joint probability density function is

$$f\left(\mathbf{x}, \boldsymbol{\mu}, \mathbf{C}_x\right) = \frac{1}{\sqrt{\left(2\pi\right)^N \det \mathbf{C}_x}} \exp\left[-\frac{1}{2}\left(\mathbf{x} - \boldsymbol{\mu}\right)^T \mathbf{C}_x^{-1}\left(\mathbf{x} - \boldsymbol{\mu}\right)\right] \tag{3.9}$$

where $\mathbf{C}_x$ is the $N \times N$ covariance of $\boldsymbol{x}$, $det(\mathbf{C}_x)$ is determinant of $\mathbf{C}_x$, and

$$\boldsymbol{\mu} = \int_{-\infty}^{\infty} \boldsymbol{x}\ f(\boldsymbol{x})\ d\boldsymbol{x} \tag{3.10}$$

$$\mathbf{C}_x = \int_{-\infty}^{+\infty} \left(\boldsymbol{x} - \boldsymbol{\mu}\right)\left(\boldsymbol{x} - \boldsymbol{\mu}\right)^T f(\mathbf{x})\ d\boldsymbol{x} \tag{3.11}$$

If $\boldsymbol{x}$ is a multivariate normal random vector with expected values defined by the vector $\boldsymbol{\mu}_x$ and covariance matrix $\mathbf{C}_x$, then $\mathbf{y} = \mathbf{A}\mathbf{x}$ is also multivariate normally distributed random, with mean and covariance of

$$\boldsymbol{\mu}_y = \mathbf{A}\boldsymbol{\mu}_x \tag{3.12}$$

and

$$\mathbf{C}_y = \mathbf{A}\mathbf{C}_x\mathbf{A}^T \tag{3.13}$$

where $\mathbf{A}$ is an operator. This is the most general expression for *propagation error* from one set of variables to another. If $\boldsymbol{y}$ and $\boldsymbol{x}$ are related nonlinearly, $\mathbf{y} = f(\boldsymbol{x})$, then:

$$\mathbf{C}_y = \mathbf{J}\mathbf{C}_x\mathbf{J}^T \tag{3.14}$$

where $\mathbf{J}$ is the Jacobian matrix of operator $\mathbf{A}$:

$$\mathbf{J}\left(\boldsymbol{x}\right) = \left[\frac{\partial f}{\partial x_1} \quad \dots \quad \frac{\partial f}{\partial x_N}\right] = \begin{bmatrix} \frac{\partial f_1}{\partial x_1} & \frac{\partial f_1}{\partial x_2} & \dots & \frac{\partial f_1}{\partial x_N} \\ \frac{\partial f_2}{\partial x_1} & \frac{\partial f_2}{\partial x_2} & \dots & \frac{\partial f_2}{\partial x_N} \\ \vdots & \vdots & \dots & \vdots \\ \frac{\partial f_M}{\partial x_1} & \frac{\partial f_M}{\partial x_2} & \dots & \frac{\partial f_M}{\partial x_N} \end{bmatrix} \tag{3.15}$$

The rows of $\mathbf{J}(x)$ are gradients of $\boldsymbol{f}\left(\boldsymbol{x}\right)$.

3.3 Marginal Probability Density

Let X and Y be two spaces with random variables $\boldsymbol{x} = \{x_1, x_2, ...\}$ and $\boldsymbol{y} = \{y_1, y_2, ...\}$ whose joint probability density is $f\left(\boldsymbol{x}, \boldsymbol{y}\right)$. The marginal probability densities are defined as:

$$f_X\left(\boldsymbol{x}\right) = \int_Y f\left(\boldsymbol{x}, \boldsymbol{y}\right) d\boldsymbol{y} \tag{3.16}$$

and

$$f_Y\left(\boldsymbol{y}\right) = \int_X f\left(\boldsymbol{x}, \boldsymbol{y}\right) d\boldsymbol{x} \tag{3.17}$$

The variables $\boldsymbol{x}$ and $\boldsymbol{y}$ are independent if the joint probability density equals the product of two marginal probability densities:

$$f(\boldsymbol{x}, \boldsymbol{y}) = f_X(\boldsymbol{x}) f_Y(\boldsymbol{y}) \tag{3.18}$$

The conjunction of states of information is used to combine information obtained from measurements with information provided by a physical theory and is shown to be the basis of the inverse problem theory.

3.4 Homogeneous Probability Distributions

Let P be a probability distribution defined over a subset A of the space S, with the probability density function $f(\mathbf{x})$:

$$P(A) = \int_A f(\mathbf{x})\, d\mathbf{x} \tag{3.19}$$

Assuming that a change of coordinates over space S is represented by:

$$\mathbf{x}^* = \mathbf{x}^*(\mathbf{x}) \tag{3.20}$$

Consequently, the probability distribution P in new coordinate will be:

$$P(A) = \int_A f^*(\mathbf{x}^*)\, d\mathbf{x}^* \tag{3.21}$$

where $f^*(\mathbf{x}^*)$ is probability density function in new coordinate. From properties of integral it is deduced that, $f^*(\mathbf{x}^*)$ and $f(\mathbf{x})$ are related as:

$$f^*(\mathbf{x}^*) = f(\mathbf{x}) \mid \frac{\partial \mathbf{x}}{\partial \mathbf{x}^*} \mid \tag{3.22}$$

where $\mid \frac{\partial \mathbf{x}}{\partial \mathbf{x}^*} \mid$ represents the absolut value of the Jacobian of the transformation. By using the Jacobian rule (3.22), the probability density representing the homogeneous probability distribution can be computed in any coordinate system if the expression in one system is known.

The *homogeneous probability distribution* is the probability distribution that assigns to each region of the space a probability proportional to the volume of the region. In an arbitrary system of coordinates $\{u, v, w\}$ in which the volume element of the space is $dV(u, v, w) = g(u, v, w)\, dudvdw$ the homogeneous probability distribution is represented by the probability density:

$$h(u, v, w) = k\ g(u, v, w) \tag{3.23}$$

where k is a constant that may have a physical dimension. In particular, in Cartesian coordinates $\{x, y, z\}$, where the volume element is $dV(x, y, z) = dxdydz$. Therefore, the probability density representing the homogeneous probability distribution is constant i.e., $f(x, y, z) = k$. Note that, in general, the homogeneous probability density is not constant, and the homogeneous probability distribution can be represented by a constant probability density only if the space is flat, particularly in case that a Cartesian coordinates is used.

Of particular interests are positive parameters like temperature, frequency, conductivity, permittivity, velocity etc that occur in pair of mutually reciprocal parameters. Such positive parameters have probability density of the form

$$f(x) = \frac{k}{x} \tag{3.24}$$

The homogeneous probability density of the reciprocal parameter $y = \frac{1}{x}$ can be obtained using the Jacobian rule (equation (3.22)) as:

$$f(y) = \frac{k}{y} \tag{3.25}$$

Introducing the logarithm of these parameters as

$$x^* = \log \frac{x}{x_0}, \qquad y^* = \log \frac{y}{y_0} \tag{3.26}$$

the Jacobian rule yields the following homogeneous probability density for new parameters x^* and y^*:

$$f'(x^*) = k, \qquad f'(y^*) = k \tag{3.27}$$

where x_0 and y_0 are arbitrary positive constants. The positives parameters of this type with the probability density $f(u) = k/u$ was first described by Jeffreys (1939), and to honor him, such parameters are called *Jefferys parameters*. In summary, the homogeneous probability density for a Jeffreys quantity u is $f(u) = k/u$. The probability density $1/x$ is a particular case of the lognormal probability density. Parameters accepting probability densities like the log-normal or its limit *i.e.*, the $\frac{1}{x}$ will be as common as their inverses, and so are *Jeffrey's parameters*. The lognormal probability density is defined by

$$f(x \mid \mu, s) = \frac{1}{xs\sqrt{2\pi}} \exp\left\{-\frac{(\log x - \mu)^2}{2s^2}\right\} \tag{3.28}$$

If x follows the lognormal distribution with parameters $\mu,\ s$, then $\log x$ follows the normal distribution with mean and standard deviation $m,\ v$, respectively. The mean, m, and variance, v, of a lognormal random variable are functions of the lognormal distribution parameters $\mu,\ s$ as:

$$m = \exp\left\{\mu + s^2/2\right\}, \qquad v = \exp\left\{\left(2\mu + s^2\right)\left(\exp s^2 - 1\right)\right\} \tag{3.29}$$

Conversely, lognormal distribution parameters can be computed from m and v:

$$\mu = \log\left(\frac{m^2}{\sqrt{m^2 + v}}\right), \qquad s = \sqrt{\log\left(\frac{v}{m^2} + 1\right)} \tag{3.30}$$

Note that when the dispersion parameter s tends to ∞, the probability density tends to the function $\frac{1}{x}$, that is the homogeneous probability density for a Jeffreys quantity (Figure (3.3)).

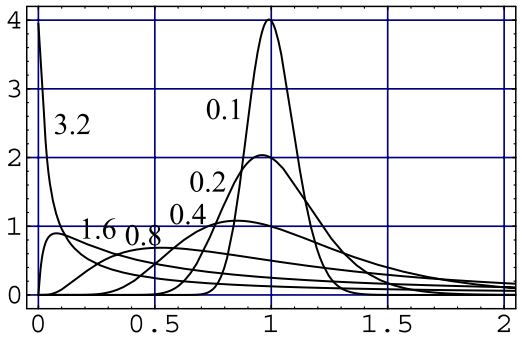

Figure 3.3: The lognormal probability density (equation (3.28)). Note that when the dispersion parameter s tends to ∞, the probability density tends to the function $1/x$, the homogeneous probability density for a Jeffreys quantity [138].

3.5 Probabilistic Formulation of Inverse Problems

The inverse problems can be generally dealt with probabilistic approach, where the a priori information on the model parameters is represented by a probability distribution over the model space. This approach explains how the *a priori* probability distribution can be transformed into the *a posteriori* probability distribution by incorporating a physical theory (forward formula) and the actual result of the observations (with their uncertainties). The general theory of probabilistic inversion has a simple formulation and is applicable to any kind of inverse problem, either including linear or strongly nonlinear problems ([86], [138]).

3.5.1 Forward and Inverse Problems

Given a complete description of a physical system, physical theories (forward problem) can predict the outcome of some measurements which are commonly called data. In general a forward problem which relates the model parameters $\boldsymbol{m}$ to the theoretical data values $\mathbf{d}$ can be represented by:

$$\mathbf{d} = g\left(\mathbf{m}\right) \tag{3.31}$$

where g is called forward operator that in general is nonlinear, $\mathbf{d} = (d_1, d_2, ...d_N)$ and $\mathbf{m} = (m_1, m_2, ...m_M)$ are data and model parameters. The inverse problem consists of using the result of some actual observations to retrieve the values of parameters that produce those measurements. The forward problem has a unique solution, while the inverse problem has non-unique solutions. Therefore, to reduce the non-uniqueness in the inverse problems, it is necessary to incorporate the available *a priori* information on the model parameters, and the data uncertainties have to be represented carefully, as well.

3.5.2 Data and Model Probability Density Function

Probabilistic framework is based on the conjunction of states of information between data and model, to jointly retrieve the unknown parameters. As in any measurement, the data is determined with an associated uncertainty and is described by a probability density, $\rho_D(\mathbf{d})$, over the data space, D. In geophysics, the source of data uncertainties are instrumental errors, positioning, environmental noise and human factors. By definition, *a priori* information on model parameters is the information available on model parameters independent of the measured data. Similarly, the model *a priori* information can be described by a probability density $\rho_M(\mathbf{m})$ in the model space, M.

As the *a prior* information on model parameters are obtained independently from the measurements, the information about the model parameters and the observations (data) can be combined through a joint probability density function in data-model $D \times M$ space as:

$$\rho(\mathbf{d}, \mathbf{m}) = \rho_D(\mathbf{d}) \ \rho_M(\mathbf{m}) \tag{3.32}$$

Moreover, the physical theory (forward problem) provides some information by predicting the relation between data and model that this correlation can be described by a probability density function presented by $\mathbf{\Theta}(\mathbf{d}, \mathbf{m})$. Finally, the posteriori state of information, $\sigma(\mathbf{d}, \mathbf{m})$, is constructed by conjunction of experimental information, $\rho(\mathbf{d}, \mathbf{m})$, with the theoretical information, $\Theta(\mathbf{d}, \mathbf{m})$, to give information in data-model space together:

$$\sigma(\mathbf{d}, \mathbf{m}) = k \frac{\rho(\mathbf{d}, \mathbf{m}) \ \Theta(\mathbf{d}, \mathbf{m})}{\mu(\mathbf{d}, \mathbf{m})} \tag{3.33}$$

where k is the normalization constant, and $\mu(\mathbf{d}, \mathbf{m})$ presents the homogeneous probability density state of information. Equation (3.33) is general and solves a variety of inverse problems.

The posteriori information in the model space is determined by the marginal probability density function as:

$$\sigma_M(\mathbf{m}) = \int \sigma(\mathbf{d}, \mathbf{m}) \ d\mathbf{d} \tag{3.34}$$

similarly, the posteriori information in the data space is given by:

$$\sigma_D(\mathbf{d}) = \int \sigma(\mathbf{d}, \mathbf{m}) \ d\mathbf{m} \tag{3.35}$$

Combination of equation (3.32) and (3.33) gives:

$$\sigma_M(\mathbf{m}) = k \ \rho_M(\mathbf{m}) \ \rho_D(g(\mathbf{m})) \tag{3.36}$$

In effect, $\rho_D(g(\mathbf{m}))$ presents the likelihood function, $L(\mathbf{m})$, which shows how good a model $\mathbf{m}$ explains the data. Figure (3.4) graphically illustrates estimation of $\sigma_M(\mathbf{m})$ and $\sigma_D(\mathbf{d})$ from joint probability density in the data-model space $\rho(\mathbf{d}, \mathbf{m})$ and information from physical theory $\Theta(\mathbf{d}, \mathbf{m})$.

Equation (3.36) is a robust tool that can directly solve a majority of inverse problems. It is mainly consists of three elements: (1) $\rho_M(\mathbf{m})$ model *a priori* probability density function; (2) $\rho_D(\mathbf{d})$ data probability density function; (3) forward problem $g(\mathbf{m})$ that sets a theoretical relation between data and model parameters. The model posterior information defined by equation (3.36) can provide very useful statistical information on model parameter, such as the mean and median values of the distribution and the uncertainties. Assuming a Gaussian distribution for data and model parameters, the probability densities are defined by:

$$\rho_D(\mathbf{d}) = \frac{1}{\sqrt{(2\pi)^n \det \mathbf{C}_D}} \exp\left[-\frac{1}{2}(\mathbf{d} - \mathbf{d}_{obs})^T \mathbf{C}_D^{-1}(\mathbf{d} - \mathbf{d}_{obs})\right] \tag{3.37}$$

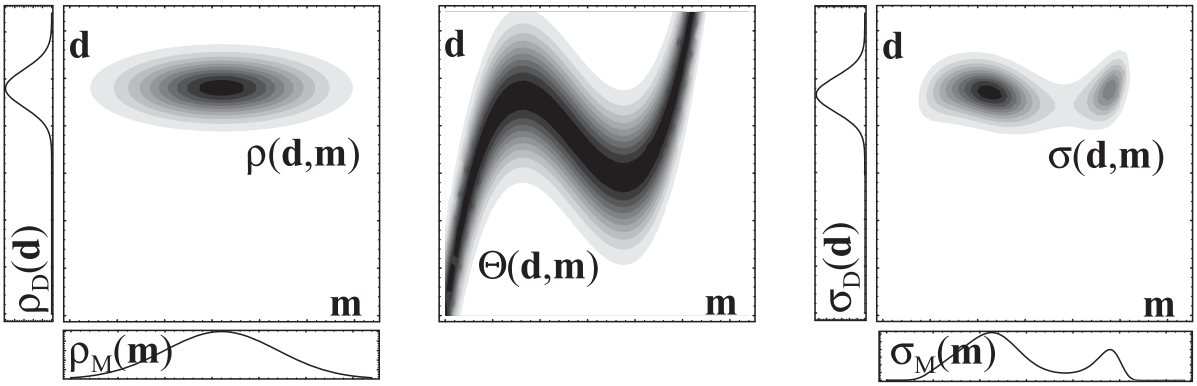

Figure 3.4: (left) The model and data probability densities, $\sigma_M(\mathbf{m})$ and $\sigma_D(\mathbf{d})$, respectively represent the information on the model *a prior* information and data. The joint probability density in the space $D \times M$ represents both states of information. (middle) The physical correlations between $\mathbf{d}$ and $\mathbf{m}$ that is predicted by a physical theory with some uncertainties. (right) The combination of the information that yields the marginal probability densities. Comparison of $\sigma_M(\mathbf{m})$ and $\rho_M(\mathbf{m})$ shows how the information about the model is retrieved from data and theoretical law (taken from [138]).

and

$$\rho_M(\mathbf{m}) = \frac{1}{\sqrt{(2\pi)^n \det \mathbf{C}_M}} \exp\left[-\frac{1}{2}(\mathbf{m}-\mathbf{m}_{prior})^T \mathbf{C}_M^{-1}(\mathbf{m}-\mathbf{m}_{prior})\right] \tag{3.38}$$

where $\mathbf{C}_D$ is data covariance matrix, and $\mathbf{C}_M$ is the model covariance matrix, $\mathbf{d}_{obs}$ and $\mathbf{m}_{prior}$ are observed data and priori model parameters. Substituting equation (3.37) and (3.38) in (3.36) yields the *a posteriori* information in the model space by the marginal probability density [86]:

$$\begin{aligned}\sigma_M(\mathbf{m}) &= k'\sqrt{\frac{\det\left(\mathbf{C}_M^{-1}+\mathbf{J}^T\mathbf{C}_D^{-1}\mathbf{J}\right)}{\det\left(\mathbf{C}_M^{-1}\right)}}\times \\ &\exp\left\{-\frac{1}{2}\left[(\mathbf{m}-\mathbf{m}_{prior})^T\mathbf{C}_M^{-1}(\mathbf{m}-\mathbf{m}_{prior})+(g(\mathbf{m})-\mathbf{d}_{obs})^T\mathbf{C}_D^{-1}(g(\mathbf{m})-\mathbf{d}_{obs})\right]\right\}\end{aligned} \tag{3.39}$$

where the matrix $\mathbf{J}$ with the elements $J_{kl} = \frac{\partial g_k}{\partial m_l}$ is the Jacobian matrix, and k' is the normalizing factor. If the non-linearity in $\mathbf{d} = g(\mathbf{m})$ is weak, then the Jacobian matrix, $\mathbf{J}$, will be approximately constant and equation (3.39) simplifies to:

$$\begin{aligned}\sigma_M(\mathbf{m}) &= k'\times \\ &\exp\left\{-\frac{1}{2}\left[(\mathbf{m}-\mathbf{m}_{prior})^T\mathbf{C}_M^{-1}(\mathbf{m}-\mathbf{m}_{prior})+(g(\mathbf{m})-\mathbf{d}_{obs})^T\mathbf{C}_D^{-1}(g(\mathbf{m})-\mathbf{d}_{obs})\right]\right\}\end{aligned} \tag{3.40}$$

If the forward equation is linear, *i.e.*, $\mathbf{d} = \mathbf{G}\mathbf{m}$ then the posterior probability density $\sigma_M(\mathbf{m})$ is also Gaussian and the equation (3.39) becomes:

$$\begin{aligned}\sigma_M(\mathbf{m}) &= k'\times \\ &\exp\left\{-\frac{1}{2}\left[(\mathbf{m}-\mathbf{m}_{prior})^T\mathbf{C}_M^{-1}(\mathbf{m}-\mathbf{m}_{prior})+(\mathbf{G}\mathbf{m}-\mathbf{d}_{obs})^T\mathbf{C}_D^{-1}(\mathbf{G}\mathbf{m}-\mathbf{d}_{obs})\right]\right\}\end{aligned} \tag{3.41}$$

Assuming that there is no *a prior* information on the model parameters, $\mathbf{C}_M^{-1} \to 0$, and hence, the posterior probability density in equation (3.39) is written as:

$$\sigma_M(\mathbf{m}) = k'' \times \exp\left[-\frac{1}{2}(g(\mathbf{m})-\mathbf{d}_{obs})^T\mathbf{C}_D^{-1}(g(\mathbf{m})-\mathbf{d}_{obs})\right] \tag{3.42}$$

where k'' is the normalizing factor. The solution of the inversion problem is usually given in terms of some posterior *pdf* parameters. In particular, if the model space is a linear space, consequently, the

probability density $\sigma_M(\mathbf{m})$ will be close to a Gaussian distribution, and the mean value of model $< \mathbf{m} >$ is obtained from:

$$< \mathbf{m} >= \int_M \mathbf{m}\, \sigma_M\left(\mathbf{m}\right) d\mathbf{m} \tag{3.43}$$

with the standard deviation of:

$$u_m = \sqrt{diag(\widetilde{\mathbf{C}}_M)} \tag{3.44}$$

where $\widetilde{\mathbf{C}}_M$ is the posterior model covariance matrix defined by:

$$\widetilde{\mathbf{C}}_M = \int_M \left(\mathbf{m} - < \mathbf{m} >\right)\left(\mathbf{m} - < \mathbf{m} >\right)^T \sigma_M\left(\mathbf{m}\right) d\mathbf{m} \tag{3.45}$$

3.6 Solving the Inverse Problem

The solution of an inverse problem essentially consists of estimating a probability distribution over the space of all possible models of the physical system under study. If the probability distributions are similar to a Gaussian or a generalized Gaussian distribution, then the solving the inverse problem will be estimation of the point around which the probability is maximum, with the associated variance and covariance.

Among many, the least squares (LSQR) are popular for solving inverse problems because they lead to the easiest computations. The only drawback with LSQR methods is their strong sensitivity to outliers in a data set. The LSQR criterion assumes that distributions of all uncertainties in the problem are Gaussian. When the forward problem equation, *i.e.*, $g(\mathbf{m})$, is linear, posterior uncertainties are Gaussian, and an explicit expression is obtained for the posterior probability distribution. When the forward equation is nonlinear, the posterior probability is not Gaussian, however, if nonlinearity is weak, finding the maximum likelihood point of the distribution and estimating the shape of the distribution around this point (*i.e.*, estimating the covariance matrix of the distribution) can satisfactorily solve the problem.

3.6.1 Nonlinearity in Inverse Problems

There are different degrees of nonlinearity in inverse problems. Figure (3.5) illustrates some regimes in the aspect of nonlinearity: linear problem, linearisable problem, weakly nonlinear problem, and strongly nonlinear problem. The gray oval in Figure (3.5) represents the joint probability density function, $\rho\left(\mathbf{d},\mathbf{m}\right) = \rho_M(\mathbf{m})\rho_D\left(\mathbf{d}\right)$, in data-model space $(D \times M)$ which is the combination of prior information on the model parameters, $\rho_M(\mathbf{m})$, and information from data, $\rho_D\left(\mathbf{d}\right)$. In fact, only the linearity degree of forward function inside the domain of gray area is important, regardless of the intrinsic nonlinearity of the function itself.

I. Linear problem: Figure (3.5a) presents strictly linear problems. The relationship between data and model parameters (forward equation) is linear, $\mathbf{d} = \mathbf{G}\mathbf{m}$, as represented by a straight line. The prior probability density $\rho(\mathbf{d},\mathbf{m})$ induces on this straight line the posterior probability density $\sigma(\mathbf{d},\mathbf{m})$ whose marginal over the model space gives the posterior probability density over the model parameter space, $\sigma_M(\mathbf{m})$. If the prior probability densities are Gaussian, then the posterior probability distribution will also be Gaussian.

II. Linearizable problem: Figure (3.5b) illustrates the linearizable problems, where the forward equation $\mathbf{d} = g\left(\mathbf{m}\right)$ can be linearized around the prior model $\mathbf{m}_{prior}$:

$$\mathbf{d} \simeq \mathbf{d}_{prior} + \mathbf{F}_{prior}\left(\mathbf{m} - \mathbf{m}_{prior}\right) \tag{3.46}$$

where $\mathbf{d}_{prior} = g\left(\mathbf{m}_{prior}\right)$ and $\mathbf{F}$ represents the derivative matrix with the elements defined by:

$$F_{ij} = \left(\frac{\partial g_i}{\partial m_j}\right)_{\mathbf{m}_{prior}} \tag{3.47}$$

The equation (3.46) is linear inside the domain of significant probability. There is no practical difference between this problem and the strictly linear problem. The posterior probability density is still approximately Gaussian.

III. Weakly nonlinear problem: Figure (3.5c) depicts a weakly nonlinear problem. The relationship between data $\mathbf{d}$ and model parameters $\mathbf{m}$ is approximately linear inside the domain of significant prior probability (*i.e.*, inside the gray oval of the figure). The posterior distribution is just as simple as the prior distribution. For instance, if the prior is Gaussian the posterior will be also Gaussian. The forward equation is linearized around a starting model, $\mathbf{m}_0$, and a better model is looked for using iterating such an algorithm.

$$\mathbf{d} = \mathbf{d}_0 + \mathbf{F}_0 \left(\mathbf{m} - \mathbf{m}_0 \right) \tag{3.48}$$

where $\mathbf{d}_0 = g\left(\mathbf{m}_0\right)$.

IV. Strongly nonlinear problem: Figure (3.5d) displays a nonlinear problem. The forward equation cannot be linearized, and even if the prior distribution is Gaussian, the posterior distribution can be very complicated and far from a Gaussian function. Special methods are required to solve the problem.

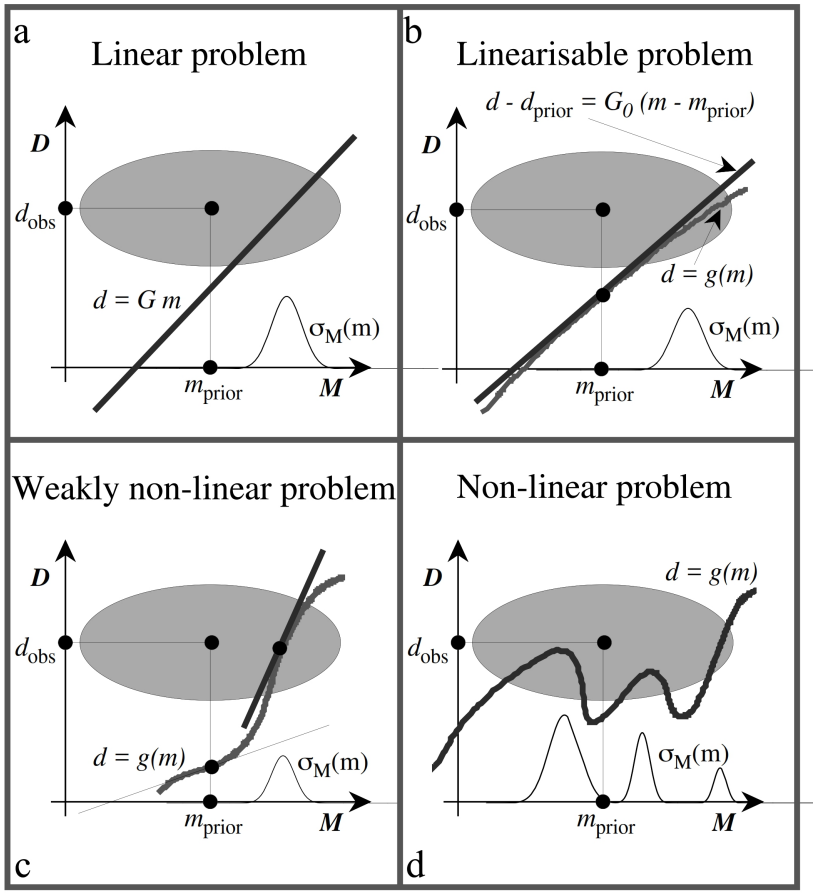

Figure 3.5: Four domains of nonlinearity in inverse problems. (a) linear problem; (b) linearizable problem; (c) weakly-linear problem; (d) nonlinear problem. The gray oval indicates the domain of significant prior probability [86].

3.6.2 The Least Squares (LSQR) Problem

Least-squares techniques are applicable when all the priori probability densities over data and model spaces, *i.e.*, $\rho_D\left(\mathbf{d}\right)$ (equation (3.37)) and $\rho_M(\mathbf{m})$ (equation (3.38)) are Gaussian. As already explained, the combination of these types of information leads to the a posteriori probability density in the model space that regardless of nonlinearity of the forward problem, $g\left(\mathbf{m}\right)$, is given by:

$$\sigma_M(\mathbf{m}) = const.\ e^{-S(\mathbf{m})} \tag{3.49}$$

where $S(\mathbf{m})$ is the misfit function that is defined by:

$$S(\mathbf{m}) = \frac{1}{2}\left[(g(\mathbf{m}) - \mathbf{d}_{obs})^T \mathbf{C}_D^{-1} (g(\mathbf{m}) - \mathbf{d}_{obs}) + (\mathbf{m} - \mathbf{m}_{prior})^T \mathbf{C}_M^{-1} (\mathbf{m} - \mathbf{m}_{prior})\right] \tag{3.50}$$

and $\mathbf{C}_M$ and $\mathbf{C}_D$ are the model and data priori covariance matrices that evaluate the uncertainties in data and model. The misfit function is also called the cost function, objective function, least-squares function, or chi-squared function. For uncorrelated uncertainties the covariance matrices become diagonal with the elements, $(\mathbf{C}_D)^{ij} = \left(\sigma_{xD}^i\right)^2 \delta^{ij}$ and $(\mathbf{C}_M)^{lk} = \left(\sigma_{xM}^l\right)^2 \delta^{lk}$ where $\left(\sigma_{xD}^i\right)$ and $\left(\sigma_{xM}^l\right)$ indicate the uncertainty of the individual data and priori model parameters, and δ^{ij} and δ^{lk} is Kronecker delta function defined by:

$$\delta^{ij} = \begin{cases} 0 & \text{if } i \neq j \\ 1 & \text{if } i = j \end{cases} \tag{3.51}$$

The inverse problem is solved by maximizing $\sigma_M(\mathbf{m})$ or equivalently by minimizing the misfit function $S(\mathbf{m})$.

Linear Problems
If the forward equation, $\mathbf{d} = g(\mathbf{m})$ is linear (*i.e.*, $\mathbf{d} = \mathbf{G}\mathbf{m}$), the misfit function will be quadratic:

$$S(\mathbf{m}) = \frac{1}{2}\left[(\mathbf{G}\mathbf{m} - \mathbf{d}_{obs})^T \mathbf{C}_D^{-1} (\mathbf{G}\mathbf{m} - \mathbf{d}_{obs}) + (\mathbf{m} - \mathbf{m}_{prior})^T \mathbf{C}_M^{-1} (\mathbf{m} - \mathbf{m}_{prior})\right] \tag{3.52}$$

and then $\sigma_M(\mathbf{m})$ is written as:

$$\sigma_M(\mathbf{m}) = const. \times \exp\left[-\frac{1}{2}(\mathbf{m} - \widetilde{\mathbf{m}})^T \widetilde{\mathbf{C}}_m^{-1} (\mathbf{m} - \widetilde{\mathbf{m}})\right] \tag{3.53}$$

This implies that $\sigma_M(\mathbf{m})$ is a Gaussian probability density, and $\widetilde{\mathbf{m}}$ and $\widetilde{\mathbf{C}}_m^{-1}$ are center and covariance matrix of the posterior probability density and are expressed by:

$$\begin{aligned} \widetilde{\mathbf{m}} &= \mathbf{m}_{prior} + \left(\mathbf{G}^T \mathbf{C}_D^{-1} \mathbf{G} + \mathbf{C}_M^{-1}\right)^{-1} \mathbf{G}^T \mathbf{C}_D^{-1} (\mathbf{d}_{obs} - \mathbf{G}\mathbf{m}_{prior}) \\ &\equiv \mathbf{m}_{prior} + \mathbf{C}_M \mathbf{G}^T \left(\mathbf{G}\mathbf{C}_M\mathbf{G}^T + \mathbf{C}_D\right)^{-1} (\mathbf{d}_{obs} - \mathbf{G}\mathbf{m}_{prior}) \end{aligned} \tag{3.54}$$

and the covariance matrix is computed by:

$$\widetilde{\mathbf{C}}_M = \left(\mathbf{G}^T \mathbf{C}_D^{-1} \mathbf{G} + \mathbf{C}_M^{-1}\right)^{-1} \tag{3.55}$$

In effect, $\widetilde{\mathbf{m}}$ is a point that minimizes the least square misfit function in equation (3.52). Having no a priori information on model, means a very large model covariance matrix, then $\mathbf{C}_M \to \infty$ or $\mathbf{C}_M^{-1} \to 0$, and formulas (3.54) and (3.55) become:

$$\widetilde{\mathbf{m}} = \left(\mathbf{G}^T \mathbf{C}_D^{-1} \mathbf{G}\right)^{-1} \mathbf{G}^T \mathbf{C}_D^{-1} (\mathbf{d}_{obs}) \tag{3.56}$$

$$\widetilde{\mathbf{C}}_M = \left(\mathbf{G}^T \mathbf{C}_D^{-1} \mathbf{G}\right)^{-1} \tag{3.57}$$

In summary, in the linear case $\mathbf{d} = \mathbf{G}\mathbf{m}$, a priori information in model space is represented by a Gaussian function with the mean value of $\mathbf{m}_{prior}$ and covariance of $\mathbf{C}_M$ that will result in a posteriori model probability density $\sigma_M(\mathbf{m})$ with the mean and covariance of $\widetilde{\mathbf{m}}$ and $\widetilde{\mathbf{C}}_M$, respectively. The comparison of priori and posterior uncertainties, $\mathbf{C}_M$ and $\widetilde{\mathbf{C}}_M$, indicates how much the inversion process could resolve the parameters.

Nonlinear Problems
When the forward equation is nonlinear, $\mathbf{d} = g(\mathbf{m})$, the posterior probability density, $\sigma_M(\mathbf{m})$, will not be Gaussian. The further the relation $\mathbf{d} = g(\mathbf{m})$ is nonlinear the further the $\sigma_M(\mathbf{m})$ is far from being a Gaussian function. If the forward equation can be linearized around $\mathbf{m}_{prior}$ (Figure (3.5b)):

$$\mathbf{d} \simeq g(\mathbf{m}_{prior}) + \mathbf{F}_{prior}(\mathbf{m} - \mathbf{m}_{prior}) \tag{3.58}$$

then the a posteriori probability density in model space is approximately Gaussian, with the mean and covariance matrix of:

$$\begin{aligned} \widetilde{\mathbf{m}} &\approx \mathbf{m}_{prior} + \left(\mathbf{F}^T\mathbf{C}_D^{-1}\mathbf{F} + \mathbf{C}_M^{-1}\right)^{-1}\mathbf{F}^T\mathbf{C}_D^{-1}(\mathbf{d}_{obs} - g(\mathbf{m}_{prior})) \\ &= \mathbf{m}_{prior} + \mathbf{C}_M\mathbf{F}^T\left(\mathbf{F}\mathbf{C}_M\mathbf{F}^T + \mathbf{C}_D\right)^{-1}(\mathbf{d}_{obs} - g(\mathbf{m}_{prior})) \end{aligned} \tag{3.59}$$

and

$$\widetilde{\mathbf{C}}_M \approx \left(\mathbf{F}^T\mathbf{C}_D^{-1}\mathbf{F} + \mathbf{C}_M^{-1}\right)^{-1} \tag{3.60}$$

So, solving an inverse problem that can be linearized is reduced to solving a linear problem. In the case that linearization is not applicable (Figure (3.5c)), but $g(\mathbf{m})$ is quasi-linear inside the gray oval where posterior density is significant, the iterative algorithms can be used to estimate the model that is the point maximizing $\sigma_M(\mathbf{m})$ or equivalently minimize the misfit function $S(\mathbf{m})$. For example, using a quasi-Newton method, the iterative relation converges to a local optimal point:

$$\mathbf{m}_{n+1} = \mathbf{m}_n - \mu_n\left(\mathbf{F}_n^T\mathbf{C}_D^{-1}\mathbf{F}_n + \mathbf{C}_M^{-1}\right)^{-1}\left[\mathbf{F}_n^T\mathbf{C}_D^{-1}(\mathbf{d}_n - \mathbf{d}_{obs}) + \mathbf{C}_M^{-1}(\mathbf{m}_n - \mathbf{m}_{prior})\right] \tag{3.61}$$

where $\mathbf{d}_n = g(\mathbf{m}_n)$, $\mathbf{F}_n = \mathbf{F}(\mathbf{m}_n)$ that is defined by $(F_n)_{ij} = \left(\frac{\partial g_i}{\partial m_j}\right)_{\mathbf{m}_n}$, and $\mu_n \leq 1$ is a positive quantity that has to be set appropriately. If there is one global optimum, then the algorithm converges to it. If there are several local optimal points, the algorithms must be initiated at a point $\mathbf{m}_0$ that is close enough to the global optimum. The a posteriori covariance operator can be estimated as:

$$\widetilde{\mathbf{C}}_M \approx \left(\mathbf{F}^T\mathbf{C}_D^{-1}\mathbf{F} + \mathbf{C}_M^{-1}\right)^{-1} \tag{3.62}$$

The main computational difference between this nonlinear solution and the linearized solution in equation (3.59) is that, the predicted data for the current model $\mathbf{d}_n = g(\mathbf{m}_n)$, has to be computed at each iteration without using any linear approximation. The problems that their nonlinearity is strong, Figure (3.5d), requires more sophisticated methods to solve.

To this end, worth noting that the most trivial use of the posterior covariance operator $\widetilde{\mathbf{C}}_M$ is to interpret the square roots of the diagonal elements (variances) as *uncertainty bars* on the posterior values of the model parameters. However, a direct examination of the off-diagonal elements of a covariance operator is not easy, and it is much better to evaluate the correlation coefficients:

$$\rho^{ij} = \frac{\widetilde{\mathbf{C}}_M^{ij}}{\sqrt{\widetilde{\mathbf{C}}_M^{ii}\widetilde{\mathbf{C}}_M^{jj}}}, \quad -1 \leq \rho^{ij} \leq 1 \tag{3.63}$$

If the posterior correlation between model parameters m^i and m^j is close to zero, the posterior uncertainties are uncorrelated. If the correlation is close to $+1$, the uncertainties are highly correlated. A strong correlation on uncertainties means that the two parameters have not been independently resolved by the data set and that only some linear combination of the parameters is resolved.

3.6.3 Uncertainties in the Forward Modelization

Assume that the data and model spaces are linear with homogeneous probability densities $\mu_D(\mathbf{d})$ and $\mu_M(\mathbf{m})$ that are constant. A Gaussian probability density choice, yields the joint probability density of data and model as:

$$\Theta(\mathbf{d},\mathbf{m}) = \frac{1}{\sqrt{(2\pi)^n \det \mathbf{C}_T}} \exp\left[-\frac{1}{2}(g(\mathbf{m}) - \mathbf{d}_{obs})^T\mathbf{C}_T^{-1}(g(\mathbf{m}) - \mathbf{d}_{obs})\right] \tag{3.64}$$

where $\mathbf{C}_T$ presents a covariance operator that imposes some Gaussian uncertainties on $d \approx g(\mathbf{m})$. When theoretical uncertainties cannot be neglected, the Gaussian model in equation (3.64) or preferably a realistic account of the modelization uncertainties can be used. Hence, thanks to Gaussian simplicity the $\mathbf{C}_D$ just has to be replaced with $\mathbf{C}_D + \mathbf{C}_T$ in equation (3.41).

Chapter 4

Attenuation Estimation Methods: Existing Methods and Their Performance

4.1 Introduction

Ground Penetrating Radar method can provide qualitative information about shallow stratigraphy and quantitative information about electromagnetic properties of the different geomaterials composing the stratigraphic sequence. The electromagnetic properties can be derived from wave velocity and attenuation of the radar signals that propagate inside the materials [56]. Propagating electromagnetic waves are subject to frequency dependent attenuation which depends on the effective conductivity. The effective conductivity is a function of the real component of the electric conductivity and the complex component of the dielectric permittivity. The velocity depends on the dielectric permittivity and the magnetic permeability of medium *e.g.,* [6]. Table (4.1) reports typical relative permittivity, electrical conductivity, velocity, attenuation and intrinsic loss tangent observed in common geological materials at 100 MHz [21]. Some basic methods have been proposed to estimate the attenuation, for example: amplitude decay [142], [43], spectral ratio (e.g., [46], [12]) and frequency shift [116], [75], [152], [51], [11], [70], [73], [26], [63], [71], [151]. Wave intrinsic attenuation results in signal amplitude decay with increasing distance, and progressive loss of high frequencies that leads to pulse broadening. Hence, by measuring the shift in the signal spectrum through time using time-frequency analysis, or amplitude spectrum variation it is possible to isolate the frequency dependent component of attenuation. Understanding the full attenuation response requires additional low-frequency resistivity measurements [11]. In this chapter, the main approaches of loss tangent (the ratio of imaginary to real part of complex permittivity) estimation are reviewed and several examples are provided from terrestrial and planetary investigations.

4.2 Intrinsic, Scattering and Total Attenuation

It is noted in Chapter 1 that intrinsic or absorption attenuation of electromagnetic waves is caused by conductivity, dielectric permittivity relaxation mechanisms, and the magnetic permeability (only for magnetic materials). Intrinsic attenuation is in general frequency dependent and leads to conversion of energy to heat. Intrinsic attenuation coefficient α_i is expressed by:

$$\alpha_i = \omega\sqrt{\mu\varepsilon'}\left\{\frac{1}{2}\left[\sqrt{1+\left(\frac{\sigma_e}{\omega\varepsilon'}\right)^2}-1\right]\right\}^2 = \omega\sqrt{\mu\varepsilon'}\left\{\frac{1}{2}\left[\sqrt{1+tan\delta^2}-1\right]\right\}^2 \quad (Np/m) \tag{4.1}$$

where $\sigma_e = \sigma + \omega\varepsilon''$ is effective conductivity, and $\varepsilon = \varepsilon' - j\varepsilon''$ is complex permittivity. For the low loss media with $tan\delta = \sigma_e/\omega\varepsilon'' << 1$ equation (4.1) is approximated by:

$$\alpha_i \approx \frac{\omega}{2V} tan\delta \tag{4.2}$$

In addition to the absorption (intrinsic) attenuation of electromagnetic waves, inclusions, on a wide range of scales, embedded in the homogeneous background of the medium scatters the incident wave in all directions. Therefore, the total attenuation coefficient is given by the summation of intrinsic α_i and scattering α_s attenuation coefficients:

$$\alpha = \alpha_i + \alpha_s \tag{4.3}$$

It is worth to note that, intrinsic attenuation provides information about the lithology and scattering attenuation can provide information about the structure of the target, independently [58]. The effects of scattering in the recorded data are originated from both multipathing and volume scattering within a medium. Particularly, in ice the scattering attenuation is much larger than that of absorption and in high temperature glaciers severely limits the penetrating depth. In this situation, the radar operating frequency requires to be low enough to achieve the deep penetration.

Table 4.1: Typical relative permittivity, electrical conductivity, velocity, attenuation and loss tangent observed in common geological materials at 100 MHz [21].

Material	$\boldsymbol{\varepsilon'_r}$	$\boldsymbol{\sigma}$ $\boldsymbol{(mS/m)}$	$\boldsymbol{V}$ $\boldsymbol{(m/ns)}$	$\boldsymbol{\alpha_i}$ $\boldsymbol{(dB/m)}$	$\boldsymbol{\tan\delta}$
Air	1	0	0.30	0	0
Distilled water	80	0.01	0.033	0.002	0.0002
Fresh water	80	0.5	0.033	0.1	0.011
Sea water	80	30000	0.01	1000	99
Dry sand	3-5	0.01	0.15	0.01	0.005
Saturated sand	20-30	0.1-1.0	0.06	0.03-0.3	0.006
Limestone	4-8	0.5-2	0.12	0.4-1	0.17-0.4
Shales	5-15	1-100	0.09	1-100	0.32-30
Silts	5-30	1-100	0.07	1-100	0.26-23
Clays	5-40	2-1000	0.06	1-300	0.26-62
Granite	4-6	0.01-1	0.13	0.01-1	0.004-0.44
Dry salt	5-6	0.01-1	0.13	0.01-1	0.004-0.44
Ice	3-4	0.01	0.16	0.01	0.0056

In literature, intrinsic attenuation sometimes is described by the quality factor, Q_i, that equals the reciprocal of loss tangent:

$$Q_i^{-1} = tan\delta = \frac{\sigma_e}{\omega\varepsilon'} = \frac{\varepsilon''}{\varepsilon'} + \frac{\sigma_s}{\omega\varepsilon'} \tag{4.4}$$

and consequently:

$$\alpha_i \approx \frac{\omega}{2Q_iV} \tag{4.5}$$

In addition the total loss can be described as

$$Q^{-1} = Q_s^{-1} + Q_i^{-1} \tag{4.6}$$

where Q_s^{-1} accounts for scattering component of total quality factor, Q^{-1}. The loss tangent gives a measure of the frequency dependent dissipation of electromagnetic waves caused by conduction and different mechanisms of dielectric relaxation (atomic, molecular and volume polarization) that produce the imaginary part of the permittivity [6]. The term $(\varepsilon''/\varepsilon')$ accounts for the polarization component of intrinsic attenuation and $\sigma_s/\omega\varepsilon'$ accounts for that of conduction mechanism. In the media with low conductivity ($\sim \sigma_s < 0.001\ S/m$) the dielectric relaxation term *i.e.*, $(\varepsilon''/\varepsilon')$, is dominant over $\sigma_s/\omega\varepsilon'$, hence, if ε'' and ε' have very similar variation over the GPR frequency range, the $tan\delta$ will be almost invariant in this range of frequency. There are many materials that fall into this category, however, in water ε' is almost invariant, but ε'' varies strongly above 500 MHz, and therefore the attenuation strongly depends on frequency at the high end of the GPR spectrum (e.g., 500 MHz−1.5 GHz). For Clays Q_i^{-1} can be strongly frequency dependent in the GPR frequency range, as well. If the conductivity is high the $\sigma_s/\omega\varepsilon'$ term cannot be ignored and loss tangent will be frequency-dependent.

As an example, for $\sigma_s = 0.005\ S/m$ and lab measurements of $(\varepsilon''/\varepsilon')$ [76], Figure (4.1) presents Q_i^{-1} and its components in equation (4.4) versus frequency. The dielectric relaxation term, $(\varepsilon''/\varepsilon')$, for the frequencies $> 40\ MHz$ is almost constant whereas the term $(\sigma_s/\omega\varepsilon')$ decays with increasing frequency, and its behavior dominates the Q_i^{-1} variation with frequency. The upper limit of frequency independence is related to the dielectric relaxation of water that occurs at frequencies above $\sim 1\ GHz$.

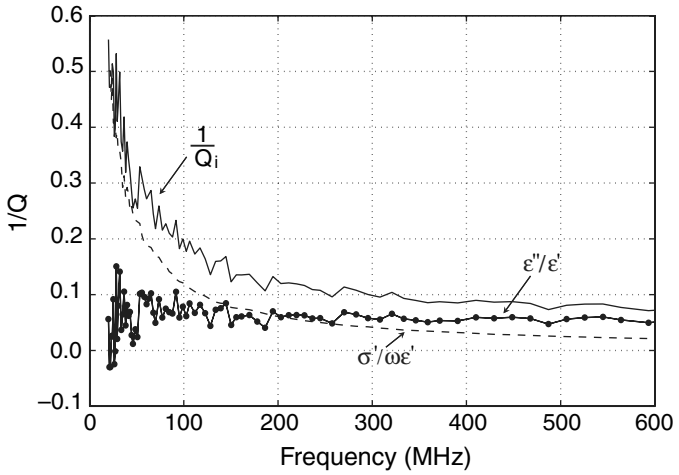

Figure 4.1: Intrinsic total Q_i^{-1} and its constituting components variation with frequency for a $\sigma = 0.005\ S/m$ and $\varepsilon''/\varepsilon'$ lab measurements of a dolomite sample in the Ellenburger dolomite outcrop [76].

4.3 Frequency Dependent Attenuation of GPR Pulses

In the frequency band of Ground-penetrating radar (10 MHz–1 GHz), the effective dielectric permittivity is approximately independent of frequency over a broad range of earth materials. It is therefore often assumed that GPR signal propagation is approximately frequency independent in many if not most of materials [11]. As frequency increases, attenuation increases as well.

There are typically three mechanisms that lead to significant frequency dependence (attenuation mechanisms) in the GPR frequency band [13], (Figure (4.2)). For many materials, at the low end of the frequency spectrum (< 10 MHz) ionic or DC conductivity dominates the frequency dependence of the dielectric spectra. In $10 - 1000$ MHz a dielectric relaxation is observed that can be attributed to bound-water relaxation, grain geometry, or a form of Maxwell-Wagner relaxation. At frequencies ≥ 1 GHz, water relaxation begins to dominate the dielectric spectrum.

While frequency dependent attenuation and velocity dispersion are necessarily linked, the functional form of dielectric relaxation in the GPR frequency range is such that velocity dispersion is weak while the attenuation coefficient can vary by $1 - 2$ orders of magnitude (Figure (4.2)). These variations in the dielectric spectrum can be used to obtain new information about the subsurface, such as information that can be related to parameters critical to hydrology, soil mechanics or other fields, such as soil moisture or clay content [13], [14]. With increasing conductivity, EM velocity dispersion may occur. However, increasing ε' stabilizes the velocity for high conductivity (Figure (4.2), right panel). This is true for most geologic materials because increasing conductivity is commonly caused by the presence of ions dissolved in water, which also increases the relative permittivity. In the presence of conductivity, and for a relatively large relative dielectric permittivity, the intrinsic attenuation Q_{in}^{-1} is a function of frequency, whereas the velocity dispersion is negligible.

Further, Turner and Siggins [144] made attenuation measurements on a range of geological materials to quantify the dielectric behavior of the materials at radar frequencies. Their results show a wide variation in attenuation rate between different sand types, but the variation with frequency above 10 MHz is almost linear for each material. For a variety of dry rocks over a frequency range of 10 MHz to 1 GHz the attenuation almost presents a linear behavior versus frequency. This resulted in conclusion that the attenuation of radio waves in some geological materials can be approximated by a linear function of frequency over the bandwidths of typical subsurface radar pulses. This characteristic is attributed to the

presence of a number of competing mechanisms e.g., dielectric loss mechanisms with differing relaxation times.

The presence of water in most soils and rocks commonly causes increase in attenuation with frequency in these materials at radar frequencies. This increased attenuation occurs because at these frequencies the highly polar water molecules begin to lag behind the applied field and increase the total real effective conductivity.

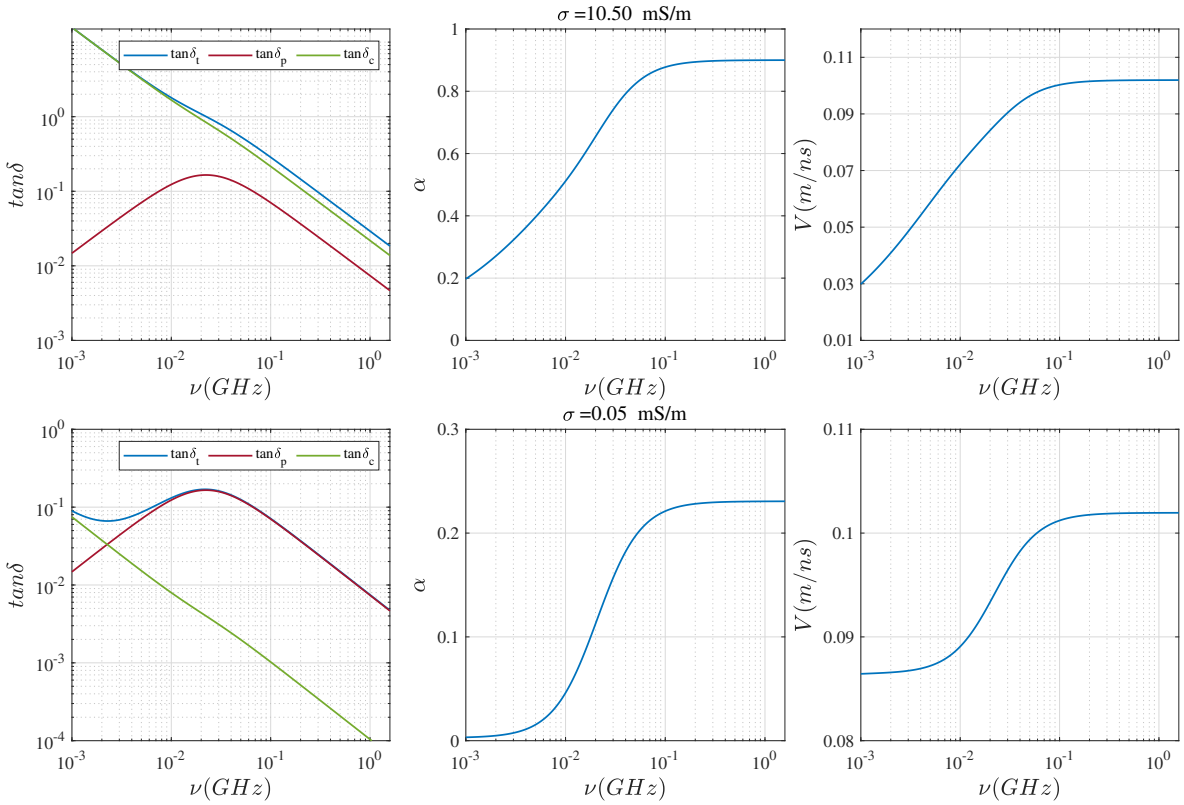

Figure 4.2: (left) loss tangent components; (middle) intrinsic attenuation; and (right) velocity variations versus GPR frequency range for typical water-saturated carbonate rocks. Different mechanisms dominate the frequency dependence over different frequency bands.

4.4 Methods of Loss Tangent Estimation

Electromagnetic waves undergo attenuation as they propagate through a lossy medium like earth. There are several methods for estimation of attenuation that in principle use amplitude spectrum information, spectrum shift or a combination of both. The basic approaches to estimate the attenuation of traveling EM waves in a medium can be classified as:

1. **Spectral ratio** (*e.g.*, [118], [46]): ratio of the amplitude spectra of propagating waves between two spatially separated depths are computed.

2. **Frequency shift** (e.g., [75], [11]): variation of maximum or centroid frequency versus time is used to estimate the attenuation.

3. **Amplitude or power decay** ([142], [43]): ratio of received amplitudes or powers at two different arrival times is computed.

The spectral ratio and frequency shift are performed in frequency domain, and amplitude decay is essentially a time domain approach.

4.4.1 Spectral Ratio

For plane-wave vertical-propagation through a homogeneous medium, the change in amplitude spectrum in a time interval $\Delta\tau$ can be modeled as:

$$A(\nu, \tau_2) = A(\nu, \tau_1)\ e^{\Delta\beta}\ e^{-\alpha V \Delta\tau} \tag{4.7}$$

where V is phase velocity, $\Delta\beta$ is a term that captures frequency-independent amplitude-scaling effects caused by phenomena such as geometric spreading, source signature, and reflection and transmission losses. For the given travel-times, $\tau_1,\ \tau_2$, the ratio of two amplitude spectra is related to α as ([118], [46]):

$$ln\left(\frac{A(\nu, \tau_1)}{A(\nu, \tau_2)}\right) = \Delta\beta - \alpha V \Delta\tau \tag{4.8}$$

considering that

$$Q = \frac{\omega}{2V\alpha} = \frac{\pi\nu}{V\alpha} \tag{4.9}$$

substituting equation (4.9) in (4.8) yields:

$$ln\left(\frac{A(\omega, \tau_1)}{A(\omega, \tau_2)}\right) = \Delta\beta - \frac{\omega\Delta\tau}{2Q} \tag{4.10}$$

This equation describes the spectral ratio method of attenuation estimation. The equation is only locally linear, and the intercept will be non-zero and depends on the band over which the analysis is done. Fitting a line to equation (4.10) which is assumed linear over the GPR bandwidth yields slope that determines $1/Q$, and the intercept term $\Delta\beta$ that however on its own does not have value. A non linear function can be fit to equation (4.10), as well. Number of studies show that the Q in equation (4.10) is rarely constant in the GPR range.

To this end, we note that the spectral ratio method is simple in principle, but in practice determining the Q-factor is complicated by overlapping wavelets which lead to amplitude spectra that do not reflect the wavelet spectrum. The amplitude spectrum of the waves may be affected by many factors, such as geometric spreading, receiver coupling, transmission-reflection loses and radiation pattern [152]. However, the amplitude spectrum form may not be influenced by these factors since these factors are not always necessarily frequency dependent.

Spectral ratio method can be more efficient as long as an appropriate bandwidth is chosen to avoid adverse effect of additive noise and numerical errors [48]. Contrary to the methods based on frequency-shift, the spectral ratio method uses the entire amplitude spectrum. The main advantage of spectral ration methods is that they are independent from the source spectrum.

4.4.2 Amplitude Decay

This method that purely relies on the amplitude information is one of the simplest methods of computing attenuation based on the decay of amplitudes. The ratio of amplitude at two different travel-times, τ_1 and τ_2 is related to the attenuation coefficient α by [142]:

$$ln\left(\frac{A(z_1, \tau_1)}{A(z_2, \tau_1)}\right) = \alpha\,(2\Delta z) = \alpha V \Delta\tau \tag{4.11}$$

that in term of Q^{-1} is written as:

$$ln\left(\frac{A(z_1, \tau_1)}{A(z_2, \tau_2)}\right) = Q^{-1}\frac{\omega}{2}\Delta\tau = Q^{-1}\pi\nu\Delta\tau \tag{4.12}$$

where ν is the dominant frequency of the transmitted pulse. The Q^{-1} can be attributed to total loss as discussed in Chapter 5. Figure (4.3) presents the attenuation of an electromagnetic wave amplitude versus a distance. The signal amplitude decays exponentially in the direction of field translation while the field shape remains invariant. The major drawback of this approach is that the transmission and reflection at subsurface interfaces can result in significant losses and amplitude decay of a radar wavelet.

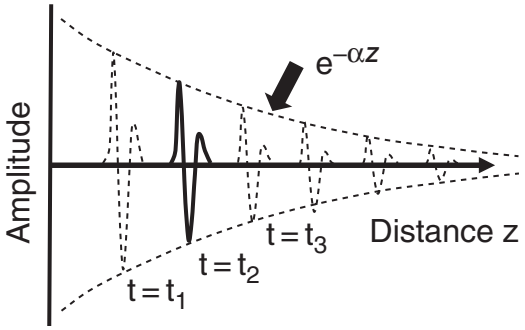

Figure 4.3: Amplitude decay of EM waves in lossy medium [2].

4.4.3 Frequency Shift

In addition to the signal amplitude decay with increasing distance, attenuation causes electromagnetic wave broadening since the high-frequency content of the spectrum dissipates faster than the low-frequency part. In other words, the dominant (maximum) and central frequency of the pulse will downshift to lower values as the wave propagates in a lossy medium [75], [116], [51]. For example, Figure (4.4) presents a synthetic pulse and the centroid frequency downshift with time.

The geometrical energy spreading is almost independent of frequency. Radar wavelets can change in shape at subsurface interfaces, but this is not so common in environments well suited for GPR. The progressive broadening of arrivals down a trace is less likely to be caused by interface reflection and transmission effects [51]. It is, however likely, in some cases where transmission and reflection coefficients are frequency-dependent, depending on the materials' frequency dependence on either side e.g., reflection between sand and clay.

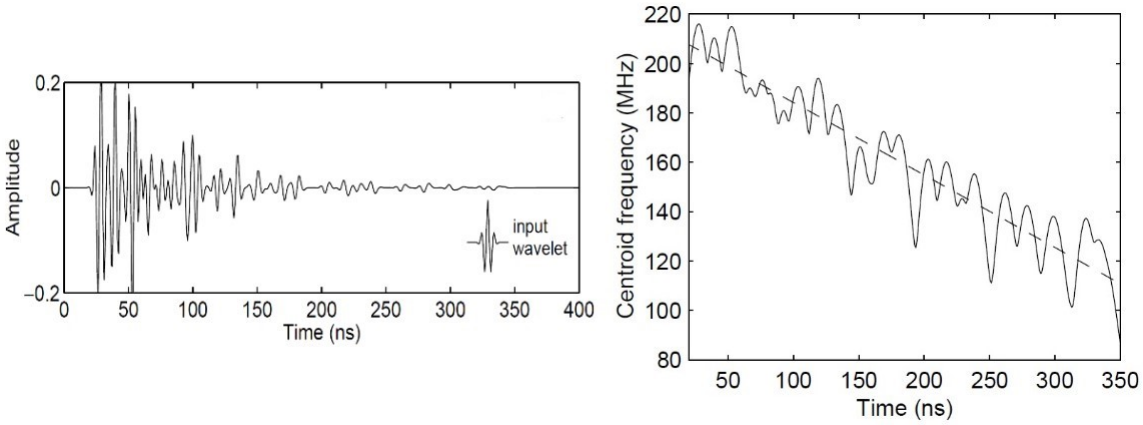

Figure 4.4: (left) A synthetic trace, (right) Variation of central frequency through time (Taken from [51]).

The frequency shift method to estimate attenuation offers certain advantages over other methods because the frequency shift is less corrupted by the adverse effects of scattering, geometric spreading, receiver coupling variations, transmission-reflection losses, and radiation/reception pattern effects, whereas, the amplitudes are easily contaminated by these factors. Indeed, the frequency-shift (equivalently pulse-broadening) of an EM pulse is relatively insensitive to these effects [75], [116].

Centroid Frequency Shift Method

Centroid frequency is referred to the geometric center of the frequency band. The centroid frequency downshift is linked to attenuation and can be attributed to dielectric losses. Figure (4.5) illustrates a pictorial description of centroid frequency downshift for a Gaussian spectra. The intrinsic attenuation of EM waves, over the bandwidths of typical radar pulses propagating in many geological materials,

is a linear function of frequency and can be characterized by a constant value [144]. Hence, assuming that the attenuation linearly depends on the frequency, *i.e.*, $\alpha_i(\nu) = \alpha_0\nu$, the centroid of traveling wave amplitude-spectrum is related to the attenuation coefficient as [75], [116]:

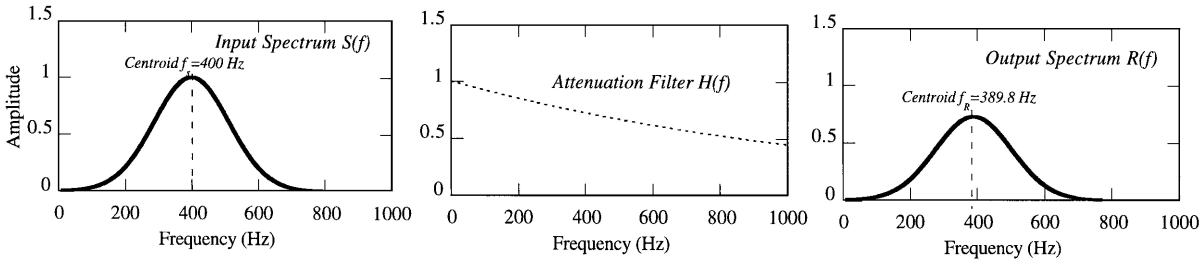

Figure 4.5: A source wavelet of Gaussian shape with the centroid frequency of 400 MHz, the attenuation effect of the medium and the received signal. The frequency shift is visible on the received signal (Taken from [116]).

$$\nu_c = \nu_0 - \sigma_s^2 \int_{ray} \frac{\pi}{VQ}\, dl = \nu_0 - \sigma_s^2 \int_{ray} \alpha_0\, dl \tag{4.13}$$

where ν_c, ν_0 and σ_s^2 are centroid frequency of received spectrum, centroid frequency of incident pulse and the variance of source pulse amplitude , respectively. The integral is taken along the ray-path. The equation (4.13) presents a gradual downshift of the centroid frequency as $\Delta\nu = \nu_0 - \nu_c$. Liu, et al., [75] proposed a statistical based approach to estimate the attenuation coefficient from the centroid downshift of the spectrum over a range of frequency. The amplitude spectrum of the incident wave, $X(\nu)$, in general can be related to the received amplitude spectrum $Y(\nu)$ by:

$$Y(\nu) = G(\nu)\, H(\nu)\, X(\nu) \tag{4.14}$$

where $G(\nu)$ includes the effects of geometric spreading, instrument response, source and receiver coupling to the medium, antenna radiation pattern, reflection and transmission coefficients, and the phase accumulation due to propagation, and $H(\nu)$ presents the attenuation effects of the medium on the wave amplitude. For a known amplitude spectrum of the incident wave, $X(\nu)$, the centroid frequency of the received pulse is estimated by:

$$\nu_c = \frac{\int_0^\infty \nu Y(\nu) d\nu}{\int_0^\infty Y(\nu) d\nu} \tag{4.15}$$

and variance of received signal spectrum is given by:

$$\sigma_c^2 = \frac{\int_0^\infty (\nu - \nu_c)^2\, Y(\nu) d\nu}{\int_0^\infty Y(\nu) d\nu} \tag{4.16}$$

If G is independent of frequency then ν_c and σ_c^2 will be independent of G, as well. This property is the main advantageous of centroid frequency downshift approach. However, this method requires to know the incident wave spectrum priory, and commonly in literature a Ricker or Gaussian function is assumed to present the source wavelet. Note that in medium that the scattering attenuation cannot be ignored the estimated attenuation will be a combination of the intrinsic and that component of scattering attenuation which is linear with frequency.

For the spacial case where the source wavelet is Gaussian with the center operating frequency of ν_0 and spectrum variance of σ_0^2:

$$X(\nu) = \frac{1}{\sqrt{2\pi\sigma_0}} \exp\left(-\frac{(\nu - \nu_0)^2}{2\sigma_0^2}\right) \tag{4.17}$$

the centroid frequency of the received pulse in a homogeneous medium is given by [75]:

$$\nu_c(\tau) = \nu_0 - \sigma_0^2 Q^{-1} \pi\tau \tag{4.18}$$

Note that to analyze the spectral variation of EM pulse through time, the time-frequency distribution analysis by using an appropriate method like Short Time Fourier Transform (STFT) or S transform is required (see Appendix A).

Maximum (Peak) Frequency Shift Method

Maximum or peak frequency is referred to the frequency corresponding to maximum amplitude of the spectrum. Therefore, it is simply obtained by: equating the derivative of the amplitude spectrum with respect to frequency to zero. Similar to the centroid frequency variation, as the signal propagates, frequency-dependent attenuation causes a downshift of the peak of the amplitude spectrum. This spectral shift can be used to estimate attenuation. For example, assuming that the source wavelet is a Ricker wavelet defined by:

$$X(\nu) = A_0 \left(\frac{\nu}{\nu_0}\right)^2 \exp\left(-\frac{\nu^2}{\nu_0^2}\right) \tag{4.19}$$

with $A_0 = \frac{2}{\sqrt{\pi}}$, the amplitude of received spectrum after time τ can be expressed as (G is neglected):

$$Y(\nu,\tau) = X(\nu)\exp(-\alpha V\tau) = A_0 \left(\frac{\nu}{\nu_0}\right)^2 \exp\left(-\frac{\nu^2}{\nu_0^2} - \alpha V\tau\right) \tag{4.20}$$

Setting the derivative of equation (4.20) equal to zero:

$$\frac{\partial Y(\nu,\tau)}{\partial \nu}|_{(\nu=\nu_m)} = 0 \tag{4.21}$$

assumption of low loss medium yields the loss tangent as a function of frequency shift [11]:

$$\tan\delta = \frac{2}{\pi\tau}\frac{\nu_0^2 - \nu_m^2(\tau)}{\nu_0^2\nu_m(\tau)} \tag{4.22}$$

where ν_m is maximum frequency at time τ. Lauro et al., [63] obtained an equivalent relation that is expressed by:

$$\nu_m(\tau) = \nu_0 \ \exp\left[-\sinh^{-1}\left(\frac{\pi}{4}\nu_0\tan\delta\tau\right)\right] \tag{4.23}$$

It is worth noting that since a Gaussian wavelet is symmetric, the mean, centroid and maximum frequencies are coincident whereas for a Ricker wavelet because of the asymmetry these especial frequencies are different. Similarly, for source wavelet with Gaussian spectrum of standard deviation σ_g, the received spectrum after time τ is:

$$Y(\nu,\tau) = \frac{1}{\sqrt{2\pi\sigma_0}}\exp\left(-\frac{(\nu-\nu_0)^2}{2\sigma_0^2} - \alpha V\tau\right) \tag{4.24}$$

By setting the derivative of equation (4.24) equal to zero, the loss tangent is obtained as:

$$\tan\delta = \frac{\nu_0 - \nu_m(\tau)}{\pi\tau\sigma_0^2} \tag{4.25}$$

Equations (4.25) and (4.18) are same due to the symmetric property of the Gaussian wavelet.

4.5 Estimation of Attenuation in Literature

In this section several examples of loss tangent estimation with their applications are briefly described.

Grimm et al., [43] studied the radar data collected at Volcanic Tableland of the Bishop (California) Tuff for Mars-analog geophysical investigation to evaluate factors that affect radars for Mars. To estimate the total attenuation, first the energy-average trace is computed by taking the mean square over all traces at each time, then, the attenuation is estimated from a least squares fit to the logarithm of power (Figure (4.6)). This operation implicitly assumes a medium that is composed of horizontal layers or isotropic, random scatterers. The intrinsic attenuation directly is measured from vertical electric sounding. The residual attenuation that is obtained from total attenuation minus the measured absorption is attributed to the scattering.

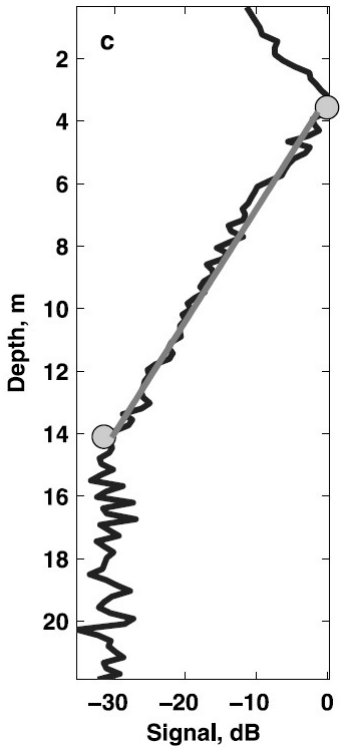

Figure 4.6: Horizontally averaged power versus depth. The fit (gray line) to the exponential decay is used to estimate the total attenuation (Taken from [43]).

Campbell et al., [17] estimate a loss tangent of $0.005 - 0.012$ using sounding radar profiles across Amazonis Planitia from the Shallow Radar (SHARAD) instrument on the Mars Reconnaissance Orbiter. The loss tangent is estimated from the ratio of variations in radar echo strength at two different time delays. The main assumptions are:

1. The surface roughness at the SHARAD wavelength scale is constant with respect to position.
2. The subsurface interface also has constant roughness on the scale of the radar wavelength in the medium.
3. The explored layer has constant dielectric loss properties.
4. The real dielectric contrasts at the surface-atmosphere and surface-subsurface interfaces are constant over some length of the detected interfaces.

As a result, the observed changes in the back-scattered power from subsurface depends only on the thickness of the layer being probed, and the loss tangent will be related to the signal attenuation in the medium as a function of traveled distance. For a round-trip distance $2z$, and initial amount of power P_0, the observed power loss is expressed by:

$$\alpha_p = \frac{P(z)}{P_0} = \exp\left[\frac{-8\pi z}{\lambda}\sqrt{\frac{\varepsilon'_r}{2}\left(\sqrt{1+\tan\delta^2}-1\right)}\right] \tag{4.26}$$

considering that

$$z = \frac{c\ \Delta\tau}{2\sqrt{\varepsilon'_r}} \tag{4.27}$$

the loss tangent is related to the power loss as:

$$\tan\delta = \sqrt{\left\{2\left[\frac{\lambda}{4\pi c\ \Delta\tau}\ln(\alpha_p)\right]^2\right\} - 1} \tag{4.28}$$

where $\Delta\tau$ is round-trip delay time, ε'_r is the real part of realtive permittivity of medium, λ is the free space radar wavelength that for SHARAD centroid frequency is $\sim 15\ m$.

Grima et al., 2009, [42] uses the power ratio and estimate $tan\delta < 0.0026$ for bulk ice in north polar deposit of Mars from SHARAD data as:

$$tan\delta = \frac{10 \log\left(\frac{P_t}{P_b}\right)}{0.091\ \nu\ \Delta\tau\ c} \tag{4.29}$$

with

$$P_t = P_s \left[\left(\frac{\sqrt{\varepsilon'_r}+1}{\sqrt{\varepsilon'_r}-1}\right)^2 - 1\right] \tag{4.30}$$

where P_t, P_s and P_b are the power of transmitted echo, power of surface echo and power of bedrock echo, respectively, and ν is the SHARAD frequency in MHz. The ε'_r is the real part of relative permittivity of the deposit that by assuming a homogeneous medium can be obtained from the time delay, $\Delta\tau$, between surface and bottom echo:

$$\varepsilon'_r = \left(\frac{\Delta\tau c}{2h}\right)^2 \tag{4.31}$$

where h is the thickness of deposit and c is the speed of light in free space.

Campbell and Morgan, 2018, [18] implement a similar approach to estimate the loss tangent based on splitting the bandwidth of SHARAD signals into radargrams with different subbands and determined the attenuation as a function of free-space wavelength, λ_1 and λ_2, as:

$$\frac{P_2}{P_1} = \frac{P_2^0}{P_1^0}\ e^{4\pi c\tau\left(\frac{1}{\lambda_1}-\frac{1}{\lambda_2}\right)\tan\delta} \tag{4.32}$$

where P_2^0 and P_1^0 are the incident power echo of two subbands, and P_2 and P_1 are those observed by the receiver.

Lauro et al., 2017, [63] estimate the loss tangent of the volcanic deposits on Mount Etna (Italy) by applying the amplitude decay and frequency shift methods in a section where a sloping interface is detected. The transmitted signal is approximated by Gaussian and Ricker wavelets, and the contribution of relaxation mechanism (polarization) and conduction terms in the loss tangent is separated. The results can offer some insights to retrieve quantitative information on electrical properties of planetary subsurface. The received spectrum is expressed as:

$$Y(\nu,\tau) = \rho X(\nu)\, e^{-j\beta 2z}\ e^{-\alpha 2z} \tag{4.33}$$

where ρ is the reflection coefficient at the interface, $X(\nu)$ is the spectrum of transmitted signal, $\beta = \omega/V = 2\pi\nu/V$, and α is attenuation coefficient that for low loss medium is $\alpha \approx \frac{\pi\nu}{V}\tan\delta$. Considering that $2z = V\tau$, equation (4.33) is written as:

$$Y(\nu,\tau) = \rho X(\nu)\, e^{-2\pi\nu j\tau}\ e^{-\pi\nu\tan\delta\tau} \tag{4.34}$$

The $\tan\delta$ is divided into two terms:

$$tan\delta = \frac{\varepsilon''}{\varepsilon'} + \frac{\sigma_s}{\omega\varepsilon'} = tan\delta_p + tan\delta_c \tag{4.35}$$

where σ_s is static conductivity, $tan\delta_p$ and $tan\delta_c$ specify polarization and conductivity contribution in loss tangent, respectively. Substituting equation (4.35) in (4.34) yields:

$$Y(\nu,\tau) = \rho X(\nu)\, e^{-2\pi\nu j\tau} e^{-\pi\nu(\tan\delta_p+\tan\delta_c)\tau} \tag{4.36}$$

then

$$Y(\nu,\tau) = \rho X(\nu)\, e^{-2\pi\nu j\tau} e^{\left(-\pi\nu\tan\delta_p-\frac{\sigma_s}{2\varepsilon'}\right)\tau} \tag{4.37}$$

note that ε' presents the real part of complex permittivity as already defined as, $\varepsilon = \varepsilon' - j\varepsilon''$. Assuming $X(\nu)$ is a Gaussian pulse with the operating centroid frequency ν_0, amplitude of X_0 and variance σ_0 the spectrum of the received echo will be:

$$Y(\nu,\tau) = \rho X_0 e^{-\frac{(\nu-\nu_0)^2}{2\sigma_0^2}} e^{-2\pi\nu j\tau} e^{\left(-\pi\nu\tan\delta_p - \frac{\sigma}{2\varepsilon' f}\right)\tau} \tag{4.38}$$

If the losses due to polarization phenomena are frequency independent the received spectrum is still a Gaussian function that its amplitude is concisely expressed by:

$$|Y(\nu,\tau)| = Y_\tau \; e^{-\frac{\left(\nu-\nu_0^{'}\right)^2}{2\sigma_0^2}} \tag{4.39}$$

where $\nu_0^{'}$ is centroid frequency of the received spectrum at time τ that is related to the ν_0 through:

$$\nu_0^{'}(\tau) = \nu_0 - \pi\sigma_0^2 \tan\delta_p \tau \tag{4.40}$$

and

$$Y_\tau = |Y_0| e^{-\pi\nu_0 \tan\delta_0 \tau + \frac{1}{2}\pi^2\sigma_0^2 \tan\delta_p^2 \tau^2} \tag{4.41}$$

where

$$tan\delta_0 = tan\delta|_{\nu=\nu_0} \tag{4.42}$$

In the case that the source wavelet is described by a Ricker wavelet, spectrum of the reflected signal cannot be analytically modeled, however, the maximum frequency variation versus time is written as:

$$\nu_0'(\tau) = \nu_0 \;\; \exp\left[-\sinh^{-1}\left(\frac{\pi}{4}\nu_0 \tan\delta_p \tau\right)\right] \tag{4.43}$$

If $\tan\delta_p \ll 1$, formula (4.43) will be linear:

$$\nu_0^{'}(\tau) \approx \nu_0 - \frac{\pi}{4}\nu_0^2 \tan\delta_p \tau \tag{4.44}$$

This procedure can retrieve the unknowns. The shifted centroid frequency at time τ, *i.e.,* ν_0', the amplitude $Y(\tau)$ and bandwidth σ_0 are obtained from a Gaussian function fit to $|Y(\nu,\tau)|$ in equation (4.39). The loss tangents, $\tan\delta_p$, $\tan\delta_0$ and ν_0 can be estimated by a polynomial regression to the logarithm of $Y(\tau)$ in equation (4.41). In addition, for the Gaussian wavelet assumption equation (4.40) and for Ricker wavelet assumption equation (4.44) can be fitted to the measured ν_0', retrieving the unknown parameters.

Bradford 2007, [11] derives the following linear approximation to the attenuation coefficient at reference frequency $\omega_0 = 2\pi\nu_0$, for low loss material:

$$\alpha \approx \alpha_{\omega_0} + \frac{\sqrt{\mu_0\varepsilon'_{\omega_0}}}{Q}(\omega - \omega_0) \tag{4.45}$$

$$\alpha = \alpha_{\omega_0} + \frac{1}{2}\sqrt{\frac{\mu_0}{\varepsilon'_{\omega_0}}}\left[\varepsilon''_{\omega_0} + \omega_0\frac{\partial\varepsilon''}{\partial\omega} - \frac{1}{2\varepsilon'_{\omega_0}}\frac{\partial\varepsilon'}{\partial\omega}\right](\omega - \omega_0) \tag{4.46}$$

then comparing with the linear approximation of α introduced by [144] finds a functional form for Q^{-1} as:

$$Q^{-1} = \frac{1}{\varepsilon'_{\omega_0}}\left[\varepsilon''_{\omega_0} + \omega_0\frac{\partial\varepsilon''}{\partial\omega} - \frac{1}{2\varepsilon'_{\omega_0}}\frac{\partial\varepsilon'}{\partial\omega}\right] \tag{4.47}$$

where $\omega_0 = 2\pi\nu_0$. For a Ricker wavelet, by evaluating the shift in the maximum of propagating signal spectrum through time, Q^{-1} is related to the peak frequency ω_m at time τ as:

$$Q^{-1} = \frac{4}{\tau}\frac{\omega_0^2 - \omega_m^2}{\omega_0^2\omega_m} \tag{4.48}$$

that is equivalent to equation (4.22). The formulation (4.47) provides a basis to invert for relaxation parameters given a differentiable relaxation model and measurements of Q^{-1} over several different pass

bands. Bradford et al., [14] showed that for radar propagating in the 1 GHz range through snow containing liquid water, Q^{-1} can be directly related to the imaginary part of the permittivity, which in turn is a simple function of liquid water content. Then with a coincident measure of radar velocity it is possible to estimate total snow water equivalent.

Ding et al., [23] analyze the Chang'E-5 LRPR data with the frequency shift method to estimate the loss tangent of the lunar regolith within a depth of ~ 2.8 m. The estimated loss tangent of the Chang'E-5 landing site ranges from 0.0148 to 0.0016.

Feng et al., [33] examine data obtained by the Lunar Penetrating Radar (LPR) onboard the Chang'E-4 mission to study the dielectric properties and stratigraphy of lunar regolith on the far side of the Moon. They evaluated the dielectric loss from the maximum penetration depth based on the radar equation. Their results suggest that regolith at the landing site has a permittivity of $2.64 - 3.85$ and a loss tangent of $0.0032 - 0.0044$, indicating that the local regolith is composed of a fine-grained, low-loss material that is much more homogeneous than that found at the Chang'E-3 landing site. The total thickness of weathered material is estimated ~ 40 m, with several regolith layers.

Eide et al., [29] implement the centroid frequency-shift method to estimate attenuation from Radar Imager for Mars' Subsurface Exploration (RIMFAX) data acquired along the Mars 2020 Perseverance rover traverse. Over Jezero Crater Floor the authors study radar attenuation in the upper 5 m of the shallow Martian subsurface and for the Q factor obtain the average value of 70.4 ± 7.7.

Analyzing Chang'E-4 LPR data, Li et al., [72] use the centroid-frequency approach and for the two-way travel time from 0 to about 450 ns report the average loss tangent $\tan\delta = 0.005 \pm 0.002$ represents an average value for the entire radar section over that interval. Then, using the obtained loss tangent estimate the bulk density and consequently the oxide content ($FeO+TiO_2$) is determined.

Bharti et al., [7] to characterize the signal sensitivity in terms of the power loss and time delay measure the along-track power of the reflectors (surface and subsurface) of SHARAD observations that cross the Mangala crater (informally named by authors). Then to determine the loss tangent of the subsurface material they fit the equation (4.28) [here $\lambda = 15\ m$ corresponds to SHARAD wavelength in free space] to measurements. To increase the total range of time delays and derive a reasonably better fit the reflectors from two radar tracks are combined. Finally, they obtain loss tangent values ranging between $0.008 - 0.009$ and attribute these values to moderate radar-absorbing material like dry, moderate-density sediments or the lower end of the range of values measured for basalt. In addition, the relative permittivity is estimated from SHARAD data.

Lai et al., [60] study Chang'E-3 and Chang'E-4 LPR data to compare dielectric properties and structure of lunar Regolith at corresponding landing sites, as two rovers are equipped with the radar sounder of same configuration. In term of attenuation, they estimate the average loss tangent by inversion of radar equation, based on ratio between received and transmitted pulses powers. The reflections are corrected for geometric spreading. Along with the traversing path of YUTU-2 rover between 0 and 105 m,the estimated average value of loss tangent is $tan\delta = 0.0039 \pm 0.0002$. Using the evaluated loss tangent, the $FeO+TiO_2$ content of lunar regolith is infered to be $11.8\% - 13\%$. At Chang'E 3 site, for $tan\delta$ and $FeO+TiO_2$content is estimated as ~ 0.02 and $24.3 \pm 3.4\ wt\%$, respectively.

Chapter 5

Estimation of Radar Pulse Attenuation: Novel Techniques

5.1 Introduction

Chapter 4 presents the general framework of basic methods for the estimation of propagating EM waves attenuation in lossy mediums, with applications to terrestrial and planetary explorations. The purpose of this chapter is to introduce novel approaches to estimating the attenuation of radar pulses for use on earth and on other planets. This technical chapter contains two parts.

In Part I, a Ricker wavelet is used to model the transmitted radar pulse, and a novel forward formula, based on the centroid-frequency shift is developed. In order to validate the new formulation, synthetic data generated by a simulated dipping sharp reflector separating two medium with different electric properties is used. Finally, the method is implemented to real datasets collected on volcanic ash to retrieve the loss tangent.

In Part II, a new variant of the previous algorithm in which the centroid-frequency shift is computed from power spectrum of the records is introduced. Using synthetic GPR data generated with the gprMax simulator over an inhomogeneous medium, these approaches are compared with the maximum frequency shift method. Then, real GPR data collected on a fractured basaltic lava flow are studied to retrieve the loss tangent values. In addition the scattering contribution is deduced from the best liner fit to the amplitude decay of the received pulses. These two proposed methods are particularly suitable in all those cases where losses are dominated by the polarization phenomena, as is the case in terrestrial and planetary dry and cold environments.

To recover the unknowns, a probabilistic inversion approach which accounts also the uncertainties due to noise content in data is used.

5.2 Part I

5.2.1 Background Theory

For a monochromatic plane electromagnetic wave that is uniform in x and y directions, with only $\hat{x}$ component that propagates along the positive z direction in a lossy medium, the electric field is given by:

$$\mathbf{E}(z,t) = \mathcal{R}\left\{\mathbf{E}(z)\, e^{j\omega t}\right\} = \widehat{\boldsymbol{x}}\, \mathcal{R}\left\{E_0\; e^{j(\omega t - \beta z)}\right\} e^{-\alpha z} \tag{5.1}$$

where as defined in Chapter 1, $\alpha = -\frac{\omega}{c}\mathcal{I}\left\{\sqrt{\varepsilon_{er}}\right\}$ and $\beta = \frac{\omega}{c}\mathcal{R}\left\{\sqrt{\varepsilon_{er}}\right\}$ are attenuation coefficient and phase constant, and E_0 is the electric field amplitude. In addition, total attenuation coefficient can be expressed by the summation of intrinsic α_i and scattering α_s attenuation coefficients, $\alpha = \alpha_i + \alpha_s$. In this part, the medium is assumed to be almost homogeneous (that means $\alpha \approx \alpha_i$), linear, isotropic and non-magnetic, thus the attenuation can be expressed according to Chapter 1 as:

$$\alpha(\omega) = -\frac{\omega}{c}\Im\left\{\sqrt{\varepsilon_{er}}\right\} = \frac{\omega}{V}\left\{\frac{1}{2}\left[\sqrt{1+tan\delta(\omega)^2}-1\right]\right\}^{1/2} = \frac{\omega}{2V}tan\delta_a(\omega),\ (Np/m) \tag{5.2}$$

where ε_{er} is the relative effective complex permittivity, $V = \frac{\omega}{\beta} = \frac{c}{\mathcal{R}\{\sqrt{\varepsilon_{er}}\}}$ (m/s) is phase velocity, and $tan\delta_a(\omega)$ is the apparent loss tangent that is used to evaluate the loss tangent:

$$tan\delta(\omega) = \sqrt{\left\{1+\frac{tan\delta_a(\omega)^2}{2}\right\}^2 - 1} \tag{5.3}$$

moreover, loss tangent has two components:

$$tan\delta(\omega) = \frac{\varepsilon''}{\varepsilon'} + \frac{\sigma_s}{\omega\varepsilon'} = tan\delta_p(\omega) + tan\delta_c(\omega) \tag{5.4}$$

where $\tan\delta_p(\omega)$ and $\tan\delta_c(\omega)$ account for polarization and conductive terms, respectively. For dry rocks, the loss tangent is a frequency-independent quantity and is mainly due to polarization processes [80], hence:

$$tan\delta \cong tan\delta_p \cong Const. \tag{5.5}$$

and for low loss materials that $tan\delta_p \ll 1$, a linear approximation of the attenuation factor expressed in equation (5.2) gives:

$$\alpha(\omega) = \frac{\omega}{V}\frac{tan\delta_a}{2} \cong \frac{\omega}{V}\frac{tan\delta}{2} \tag{5.6}$$

In dispersive materials, where the loss tangent is frequency-dependent, Taylor expansion allows to linearly approximate the attenuation coefficient around the GPR operating frequency ν_0 as follows [144], [11]. Considering that $\omega = 2\pi\nu$

$$\alpha(\nu) = \frac{\pi\nu}{V}tan\delta(\nu) = \frac{\pi\nu}{V}\left[\frac{\sigma_s}{2\pi\nu\varepsilon'} + tan\delta_p(\nu)\right] = \frac{\sigma_s}{2V\varepsilon'} + \frac{\pi\nu}{V}tan\delta_p(\nu) \tag{5.7}$$

the second term is approximated by Taylor expansion around ν_0 as:

$$\begin{aligned}\frac{\pi\nu}{V}tan\delta_p(\nu) &\approx \frac{\pi\nu_0}{V}tan\delta_p(\nu_0) + (\nu-\nu_0)\left[\frac{\pi}{V}tan\delta_p(\nu) + \frac{\pi\nu}{V}\frac{\partial tan\delta_p(\nu)}{\partial\nu}\right]_{\nu=\nu_0} \\ &= \frac{\pi\nu_0}{V}tan\delta_p(\nu_0) + \frac{\pi\nu}{V}tan\delta_p(\nu_0) - \frac{\pi\nu_0}{V}tan\delta_p(\nu_0) + (\nu-\nu_0)\left[\frac{\pi\nu}{V}\frac{\partial tan\delta_p(\nu)}{\partial\nu}\right]_{\nu=\nu_0} \\ &= \frac{\pi\nu}{V}tan\delta_p(\nu_0) + (\nu-\nu_0)\left[\frac{\pi\nu}{V}\frac{\partial tan\delta_p(\nu)}{\partial\nu}\right]_{\nu=\nu_0}\end{aligned} \tag{5.8}$$

inserting equation (5.8) in (5.7) yields:

$$\alpha(\nu) \approx \frac{\sigma_s}{2V\varepsilon'} + \frac{\pi\nu}{V}tan\delta_p(\nu_0) + (\nu-\nu_0)\left[\frac{\pi\nu}{V}\frac{\partial tan\delta_p(\nu)}{\partial\nu}\right]_{\nu=\nu_0} \tag{5.9}$$

5.2.2 Received Spectrum at Receiver

The amplitude spectrum of the received echos is the absolute value of the Fourier transform of received signals $y(t,\tau)$ that are back-scattered by discontinuities located in subsurface:

$$Y(\nu,\tau) = \left|\int_{-\infty}^{\infty} y(t,\tau)e^{-j2\pi\nu t}\,d\nu\right| = |\rho X(\nu)|\, e^{-\pi\nu\ tan\delta_a\tau} \tag{5.10}$$

where τ is two-way travel time, $X(v)$ s the spectrum of the signal emitted by the antenna, ρ is the Fresnel reflection coefficient, and $e^{-\pi\nu\ tan\delta_a\tau}$ is the attenuation term. The emitted spectrum $X(\nu)$ is generally unknown since it depends on the coupling of the antenna with the ground. Therefore, it is common to assume a theoretical function like a Ricker or a Gaussian wavelet as the transmitted signal (*e.g.*, [75], [152], [63]). Here, a Ricker wavelet is considered, whose amplitude spectrum is expressed as:

$$X(\nu) = A_0\left(\frac{\nu}{\nu_0}\right)^2\exp\left(-\frac{\nu^2}{\nu_0^2}\right) \tag{5.11}$$

where ν_0 is operating frequency and $A_0 = 2/\sqrt{\pi}$ is the amplitude. The received spectrum is obtained by combining equations (5.11) and (5.10):

$$Y(\nu,\tau) = A_0(\frac{\nu}{\nu_0})^2 \; e^{-(\frac{\nu}{\nu_0})^2} \; e^{-\pi\nu \; tan\delta_a\tau} \tag{5.12}$$

According to this relation the spectral content of the transmitted signal is affected by the attenuation factor $e^{-\pi\nu \; tan\delta_a\tau}$, which filters out the high frequency components. As already stated, this causes the maximum of transmitted-signal amplitude-spectrum and average frequency content (centroid frequency) undergo a gradual down shift as the time-depth τ increases [see Figure (4.4) and (4.5)].

5.2.3 Loss tangent Estimation: Amplitude Spectrum Analysis

As noted in Chapter 4, the centroid frequency is defined as the geometric center of the frequency band, and it is well approximated by the mean frequency, which is a statistical quantity. The entroid frequency can be computed from amplitude spectrum as:

$$\nu_{ca}(\tau) = \frac{\int_0^\infty \nu Y(\nu,\tau)d\nu}{\int_0^\infty Y(\nu,\tau)d\nu} \tag{5.13}$$

where ν_{ca} presents the centroid frequency obtained from the amplitude spectrum. Due to the presence of noise in the GPR data, which usually appears constant in the whole spectrum, equation (5.13) may overestimates the centroid frequency. This effect can be mitigated by constraining the frequency spectrum to an upper boundary frequency value, ν_{UB}. Accordingly, the definition of the centroid frequency is modified:

$$\nu_{ca}(\tau) = \frac{\int_0^{\nu_{UB}} \nu Y(\nu,\tau)d\nu}{\int_0^{\nu_{UB}} Y(\nu,\tau)d\nu} \tag{5.14}$$

by substituting equation (5.12) in (5.14) the relation describing the time-dependent centroid frequency of the received spectrum is obtained

$$\nu_{ca}(\tau) = \frac{\int_0^{\nu_{UB}} \nu \; \left(\frac{\nu}{\nu_0}\right)^2 e^{-\left(\frac{\nu}{\nu_0}\right)^2} \; e^{-\pi\nu\tan\delta_a\tau} \; d\nu}{\int_0^{\nu_{UB}} \left(\frac{\nu}{\nu_0}\right)^2 e^{-\left(\frac{\nu}{\nu_0}\right)^2} \; e^{-\pi\nu\tan\delta_a\tau} \; d\nu} \tag{5.15}$$

defining two new variables $u = \nu/\nu_0$ and $x = \frac{1}{2}\pi\nu_0\tan\delta_a\tau$,

$$\nu_{ca}(\tau) = \frac{\int_0^{\nu_{UB}} \nu \; \left(\frac{\nu}{\nu_0}\right)^2 e^{-\left(\frac{\nu}{\nu_0}\right)^2} e^{-2x\frac{\nu}{\nu_0}} \; d\nu}{\int_0^{\nu_{UB}} \left(\frac{\nu}{\nu_0}\right)^2 e^{-\left(\frac{\nu}{\nu_0}\right)^2} e^{-2x\frac{\nu}{\nu_0}} \; d\nu} = \nu_0 \frac{\int_0^{\nu_{UB}/\nu_0} u^3 e^{-(u+x)^2} e^{x^2} \; du}{\int_0^{\nu_{UB}/\nu_0} u^2 e^{-(u+x)^2} e^{x^2} \; du} \tag{5.16}$$

and by introducing the variable $\xi = u + x$,

$$\nu_c(\tau) = \nu_0 \frac{\int_x^{x_{max}} (\xi - x)^3 e^{-\xi^2} \; d\xi}{\int_x^{x_{max}} (\xi - x)^2 e^{-\xi^2} \; d\xi} \tag{5.17}$$

where $x_{max} = x + \nu_{UB}/\nu_0$. The integrals are split into different terms:

$$\nu_{ca}(\tau) = \nu_0 \frac{\int_x^{x_{max}} \xi^3 e^{-\xi^2} \; d\xi - 3x\int_x^{x_{max}} \xi^2 e^{-\xi^2} \; d\xi + 3x^2\int_x^{x_{max}} \xi e^{-\xi^2} \; d\xi - x^3\int_x^{x_{max}} e^{-\xi^2} \; d\xi}{\int_x^{x_{max}} \xi^2 e^{-\xi^2} \; d\xi - 2x\int_x^{x_{max}} \xi e^{-\xi^2} \; d\xi + x^2\int_x^{x_{max}} e^{-\xi^2} \; d\xi} \tag{5.18}$$

which gives the variation of centroid frequency as a function of operating frequency, time and loss tangent [66]

$$\nu_{ca}(\nu_0,\tau,tan\delta_a) = \nu_0 \frac{I_3(x) - 3xI_2(x) + 3x^2I_1(x) - x^3I_0(x)}{I_2(x) - 2xI_1(x) + x^2I_0(x)} \tag{5.19}$$

where $I_n(x)$ is defined as:

$$I_n(x) = \int_x^{x_{max}} \xi^n e^{-\xi^2} d\xi \tag{5.20}$$

In particular, for $n = 0,\ 1,\ 2,\ 3$ these integrals are equal to:

$$\begin{aligned} I_0(x) &= \frac{\sqrt{\pi}}{2}\ [\ erfc(x) - erfc(x_{max})] \\ I_1(x) &= \frac{1}{2}\ \ (e^{-x^2} - e^{-x_{max}^2}) \\ I_2(x) &= \frac{\sqrt{\pi}}{4}\ \ [\ erfc(x) - erfc(x_{max})] + \frac{1}{2}(xe^{-x^2} - x_{max}e^{-x_{max}^2}) \\ I_3(x) &= \frac{1}{2}\ \ (e^{-x^2} - e^{-x_{max}^2}) + \frac{1}{2}\ (x^2e^{-x^2} - x_{max}^2 e^{-x_{max}^2}) \end{aligned} \tag{5.21}$$

where $erfc(x)$ is the complementary error function:

$$erfc(x) = \frac{2}{\sqrt{\pi}} \int_x^{\infty} e^{-\xi^2} d\xi \tag{5.22}$$

Equation (5.19) is a nonlinear expression that defines the relation between the measured centroid frequencies and the model parameters, that are, the operating frequency ν_0 and the medium apparent loss tangent $tan\delta_a$. The centroid frequency is computed from the spectrum amplitude at different time delays τ, and then the computed centroid-frequency versus time is used to retrieve the loss tangent through a probabilistic inversion approach [138], [86] (see Chapter 3).

For $x \ll 1$ and $\nu_{UB} \to \infty$ a linear approximation of equation (5.19) can be obtained:

$$\nu_c(\tau) \approx\ \nu_c(0) + \nu_0\ \ \left.\frac{\partial F(x)}{\partial x}\right|_{x=0} x \tag{5.23}$$

where the function $F(x)$ is defined as:

$$F(x) \equiv \frac{\nu_c(\tau)}{\nu_0} \tag{5.24}$$

and considering:

$$F(x) = \frac{N(x)}{D(x)} \tag{5.25}$$

we have:

$$\frac{\partial F(x)}{\partial x} = \frac{D\frac{\partial N(x)}{\partial x} - N\frac{\partial D(x)}{\partial x}}{D^2} \tag{5.26}$$

where

$$N(x) = I_3(x) - 3xI_2(x) + 3x^2 I_1(x) - x^3 I_0(x) \tag{5.27}$$

$$D(x) = I_2(x) - 2xI_1(x) + x^2 I_0(x) \tag{5.28}$$

$$\frac{\partial N(x)}{\partial x} = \frac{\partial I_3(x)}{\partial x} - 3x\frac{\partial I_2(x)}{\partial x} + 3x^2\frac{\partial I_1(x)}{\partial x} - x^3\frac{\partial I_0(x)}{\partial x} - 3I_2(x) + 6xI_1(x) - 3x^2 I_0(x) \tag{5.29}$$

and

$$\frac{\partial D(x)}{\partial x} = \frac{\partial I_2(x)}{\partial x} - 2x\frac{\partial I_1(x)}{\partial x} + x^2\frac{\partial I_0(x)}{\partial x} - 2I_1(x) + 2xI_0(x) \tag{5.30}$$

for $v_{UB} \to \infty$ ($i.e.,\ x_{max} \to \infty$):

$$\nu_c(0) =\ \nu_0\frac{2}{\sqrt{\pi}}, \quad I_1(0) = \frac{1}{2}\ , \quad I_2(0) = \frac{\sqrt{\pi}}{4}\ , \quad I_3(0) = \frac{1}{2} \tag{5.31}$$

consequently

$$\left.\frac{\partial F(x)}{\partial x}\right|_{x=0} = -\frac{3\pi - 8}{\pi} \tag{5.32}$$

Finally, substituting equations (5.32) and (5.31) in (5.23), the linear approximation of centroid frequency will be:

$$\nu_c(\tau) \approx \ \nu_0 \frac{2}{\sqrt{\pi}} - \frac{3\pi - 8}{\pi} \nu_0^2 \tan\delta_a \ \tau \tag{5.33}$$

As expressed in Chapter 4, the variation of maximum frequency assuming a Ricker wavelet for source pulse is given by:

$$\nu_m(\tau) = \nu_0 \ \exp\left[-\sinh^{-1}\left(\frac{\pi}{4}\nu_0 \tan\delta_a \tau\right)\right] \tag{5.34}$$

defining $x_h = \frac{\pi}{4}\nu_0 \ tan\delta_a \tau$, equation (5.34) can be expressed as:

$$\nu_m(\tau) = \nu_0 \ \exp\left[-\sinh^{-1}(x_h)\right] \tag{5.35}$$

For $x_h \to 0$, $\sinh^{-1}(x_h) \simeq x_h$ and consequently the linear approximation of $\nu_m(\tau)$ will be:

$$\nu_m(\tau) = \nu_0 e^{-x_h} \simeq \nu_0(1 - x_h) = \nu_0 - \frac{\pi}{4}\nu_0^2 \ tan\delta_a \ \tau \tag{5.36}$$

Jacobian Matrix in Inversion Process

The Jacobian matrix that is required in solution of the inverse problem is obtained from the partial derivatives of the centroid frequency as a function of $\tan\delta_a$ and ν_0 whose row numbers depends on the number of data N:

$$J_{ca_i} = \left[\frac{\partial \nu_{ca}(\tau_i)}{\partial \nu_0}, \frac{\partial \nu_{ca}(\tau_i)}{\partial \tan\delta_a}\right] \tag{5.37}$$

where $i = 1, 2, \ldots, N$, and N is number of data. Starting from equation (5.24), $F(x) = \frac{\nu_c(\tau)}{\nu_0}$, the partial derivatives of $\nu_c(\tau)$ with respect to model parameters (*i.e.*, $\tan\delta_a$ and ν_0) are given by:

$$\frac{\partial \nu_c(\tau)}{\partial \nu_0} = F(x) + \nu_0 \frac{\partial F(x)}{\partial x}\frac{\partial x}{\partial \nu_0} = F(x) + x\frac{\partial F(x)}{\partial x} \tag{5.38}$$

and

$$\frac{\partial \nu_c(\tau)}{\partial \tan\delta_a} = \nu_0 \frac{\partial F(x)}{\partial x}\frac{\partial x}{\partial \tan\delta_a} = \nu_0 \frac{x}{\tan\delta_a}\frac{\partial F(x)}{\partial x} \tag{5.39}$$

Estimation of Uncertainty

Solution of inversion problem requires the knowledge of data covariance matrix, $\boldsymbol{C_d}$, as well. If the data uncertainties u_d are uncorrelated, $\boldsymbol{C_d}$ is defined by $C_{dij} = u_{di}^2 \delta_{ij}$ where δ_{ij} is the delta Kronecker function. To compute the uncertainties associated with the data, it is assumed that the received signal $y(t, \tau)$ is affected by an additive white-Gaussian noise with zero mean and standard deviation u_n, $n(t) \simeq N(0, u_n^2)$, that is:

$$y(t, \tau) = y_{nf}(t, \tau) + n(t) \tag{5.40}$$

where $y_{nf}(t, \tau)$ is the noise-free signal. The uncertainty on the centroid frequency u_d is computed through the statistical propagation formula:

$$u_d = \sqrt{(\Delta\nu_{ca})^2 + (\Delta\nu_{ca}^n)^2} \tag{5.41}$$

where $\Delta\nu_{ca}$ is the uncertainty associated to the numerical discretization of the spectrum [see also equation (4.16)]:

$$\Delta\nu_{ca} = \sqrt{\frac{\sum_{k=1}^{K}(\nu_k - \nu_{ca})^2 \ Y_k}{\sum_{k=1}^{K} Y_k}} \tag{5.42}$$

where $Y_k = Y(\nu_k)$ presents the amplitude of the spectrum at frequency $\nu_k = \nu(k)$, and K is the index of maximum boundary-value of frequency $\nu(K) = \nu_{UB}$, and $\Delta\nu_{ca}^n$ is the uncertainty associated to the white-Gaussian noise:

$$\Delta\nu_{ca}^n = \frac{\partial\nu_{ca}}{\partial n} u_n \tag{5.43}$$

The theoretical uncertainty due to noise $\Delta\nu_{ca}^n$ is derived in following. The centroid frequency is numerically computed by:

$$\nu_{ca} = \frac{\sum_{k=1}^{K} \nu_k \, Y_k}{\sum_{k=1}^{K} Y_k} \tag{5.44}$$

The spectrum amplitude equals to the absolute value of the Fourier transform of signal $y(t)$, *e.g.*, [93]:

$$Y_k = \left| \sum_{n=1}^{N} y(t_n) \, e^{j2\pi\nu_k t_n} \right| = \sqrt{Y_{re}^2 + Y_{im}^2} \tag{5.45}$$

where the real and imaginary parts of the spectrum amplitude are obtained by:

$$Y_{re} = \sum_{n=1}^{N} y(t_n) \cos(2\pi\nu_k t_n) \tag{5.46}$$

and

$$Y_{im} = \sum_{n=1}^{N} y(t_n) \sin(2\pi\nu_k t_n) \tag{5.47}$$

It follows that uncertainty on centroid frequency due to the noise $\Delta\nu_{ca}^n$ can be computed from equations (5.44) to (5.47) through error propagation formula:

$$\Delta\nu_{ca}^n = \sqrt{\sum_{k=1}^{K} \left[\frac{\partial\nu_{ca}}{\partial Y_k} \Delta Y_k \right]^2} = \sqrt{\sum_{k=1}^{K} \left[\frac{\partial\nu_{ca}}{\partial Y_k} \frac{\partial Y_k}{\partial n} \right]^2} u_n \tag{5.48}$$

where $\Delta Y_k = \frac{\partial Y_k(\nu)}{\partial n} u_n$ (u_n is standard deviation of noise content). The partial derivative of centroid frequency respect to the amplitude spectrum is derived from equation (5.44):

$$\frac{\partial\nu_{ca}}{\partial Y_k} = \frac{\nu_k \sum_{k=1}^{K} Y_k \; - \; \sum_{k=1}^{K} \nu_k \, Y_k}{\left[\sum_{k=1}^{K} \; Y_k \right]^2} = \frac{\nu_k \; - \; \nu_{ca}}{\sum_{k=1}^{K} Y_k} \tag{5.49}$$

and partial derivative respect to noise is obtained from equation (5.45):

$$\frac{\partial Y_k}{\partial n} = \frac{Y_{re} \; \sum_{n=1}^{N} \cos(2\pi\nu_k t_n) \; + Y_{im} \sum_{n=1}^{N} \sin(2\pi\nu_k t_n)}{Y_k} \tag{5.50}$$

Note that the interaction between the GPR signals and a subsurface interface is actually very complicated, due to several factors (e.g., the interface roughness, lack of a sharp boundary, lateral returns). All these unknown variables introduce additional uncertainties into the data, which could become noticeable when the level of noise is very low. In such condition neglecting these contributions might produce an underestimation on the centroid or maximum frequencies uncertainties. A possible approach to mitigate this problem is to introduce an additional uncertainty computed from the signal bandwidth (BW). Thus, the uncertainty expressed in equation (5.41) is modified as:

$$u_{dm} = \sqrt{u_d^2 + u_{BW}^2} \tag{5.51}$$

where u_{BW} is proportional to the bandwidth.

5.2.4 GPRMax Software for Electromagnetic Simulation

gprMax Key Features

Modeling the GPR responses has a prominent role in understanding the Ground Penetrating Radar and provides the means for testing new data processing techniques and interpretation software. gprMax is an open source software that simulates electromagnetic wave propagation [38], [37], [149]. It solves Maxwell's equations in 3D using the Finite-Difference Time-Domain (FDTD) method. gprMax was originally designed for modeling Ground Penetrating Radar but can also be used to model electromagnetic wave propagation for many other applications.

The FDTD model represents a discretized version of the real problem in a limited size. The main reasons for the use of the FDTD method are: its ease of implementation in a computer programme, and its fine scalability when compared with other popular electromagnetic modeling methods such as the finite-element and integral techniques. However, the main drawbacks of the FDTD technique are: the need to discretize the volume of the problem space which could lead to excessive computer memory requirements and the staircase representation of curved interfaces.

gprMax has the ability to represent dispersive materials using a single-pole Debye model. Many materials can be adequately represented using this approach for the typical frequency ranges associated with GPR. However, multi-pole Debye is often used to simulate the electric susceptibility of materials such as water and soils. Electric susceptibility that relates the polarization density to the electric field includes both the real and imaginary parts of the complex electric permittivity variation. gprMax can be used to create soils with more realistic dielectric and geometrical properties based on a semi-empirical model, that was initially suggested by [24], [44] and is used to describe the dielectric properties of the soil. The model relates relative permittivity of the soil to bulk density, sand particle density, sand fraction, clay fraction and water volumetric fraction. This approach can model a more realistic soil with a stochastic distribution of these parameters. The real and imaginary parts of this semi-empirical model can be approximated using a multi-pole Debye function plus a conductive term. gprMax also includes predefined models of antennas that behave similarly to the commercial antennas.

One of the main challenging issues in modeling GPR is the truncation of the computational domain at a finite distance from the sources and targets where the values of the electromagnetic field cannot be calculated directly by the numerical method. Therefore, approximate conditions known as Absorbing Boundary Condition (ABC) are applied at a sufficient distance from the source to truncate, and therefore, to limit the computational space. The role of ABC is to absorb any waves impinging on boundaries, hence simulating an unbounded space. The computational space (*i.e.*, model space) that is limited by the ABC should contain all important features of the problems geometry such as all sources and output points and important targets. Figure (5.1) displays GPR forward problem showing computational domain bounded by an absorbing boundary condition (ABC). The gprMax uses efficient and well-performing Perfectly Matched Layer (PML) absorbing boundary conditions. A PML that is based on a recursive integration approach to the complex frequency shifted is adopted in gprMax with the ability to customize the parameters of PML optimizing its performance. In summary, some key features of gprMax are: an easy to use-command interface, the ability to model dispersive materials, the modeling of complex shaped targets, and the simulation of unbounded space using powerful absorbing boundary conditions.

Numerical Solutions Using FDTD Approach

All electromagnetic phenomena on a macroscopic scale are described by the well-known Maxwell's equations that are first order partial differential equations, expressing the relations between the fundamental electromagnetic field quantities and their dependence on their sources. In Maxwell's equations, the field vectors are assumed to be single-valued, bounded, continuous functions of position and time. In order to simulate the GPR response from a particular target or set of targets, the Maxwell's equations have to be solved subject to the geometry of the problem and the initial conditions. The GPR forward problems are classified as an initial value-open boundary problem. Therefore in order to obtain a solution, an initial condition (*i.e.*, excitation of the GPR transmitting antenna) has to be defined to allow for the resulting fields to propagate through space reaching a zero value at infinity since there is no specific boundary which limits the geometry of the problem. Although the first part (*i.e.*, specification of the source) is easy to accommodate, the second part cannot be easily tackled using a finite computational space.

The FDTD approach to the numerical solution of Maxwell's equations discretizes both the space and time domains. Thus the spatial, Δx, Δy and Δz, and temporal, Δt, discretization steps play a very significant role in modeling. The smaller the steps are the closer the FDTD model is to a real representation of the problem. The building block of the discretized FDTD grid is called Yee cell named after Kane Yee who pioneered the FDTD method. Figure (5.2) presents an 3D illustration of Yee cell. By assigning appropriate constitutive parameters to the locations of the electromagnetic field components, complex shaped targets can be included easily in the models. However, objects with curved boundaries will be represented using a staircase approximation.

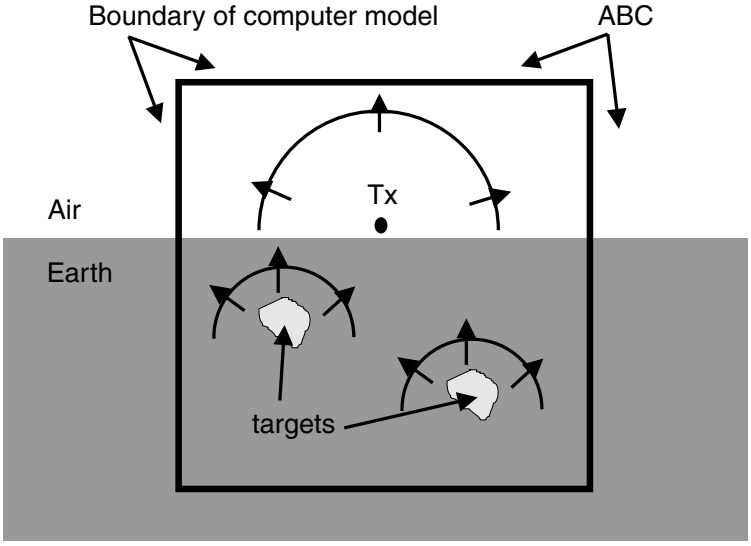

Figure 5.1: A view of the model space bounded by Absorbing Boundary Condition.

gprMax is fundamentally based on solving Maxwell's equations in 3D using the FDTD method, transverse electromagnetic (TEM) mode. However, it can also be used to carry out simulations in 2D using the transverse magnetic (TM) mode. A 2D simulation is achieved by specifying a computational domain that has only a single cell dimension in one direction (that direction is considered the infinite direction). In this case the electric and magnetic field components on the two faces of the single cell slice in the invariant direction are set to zero. In 3D simulation the Maxwell's equations in linear, isotropic nondispersive materials are written as six coupled partial differential equations (*e.g.*, [30]):

$$\begin{aligned}
\frac{\partial E_x}{\partial t} &= \frac{1}{\varepsilon}\left(\frac{\partial H_z}{\partial y} - \frac{\partial H_y}{\partial z} - J_{Sx} - \sigma_s E_x\right) \\
\frac{\partial E_y}{\partial t} &= \frac{1}{\varepsilon}\left(\frac{\partial H_x}{\partial z} - \frac{\partial H_z}{\partial x} - J_{Sy} - \sigma_s E_y\right) \\
\frac{\partial E_z}{\partial t} &= \frac{1}{\varepsilon}\left(\frac{\partial H_y}{\partial x} - \frac{\partial H_x}{\partial y} - J_{Sz} - \sigma_s E_z\right)
\end{aligned} \tag{5.52}$$

and

$$\begin{aligned}
\frac{\partial H_x}{\partial t} &= \frac{1}{\mu}\left(\frac{\partial E_y}{\partial z} - \frac{\partial E_z}{\partial y} - M_{Sx} - \sigma_m H_x\right) \\
\frac{\partial H_y}{\partial t} &= \frac{1}{\mu}\left(\frac{\partial E_z}{\partial x} - \frac{\partial E_x}{\partial z} - M_{Sy} - \sigma_m H_y\right) \\
\frac{\partial H_z}{\partial t} &= \frac{1}{\mu}\left(\frac{\partial E_x}{\partial y} - \frac{\partial E_y}{\partial x} - M_{Sz} - \sigma_m H_z\right)
\end{aligned} \tag{5.53}$$

and in 2D the equations reduce to the corresponding 2D form as:

$$\frac{\partial E_z}{\partial t} = \frac{1}{\varepsilon}\left(\frac{\partial H_y}{\partial x} - \frac{\partial H_x}{\partial y} - J_{Sz} - \sigma_s E_z\right) \tag{5.54}$$

and

$$\begin{aligned}\frac{\partial H_x}{\partial t} &= \frac{1}{\mu}\left(-\frac{\partial E_z}{\partial y} - M_{Sx} - \sigma_m H_x\right)\\ \frac{\partial H_y}{\partial t} &= \frac{1}{\mu}\left(\frac{\partial E_z}{\partial x} - M_{Sy} - \sigma_m H_y\right)\end{aligned} \tag{5.55}$$

where σ_s is static electric conductivity, σ_m is magnetic conductivity (equivalent magnetic loss) in Ω/m, J_S and M_S are independent source of electric and magnetic fields.

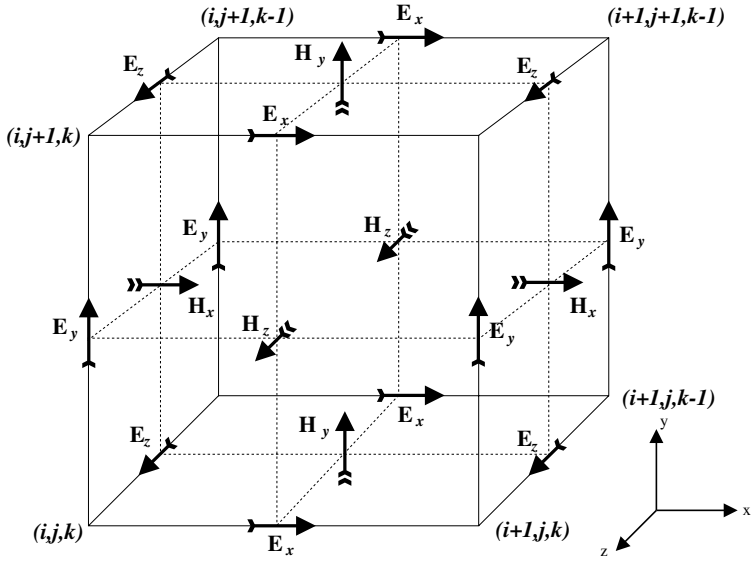

Figure 5.2: Single FDTD Yee cell.

These equations are discretized in both space and time domain and are applied in each FDTD cell. The numerical solution is obtained directly in the time domain in an iterative fashion. In each iteration the electromagnetic fields propagate in the FDTD grid and each iteration corresponds to an elapsed simulated time of one Δt. Hence by specifying the number of iterations we can instruct the FDTD solver to simulate the fields for a given time window. Note that, to obtain a solution directly in the time domain using the FDTD method the values of Δx, Δy and Δz can not be assigned independently. FDTD is a conditionally stable numerical process. The stability condition is known as the CFL condition and is given by:

$$\Delta t \leq \frac{1}{c\sqrt{\frac{1}{\Delta x^2} + \frac{1}{\Delta y^2} + \frac{1}{\Delta z^2}}} \tag{5.56}$$

where c is the speed of light. The equation states that Δt is bounded by the values of Δx, Δy and Δz. In 2D case the stability condition is obtained by letting $\Delta z \to \infty$.

There is no specific guideline for choosing the right spatial discretization for a given problem. In general, it depends on the required accuracy, the frequency content of the source pulse and the size of the targets. Obviously, all targets present in a model must be adequately resolved. The other important factor which influences the spatial discretization is the errors associated with numerically induced dispersion. This means that contrary to the real world where electromagnetic waves propagate with the same velocity regardless of their direction and frequency (assuming no dispersive media and far-field conditions) in the discrete media this is not the case. However, the error can be minimized according to the following

rule-of-thumb: the discretization step should be at least ten times smaller than the smallest wavelength of the propagating electromagnetic fields, $\Delta l \leq \lambda/10$. Note that in general low-loss media wavelengths are much smaller compared to free space.

5.2.5 Synthetic Model Analysis - Sloping Interface

To validate the proposed approach, a two-layer synthetic model with a sloping interface is used (Figure (5.3)). GPR data are simulated using gprMax. A 2D model is simulated by setting the third dimension equals to the spatial discretization. The simulations are carried out considering two scenarios having different electrical properties of the first layer, to model low-loss and high-loss cases. The complex permittivity of the first layer ε_1 is described by a Debye relaxation model:

$$\varepsilon_1 = \varepsilon_\infty - j\frac{\sigma_1}{\omega} + \sum_{p=1}^{N} \frac{\Delta\varepsilon_p}{1 + j\omega\tau_p} \tag{5.57}$$

where ε_∞ is the real part of complex permittivity at infinity (very large) frequencies, σ_1 is the conductivity, N the number of Debye poles, τ_p is the relaxation time of p^{th} pole, and $\Delta\varepsilon_p = \varepsilon_s - \varepsilon_\infty$, and ε_s is the real part of the complex permittivity at zero (very low) frequencies. Note that, $\Delta\varepsilon_p$ is always positive and $\varepsilon_\infty > \varepsilon_0$. The second layer is described as a conductive material with

$$\varepsilon_2 = \varepsilon_2' - j\sigma_2/\omega \tag{5.58}$$

The parameters of two layers are reported in Table (5.1), and the electrical properties of the first layer as a function of frequency are shown in Figure (5.4). The receiving antennas are modeled by two Hertzian dipoles with electric field polarization perpendicular to the plane containing the discontinuity, which corresponds to the TE mode. A Ricker wavelet is considered as transmitted signal. The simulated GPR cross section at 1 GHz obtained with gprMax is shown in Figure (5.3) where the discretization cell-size is 0.003 m, and the simulation time is set to 20 ns. These datasets are contaminated by a white Gaussian noise that produces a signal to noise ratio (SNR) of about 35 dB on the signal reflected at the start of the slope (first trace in the cross section).

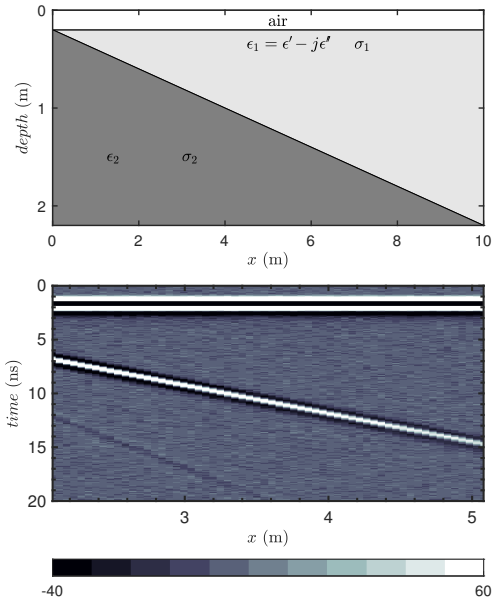

Figure 5.3: Synthetic model and related radargram: (upper panel) two layers having different electric properties separated by a slopping interface. (Lower panel) radar cross section generated using gprMax starting from the model considering a discretization of 3 mm in all dimensions. The data in cross section are contaminated with a white Gaussian noise which produces a SNR of 35 dB at the reflected signal at the start of slope.

The proposed inversion procedure is implemented as follows: The reflected signal by the interface on each trace is selected with a Hann time window, six times larger than the inverse of operating frequency

($W_H > 6/\nu_0$), and the related spectrum amplitude is computed by using FFT algorithm. Maximum and centroid frequencies, with the associated uncertainties and *SNR* are estimated for each GPR trace. Figure (5.5) presents the extracted maximum and centroid frequency vs. two-way travel time, and variation of *SNR* with time.

Table 5.1: Electric parameters of the mediums that are used in gprMax simulations

Medium	ε_∞	ε_2	σ_1, σ_2 S/m	$< tan\delta_a >$ $(0.5 - 1.5$ GHz)	N	$\Delta\varepsilon_p$	$\tau_p(ns)$
Low loss	4	6	3.5×10^{-5}, 0.5	1.84×10^{-2}	3	0.1	2.1, 0.25, 0.0395
High loss	3	6	2.0×10^{-4}, 0.5	1.04×10^{-1}	3	0.5	2.1, 0.25, 0.0395

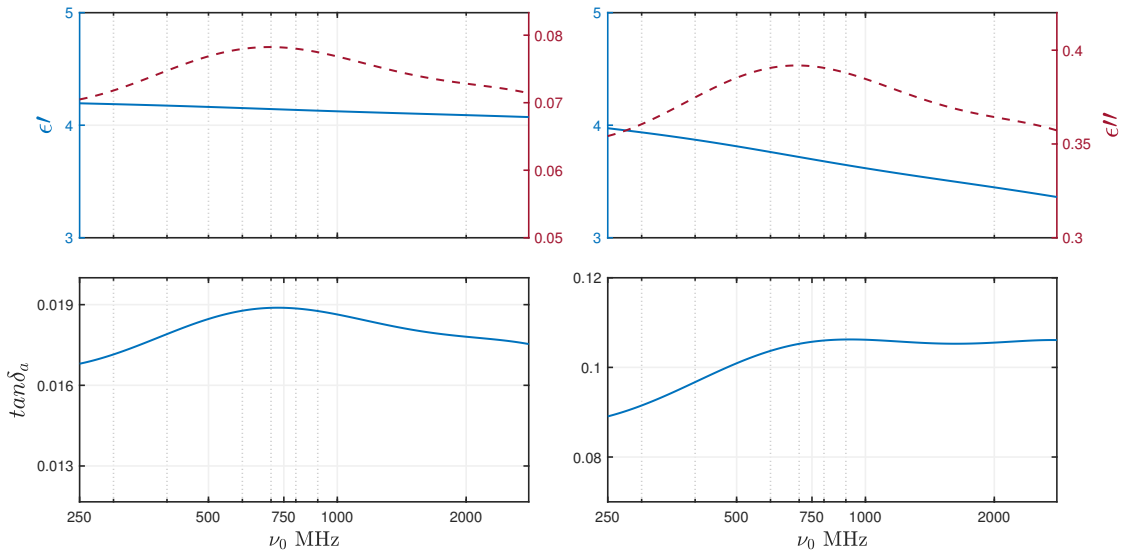

Figure 5.4: Complex relative permittivity and apparent loss tangent of the first layer as a function of frequency. (Upper panel) real (solid lines) and imaginary (dashed lines) parts of relative permittivity for the low loss and the high loss scenarios, respectively. (Lower panel) apparent loss tangent computed for the low loss and the high loss scenarios.

The posterior probability density functions distribution and the marginal pdfs obtained by maximum and centroid frequency approaches are shown in Figure (5.6). In the inversion procedure $\nu_{UB} = 2\ GHz$ is imposed. These distribution and pdfs are peaked around the true values. More precisely, the results of the inversion are given by the average $< \mathbf{m} >$, (equation (3.43)) with the related standard deviations estimated from the marginal pdfs (equation (3.45)). This procedure is applied to two different models with the properties in Table (5.1), considering different level of noise (*SNR*) and various frequency upper boundaries. Figure (5.7) illustrates the inversion results of the centroid frequency-shift method for low loss (upper panel) and high loss (lower panel) scenarios. The estimated parameters, $tan\delta_a$ and ν_0 values, are plotted for different ν_{UB} , as a function of the *SNR*. In both scenarios, the upper boundary frequency has a significant effect only when the *SNR* is low, as shown by the divergence of the different curves below 45 dB (Figure (5.7)). The comparison between centroid and maximum frequency methods is also reported for low loss (Figure (5.8) upper panel) and high (Figure (5.8) lower panel) loss scenarios, where the estimated $tan\delta_a$ values are compared with the apparent loss tangent of the first layer, averaged in the range $0.5 - 1.5$ GHz (Table (5.1)). In both scenarios, the centroid method better estimates $tan\delta_a$, regardless the *SNR* value. In the low-loss scenario the maximum frequency approach seems to slightly overestimate or underestimate $tan\delta_a$ whereas in the high-loss scenario the underestimation appears almost systematic (biased). As expected, in both methods, the uncertainties are larger for low *SNR* values, however the centroid frequency method is more precise (smaller uncertainties) at low *SNR* (below 50 dB) and the maximum frequency method at higher *SNR*.

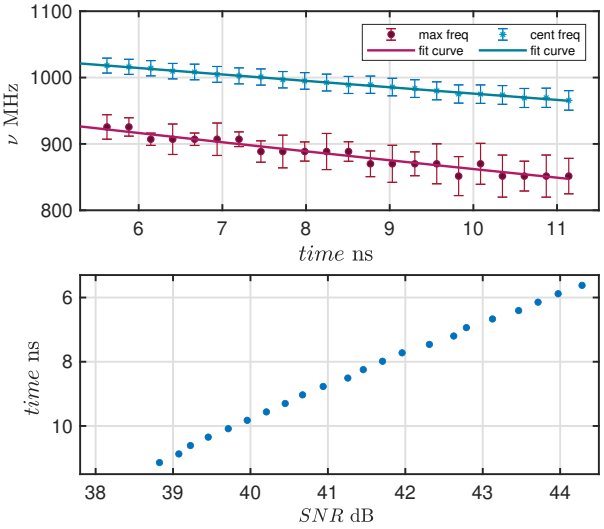

Figure 5.5: Maximum and centroid frequency vs. time delay of the received signal and variation of SNR. (upper panel) Maximum and centroid frequency retrieved from the radargram in Figure (5.3), and best-fit curves calculated with equations (5.18) and (5.34), using $\nu_{UB} = 2\ GHz$. (lower panel) estimated SNR values vs. time.

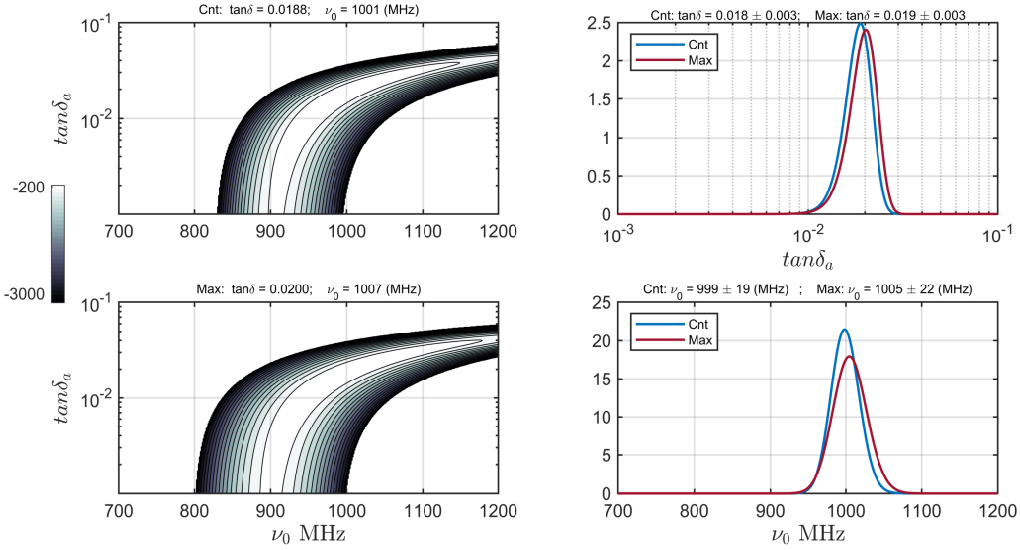

Figure 5.6: Posterior probability density functions and marginal pdfs: (left) bivariate distribution for the centroid and maximum frequency. (right) marginal pdfs for loss tangent and operating frequency retrieved by the two methods.

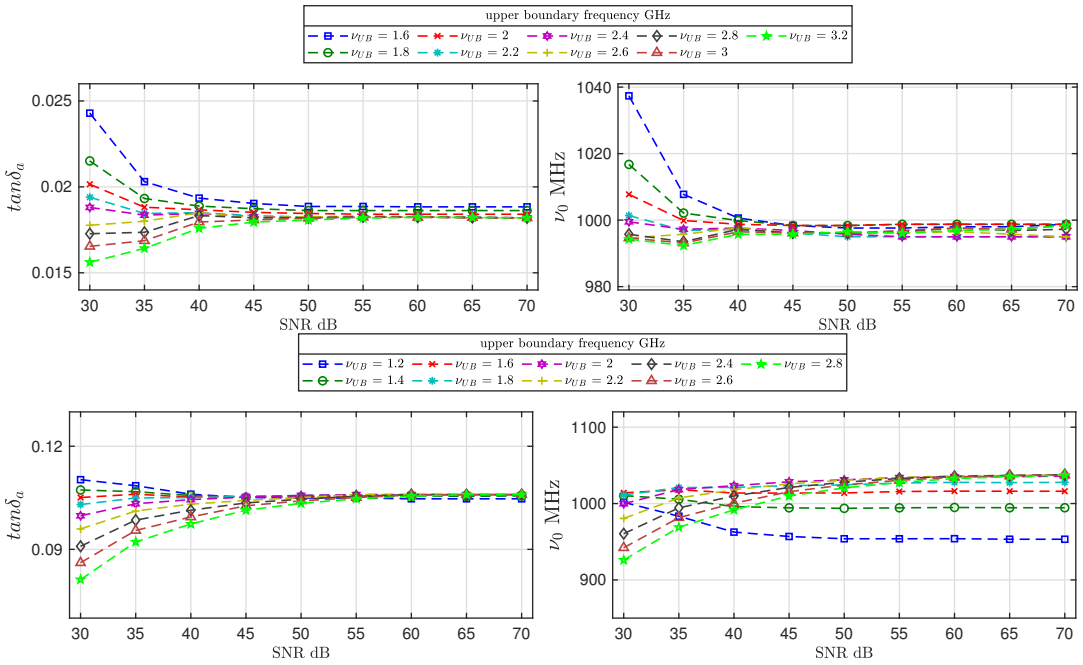

Figure 5.7: Estimated loss tangent and nominal operating frequency for various ν_{UB} vs. *SNR*. (upper) low-loss model. (lower) high-loss model.

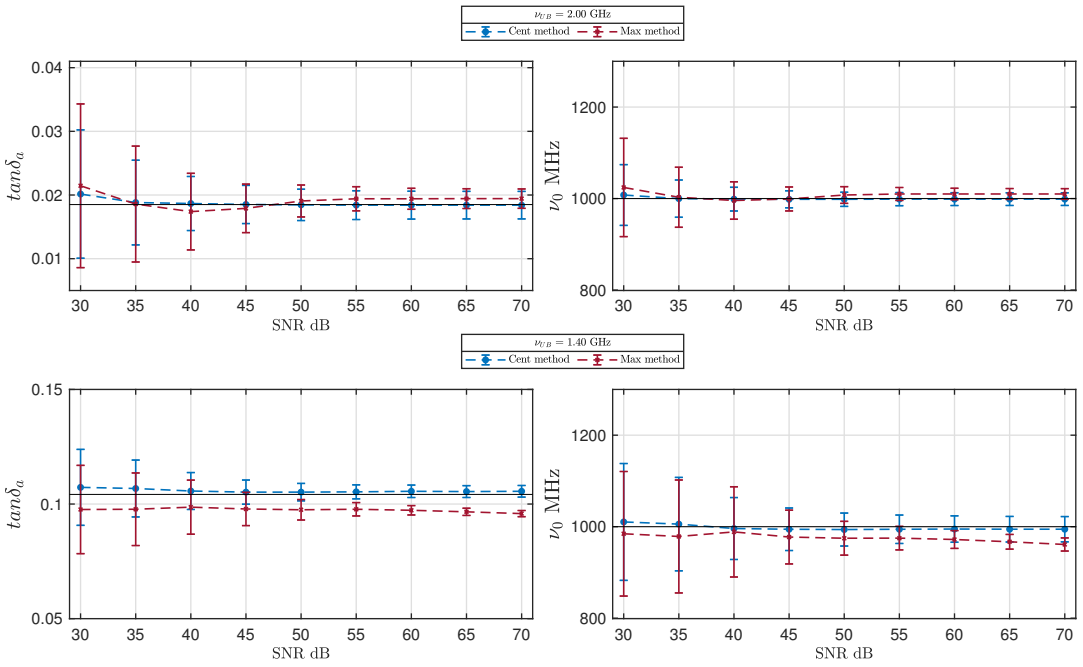

Figure 5.8: Comparison of the estimated loss tangent and operating nominal frequency for the two approaches vs. *SNR*: (upper) low-loss model; (lower) high-loss model; Bold-black lines indicate nominal frequency ($\nu_0 = 1GHz$) and mean loss tangent value of the first layer.

5.2.6 Analysis of GPR Data Collected on Mount Etna, Italy

GPR data collected on volcanic deposits [Mount Etna, Italy, Figure (5.9)] using 500 MHz and 1 GHz antennas in transverse electric TE and transverse magnetic TM configurations, were used to test the centroid method on real datasets. The data were acquired in reflection mode (single offset) using a PulseEKKO Pro™ bistatic system (Sensors & Software, Inc.) and the following acquisition parameters: step size 0.02 m, time resolution 0.1 ns at 500 MHz and 0.05 ns at 1 GHz, 100 ns time window and

stacking of 4. The GPR profiles were collected on the top of a natural scarp parallel to the edge, far from its front to avoid lateral reflections. The TE radar cross sections are shown in Figure ((5.10), left), and the two-way travel time vs. SNR of relevant back-scattered echoes from the interface is presented in Figure ((5.10), right). The radar cross sections show the presence of a clear continuous sloping interface that separates two distinct volcanic ash deposits. The analysis was performed only on data showing a linear trend of time vs. SNR [red dots in Figure (5.10)].

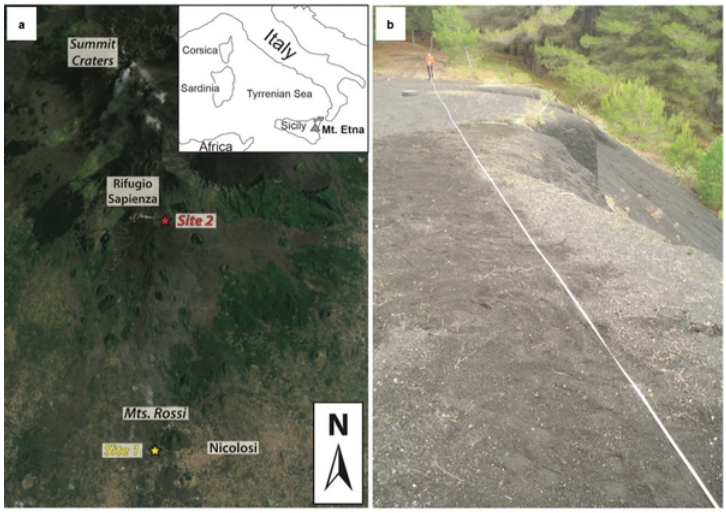

Figure 5.9: Survey area location. Satellite image of the area that locates the site 1, and Site 1 picture, which contains vesiculated lapilli, at the base of the southwestern flank of Mount Rossi, the pyroclastic cones formed during the 1669 A.D. eruption of Mount Etna.

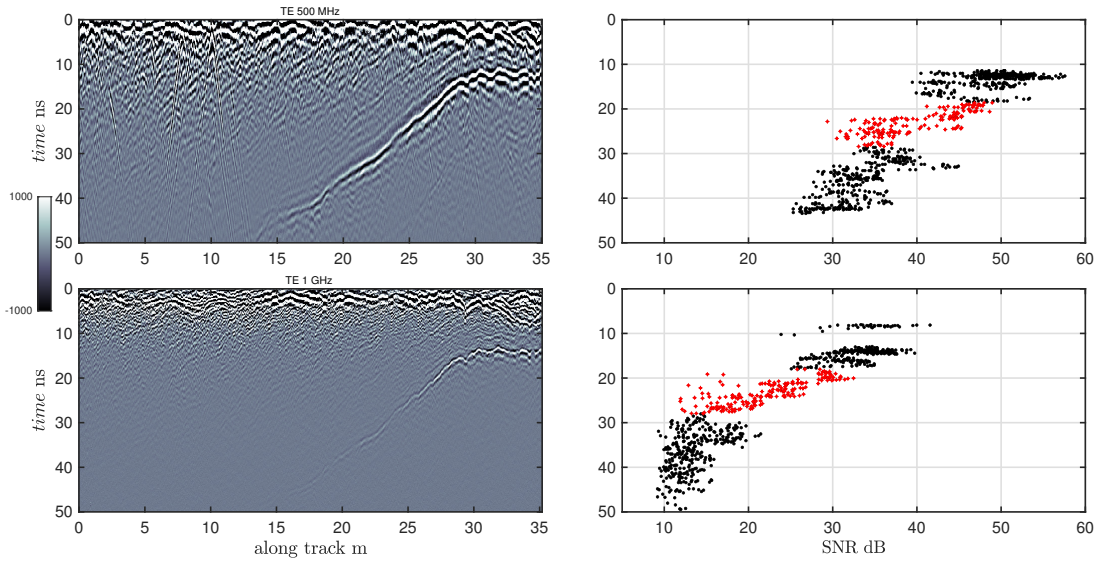

Figure 5.10: Radar data acquired on Mount Etna: (left) TE 500 MHz and TE 1 GHz radar cross sections after Dewow filtering and background removal. (right) time vs. SNR is computed from signal echoes intensity where the noise level is considered as standard deviation of the GPR signal at the end of the trace. Red dots in right panels indicate the analyzed time interval.

Loss tangent and operating frequency are estimated by applying two different inversion procedures: (1) using equation (3.40), as in the synthetic data analysis; (2) applying equation (3.42) which imposes a priori Gaussian probability density function for the operating frequency. In the latter case, we assumed a pdf centered at 500 MHz and 1 GHz having a width of 50 MHz and 100 MHz, respectively. Figure (5.11) shows the inversion results for TE and TM data as a function of different ν_{UB} values. The results for the 500 MHz data are not affected by the choice of ν_{UB} as at this frequency the SNR is high thus, the estimated loss tangent value is substantially constant in the entire ν_{UB} range. Conversely, being

the 1 GHz antenna characterized by a lower *SNR*, the data are strongly affected by the ν_{UB} value. However, the use of some a priori information strongly improves the stability of the results, providing an apparent loss tangent value that is almost constant between 1300 and 1600 MHz for both TE and TM modes. Note that in this interval also the operating frequency is constant and in good agreement with the nominal operating frequency. Table (5.2) summarizes the results of the inversion performed with a priori assumptions; the loss tangent is computed as the average of the values in the range $900 - 1200$ for the 500 MHz antenna and $1300 - 1600$ for the 1 GHz antenna, where such quantity is almost constant. Interestingly, the loss tangent values reported in Table (5.2) are also compatible with those retrieved for the same dataset in [63] [see Table (5.3)] applying different methodologies.

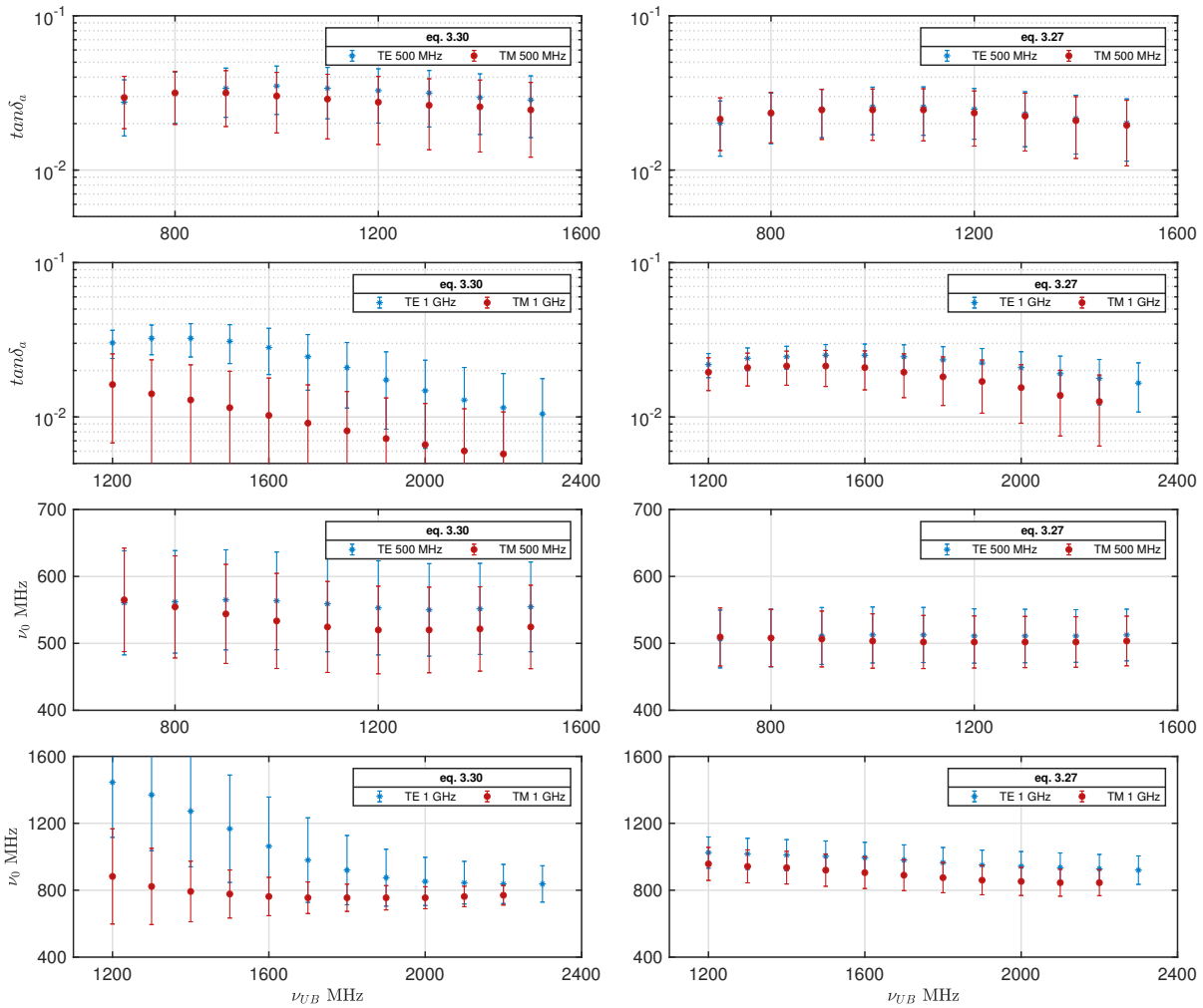

Figure 5.11: Comparison between model parameters estimated from TE (blue) and TM (red) data; loss tangent and operating frequency are plotted vs. upper boundary frequency. (left) no a priori information is applied, (right) a priori information is imposed.

Table 5.2: Inversion results of the GPR data collected on the ash deposit.

Configuration	ν_{up} *MHz*	ν_0 *MHz*	$tan\delta_a$
TM 500 MHz	900-1200	502±38	0.022±0.009
TE 500 MHz	900-1200	511±40	0.023±0.009
TM 1 GHz	1300-1600	905±95	0.021±0.006
TE 1 GHz	1300-1600	980±90	0.025±0.005

Table 5.3: The estimated loss tangent and nominal frequency on the ash deposit by [63].

Configuration	$v_0\ MHz$	$tan\delta_a$
TM 500 MHz	440±10	0.030±0.005
TE 500 MHz	450±10	0.034±0.007
TM 1 GHz	840±30	0.025±0.003
TE 1 GHz	870±20	0.028±0.004

5.2.7 Discussion

The estimation of attenuation and loss tangent from GPR data has important implications in terrestrial and planetary investigations, and in combination with the information coming from the velocity it can help to discriminate different probed materials. The proposed procedure introduces a new forward formula relating the downshift of centroid frequency to the loss tangent of the investigated material, assuming a Ricker wavelet as transmitted signal. The model parameter, loss tangent and operating frequency, are retrieved using a probabilistic inversion approach.

The test performed with the synthetic data has shown that, in the case of low-loss materials, this method produces comparable results to those computed with the maximum frequency approach. The centroid-frequency method appears to be more accurate in a high-loss environment, and it is, in general, more precise (smaller uncertainties) when the noise level is higher. An important aspect that was presented is the role of upper boundary frequency in the computation of the centroid frequency. In fact, when the material is lossy and filters out the high-frequency component of the spectrum, the noise at high frequency might become dominant, affecting the correct estimation of the centroid frequency. The proposed method being based on estimation of the signal average frequency content, also could be applied in more complex scenarios in which the material is inhomogeneous and/or where defined and continuous reflectors are absent. This approach can be useful on earth, where a high-loss environment prevents a deep signal penetration, and the detection of clear reflectors could be difficult. Given the increasing interest in applying GPR to subsurface planetary exploration, this method also could be particularly suitable for the dry and cold environments typical of the moon and Mars. In fact, in these planetary bodies, the shallow subsurface is dominated by fine materials (regolith) mixed with rocky inclusions. In this scenario, the stratifications are difficult to detect due to the lack of liquid water or wet sediments that usually enhance the reflections at the interfaces between materials.

5.3 Part II

5.3.1 Problem Outline

Ground Penetrating Radar (GPR) is a well-established geophysical technique capable of probing the subsurface at shallow depth, using a short burst of electromagnetic energy. This technique has been successfully applied in Solar System exploration [2] to investigate the internal structure of planets, moons, and other Small Solar System bodies [109], [104], [124], [92], [111]. The main difference between terrestrial and planetary GPR exploration is the temperature and moisture conditions of the subsurface. Planets and other extraterrestrial bodies are usually very cold (the only exception is Venus) and very dry; these conditions favor the signal penetration but, at the same time, drastically reduce (especially the lack of water) the dielectric contrasts between materials, making the detection of interfaces and single targets particularly difficult. Moreover, the shortage of direct information from in situ geological studies does not allow to impose strong constraints on the geophysical interpretation. Thus, the estimation of the electromagnetic parameters from the radar data represents fundamental information trying to understand the geological nature of the subsurface.

Any radar signal propagating in a material is subjected to attenuation due to intrinsic losses and scattering losses [43], [46]. The former is due to the electrical and magnetic properties of the medium, and the latter to the presence of inhomogeneities. The evaluation of these two contributions can provide

information on the chemical and mineralogical composition, *i.e.*, titanium and iron content [120], [72] and on the inhomogeneities present in the material [103].

Estimation of the intrinsic and scattering losses can be achieved using different methods [46], [43], [142]. The overall attenuation is usually computed from the signal amplitude decay. The intrinsic losses can be determined by the spectral ratio method which, however, is affected by the shape of the reference wavelet spectrum. A second approach is given by the frequency shift method which offers certain advantages with respect to the spectral ratio method, being less affected by geometric spreading, receiver coupling variations, transmission/reflection losses, and radiation/reception pattern effects. Once the intrinsic losses have been computed, the scattering contribution can be calculated by subtracting such quantity from the overall attenuation.

In this part, a new variant of the proposed method in the previous section is introduced, and a new forward formula is developed. Then a synthetic dataset, simulated by gprMax considering a fractal model, is examined. To increase the validity of solutions, two methods are simultaneously implemented to estimate the absorbing loss tangent of the medium with the stochastically distributed properties. The scattering contribution is deduced from the total loss inferred from the best fit to the amplitude decay of received pulses. In addition, theses newly developed methods are compared with maximum frequency shift analysis. Finally, the absorbing and scattering loss of the subsurface of Volcano Mount Etna, Italy are evaluated from the collected GPR data.

5.3.2 Loss Tangent Estimation: Power Spectrum Analysis

The inverse of the quality factor Q^{-1} is composed of scattering losses, Q_s^{-1}, and intrinsic losses Q_i^{-1}, and describes the total attenuation of the signal:

$$Q^{-1} = Q_s^{-1} + Q_i^{-1} \tag{5.59}$$

where Q_i^{-1} is equal to the loss tangent, $tan\delta$, as defined in equation (4.4). The centroid frequency is a statistical quantity that represents an average frequency of the spectrum of the pulse and can be evaluated at different time depth τ computing the received amplitude spectrum $Y(\nu,\tau)$ using the Short-Time Fourier Transform ($STFT$). In the previous part, the centroid frequency was computed from amplitude spectrum and to reduce the effect of noise content an upper boundary frequency ν_{UB} was introduced [see equations (5.14) and (5.19)]. The centroid frequency can also be computed using power spectrum $Y^2(\nu,\tau)$ [147]. Therefore, considering an upper boundary frequency, the centroid frequency is computed as:

$$\nu_{cp}(\nu_0, tan\delta, \tau) = \frac{\int_0^{\nu_{UB}} \nu Y^2(\nu,\tau) d\nu}{\int_0^{\nu_{UB}} Y^2(\nu,\tau) d\nu} = \frac{\int_0^{\nu_{UB}} \nu X^2(\nu)\ e^{-2\pi\nu \tan\delta\tau}\ d\nu}{\int_0^{\nu_{UB}} X^2(\nu)\ e^{-2\pi\nu \tan\delta\tau}\ d\nu} \tag{5.60}$$

that for a source pulse of the Ricker function shape becomes:

$$\nu_{cp}(\nu_0, tan\delta, \tau) = \frac{\int_0^{\nu_{UB}} \nu \left(\frac{\nu}{\nu_0}\right)^4 e^{-2\left(\frac{\nu}{\nu_0}\right)^2}\ e^{-2\pi\nu \tan\delta\tau}\ d\nu}{\int_0^{\nu_{UB}} \left(\frac{\nu}{\nu_0}\right)^4 e^{-2\left(\frac{\nu}{\nu_0}\right)^2}\ e^{-2\pi\nu \tan\delta\tau}\ d\nu} \tag{5.61}$$

solving the integrals in 5.61 yields the analytic formula of the centroid frequency as a function of τ, v_0, and $tan\delta$:

$$\nu_{cp}(\nu_0, tan\delta, \tau) = \frac{\nu_0}{\sqrt{2}} \frac{I_5(\chi) - 5\chi I_4(\chi) + 10\chi^2 I_3(\chi) - 10\chi^3 I_2(\chi) + 5\chi^4 I_1(\chi) - \chi^5 I_0(\chi)}{I_4(\chi) - 4\chi I_3(\chi) + 6\chi^2 I_2(\chi) - 4\chi^3 I_1(\chi) + \chi^4 I_0(\chi)} \tag{5.62}$$

where $\chi = \sqrt{2}x = \frac{\sqrt{2}}{2}\pi\nu_0\ tan\delta\tau$. The details of equation (5.62) derivation is as follows: Recalling the equation (5.61):

$$\nu_{cp}(\nu_0, tan\delta, \tau) = \frac{D_1}{D_2} \tag{5.63}$$

where

$$\begin{aligned} D_1 &= \int_0^{\nu_{UB}} \nu \left(\frac{\nu}{\nu_0}\right)^4 e^{-2\left(\frac{\nu}{\nu_0}\right)^2}\ e^{-2\pi\nu \tan\delta\tau}\ d\nu = \int_0^{\nu_{UB}} \nu \left(\frac{\nu}{\nu_0}\right)^4 e^{-2\left[\left(\frac{\nu}{\nu_0}\right)^2 + 2x\left(\frac{\nu}{\nu_0}\right)\right]}\ d\nu \\ &= e^{2x^2} \int_0^{\nu_{UB}} \nu \left(\frac{\nu}{\nu_0}\right)^4 e^{-2\left[\left(\frac{\nu}{\nu_0}\right)^2 + 2x\left(\frac{\nu}{\nu_0}\right)\right]}\ d\nu = \nu_0^2 e^{2x^2} \int_0^{\nu_{UB}} \left(\frac{\nu}{\nu_0}\right)^5 e^{-2\left(\frac{\nu+x\nu_0}{\nu_0}\right)^2}\ \frac{d\nu}{\nu_0} \end{aligned} \tag{5.64}$$

by defining the new variable $p = \sqrt{2}\left(\frac{\nu}{\nu_0} + x\right)$, D_1 is written as:

$$D_1 = \frac{1}{\sqrt{2^6}}\nu_0^2 e^{\chi^2}\int_{\chi}^{\chi+\frac{\nu_{UB}}{\nu_0}} (p-\chi)^5 e^{-p^2} dp \tag{5.65}$$

giving rise to:

$$D_1 = \frac{1}{\sqrt{2^6}}\nu_0^2 e^{\chi^2}\left[I_5(\chi) - 5\chi I_4(\chi) + 10\chi^2 I_3(\chi) - 10\chi^3 I_2(\chi) + 5\chi^4 I_1(\chi) - \chi^5 I_0(\chi)\right] \tag{5.66}$$

proceeding a similar procedure for D_2 gives:

$$D_2 = \frac{1}{\sqrt{2^5}}\nu_0 e^{\chi^2}\left[I_4(\chi) - 4\chi I_3(\chi) + 6\chi^2 I_2(\chi) - 4\chi^3 I_1(\chi) + \chi^4 I_0(\chi)\right] \tag{5.67}$$

where $I_n(\chi)$ for $n = 1, 2, 3, 4, 5$ is expressed as:

$$\begin{aligned}
I_0(\chi) &= \frac{\sqrt{\pi}}{2}\left[erfc(\chi) - erfc(\chi_{max})\right] \\
I_1(\chi) &= \frac{1}{2}\left(e^{-\chi^2} - e^{-\chi_{max}^2}\right) \\
I_2(\chi) &= \frac{\sqrt{\pi}}{4}\left[erfc(\chi) - erfc(\chi_{max})\right] + \frac{1}{2}\left(\chi e^{-\chi^2} - \chi_{max} e^{-\chi_{max}^2}\right) \\
I_3(\chi) &= \frac{1}{2}\left(e^{-\chi^2} - e^{-\chi_{max}^2}\right) + \frac{1}{2}\left(\chi^2 e^{-\chi^2} - \chi_{max}^2 e^{-\chi_{max}^2}\right) \\
I_4(\chi) &= \frac{1}{2}\left(\chi^3 e^{-\chi^2} - \chi_{max}^3 e^{-\chi_{max}^2}\right) + \frac{3}{2} I_2(\chi) \\
I_5(\chi) &= \frac{1}{2}\left(\chi^4 e^{-\chi^2} - \chi_{max}^4 e^{-\chi_{max}^2}\right) + 2 I_3(\chi)
\end{aligned} \tag{5.68}$$

where $\chi_{max} = \chi + \nu_{UB}/\nu_0$, and $erfc(\chi)$ presents complementary error function:

$$erfc(\chi) = 1 - erf(\chi) = 1 - \frac{2}{\sqrt{\pi}}\int_0^{\chi} e^{-\xi^2} d\xi \; = \frac{2}{\sqrt{\pi}}\int_{\chi}^{\infty} e^{-\xi^2} d\xi \tag{5.69}$$

The probabilistic inversion approach is employed to estimate the loss tangent from equation (5.62). The following presents derivation of the Jacobian matrices and uncertainty which are required in inversion process. Equation (5.62) is written as:

$$\nu_{cp}(\nu_0, tan\delta, \tau) = \frac{\nu_0}{\sqrt{2}} F(\chi) = \frac{\nu_0}{\sqrt{2}} \frac{N(\chi)}{D(\chi)} \tag{5.70}$$

where the partial derivatives are computed by:

$$\frac{\partial \nu_{cp}(\nu_0, tan\delta, \tau)}{\partial \nu_0} = \frac{1}{\sqrt{2}} F(\chi) + \frac{\nu_0}{\sqrt{2}} \frac{\partial F(\chi)}{\partial \chi} \frac{\partial \chi}{\partial \nu_0} = \frac{1}{\sqrt{2}} F(\chi) + \frac{\chi}{\sqrt{2}} \frac{\partial F(\chi)}{\partial \chi} \tag{5.71}$$

$$\frac{\partial \nu_{cp}(\nu_0, tan\delta, \tau)}{\partial \tan\delta} = \frac{\nu_0}{\sqrt{2}} \frac{\partial F(\chi)}{\partial \chi} \frac{\partial \chi}{\partial \tan\delta} = \frac{\nu_0}{\sqrt{2}} \frac{\chi}{\tan\delta} \frac{\partial F(\chi)}{\partial \chi} \tag{5.72}$$

the partial $\frac{\partial F(\chi)}{\partial \chi}$ derivative can be written as:

$$\frac{\partial F(\chi)}{\partial \chi} = \frac{N_1(\chi) - N_2(\chi)}{D(\chi)^2} \tag{5.73}$$

with

$$\begin{aligned}
N_1(\chi) = D(\chi) \times [&\frac{\partial I_5(\chi)}{\partial \chi} - 5\chi \frac{\partial I_4(\chi)}{\partial \chi} + 10\chi^2 \frac{\partial I_3(\chi)}{\partial \chi} - 10\chi^3 \frac{\partial I_2(\chi)}{\partial \chi} + 5\chi^4 \frac{\partial I_1(\chi)}{\partial \chi} - \chi^5 \frac{\partial I_0(\chi)}{\partial \chi} \\
&- 5I_4(\chi) + 20\chi I_3(\chi) - 30\chi^2 I_2(\chi) - 20\chi^3 I_1(\chi) - 5\chi^4 I_0(\chi)]
\end{aligned} \tag{5.74}$$

and

$$N_2(\chi) = N(\chi) \times \ [frac\partial I_4(\chi)\partial\chi - 4\chi\frac{\partial I_3(\chi)}{\partial\chi} + 6\chi^2\frac{\partial I_2(\chi)}{\partial\chi} - 4\chi^3\frac{\partial I_1(\chi)}{\partial\chi} + \chi^4\frac{\partial I_0(\chi)}{\partial\chi} \\ - 4I_3(\chi) + 12\chi\ I_2(\chi) - 12\chi^2 I_1(\chi) + 4\chi^3 I_0(\chi)] \tag{5.75}$$

where

$$D(\chi) = I_4(\chi) - 4\chi I_3(\chi) + 6\chi^2\ I_2(\chi) - 4\chi^3\ I_1(\chi) + \chi^4\ I_0(\chi) \tag{5.76}$$

$$N(\chi) = I_5(\chi) - 5\chi I_4(\chi) + 10\chi^2 I_3(\chi) - 10\ \chi^3 I_2(\chi) + 5\ \chi^4 I_1(\chi) - \chi^5 I_0(\chi) \tag{5.77}$$

the partial derivatives $\frac{\partial I_n(\chi)}{\partial\chi}$ is obtained from:

$$\frac{\partial I_n(\chi)}{\partial\chi} = -\chi^n e^{-\chi^2} + \chi^n_{max} e^{-\chi^2_{max}} \tag{5.78}$$

$$J_{cp_i} = \left[\frac{\partial\nu_{cp}(\tau_i)}{\partial\nu_0}, \frac{\partial\nu_{cp}(\tau_i)}{\partial\tan\delta_a}\right] \tag{5.79}$$

where $i = 1, 2, \ldots, N$, and N is number of data.

The estimation of uncertainty is performed in same procedure in the previous part. Assuming the errors are uncorrelated the uncertainty of the data (centroid frequency) can be examined by using propagation formula as:

$$u_d = \sqrt{(\Delta\nu_{cp})^2 + \left(\Delta\nu^n_{cp}\right)^2} \tag{5.80}$$

where $\Delta\nu_{cp}$ is the uncertainty associated to the numerical discretization of the spectrum, and $\Delta\nu^n_{cp}$ is the uncertainty on centroid frequency due to the noise. The numerical uncertainty is defined by [147]:

$$\Delta\nu_{cp} = \sqrt{\frac{\sum_{k=1}^{K}(\nu_k - \nu_{cp})^2\ Y_k^2}{\sum_{k=1}^{K} Y_k^2}} \tag{5.81}$$

where $Y_k = Y(\nu_k)$ presents the amplitude of the spectrum at frequency $\nu_k = \nu(k)$, and K is the index of maximum boundary-value of frequency $\nu(K) = \nu_{UB}$, and $\Delta\nu^n_{cp}$ is the uncertainty associated to the white-Gaussian noise:

$$\Delta\nu^n_{cp} = \frac{\partial\nu_{cp}}{\partial n} u_n \tag{5.82}$$

To theoretically estimate the uncertainty due to noise $\Delta\nu^n_{cp}$, we start from the centroid frequency that is numerically computed by:

$$\nu_{cp} = \frac{\sum_{k=1}^{K}\nu_k\ Y_k^2}{\sum_{k=1}^{K} Y_k^2} \tag{5.83}$$

The spectrum amplitude Y_k equals to the absolute value of the Fourier transform of signal $y(t)$:

$$Y_k = \left|\sum_{n=1}^{N} y(t_n)\, e^{j2\pi\nu_k t_n}\right| = \sqrt{Y_{re}^2 + Y_{im}^2} \tag{5.84}$$

where the real Y_{re} and imaginary Y_{im} parts of the spectrum amplitude are obtained by:

$$Y_{re} = \sum_{n=1}^{N} y(t_n)\cos(2\pi\nu_k t_n) \tag{5.85}$$

and

$$Y_{im} = \sum_{n=1}^{N} y(t_n)\sin(2\pi\nu_k t_n) \tag{5.86}$$

The uncertainty on centroid frequency due to the noise content $\Delta\nu_{cp}^{n}$ can be computed from error propagation formula:

$$\Delta\nu_{cp}^{n} = \sqrt{\sum_{k=1}^{K}\left[\frac{\partial\nu_{cp}}{\partial Y_k}\Delta Y_k\right]^2} = \sqrt{\sum_{k=1}^{K}\left[\frac{\partial\nu_{cp}}{\partial Y_k}\frac{\partial Y_k}{\partial n}\right]^2}\ u_n \tag{5.87}$$

where $\Delta Y_k = \frac{\partial Y_k(\nu)}{\partial n}u_n$ (u_n is standard deviation of noise content). The partial derivative of centroid frequency is derived from equation (5.83):

$$\frac{\partial\nu_{cp}}{\partial Y_k} = \frac{2\sum_{k=1}^{K}\nu_k Y_k\ \sum_{k=1}^{K}Y_k^2 - \ 2Y_k\sum_{k=1}^{K}\nu_k\ Y_k^2}{\left[\sum_{k=1}^{K}\ Y_k^2\right]^2} = \frac{2\sum_{k=1}^{K}\nu_k Y_k\ -\ 2\nu_{cp}Y_k}{\sum_{k=1}^{K}Y_k^2} \tag{5.88}$$

and partial derivative respect to noise is obtained by:

$$\frac{\partial Y_k}{\partial n} = \frac{Y_{re}\ \sum_{n=1}^{N}\cos\left(2\pi\nu_k t_n\right)\ + Y_{im}\sum_{n=1}^{N}\sin\left(2\pi\nu_k t_n\right)}{Y_k} \tag{5.89}$$

This equation offers an innovative formula to evaluate the uncertainty of estimated centroid frequency sequences which are used in inversion process. The uncertainty expressed in equation (5.80) is modified to include additional uncertainties:

$$u_{dm} = \sqrt{u_d^2 + u_{BW}^2} \tag{5.90}$$

where u_{BW} is assumed to be proportional to the bandwidth.

5.3.3 Synthetic Model Analysis - Heterogeneous Soil

To study the effect of the GPR signal propagating in a heterogeneous soil, synthetic radar data have been generated through gprMax using a stochastic distribution of the dielectric properties [37], [149]. In simulation, the transmitting and receiving antennas are two Hertzian dipoles in TE mode and the source wavelet is a Ricker function with a nominal frequency of $\nu_0 = 1\ GHz$. The step size of both antennas is set to 0.02 m. The complex permittivity is defined using the Peplinski model [100] and [101]:

$$\begin{aligned}\varepsilon'_{(1.4-18\ GHz)} &= \left[1 + \frac{\rho_b}{\rho_{sn}}\left(\varepsilon_{sn}^{a} - 1\right) + m_u^{\beta'}\varepsilon_w'^{a} - m_u\right]^{\frac{1}{a}}\\ \varepsilon'_{(0.3-1.3\ GHz)} &= 1.15\varepsilon'_{(1.4-18\ GHz)} - 0.68\end{aligned} \tag{5.91}$$

and the imaginary part of permittivity is:

$$\varepsilon'' = m_u^{\frac{\beta''}{a}}\left[\frac{\sigma_f}{\omega}\frac{\left(\rho_{sn} - \rho_b\right)}{\rho_{sn}m_u} - \varepsilon_w''\right] \tag{5.92}$$

with the parameters definition as:

$$\begin{aligned}\varepsilon_{sn} &= \left(1.01 + 0.44\rho_{sn}\right)^2 - 0.062\\ \beta' &= 1.2748 - 0.519S - 0.152C\\ \beta'' &= 1.33797 - 0.603S - 0.166C\end{aligned} \tag{5.93}$$

and the complex permittivity of water, ε_w, is obtained by:

$$\varepsilon_w = \varepsilon_{w,\infty} + \frac{\varepsilon_{w,s} - \varepsilon_{w,\infty}}{1 + j\omega t_{0,\omega}} \tag{5.94}$$

The term σ_f is a linearly proportional term to the static conductivity σ:

$$\begin{aligned}\sigma_{f(1.4-18\ GHz)} &= -1.645 + 1.939\rho_b - 2.25622S + 1.594C\\ \sigma_{f(0.3-1.3\ GHz)} &= 0.0467 + 0.2204\rho_b - 0.411S + 0.66144C\end{aligned} \tag{5.95}$$

where: m_u is the water volumetric fraction, ρ_b is the bulk density of soil in g/cm^3, ε_{sn} is the relative permittivity of the sand particles, $a = 0.65$ is an experimentally derived constant, and S and C are the sand and clay fractions, respectively, $t_{0,\omega} = 9.23\ ps$ is the relaxation time of the water, $\varepsilon_{w,s} = 80.1$ and $\varepsilon_{w,\infty} = 4.9$ are relative electrical permittivity of water for zero and infinity frequencies. Table (5.4) presents the parameters that have been set to produce a model which its loss tangent is quite constant over the investigated frequency range.

Table 5.4: The heterogeneous soil's properties used in gprMax simulation.

ρ_{sn}, sand particles density g/cm^3	ρ_b, bulk density of the soil g/cm^3	S sand fraction	C clay fraction	m_u water volumetric fraction	Centroid frequency (GHz)
2.99	1.59	0.984	0.16	0.015-0.025	1.0

In addition to clearly discriminate the primary reflections we add an additional material with relative dielectric permittivity $\varepsilon'_{r_{base}} = 9$ and conductivity 0.002 S/m as an interface layer under inhomogeneous media, which can be used for comparative study. Figure (5.12) shows the spatial distribution of: real and imaginary part of the soil's relative permittivity, conductivity and the relevant loss tangent (summation of both polarization and conductive components, see equation (4.4)). The variation of loss tangent in frequency band of $\sim 0.5 - 1.5$ HGz is shown in Figure (5.13). It follows that the mean loss tangent is $< \tan\delta >= 0.0129 \pm 0.0024$. The produced synthetic radargram by gprMax is shown in Figure (5.14, left). Singular value decomposition (SVD), having the first 3 dominant eigenvalues filtered out, is applied to the simulated data [Figure (5.14, right)]. The bright horizontal continuous reflections appear in the radar cross section at $\sim 45\ ns$, present the interface between soil and bedrock. In addition, the synthetic data is contaminated by a normally distributed random noise with zero mean and standard deviation equal to 2% of signal amplitude.

Figure (5.15) for example presents a single trace extracted from the radargram, and its time-frequency distribution obtained by STFT with a 10 ns time window of Hann type. The computed spectrogram indicates that at the earliest times, the spectral components in the range of 0 to $\sim 250 MHz$ are dominant.

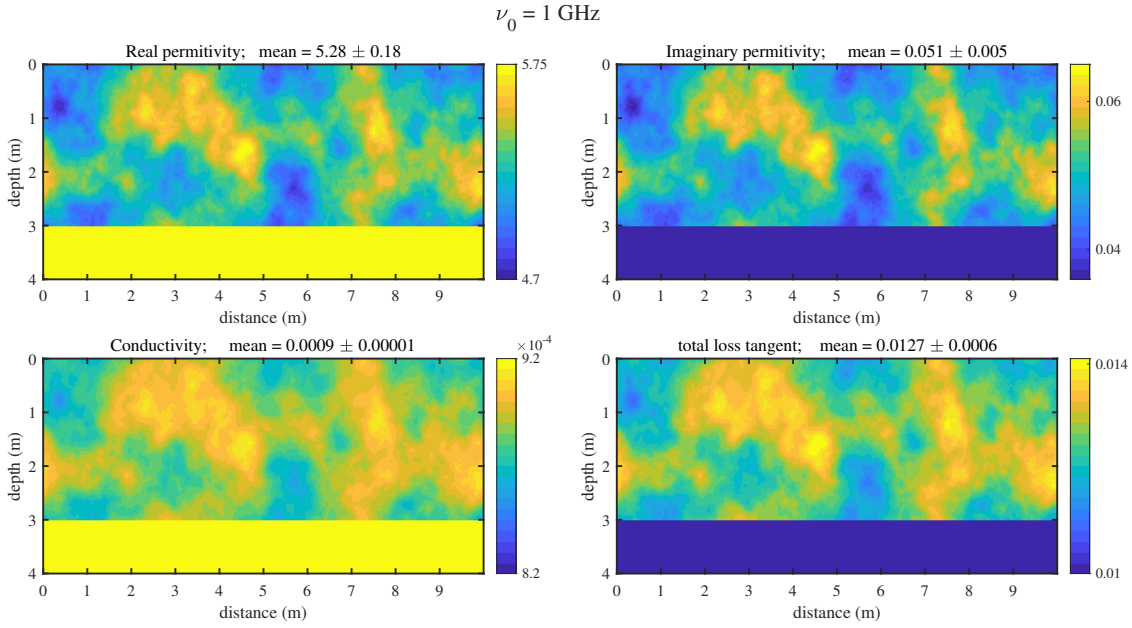

Figure 5.12: The simulated fractal model by gprMax. Real and imaginary parts of relative permitivity, static conductivity and loss tangent. The quantities on panels represent the mean value in the operating frequency 1.0 GHz.

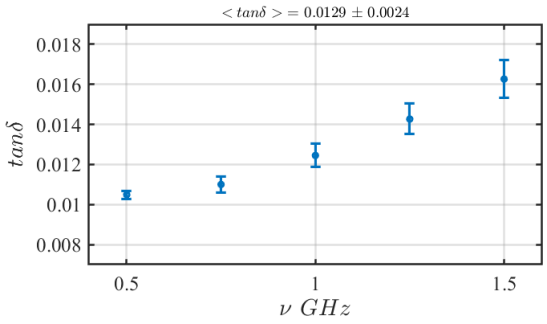

Figure 5.13: The variation of model's loss tangent in the frequency range of 0.5-1.5 GHz.

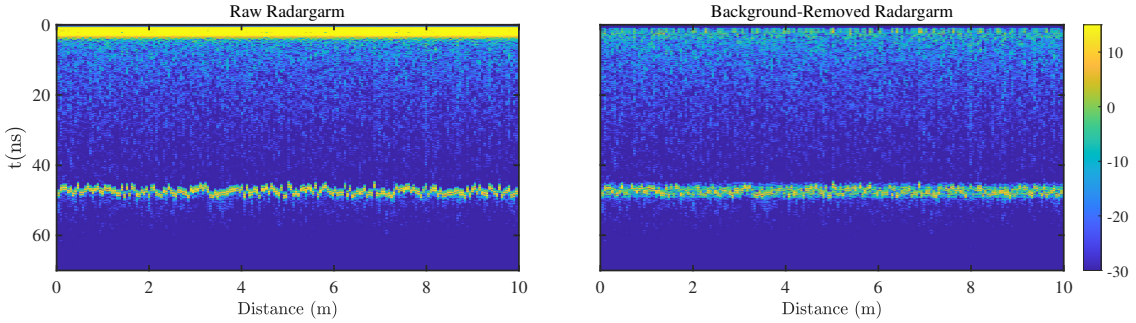

Figure 5.14: The produced radargram over the synthetic model presented in Figure (5.12). The background is removed using SVD, excluding the first 3 eigenvalues. The bright reflection at $\sim 45\ ns$ indicates the interface at depth 3 m.

Figure (5.16) displays an example of centroid frequency behavior as a function of time for processed (left panel) and raw data (right panel). The centroid frequency is computed applying different values of ν_{UB} and compared with the theoretical trend considering the average loss tangent value ($tan\delta = 0.013$). A general decreasing trend with time is obvious.

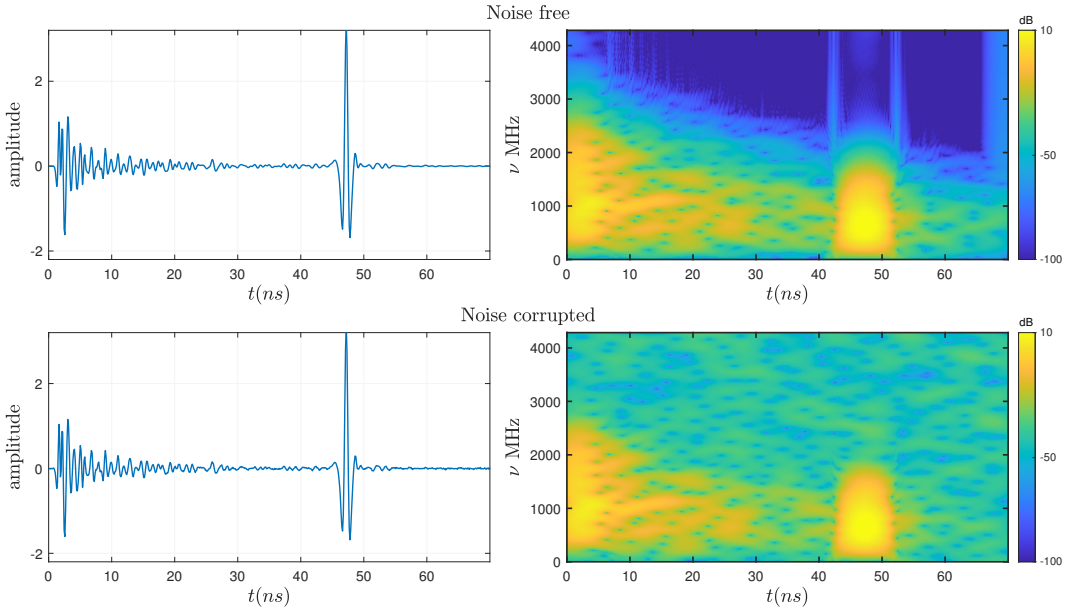

Figure 5.15: A trace and its time-frequency distribution calculated by STFT with a 10 ns Hann window. Upper pannel is noise-free trace and lower panel presents the same trace contaminated by a random noise.

The loss tangent $tan\delta$ and the nominal frequency ν_0 are estimated by using a probabilistic inversion approach using both forward formula introduced in equation (5.19) and (5.62) in different time intervals

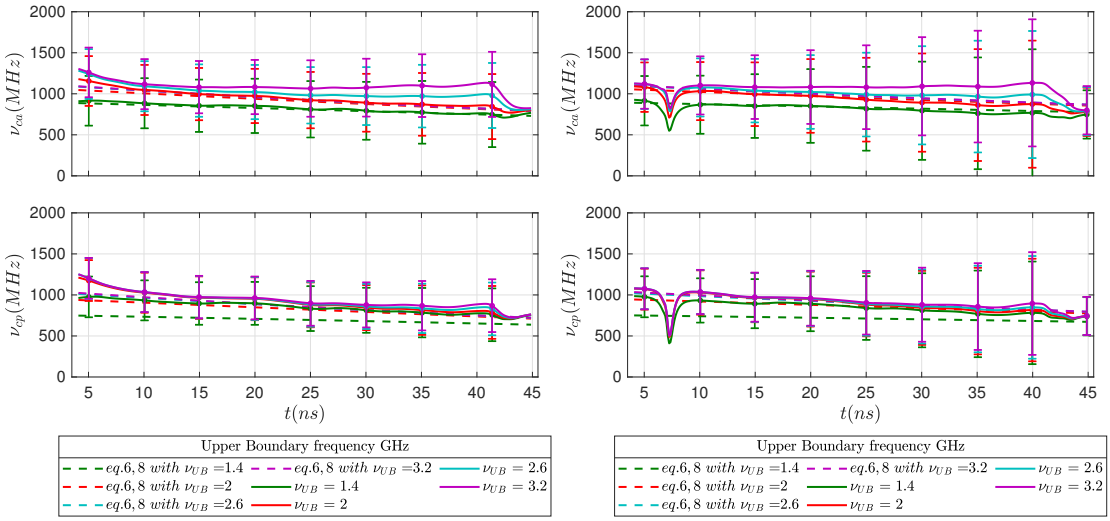

Figure 5.16: The theoretical and observed centroid frequency variation versus time for the 30 traces, considering various ν_{UB} and $tan\delta = 0.013$. Left panel obtained from processed data and right from raw data.

from 3 ns to a time delay t_{max}. Figure (5.17) and (5.18) illustrate the retrieved solutions as a function of t_{max} for different upper boundary frequency values from processed and raw data, respectively. Note that the estimated parameters indicates the average of all model parameters (ν_0 and $tan\delta$) over all traces, and a priori information for the nominal frequency ν_0 is incorporated into the inversion process through a Gaussian probability density function with the mean value of 1 GHz and standard deviation of 50 MHz (for detail see [66]). For appropriate values of ν_{UB} both centroid frequency shift approaches determine a loss tangent value which is consistent with the average value ($\sim tan\delta = 0.013 \pm 0.002$) for all time intervals whereas comparing the results from raw and processed data suggests that background removal slightly impacts the solution, particularly in larger time delay. Maximum frequency shift analysis underestimates the loss tangent. The upper boundary frequency has significant effect in the case of amplitude inversion analysis, especially at larger time-depth where the noise content becomes prominent. The estimated nominal frequency values ν_0 by amplitude spectrum method are well consistent with the true value (1 GHz) but those obtained by the power spectrum method are less accurate, particularly for $\nu_{UB} < 2\ GHz$.

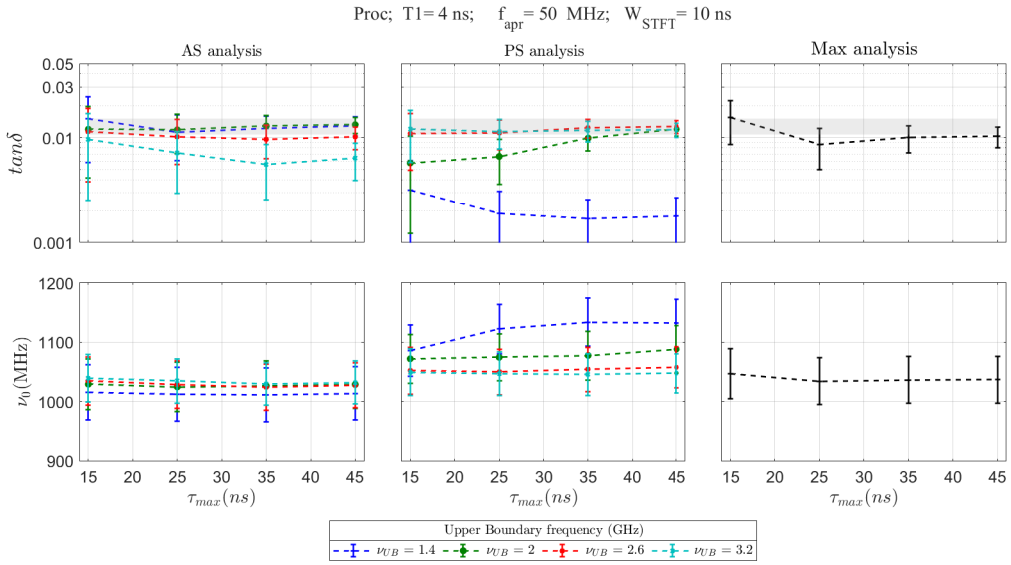

Figure 5.17: Processed data inversion. The results of simulated data inversion for absorption loss tangent and nominal frequency from amplitude spectrum and power spectrum and maximum frequency shift analysis. The gray region shows the variability of loss tangent estimated by the input dielectric model.

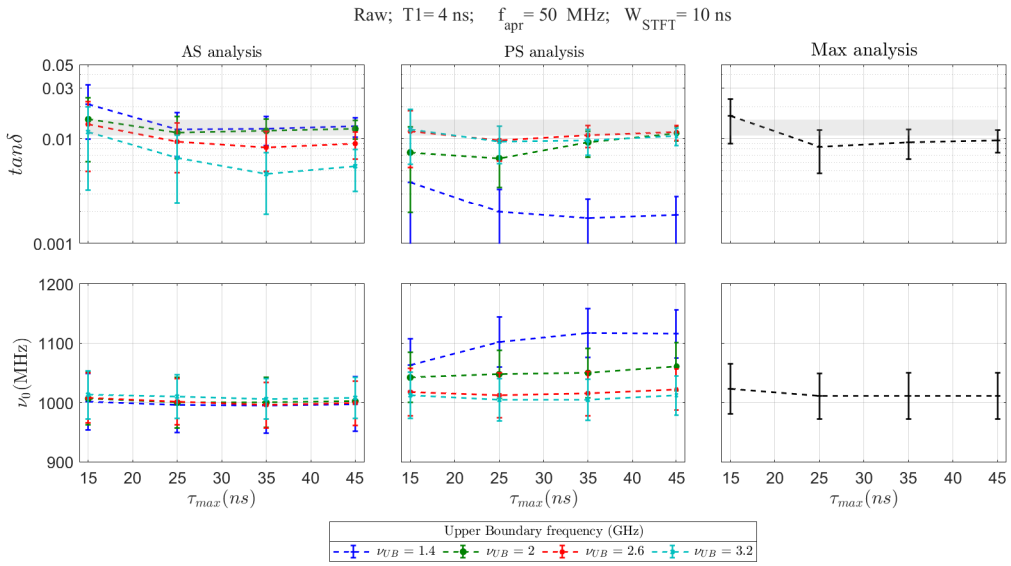

Figure 5.18: Raw data inversion. The results of simulated data inversion for absorption loss tangent and nominal frequency from amplitude spectrum and power spectrum and maximum frequency shift analysis. The gray region shows the variability of loss tangent estimated by the input dielectric model.

The loss tangent values are estimated as a function of GPR position along track and compared with the total loss Q^{-1} that is computed by a linear least-square fit of the amplitude decay in the time interval $3 - 40\ ns$ (Figure (5.19)). The total loss Q^{-1} values are in general larger than the loss tangent values that can be attributed to the additional scattering losses Q_s^{-1} generated by the heterogeneity of the investigated medium. To compute the loss tangent values, the upper boundary frequency is considered as 2.0 GHz and 2.6 GHz in amplitude and power spectrum analysis, respectively.

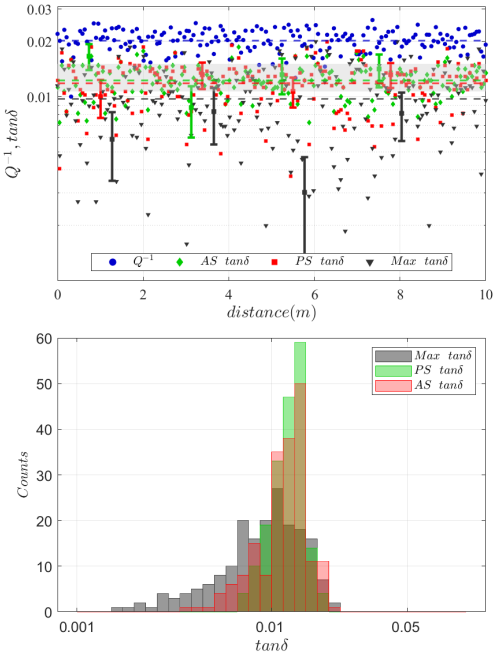

Figure 5.19: Separation of total loss into its components for simulated medium. Upper panel shows the constituting terms of loss along the track. The results are obtained considering $t_{max} = 40\ ns$ and $\nu_{UB} = 2.0,\ 2.6\ GHz$ for amplitude and power spectrum analysis. The gray region shows the variability of the loss tangent estimated by the input dielectric model. Dashed-lines present the mean values of each quantity.

5.3.4 Analysis of GPR Data Collected on Mount Etna, Italy

The GPR datasets were collected on volcanic deposit on Mount Etna Italy using 500 MHz and 1 GHz antennas in transverse electric (TE) and transverse magnetic (TM) configurations. These datasets can be considered as good analog of Martian and Lunar terrains. The data were acquired in reflection mode (single offset) using a $PulseEKKO\ Pro^{TM}$ bistatic system (Sensors & Software, Inc.). The data processing includes Dewow and background noise removal. The presented radargram cross sections in Figure (5.20) shows a complex stratigraphy composed of lava flow deposits. Several irregularly distributed hyperbolic reflectors are detected all over the radar section, while there is not any prominent interface across the entire radar profile. These hyperbolic reflectors are more visible in 500 MHz cross sections. The radargrams suggest a medium that is composed of irregular scatterers. Such a volcanic deposit could be a nice analog for Mars geophysical investigation. Since the higher frequency pulses are attenuate more rapidly with distance, the 1 GHz radargrams present poor information at deep parts, whereas the resolution of radar image at shallow parts is better than those provided by 500 MHz antenna.

The Average Time Amplitude (ATA) on the radar sections versus time in Figure (5.21) clearly shows the signals drop to noise level at the time 40 ns and 20 ns for antennas 500 MHz and 1 GHz, respectively.

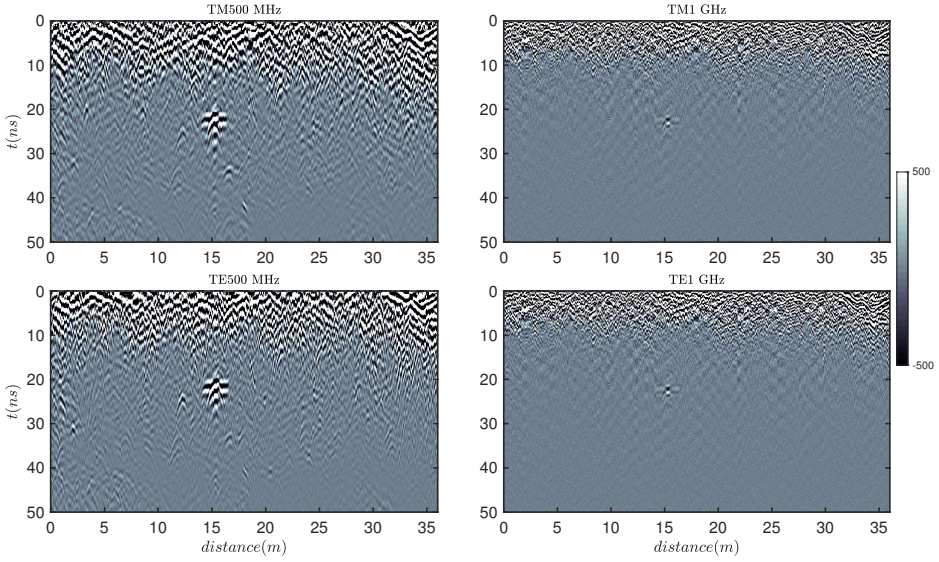

Figure 5.20: Radar data acquired on Mount Etna: TM500 MHz, TM1 GHz, TE500 MHz, and TE1 GHz radar cross sections after Dewow filtering and background removal. Radargrams are dominated by hyperbolic returns from small-scale scatterers, there is no prominent discontinuity. A hyperbolic reflection is present in $20 - 30$ ns interval.

The loss tangent of the stratigraphy is computed by means of the described methods based on the centroid frequency shift. All traces are interpreted at various time intervals with the starting time of 3ns for a range of ν_{UB}. Figures (5.22)-(5.25), in detail illustrate the retrieved parameters from analysis of radar section of antennas, in different time-depth intervals. The power spectrum solution seems to be less dependent on the ν_{UB} which is due to more stability of this method relative to noise. The TE and TM configurations with the same antenna yield basically similar results that only slightly differ in the details.

Finally, we performed a trace-by-trace analysis to compare Q^{-1} values with the loss tangent quantities. The inverse quality factor Q^{-1} was estimated by performing a linear fit on the amplitude decay plots in the time interval $3 - 16$ ns. These values are reported in Figure (5.26) (solid black and gray lines) and are compared to the loss tangent values computed with the amplitude and power spectrum methods for the same time interval and upper boundary frequencies $\nu_{UB} = 1.4$ GHz (red solid line at 500 MHz) and $\nu_{UB} = 2.4$ GHz (blue solid line at 1000 MHz). The plots reported in Figure (5.26) show that the quality factors Q^{-1} are always larger than the loss tangent values, regardless frequency and antennas configuration (Table 5.5). Moreover, Q^{-1} at 500 MHz is larger than that at 1000 MHz, whereas the loss tangent is frequency independent. According to equation (5.59), the difference in Q^{-1} can be ascribed to the scattering losses that are larger at 500 MHz, as also suggested by numbers and dimensions of the features present in the radar sections.

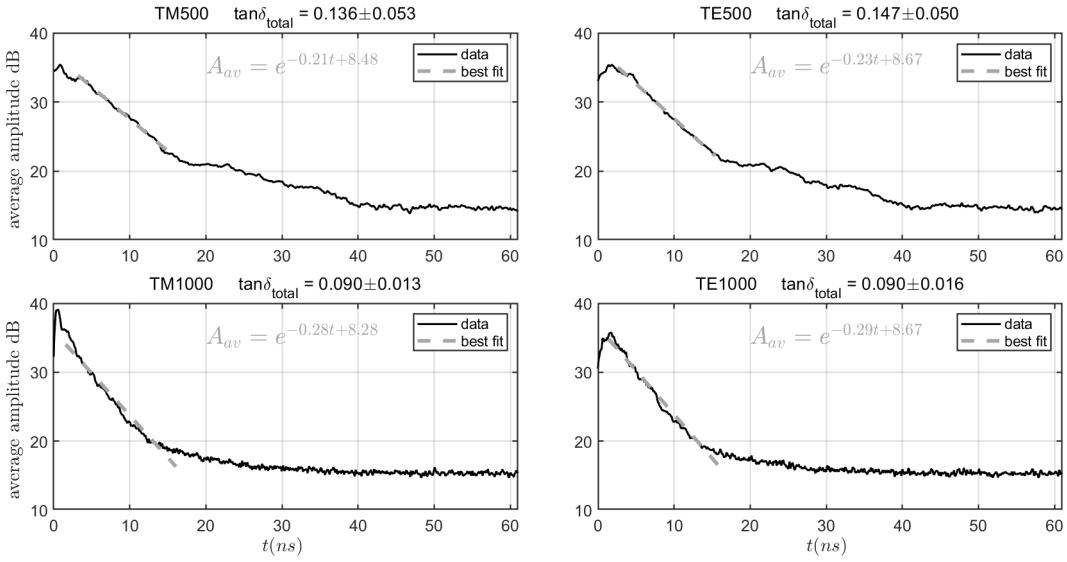

Figure 5.21: The average amplitude of all recorded signals over the cross section. The total loss tangent is estimated by linear fitting to the segment in $3-16$ ns as: 0.136 ± 0.053, 0.147 ± 0.050, 0.090 ± 0.013, 0.090 ± 0.016, from TM500 MHz, TE500 MHz, TM1 GHz and TE1 GHz, respectively.

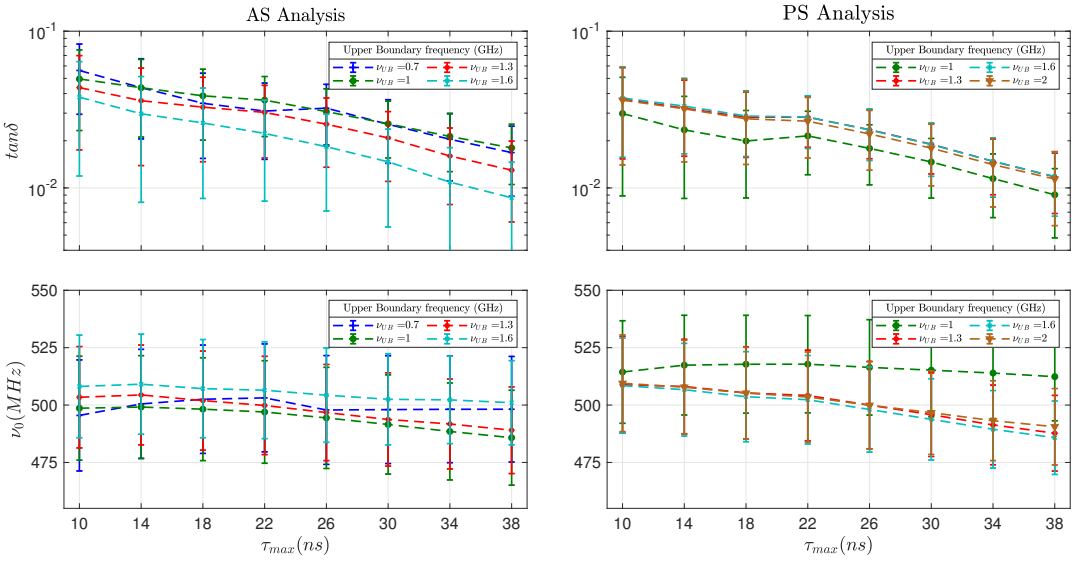

Figure 5.22: The results of TE500 MHz data inversion. (upper panel) Loss tangent estimated from amplitude spectrum and from power spectrum. (lower panel) Nominal frequency estimated from amplitude spectrum and from power spectrum. In all cases the time interval starts from 3 ns.

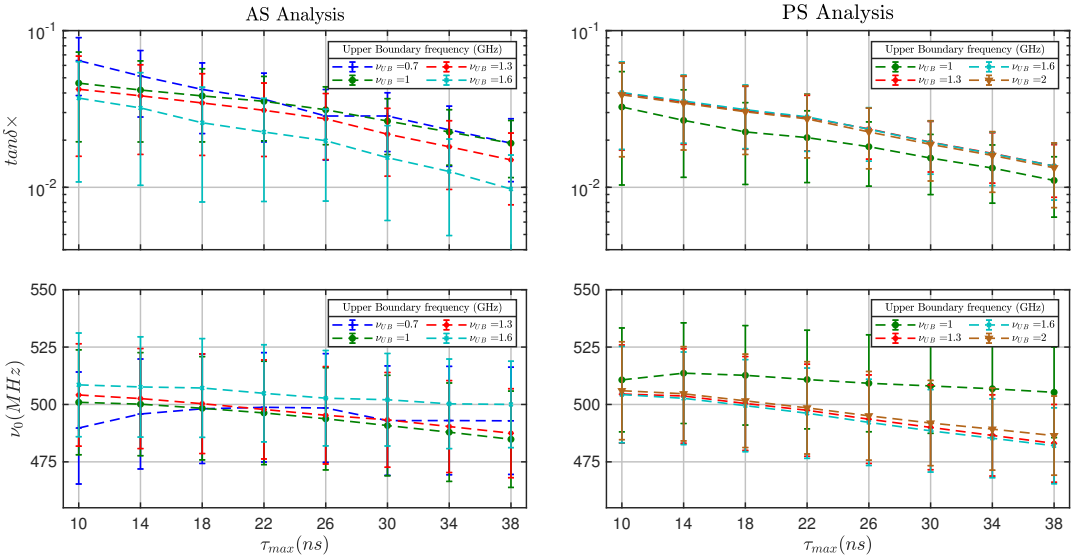

Figure 5.23: The results of TM500 MHz data inversion. (upper panel) Loss tangent estimated from amplitude spectrum and from power spectrum. (lower panel) Nominal frequency estimated from amplitude spectrum and from power spectrum. In all cases the time interval starts from 3 ns.

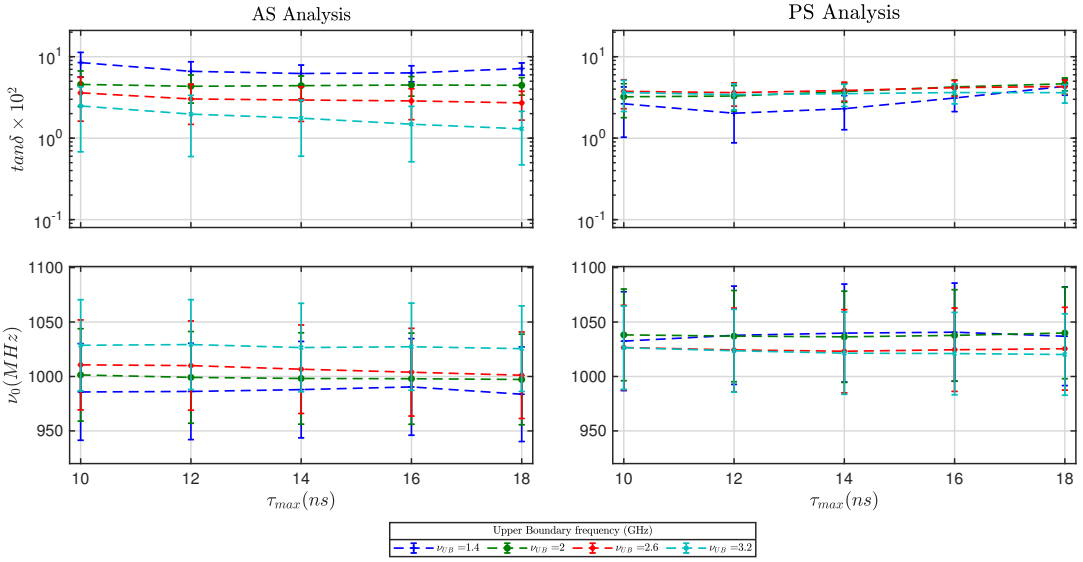

Figure 5.24: The results of TE 1000 MHz data inversion. (upper panel) Loss tangent estimated from amplitude spectrum and from power spectrum. (lower panel) Nominal frequency estimated from amplitude spectrum and from power spectrum. In all cases the time interval starts from 3 ns.

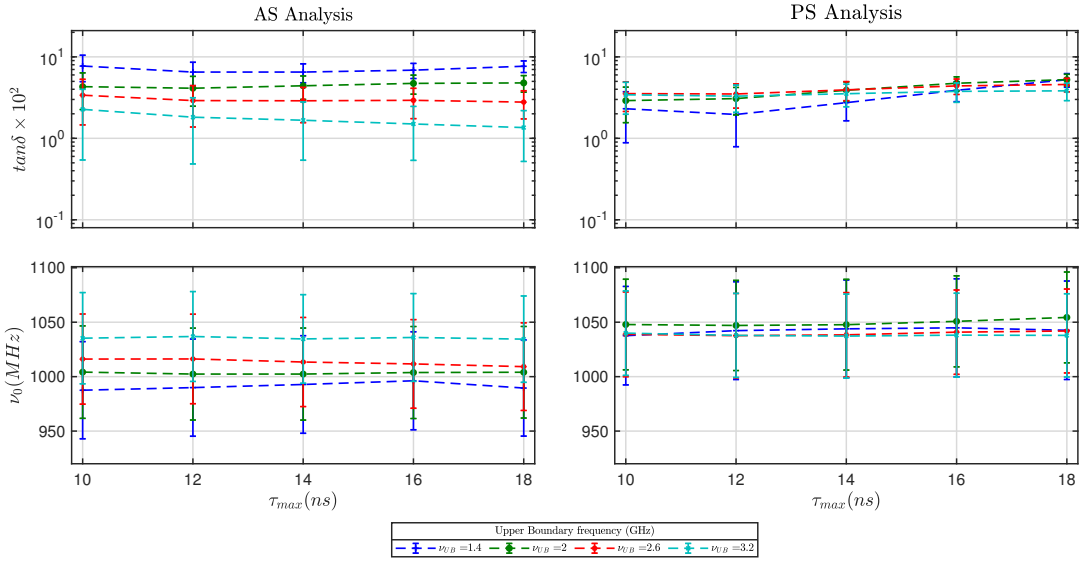

Figure 5.25: The results of TM 1000 MHz data inversion. (upper panel) Loss tangent estimated from amplitude spectrum and from power spectrum. (lower panel) Nominal frequency estimated from amplitude spectrum and from power spectrum. In all cases the time interval starts from 3 ns.

Moreover, the total attenuation of each trace is estimated by performing the best fit to the amplitude decay in the time interval $3 - 16$ ns where it presents a linear behavior [see Figure (5.21)]. Such values are compared with the loss tangent computed from power spectrum analysis in the same time interval considering $\nu_{UB} = 1.4\ GHz$ and $\nu_{UB} = 2.4\ GHz$, respectively, for the 500 MHz and 1 GHz antenna (Figure(5.26)). Note that, the results obtained from amplitude spectrum method is not shown for brevity, as they are well compatible to those retrieved from power spectrum method. The summary of results in Table (5.5) evidently shows that the scattering loss tangent is dominant component of total loss. Importantly, this term differs significantly for the 500 MHz and 1 GHz antenna as it is expected for scattering loss.

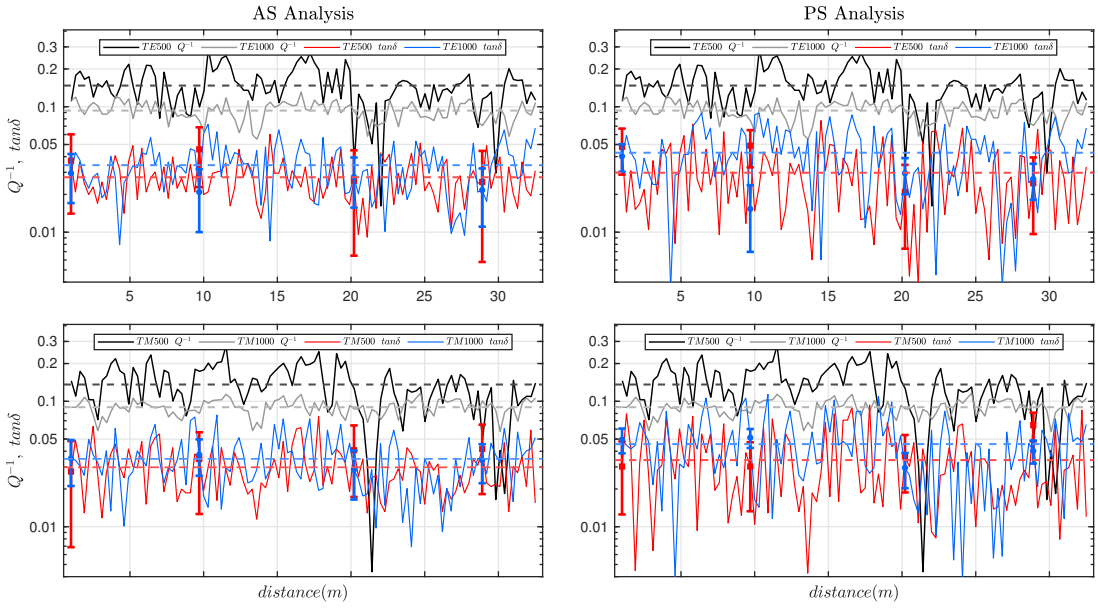

Figure 5.26: Total loss and loss tangent estimation from real data. (upper panel) total loss and loss tangent obtained from TM500 MHz and TM1 GHz antennas. (lower panel) total loss and loss tangent obtained from TE500 MHz and TE1 GHz antennas.

Table 5.5: Summary of results obtained from real data analysis.

Antenna	time interval ns	v_{UB} GHz	Q^{-1}	Q_s^{-1}	*AS*, $tan\,\delta$	*PS*, $tan\,\delta$
TM500 MHz	3 -16	1.4	0.136±0.053	0.107±0.048	0.029±0.012	0.030±0.013
TE500 MHz	3-16	1.4	0.147±0.050	0.122±0.050	0.027±0.010	0.030±0.017
TM1 GHz	3-16	2.4	0.089±0.013	0.055±0.021	0.034±0.016	0.035±0.016
TE1 GHz	3-16	2.4	0.093±0.016	0.059±0.021	0.034±0.014	0.043±0.022

5.3.5 Discussion

GPR attenuation is partially intrinsic (associated with the real conductivity and dielectric relaxation) and partially scattering (associated with the medium heterogeneity). For GPR frequency range, the polarization term of loss tangent for most of geological materials is frequency independent, while the intrinsic attenuation will be a function of frequency if the contribution of conductivity σ_s is not negligible. The introduced approaches assume the low loss media ($\sigma_s < 1\ mS/m$) with attenuation coefficient that is linearly depends on frequency (equation (4.13)), and hence, retrieve the polarization term of intrinsic attenuation. For low value of static conductivity the attenuation coefficient is given by:

$$\alpha_i \approx \frac{\omega}{2V}\ tan\delta = \frac{\omega}{2V}\ (tan\delta_p + tan\delta_c) = \frac{\omega}{2V}\ \left(\frac{\varepsilon''}{\varepsilon'} + \frac{\sigma_s}{\omega\varepsilon'}\right) \tag{5.96}$$

where very small static conductivity leads to

$$\alpha_i \approx \frac{\omega}{2V}\ tan\delta_p = \frac{\omega}{2V}\ \frac{\varepsilon''}{\varepsilon'} \tag{5.97}$$

In GPR frequency range permittivity components are almost frequency independent. This is a reliable assumption for dry granular basaltic materials. Hence, the attenuation coefficient linearly depends on the frequency and equation (5.97) can be written as:

$$\alpha_i(\nu) = \alpha_0\nu \tag{5.98}$$

In this scenario, the frequency-shift approaches perform well and derive total loss tangent that is equivalent to $tan\delta_p$.

If the frequency-dependent term of loss tangent *i.e.*, $\frac{\sigma_s}{\omega\varepsilon'}$, is not negligible the medium no longer is low loss:

$$\alpha_i(\nu) \approx \frac{\pi tan\delta_p}{V}\nu + \frac{\sigma_s}{2V\varepsilon'} = \alpha_0\nu + \alpha_1 \tag{5.99}$$

where as mentioned above α_1 in GPR range of frequency is almost frequency-independent. In this case, using the centroid frequency shift method only the polarization term of loss tangent ($\sim\ \alpha_0$) can be extracted [also see section (4.4.3) and equation (4.13)], and the conductivity term ($\sim \alpha_1$) is skipped.

In addition, the main assumption to separate the scattering and intrinsic attenuation, is frequency-dependent scattering, whereas this term can have both frequency dependent and frequency independent components, with maximum contribution at wavelengths close to the scatterer sizes. Therefore, separation of Q_i^{-1} and Q_s^{-1} is straightforward as long as the scattering attenuation exhibits a frequency independence behavior. For example, in the case of scattering attenuation with a linear dependence on frequency, these methods may overestimate the loss tangent.

5.3.6 Conclusion

Loss tangent estimation from GPR data in conditions where clear and continuous reflectors are absent is not straightforward; many sites, especially in planetary environments, do not show significant dielectric contrast between layers or materials and losses evaluation is complex. In these scenarios, centroid frequency shift methods can be particularly useful; it was shown that centroid-frequency shift methods utilizing amplitude and power spectrum techniques are both capable to retrieve the loss tangent in a

material lacking dielectric interfaces. Moreover, the comparison between total losses, described by the amplitude decay, and dielectric losses allows to evaluate the overall effect of the scattering due to the random distribution of the inhomogeneities. In planetary exploration, loss tangent evaluation is important to define the material composition, especially in terms of oxides, whereas the scattering component allows to determine the properties of subsurface, e.g., a fractured basalt layer or the distributions of ejecta material. Therefore, given the shortage of any in situ measurements, losses evaluation represents a fundamental tool to reduce the uncertainty on geological nature of the site.

Chapter 6

Loss Tangent Estimation: Planetary Prospecting

This chapter analyzes planetary radar-sounding data to estimate attenuation and provide new interpretations of the probed subsurface media. The Part I discusses the data acquired by the Chinese Lunar Penetrating Radar (LPR) on onboard the Yutu-2 rover of the Moon Chang'E 4 mission. After revisiting some results already published, the developed methods in Chapter 5 are implemented to estimate the loss tangent of lunar regolith-stratigraphy on the far side of the Moon from the observations (500 MHz channel) made by the LPR. The results can be able to obtain a more accurate description and characterization of the subsurface.

Part II is dedicated to Advanced Radar for Subsurface and Ionosphere Sounding (MARSIS) data studies at Ultimi Scopuli, located in SPLD, where very strong reflections beneath the ice layer and has been observed. Accordingly, first, the theoretical framework of attenuation estimation from MARSIS data is outlined. The loss tangent of SPLD at Ultimi Scopuli at 3, 4 and 5 MHz frequencies is retrieved from the linear relationship based on the ratio between basal-surface echo intensities. Then, the recent findings are presented that allow to better constrain the geological context of the investigated area by providing an estimate of the loss tangent of the area, an upper limit of the temperature, and an estimate of the dust content in the ice.

6.1 Lunar Penetrating Radar Data

6.1.1 Exploration of Moon's Nearside and Farside

Till 2019 there were 20 landings on Moon, all on the nearside whereas there was no landing on the Moon's farside because of the difficulty of communication between Earth and the farside. Figure (6.1) shows all the landing sites on the moons till 2019. The rover, Yutu-2, that carries Chang'E-4, was landed in the Von Kármán crater on the floor of the South Pole-Aitken basin on 3 January 2019, by the Chinese Lunar Exploration Program. The rover carries a landing camera, a terrain camera, a panoramic camera, a visible and near infrared imaging spectrometer, and ground penetrating radar.

Figure (6.2) presents Landing-site images taken by the lander terrain camera and Yutu-2 panoramic camera. The exploration of this region may address some fundamental questions, such as the nature of the lunar mantle, and the cause of greater crustal thickness on the farside [150].

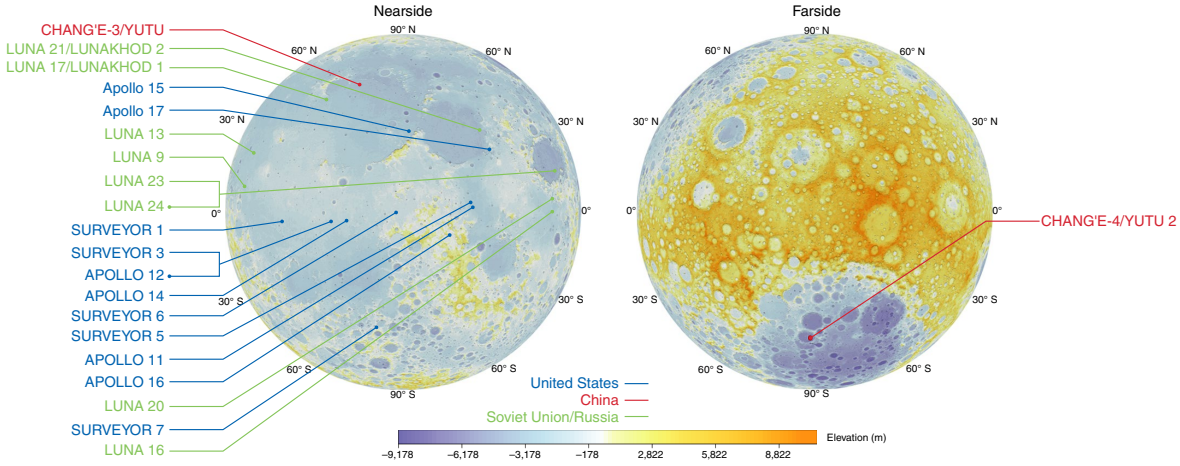

Figure 6.1: Distribution of all landings sites on the Moon till 3 January 2019. (left) nearside; (right) farside. The subsurface structure of the CE-4 landing site preserves a record of the sequence of major impact events of this region. Notably, there are several younger large (>25 km) impact craters around the Von Kármán that may contribute ejecta materials to the local regolith in the Von Kármán [150].

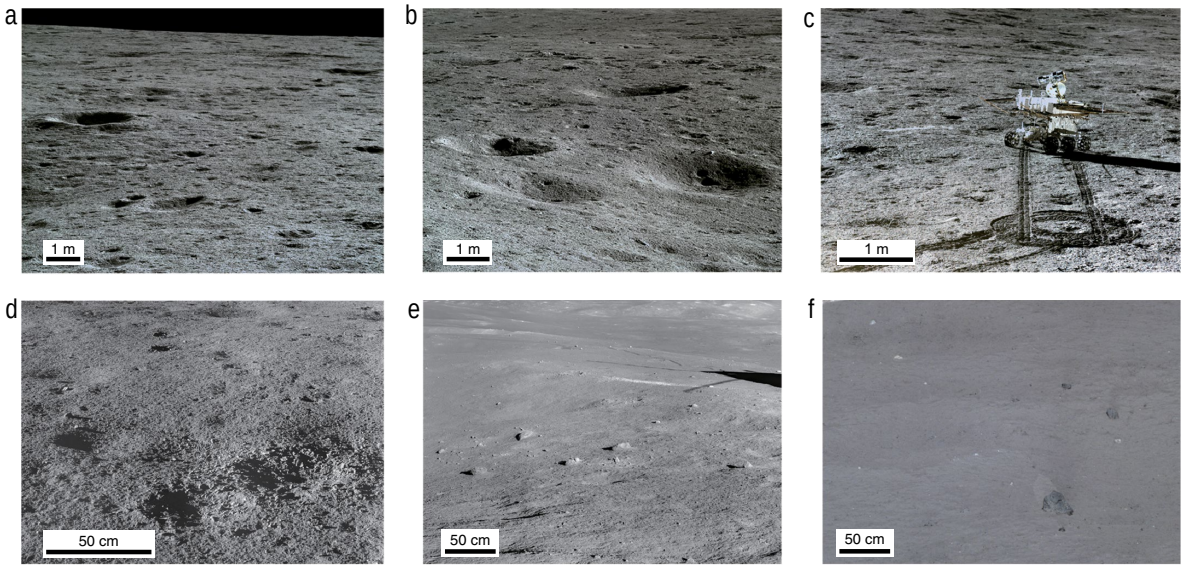

Figure 6.2: Landing-site images taken by the chang'e-4 lander terrain camera and Yutu-2 panoramic camera. (**a**), (**b**), Images of small craters around the landing site. (**c**), Rover Yutu-2. (**d**), Close-up view showing rock debris in small craters (from Yutu-2). (**e**), Small rocks near the traverse area (from Yutu-2). (**f**), Unusual dark rocks near the landing site [150].

6.1.2 Lunar Penetrating Radar Onboard th CE-3 and CE-4

In 2014, Chang'E-3 (CE-3) mission started to survey the lunar subsurface at its landing site in northern Mare Imbrium, in Moon's nearside, by using the Lunar Penetrating Radar (LPR) onboard the Yutu rover. It was the first ground penetrating radar that has operated on the Moon's surface. The LPR is an ultra-wideband carrier-free pulse radar with two channels. The first channel installed on the back of the rover, operates at a center frequency of 60 MHz with a bandwidth of 40 MHz, while the second channel installed on the underside of the rover, works at a central frequency of 500 MHz with a bandwidth of 500 MHz. The free space range resolutions are $\sim$ 50 cm and $\sim$ 25 m for 60 MHz and 500 MHz, respectively. The LPR uses one transmitting and one receiving dipole antenna for 60 MHz, and one transmitting and two bow-tie receiving antennas for 500 MHz that are attached to the bottom of the rover as shown in Figure (6.3), ([153], [134], [34]).

In 2019, Chang'E-4 (CE-4) landed on the eastern floor of Von Kármán crater on the farside of the moon. The Yutu-2 rover of CE-4 mission carried an LPR with the same configuration as CE-3 ([150], [71]).

Figure (6.4), for example, presents the Yutu-2 route in the first 9 months. The time intervals between two adjacent traces, recorded by CE-4 LPR, are 1.536 s at 60 MHz and 0.6636 s at 500 MHz. The velocity of the rover is ~ 5.5 cm/s , which gives an approximate step size of ~ 3.6 cm for the 500 MHz and ~ 8.5 cm for the 60 MHz [72]. Same as CH-3, the high-frequency system of CE-4 LPR is equipped with one transmitting and two receiving bow-tie antennas (CH2A and CH2B) that are located at the bottom of the Yutu-2 rover (~ 0.3 m above the ground) and are separated ~ 0.16 m from each other. The first receiving antenna (CH2A) in the high-frequency system is affected by a strong cross-talk. In addition, as in the CE-3 mission, the low-frequency (60 MHz) unsheilded-antennas that are installed on the back of the CE-4 rover, leading to electromagnetic coupling with the rover's metallic body, resulting in strong disturbances that largely overlap the back-scattered signals from the subsurface. These disturbances could easily be misinterpreted as subsurface reflectors [106]. Therefore, we analyze only the LPR CH2B, 500 MHz data, and other datasets are not studied here. At this frequency the structure and depth of lunar regolith can be probed within 30 m, and the structure of lunar crust can be investigated to hundreds of meters deep.

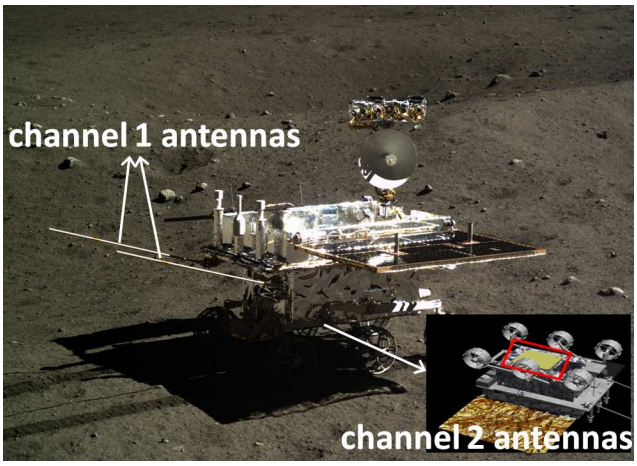

Figure 6.3: The two radar channels, 60 and 500 MHz, on the LPR. This picture was taken by the descending camera onboard the CE-3 lander. For the second channel that operates at 500 MHz, one transmitting and two receiving bow-tie antennas are attached to the bottom of the Yutu rover [134].

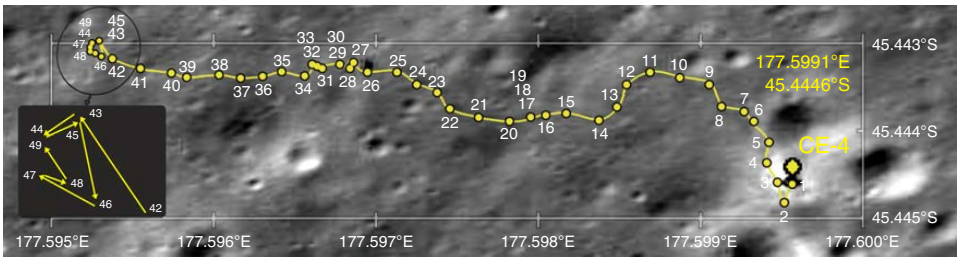

Figure 6.4: The Yutu-2 rover route during 9 months. The yellow dots represent way-points [59].

6.1.3 Data and Methods

The collected high-frequency radar data is processed by applying standard GPR signal processing steps including background subtraction, dewow filtering and geometric spreading correction. To remove the background, the mean of all traces in a moving window with a specific width is computed, and then, the mean trace is subtracted from each individual trace in the window. Two moving windows with the widths of 10 m and 50 m are chosen [53]. Comparing the final processed data, considering two window-widths, indicates that the width of the window slightly affects the processed data, as shown in Figure (6.5) and (6.6). Note that, the sequence of moving window does not have an overlap. Background subtraction

suppresses ring-down response, and dewow filtering is used to reduce the low-frequency signal due to the coupling between receiver and transmitter.

The average time amplitude (ATA) is computed for each dataset. The ATA plot in Figure (6.7) presents the variation of amplitude versus time, so estimates the signal penetration (signal attenuation). In addition ATA plot can detect the time-invariant coherent-noise level due to the so-called system residual response. The ATA plot shows that the datasets have the identical overall decay versus time and reach the noise level at around 500 ns. Several features are visible at the times about 270 ns, 330 ns and 430 ns.

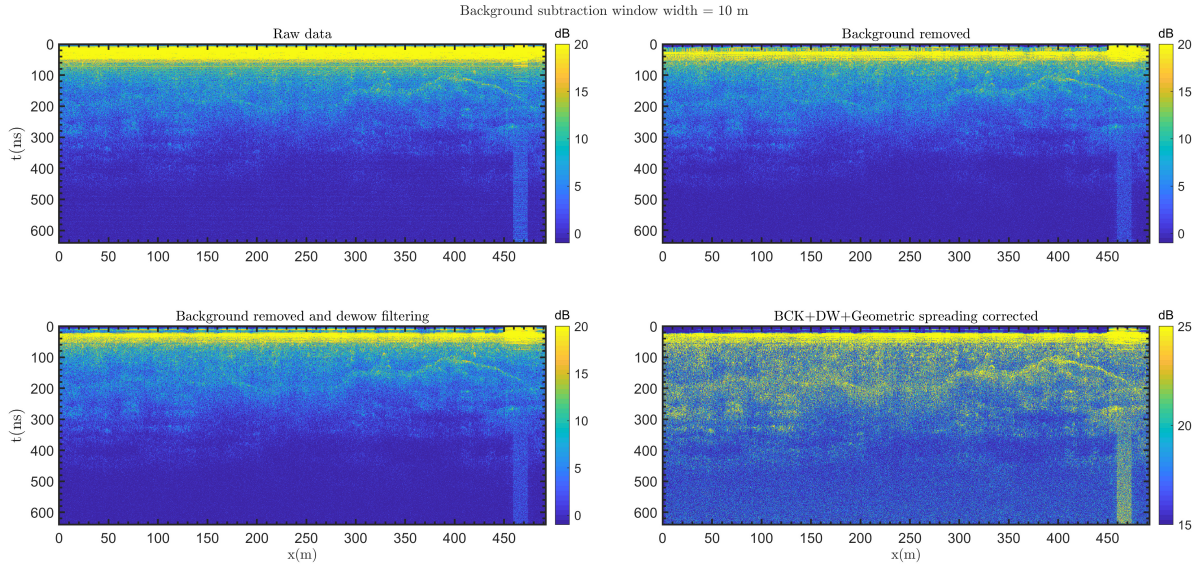

Figure 6.5: Processing steps of LPR high frequency by the window width of 10 m. (a) Raw data; (b) Raw data after background subtraction; (c) Raw data after background subtraction and dewow filtering; (d) Raw data after background subtraction, dewow filtering and geometrical spreading compensation. The sampling interval is 0.3125 ns and the average trace interval is 3.75 *cm*.

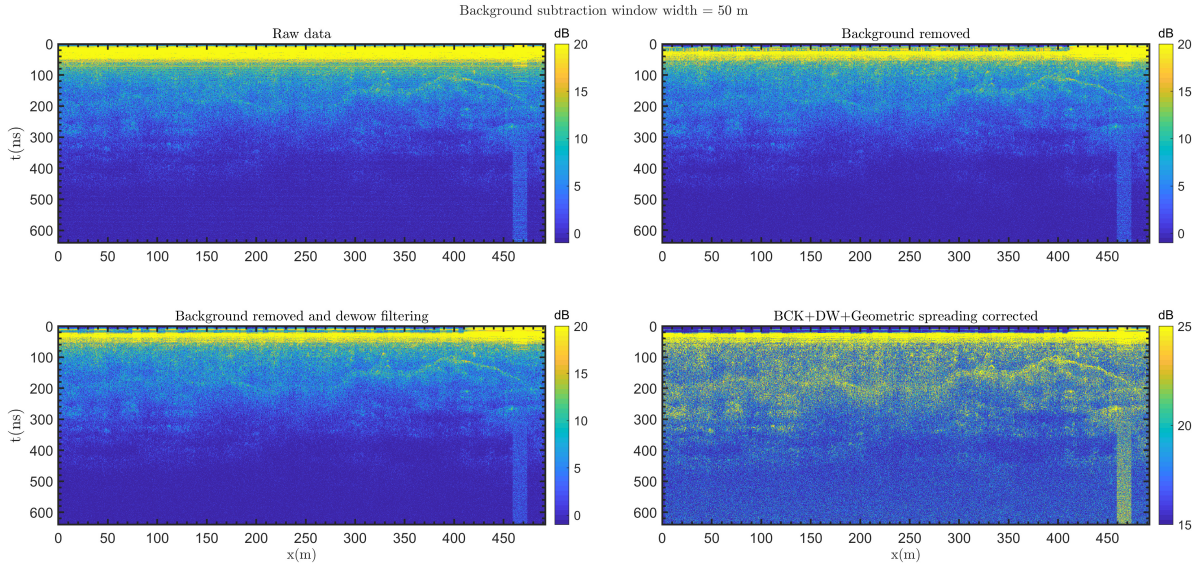

Figure 6.6: Processing steps of LPR high frequency by the window width of 50 m. Raw data; Raw data after background subtraction; Raw data after background subtraction and dewow filtering; Raw data after background subtraction, dewow filtering and geometrical spreading compensation. The sampling interval is 0.3125 ns and the average trace interval is 3.75 *cm*.

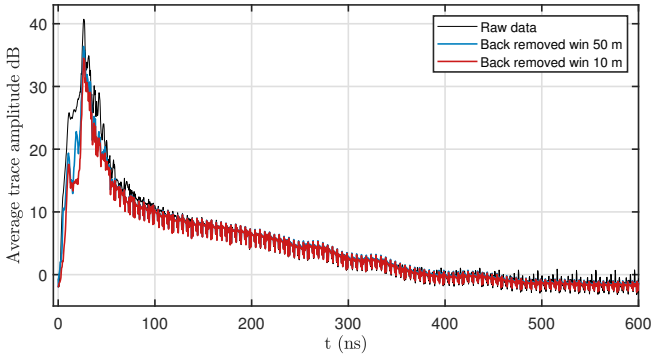

Figure 6.7: The average time amplitude (ATA) for raw and processed data.

For the first 100 meter of the track, the bulk loss tangent (intrinsic or electric loss) is estimated at various time intervals by using the frequency shift methods described in the Chapter 5. The constraint is imposed on the operating frequency by a priori Gaussian *pdf* that is centered at 500 MHz a width of 25 MHz (5 per cent of the operating central frequency). Since the two sets of processed data leads to the same results, in the following only the solution of data processed by a window of the width 10 m is presented. To exclude the direct air-waves and direct ground-waves effect, we start from the time-depth of 60 ns, and consider 6 moving time-windows with the different widths in the range of $w_t = 30 - 80\ ns$ (w_t is the width of the time window) to select a section of the radargram to estimate the bulk loss tangent. The time-windows sequentially shifts 10 ns in time-depth direction to cover all depths. Two sequential windows have an overlap of $(w_t - 10)\ ns$. Figure (6.8) presents the estimated intrinsic loss tangent. The corresponding recovered operating frequency is shown in Figure (6.9), as well. Note that upper boundary frequency value is 1.2 GHz and 2.0 GHz in amplitude and power spectrum analysis.

The imposed constraint is applied through 5 per cent uncertainty on frequency, however, the tests show that imposed constraint has its prominent effects only on the estimated frequency and the loss tangent is always almost invariant under the imposed constraint. For example, Figure (6.10) compares the estimated loss tangent when the width of imposed a priori Gaussian pdf equals to 20 and 5 per cent of centroid frequency. In addition, total loss is estimated from the linear least-square fit to the logarithm of ATA plot in the same sections in the Figure (6.8) with the same moving time-window widths. Figures (6.11) to (6.13) displays the estimated total loss and compares it with the loss tangent in Figure (6.8). The independence of the two calculations may lead to peculiar situations, in which the total loss is lower than the intrinsic loss [the most left part of Figures (6.11) to (6.13)]. These artifacts are possibly due to either laterally coherent structures, interference, or noise which may cause the ATA to deviate from the expected exponential decay.

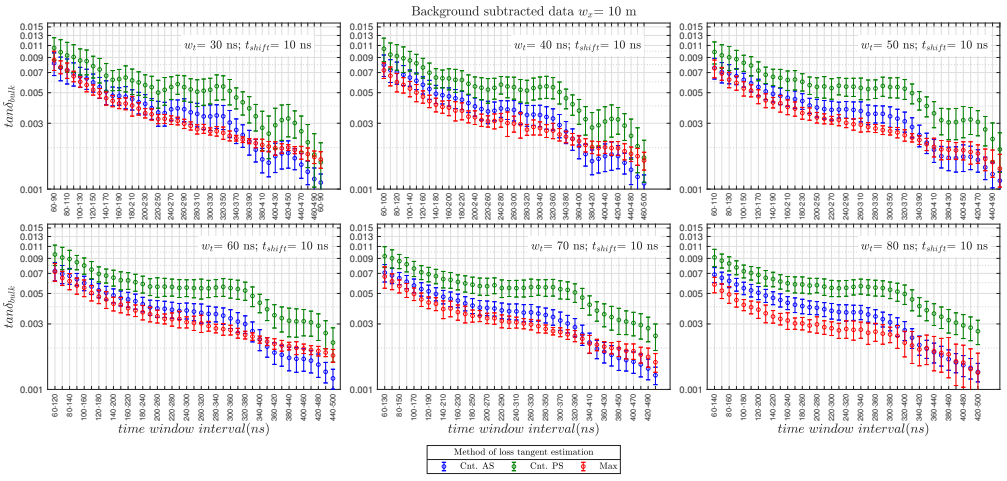

Figure 6.8: The bulk loss tangent estimated from the first 100 meters of track, at various time-depth intervals considering different moving time-window width. The reported values for each interval is average of all loss tangent values obtained from the traces in that section.

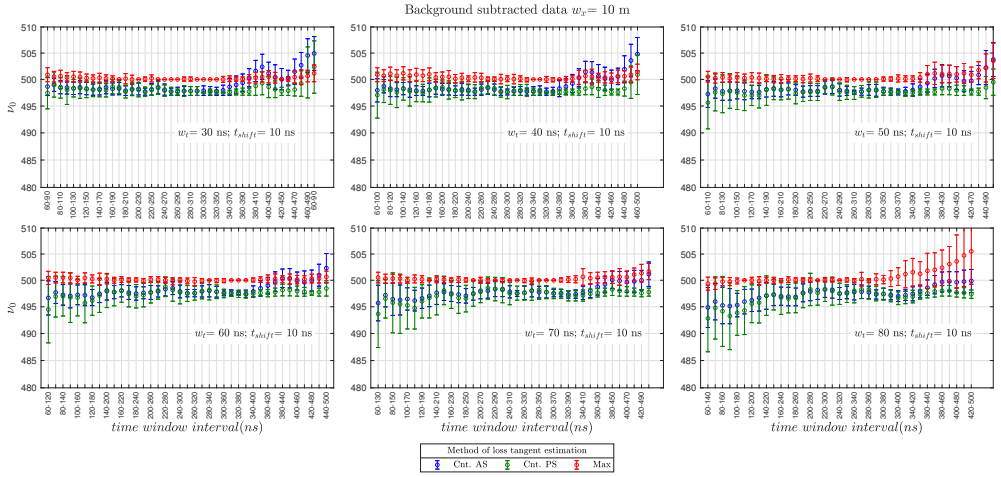

Figure 6.9: The estimated operating frequency in correspondence of Figure (6.8).

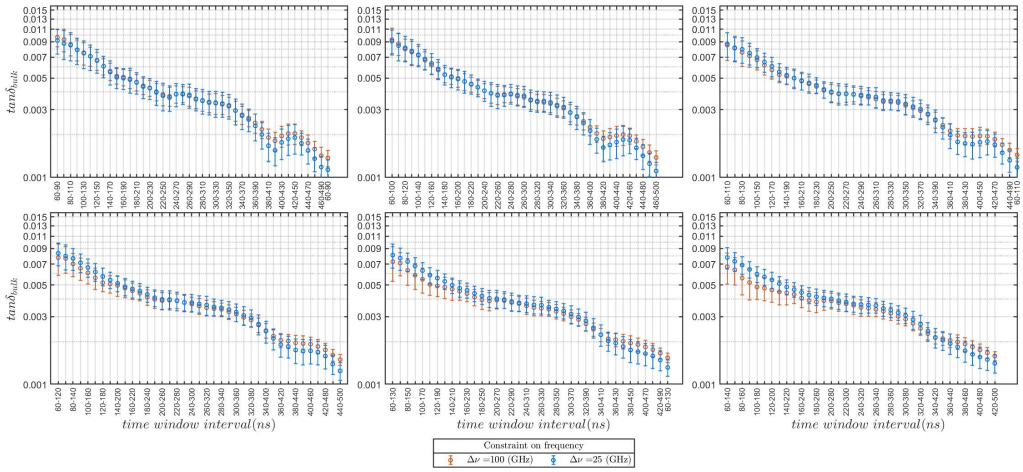

Figure 6.10: Comparing the solutions for different constraints applied trough a priori Gaussian pdf on operating frequency.

Figure 6.11: Comparing the total loss (blue) and loss tangent (intrinsic loss, red) in various time-depths for the first 100 meters along the track. The loss tangent is obtained from centroid frequency shift, amplitude spectrum analysis approach.

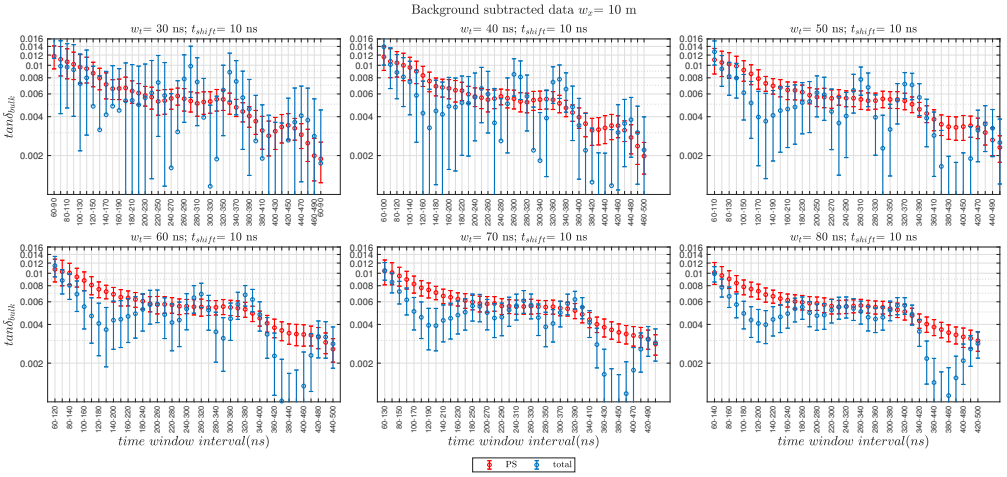

Figure 6.12: Comparing the total loss (blue) and loss tangent (red) in various time-depths for the first 100 meters along the track. The intrinsic loss is obtained from centroid frequency shift, power spectrum analysis approach.

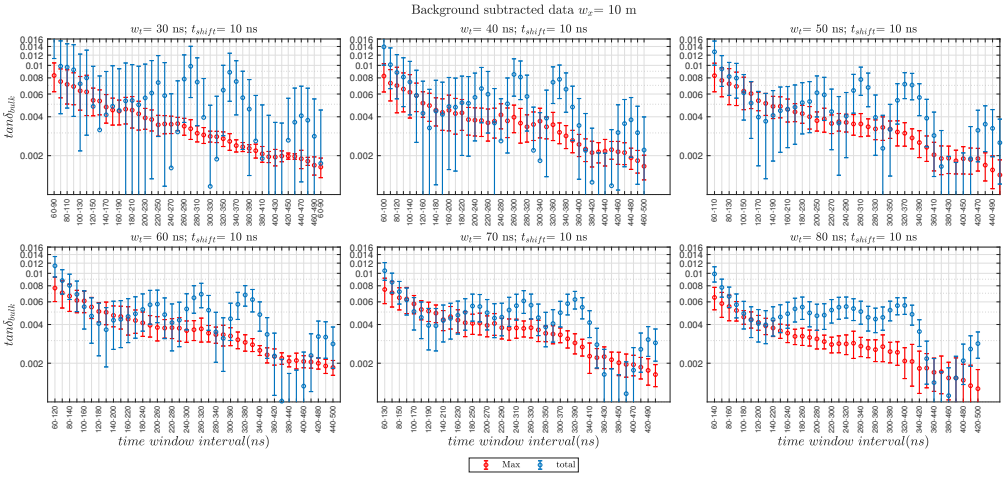

Figure 6.13: Comparing the total loss (blue) and loss tangent (red) in various time-depths for the first 100 meters along the track. The intrinsic loss tangent is obtained from maximum frequency shift, amplitude spectrum analysis.

6.1.4 Loss Tangent Estimation from the Inclined Interface

The distinct inclined interface that is visible on the radargram at distance $410 - 460$ m along the track (Figure (6.14)) can be used to estimate the loss tangent. We implement a procedure similar to that used in Chapter 5. The loss tangent is estimated by using frequency shift method, considering an upper boundary frequency of 1.2 GHz. Figure (6.15) presents the obtained probability distribution and the marginal pdfs. Both approaches yield a loss tangent around 0.006 that is in consistency with those already obtained.

To estimate the total loss, first the maximum amplitude-values around the interface, that are approximately determined by the white line in Figure (6.16, left panel), is extracted. For this purpose a window centered on the white line with the width of 16 ns is used. The blue circles in the Figure (6.16, right panel) present the maximum amplitude-values around the interface, and the total loss tangent is estimated by best linear fit to these data. Figure (6.17) displays the computed total loss considering various time intervals. The solutions shows that the evaluated total loss is very unstable respect with the selected time interval.

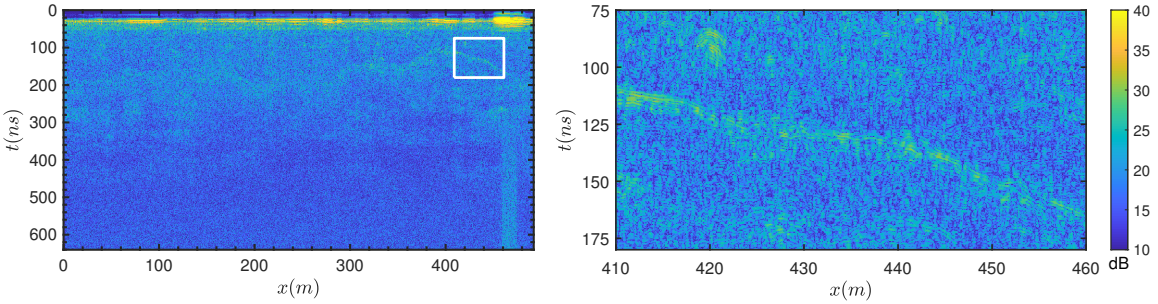

Figure 6.14: Radargram and the section including inclined interface.

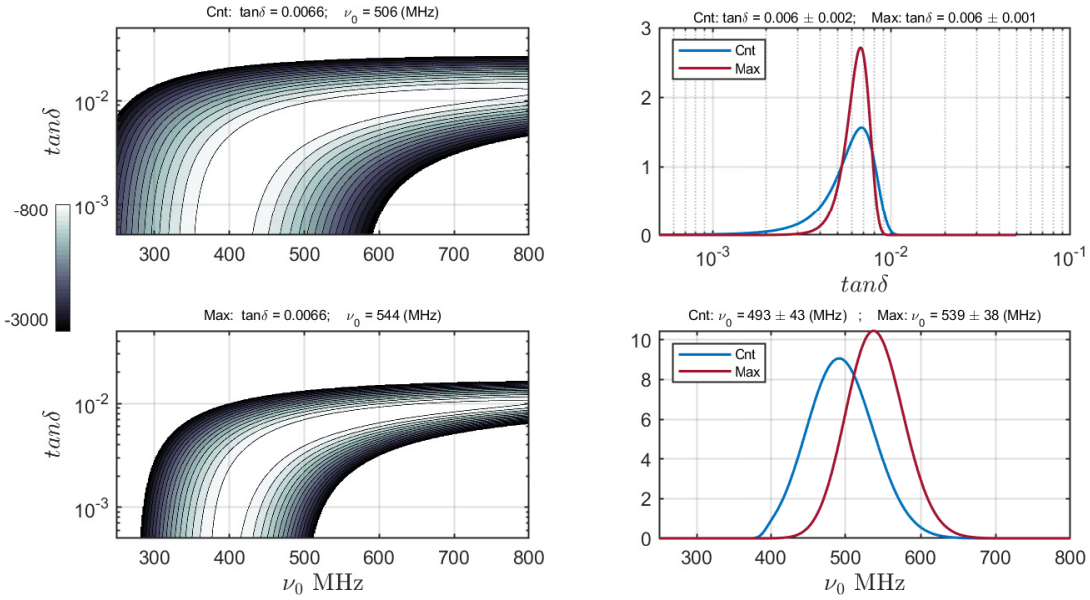

Figure 6.15: The probabilistic approach to retrieve the loss tangent and operating frequency. Posterior probability distribution and marginal PDFs determine the solutions.

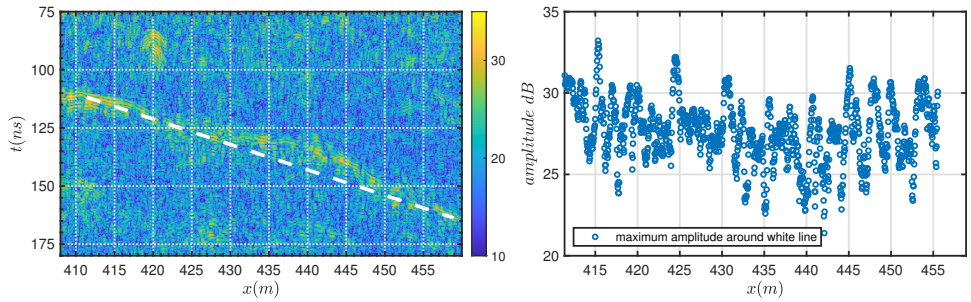

Figure 6.16: The reflection by interface and amplitude maximum value around the interface. The total loss is estimated by a linear fit to the blue data. A time window with the width of 16 ns is used to extract the maximum amplitude.

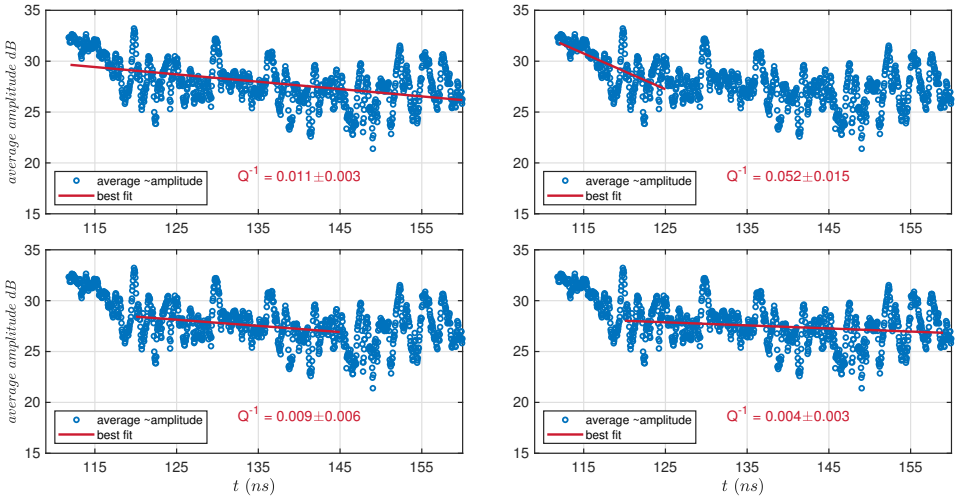

Figure 6.17: Total loss estimation from the inclined interface. The selected time interval (or selected part of interface) has prominent effect on the solutions.

6.1.5 Loss Tangent Estimation Overall of the Radargram

The intrinsic and total loss map are produced across the entire radar profile. A moving window with the width of 5 meter (∼120 traces) along the track is selected. Then, for each section that is specified by the window position along the track, the loss tangent is estimated by using the same procedure as performed in Figure (6.8). We choose a sliding time-window with the width of 30 ns, and with the starting time from 60 to 470 ns. The mean value of all loss tangent estimated in a particular subsection that is defined by the time-window and distance-window is reported as the loss tangent of that subsection. The intrinsic and total loss are obtained from frequency shift and best fit to average amplitude, respectively. In the case of total loss the sliding time-window width is 60 ns. Geometric spreading correction was applied in total loss estimation. Figure (6.18) displays the loss maps.

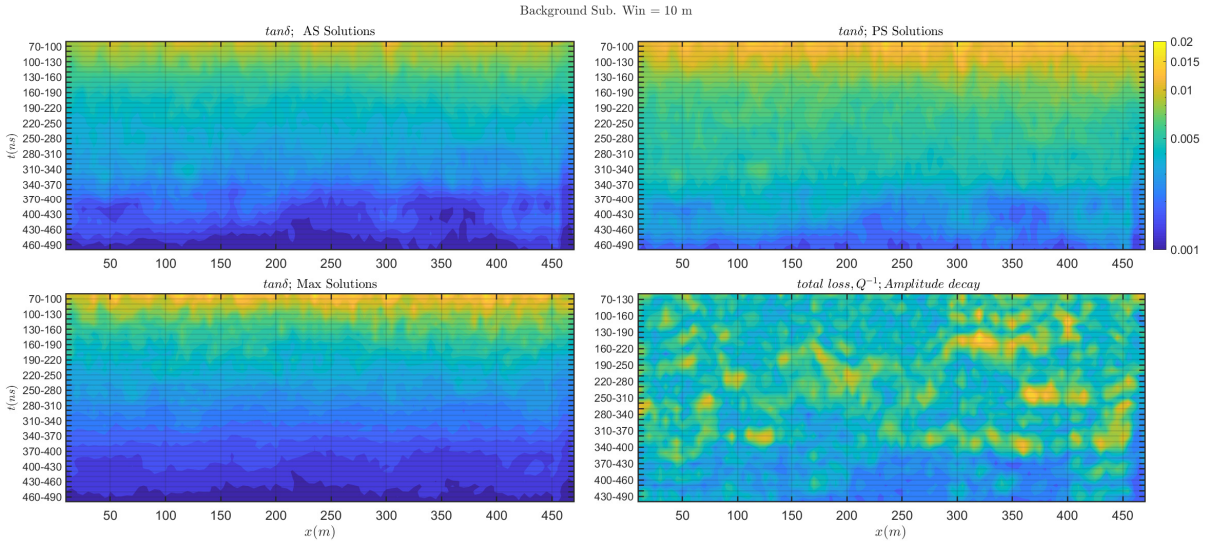

Figure 6.18: The intrinsic and total loss maps obtained from analysis overall radargram cross section. The sliding time-window width for producing intrinsic and total loss maps is 30 ns and 60 ns, respectively.

The absorption attenuation is almost constant along track while total loss presents a large variation that is caused by inhomogeneities and scatters. In addition, the average loss tangent and total loss are $tan\delta = 0.0039 \pm 0.0023$, $Q^{-1} = 0.0049 \pm 0.0020$ that is consistent with evaluation in [72]. Comparing the radargram with total and intrinsic loss maps indicates that there is some correlation between loss

tangent and radargram (Figure (6.19)). Li et al., [72], applied a tomographic inversion algorithm to the first 100 m of the radargram section to illustrate the internal structure of the deposit. Their resulting image show that in the central part of the image, there is a lens of rather uniform and transparent material (Figure 6.20). This structure is also visible on the produced image of loss tangent as presented in Figure (6.21). In agreement with [72] the velocity is assumed a constant value of 0.16 m/ns.

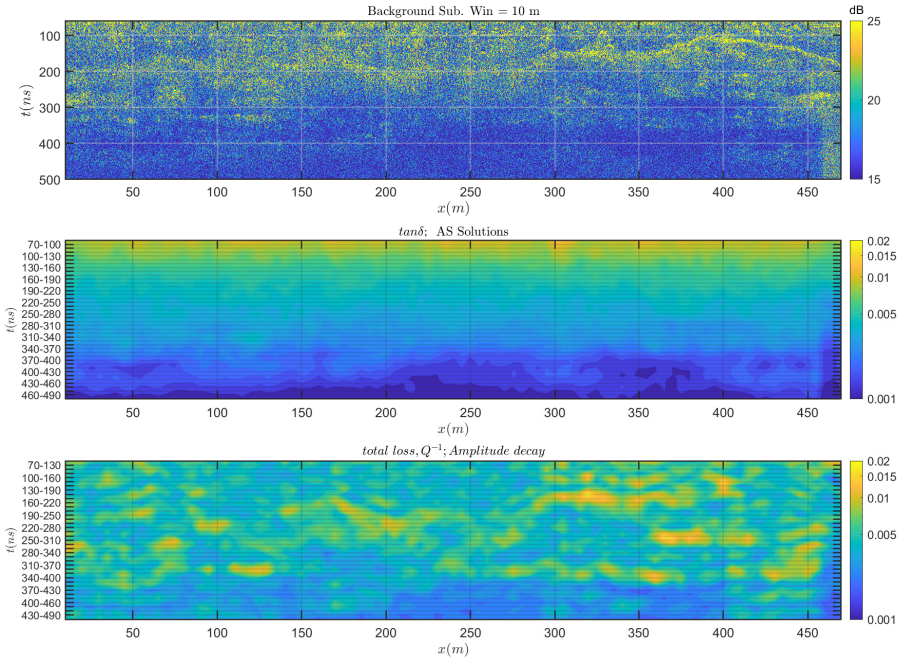

Figure 6.19: The entire radargram section in comparison with the intrinsic (loss tangent) and total loss. Several feature observed by radargram is visible also on the loss tangent image.

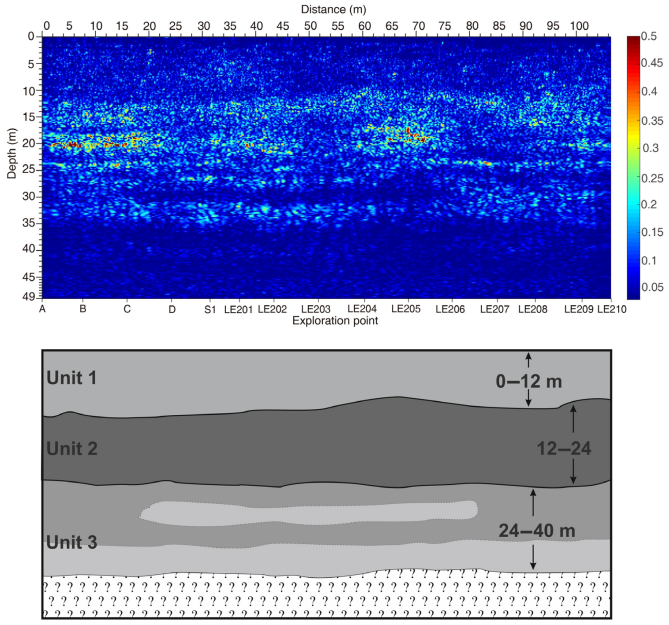

Figure 6.20: (upper panel)Tomographic reconstruction of the radar data, representing reflectivity due to electromagnetic contrast.(lower panel) Schematic of the stratigraphic sequence highlighting the contacts between units and the relevant thicknesses based on the radargram and the tomographic reconstruction [72].

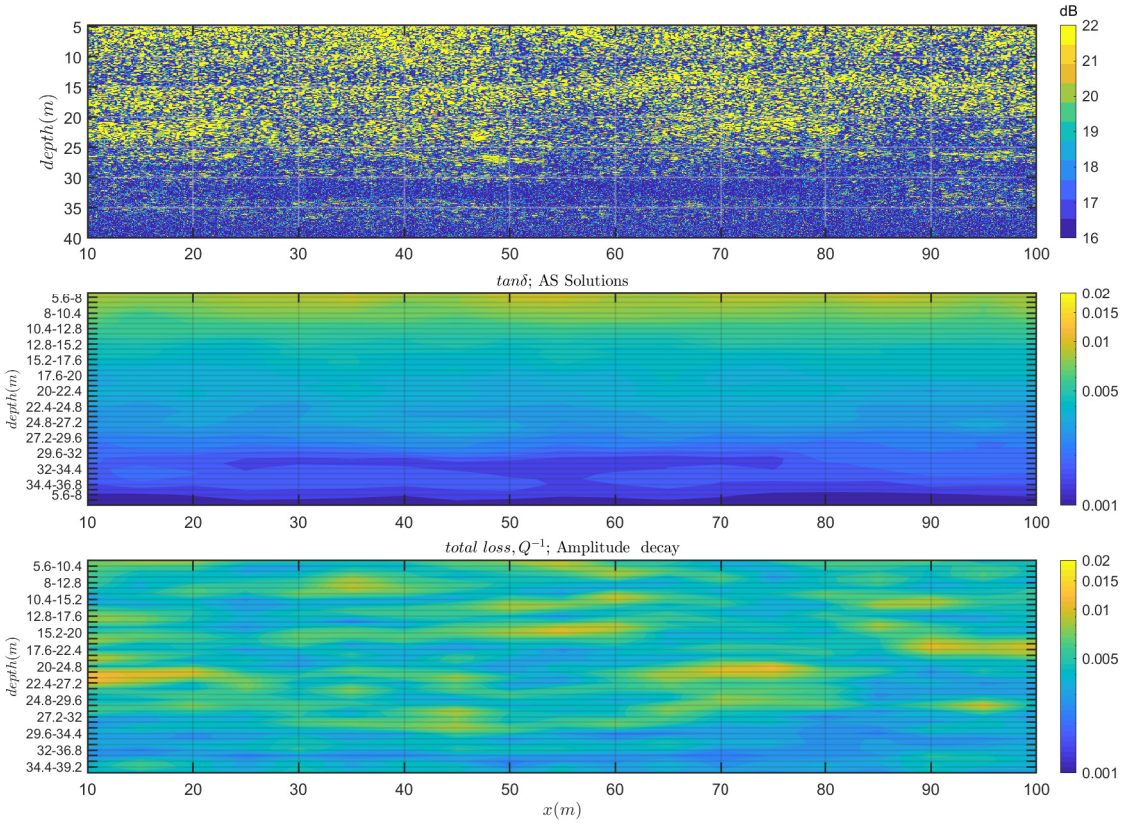

Figure 6.21: The first 100 meters of (upper panel) radargram profile and (middle panel) the reconstructed image of loss tangent and (lower panel) the image of total loss. The two way travel time is converted to depth assuming a constant velocity $v = 0.16\ m/ns$.

6.2 MARSIS Data Analysis

6.2.1 Background

The presence of liquid salty water at a depth of $\sim$ 1.5 km below the surface of the SPLD at Ultimi Scopuli was first inferred from MARSIS data [69] using an inversion method [97], from which two distinct distributions of apparent permittivity values were retrieved: (1) a high value distribution, characterizing the bright area, interpreted as evidence of basal brines; and (2) a low value distribution, detected for the surrounding areas, which is typically attributed to dry and frozen rocks or soil. Figure (6.22) shows a regional map of basal echo power normalized by the median of surface power computed along each orbit. Bright reflections are localized around 193°E, 81°S in all intersecting orbits, outlining a well-defined, 20 km wide subsurface anomaly.

Following this study, other bright basal reflections were detected in the vicinity of the site: Lauro et al., [68] applied a signal processing technique commonly used in terrestrial Radar Echo Sounding (RES) investigations to discriminate between wet and dry subglacial basal conditions, which reinforced the interpretation that the bright basal reflections were due to the presence of basal brines. Figure (6.23) presents a basal intensity map and a basal acuity map in which a strong spatial correlation between two quantities is visible. Then using a probabilistic approach in [69] the basal relative permittivity map is computed in the area where significant number of samples are available (Figure (6.24)).

Knowledge of the physical and thermal properties of the South Polar Layer Deposits (SPLD) is key to constrain the source of bright basal reflections at Ultimi Scopuli detected by the MARSIS radar sounder. In this Part based on data acquired by MARSIS at 3, 4 and 5 MHz a detailed analysis of attenuation is presented. It is shown that attenuation is frequency dependent and its behavior is consistent throughout the entire region. This suggests that the SPLD are compositionally homogeneous at Ultimi Scopuli, and the results are consistent with dust contents of 5 to 12 %. Using these values as input and plausible estimates of surface temperature and heat flux, the basal temperatures is inferred around 200 K: these

are consistent with liquid perchlorate brines within liquid vein networks as the source of the reflections. Furthermore, extrapolation of the attenuation to higher frequencies explains why SHARAD (Shallow Radar) has thus far not detected basal reflections within the SPLD at Ultimi Scopuli.

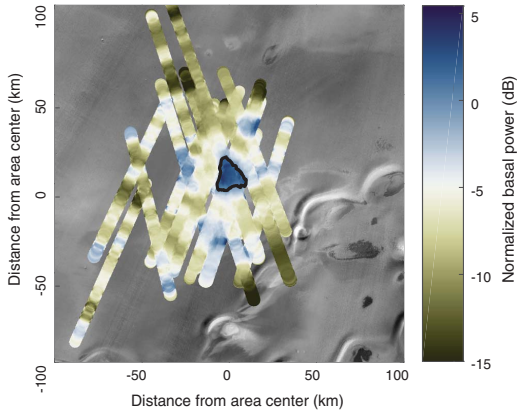

Figure 6.22: Normalized basal echo power at 4 MHz. The large blue area (positive values of the normalized basal echo power) outlined in black corresponds to the main bright area; the map also shows other, smaller bright spots that have a limited number of overlapping profiles [97].

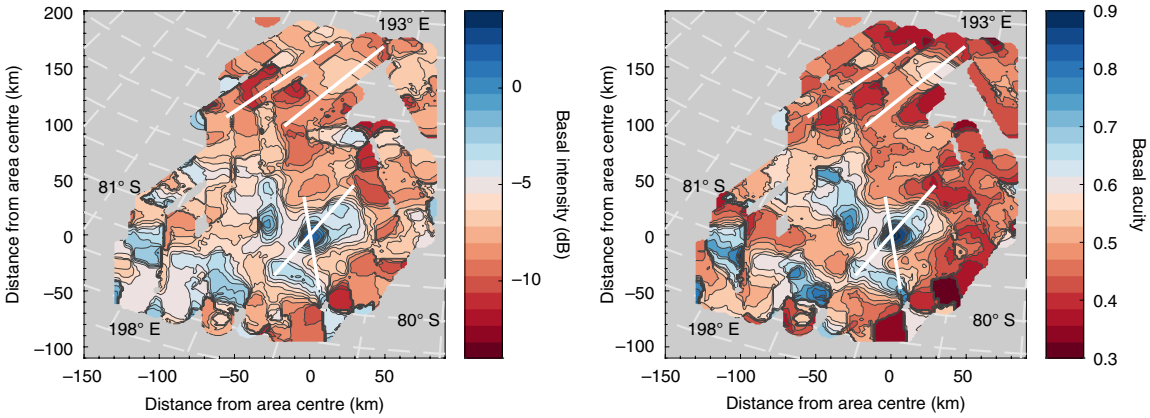

Figure 6.23: Spatial distribution of normalized basal reflectivity and acuity. (left) Normalized basal reflectivity and (right) normalized basal acuity. The quantities are computed from the radar data collected at 4 MHz. Both maps clearly show two distinct areas: an upper southern area characterized by a very low and relatively constant signal intensity, -14 to -6 dB , and acuity, 0.3 to 0.6, and a lower northern area characterized by several patches of high signal intensity, -3 to 4 dB , and acuity, 0.65 to 1 [68].

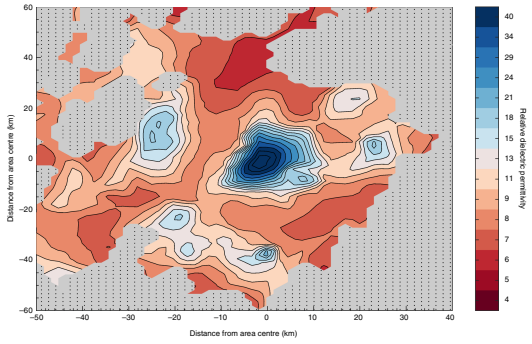

Figure 6.24: Relative dielectric permittivity map computed by inverting the radar data considering all regions where the number of samples is larger than 100. The map only shows the permittivity values retrieved from radar data having acuity values larger than 0.5. Values larger than 15 suggest the presence of liquid water [68].

6.2.2 Loss Tangent Estimation from MARSIS Data: Theoretical Aspect

Loss tangent is the fundamental parameter to estimate the SPLD dust content and signal attenuation. We present here the theoretical aspect of loss tangent estimation from MARSIS data. The aim of the inversion process is estimation of the materials composing the different detected interfaces, including any inclusion of the SPLD and its percentage, by evaluation of the values of the permittivity that would generate the observed radio echoes. The interpretation of MARSIS data requires the discrimination between signals arising from subsurface interfaces and those coming from the surface topographic features, not immediately below the radar, that have the same time delay between transmission and reception (surface clutter) [107]. In the next section, the methodology described here, is applied to radar data, and validity of the results is improved by taking into consideration constraints due to geology, local temperature, and thermal conditions of the observed zones.

We recall that the loss tangent is given by two contributions that behave differently with temperature and frequency. The dielectric response to an oscillating electric field (*e.g.*, a radar wave) is described by the complex effective dielectric permittivity of the medium as in Chapter 1:

$$\varepsilon_e = \varepsilon' - j\left(\varepsilon'' + \frac{\sigma_s}{\omega}\right) = \varepsilon'_e - j\varepsilon''_e \tag{6.1}$$

where as already defined σ_s is static conductivity, $\omega = 2\pi\nu$ is angular frequency. The real part of the dielectric permittivity ε' accounts for energy storage, and the imaginary part accounts for the energy loss due to heat caused by the polarization process (ε'') and free charge carrier migration (conduction, σ_s). The total intrinsic loss is defined through the loss tangent factor $tan\delta$ which is the sum of polarization, $tan\delta_p(\omega)$, and the conductive, $tan\delta_c(\omega)$, term (see Chapter 5):

$$tan\delta(\omega) = \frac{\varepsilon''}{\varepsilon'} + \frac{\sigma_s}{\omega\varepsilon'} = tan\delta_p(\omega) + tan\delta_c(\omega) \tag{6.2}$$

In water ice admixed dust, at MARSIS frequencies, $tan\delta_c$ strongly depends on temperature ($\propto e^{-\frac{E_a}{kT}}$) and decreases with frequency ($\propto 1/\nu$), whereas $tan\delta_p$ is both frequency and temperature independent. In case of a normally impinging wave propagating in a medium delimited by two interfaces (air-SPLD and SPLD-basal material), the ratio between basal and surface echo intensities, P_b and P_s respectively, can be written as (e.g., [69], [96], [107], [64]):

$$\frac{P_b}{P_s} = \frac{\chi_b}{\chi_s}\left[\frac{\left(1-{\rho_s}^2\right)\rho_b}{\rho_s}\right]^2 A \tag{6.3}$$

where χ_b and χ_s account for basal and surface interface roughness, ρ_b and ρ_s are basal and surface Fresnel coefficient, respectively, and A represents the attenuation factor given by:

$$\begin{aligned} A &= \exp\left(-2\int_0^H 2\alpha(z)dz\right) \simeq \exp\left(-2\int_0^H \frac{\omega}{V}\tan\delta\,(z)\,dz\right) \\ &= \exp\left(-2\int_0^H \frac{\omega}{V}\tan\delta_c\,(z)\,dz - 2\int_0^H \frac{\omega}{V}\tan\delta_p\,(z)\,dz\right) \\ &= \exp\left(-2\int_0^H \frac{\sigma_c(z)}{V}dz - 2\int_0^H \frac{\omega}{V}\tan\delta_p\,(z)\,dz\right) = \exp\left(-\frac{\sigma_{SPLD}}{\varepsilon'}\tau - \omega\tan\delta_{SPLD}\tau\right) \end{aligned} \tag{6.4}$$

and consequently equation (6.4) is written as:

$$\frac{P_b}{P_s} = \frac{\chi_b}{\chi_s}\left[\frac{\left(1-{\rho_s}^2\right)\rho_b}{\rho_s}\right]^2 \exp\left(-\tau\frac{\sigma_{SPLD}}{\varepsilon'} - \tau\omega\tan\delta_{SPLD}\right) \tag{6.5}$$

where z is the depth, H is the SPLD thickness, $\tau = \frac{2H}{V} = \frac{2H\sqrt{\varepsilon'/\varepsilon_0}}{c}$ is the two-way travel time, $\tan\delta_{SPLD}$ and σ_{SPLD} are the overall SPLD loss tangent and conductivity, respectively.

Selecting only MARSIS data with high acuity (see next section) (> 0.6) the roughness terms can be neglected: $\chi_b/\chi_s \simeq 1$; in addition, as the temperature expected for the SPLD is very low, conductivity

losses are negligible (Figure 6.25). Under these assumptions, equation (6.5), in logarithmic scale, results in a relation that linearly depends on frequency ν and time delay τ expressed as:

$$\hat{P}_n(\nu,\ \tau) \simeq\ \hat{P}_{n0} - \xi\ \nu\ \tan\delta_{SPLD}\ \tau \tag{6.6}$$

where $\hat{P}_n(\nu,\tau) = 10\ \log_{10}\left(\frac{P_b}{P_s}\right)$, $\xi = 2\pi\ 10\log_{10} e$, and $\hat{P}_{n0} = 10\ \log_{10}\left(\frac{\left(1-{\rho_s}^2\right)\rho_b}{\rho_s}\right)^2$.

Equation (6.6) is used to estimate the loss tangent using a probabilistic approach. The forward model is defined by the $\hat{P}_n = g(m)$ where m is the model parameters $m = (\hat{P}_{n0},\ \log_{10}\tan\delta_{SPLD})$. The estimation was carried out considering the data collected outside the bright areas [see Figure(6.26)], where the time delay τ varies between 13 and 25 μs; the dataset $\hat{P}_n$ was divided in 21 subsets (7 time delay intervals for each frequency) having 2 μs width. For each subset, (ν_i, τ_j), the probability distribution, p_{ij}, of $\hat{P}_n(\nu_i,\ \tau_j)$ is retrieved, and the posterior volumetric probability $\sigma_M(m)$ is computed as the product of the probability calculated for each subset p_{ij}:

$$\sigma_M(m) = p_M(m) \prod_{ij} \sqrt{\frac{\det(g_m + D^t g_d D)}{\det(g_m)}}\ p_{ij}(\hat{P}_n = g(m)) \tag{6.7}$$

where g_m is the metric of the model parameters space, g_d is the metric of the data space, $D_{kl} = \partial g_k/\partial m_l$ and $p_M(m)$ is the prior probability of the model parameters. The loss tangent marginal volumetric probability is computed as:

$$p(\tan\delta_{SPLD}) = \int \sigma_M(m)\, d\hat{P}_{n0} \tag{6.8}$$

considering that the prior probability on $\hat{P}_{n0}$ is described by a uniform distribution:

$$p\left(\hat{P}_{n0}\right) = const, \qquad \hat{P}_{n0} \in [-4,\ 1],\quad dB \tag{6.9}$$

the range of $\hat{P}_{n0}$ was computed assuming a typical rock as basal material with permittivity values $\varepsilon_b \in [8,\ 12]$ and water ice admixed with dust for the SPLD ($\varepsilon_{SPLD} \in [3.1,\ 3.5]$).

Acuity

Acuity is a term that is related directly to the local topography of the interface, and hence, can be used to quantify the roughness and is defined as the ration between maximum power and aggregate power in a time-depth interval [98]:

$$A_c = \frac{max\left\{y_r^2(t)\right\}}{\sum_{t=\tau-T/2}^{\tau+T/2} y_r^2(t)} \tag{6.10}$$

where $y_r(t)$ is the received pulse generated by a reflector located at a time depth τ, and T determines the time interval included in the aggregate.

Dust Volume Fraction Estimation

In an icy mixture, loss tangent value is strongly affected by the dust content and can be considered a reliable parameter to estimate the amount of dust. Given the water ice/dust composition of the SPLD, the overall complex permittivity ε_{SPLD} can be obtained by Maxwell-Garnett formula [128]

$$\varepsilon_{SPLD} = \varepsilon_{ice} + 3 f_v \varepsilon_{ice} \frac{\varepsilon_d - \varepsilon_{ice}}{\varepsilon_d + 2\varepsilon_{ice} - f_v(\varepsilon_d - \varepsilon_{ice})} \tag{6.11}$$

where ε_{ice} is the complex permittivity of pure water ice at 200 K, $\varepsilon_d = 8.8\times(1-j\tan\delta_d)$ ($\tan\delta_d$ is dust loss tangent) is the complex permittivity of the dust and, f_v the dust volumetric fraction. The estimation of f_v is based on a probabilistic approach where the data are described by the estimated volumetric probability $p(\tan\delta_{SPLD})$, the physical model by $g(m) = \mathcal{I}m\{\varepsilon_{SPLD}\}/\mathcal{R}e\{\varepsilon_{SPLD}\}$ (equation 6.11) and model parameters are $m = (\log_{10}(f_v), \log_{10}(tan\delta_g))$. The posterior probability is computed as:

$$\sigma_M(m) = p_M(m) \sqrt{\frac{\det(g_m + D^t g_d D)}{\det(g_m)}}\ p(tan\delta_{SPLD} = g(m)) \tag{6.12}$$

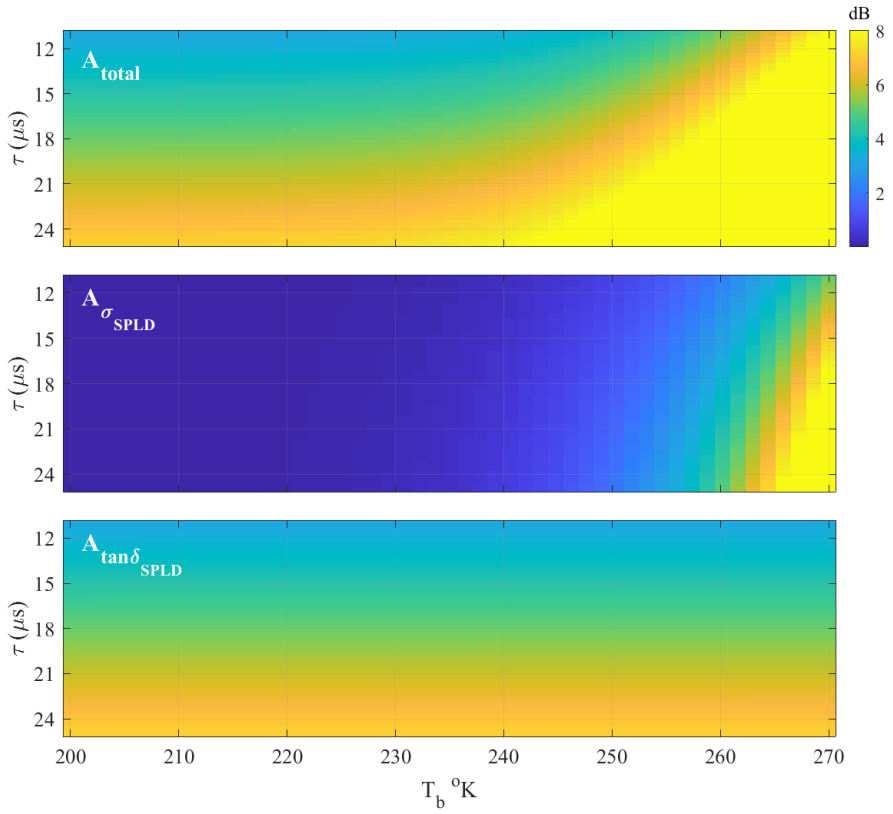

Figure 6.25: Effect of conductivity and dust loss tangent on the signal attenuation in the SPLD. Attenuation computed at 4 MHz as function of the two-way travel time and basal temperature. (upper panel) SPLD attenuation computed using Maxwell-Garnett mixing formula admixing pure water ice with 12 % dust having $\tan\delta_d = 1.7 \times 10^{-2}$. (middle panel) SPLD attenuation neglecting the dust loss tangent. (lower panel) SPLD attenuation neglecting the conductivity of water ice [65].

Given the paucity of dielectric properties measurements on Mars analogue solid samples, we considered loss tangent values of solid lunar samples available in the literature [19] which allow us to establish a lower and upper limit in the dust loss tangent values. In particular, we considered a uniform distribution for the prior probability of the dust loss tangent $p\left(tan\delta_d\right) = const$, $tan\delta_d \in [7 \times 10^{-3}, 4 \times 10^{-2}]$. We note that this range also includes the theoretical value ($tan\delta_d = 2 \times 10^{-2}$) of shergottite according to [90]. It follows that the posterior volumetric probability of f_v is given by:

$$p\left(f_v\right) = \int \sigma_M\left(m\right)\ d\tan\delta_d \tag{6.13}$$

The provided procedure and information are specifically used to explain MARSIS' bright reflections.

6.2.3 Attenuation

MARSIS acquires data at three different frequencies 3, 4 and 5 MHz, which allows the investigations of the frequency behavior of the signals propagating through the SPLD and reflected by the basal material. Absorption of radar signals propagating through a medium causes reduction of the signal intensity (attenuation) that depends on the frequency of traveling signal, length of the path, and the type of material through which the signal propagates. This parameter can be computed by two different approaches, which are dictated by the radar performance and the subsurface properties. In Radio Echo Sounding (RES) studies, attenuation is usually estimated from the measurements of the intensity of the signal reflected by internal layering [79], [77]. This method was tested on MARSIS [10] and SHARAD [119] data. Another technique measures the variation of echo power from a single subsurface interface observed at different depths. Here we combine the latter method with a procedure introduced by Picardi et al., [107] based on MARSIS data acquired at the three operating frequencies, 3, 4, and 5 MHz.

Along the same track, MARSIS simultaneously collects radar data as 3 and 4 MHz pairs, or 4 and 5 MHz pairs, generating two radar profiles for each observation (*i.e.*, each radar track). The dataset used in the present analysis consists of 132 MARSIS raw observations, acquired at Ultimi Scopuli between 2010 and 2019 (Figure (6.22)): 36 at 3 MHz, 132 at 4 MHz and 96 at 5 MHz. Such observations have been collected on a large region, were both bright and non-bright areas were detected [68].

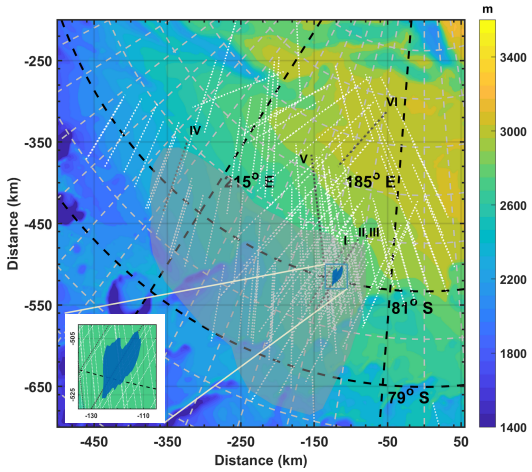

Figure 6.26: Mars Orbiter Laser Altimeter topographic map of the investigated area at Ultimi Scopuli. Dotted lines are MARSIS observations. The blue region indicates the geographic location of the main bright area. The observations in the light-gray shadowed area have not been used for data inversion, as they cross high and low basal reflectivity areas and cannot be assigned neither to bright nor to non-bright datasets. Black dotted lines refer to observations plotted in Figure (6.23): 2654 (V), 10737(II), 12685(III), 12780(VI), 14967(I), 19392(IV). Two tracks (II and III) across the central part of the main bright area, are shown by the same black dotted line on the map. The map is created using MATLAB software and MOLA data [65].

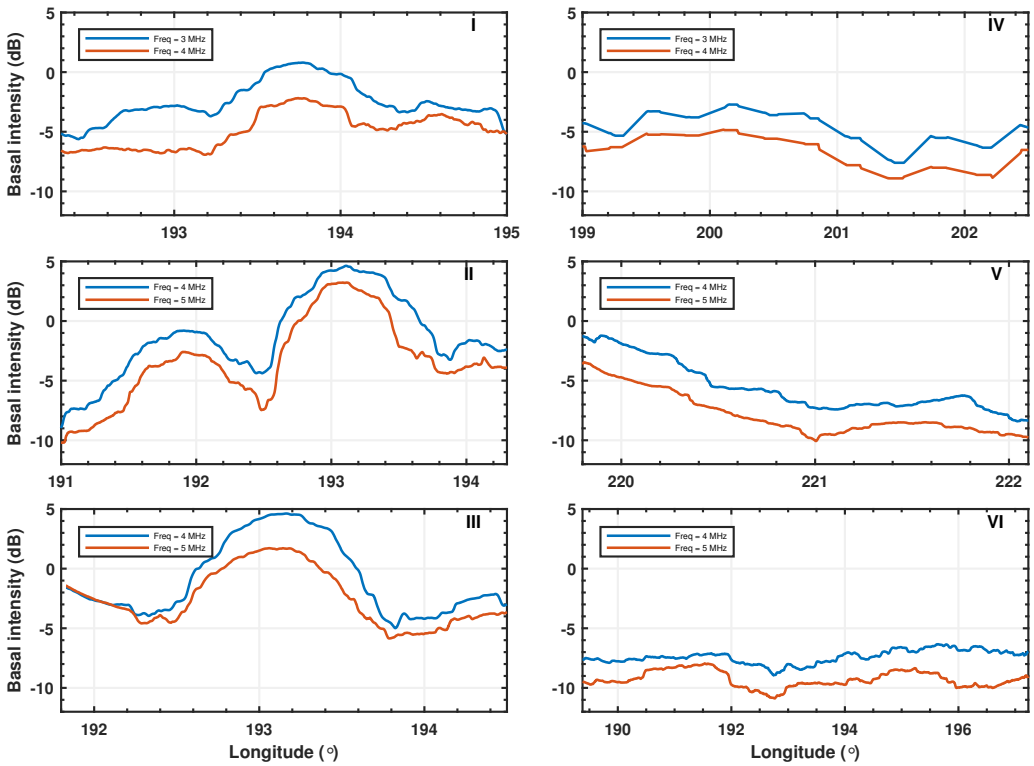

Figure 6.27: Basal normalized echo power measured at two frequencies. The plots refer to observations collected very close (I) or inside (II, III) and outside the main bright area (IV, V, VI) of Fig. 1, after applying an along track average. Note that plots II and III do not totally overlap and start/end at different locations. The difference in basal power between frequencies is approximately constant along track and does not appreciably change between observations, aside from a small segment in observation III.

Regardless of the location, inside or outside the bright areas, the echoes collected at the higher frequency have smaller amplitude than those collected at the lower frequency (Figure (6.27)). This frequency-dependent behavior can be due to: (1) the properties of the SPLD, which affect the propagation of the signals, and/or (2) to the properties of the basal interface, which control the intensity of the reflection. The latter depends on the interface roughness and the dielectric contrast between the SPLD and the underlying material. The contribution of the interface roughness can be evaluated through the computation of the signal acuity, defined as a parameter that measures the smoothness of the interface. We found that the calculated acuity values are uncorrelated (correlation coefficient <0.1) to the values of the difference in echo power between two frequencies: this implies that the roughness effect on the frequency behavior of the reflected signal is actually negligible. Furthermore, because the difference in basal echo power at two frequencies is constant both within and outside the bright areas (Figure (6.27)), we can also exclude a frequency effect due to the basal dielectric contrast, concluding that the frequency behavior of MARSIS data is primarily controlled by the properties of the SPLD.

At the MARSIS operating frequencies, the signal attenuation in water ice is frequency independent [104], unless the ice contains impurities [80], such as mineral inclusions, in which case the attenuation of signal in the mixture reflects the frequency-dependent behavior of the impurities [solid lines in Figure (6.28)]. Vice versa, while attenuation in pure water ice is temperature dependent, presence of dust modifies such behavior, so that attenuation of the radar signal in the mixture becomes temperature independent at low temperatures. Attenuation, A, in the ice-dust mixture that composes the SPLD is given by two contributions, as expressed by equation (6.5):

$$A = A_{\sigma_{SPLD}} A_{tan\delta_{SPLD}} = e^{-\frac{\sigma_{SPLD}}{\varepsilon'}\tau} e^{-2\pi\nu\ tan\delta_{SPLD}\tau} \tag{6.14}$$

The first exponential gives the attenuation due to the conductivity of the SPLD ($A_{\sigma_{SPLD}}$) [cyan dashed line in Figure (6.28)]; it is temperature dependent and frequency independent. The second exponential gives the attenuation due to the polarization phenomena and it is expressed by the loss tangent of the mixture ($A_{tan\delta_{SPLD}}$) [Black dashed lines in Figure (6.28)]; it is temperature independent and frequency dependent.

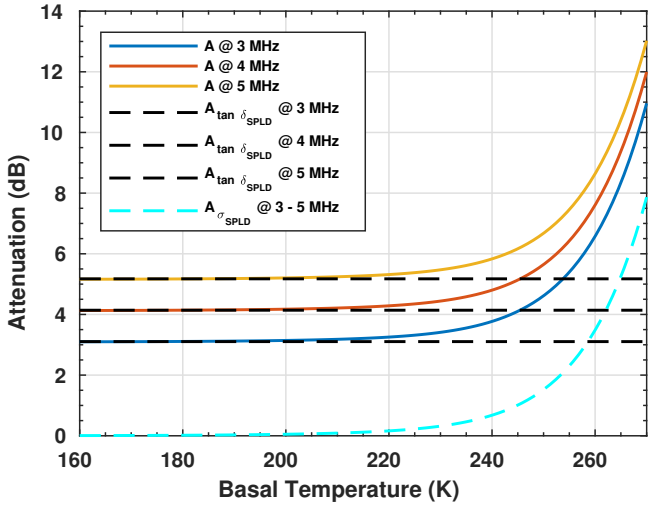

Figure 6.28: Attenuation in an ice/dust mixture at MARSIS frequencies. Solid lines are computed using Maxwell-Garnett mixing formula assuming a 12% dust content and $tan\delta_d = 1.7 \times 10^{-2}$, admixed with pure water ice. Black dashed lines are computed using the same mixing formula and negligible ice conductivity. The cyan dashed line is computed assuming negligible dust loss tangent. All curves refer to 17.5 μs two-way travel time [65].

6.2.4 Loss Tangent and Dust Estimation

The best conditions to invert equation (6.14) and retrieve the loss tangent, are realized outside of the shadowed area (Figure (6.26)): here the two-way travel time τ of the basal reflector varies between 13 μs and 25 μs and the number of samples is large at all frequencies (Figure (6.29)). Moreover, we can assume that the dielectric contrast between the SPLD and the basal material is relatively constant. This assumption is supported by the fact that dry materials have comparable dielectric permittivity.

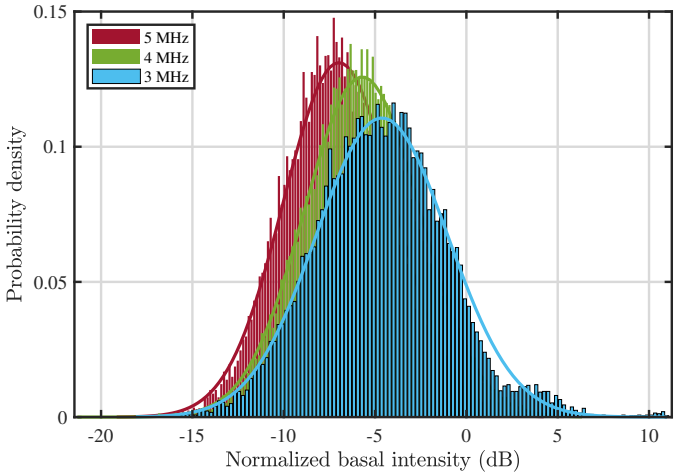

Figure 6.29: Analysis of MARSIS data collected outside the bright areas. Normalized basal power distributions at three frequencies measured for different two-way travel times, in the range $13 - 25\ \mu s$ [65].

The calculated $\tan\delta_{SPLD}$ values range between 1.5×10^{-3} (25th percentile) and 2.6×10^{-3} (75th percentile), with the highest probability density (Figure (6.30)). In the dataset collected in the bright areas (gray shadowed area in Figure (6.26)) the basal reflectivity changes abruptly along track (Figure (6.27)), as discussed in detail in [68] and the two-way travel time τ remains essentially constant. In these conditions it is not possible to apply the method described above, however the subset of data collected in the main bright area [blue region in Figure(6.26)], where the basal reflectivity is quite constant, can still be used to estimate the loss tangent from the difference in echo power at two frequencies [107]. We found values of the same order of magnitude to those estimated outside the bright areas but distributed within a larger range ($1.6\ \times 10^{-3}$ to 5.8×10^{-3}).

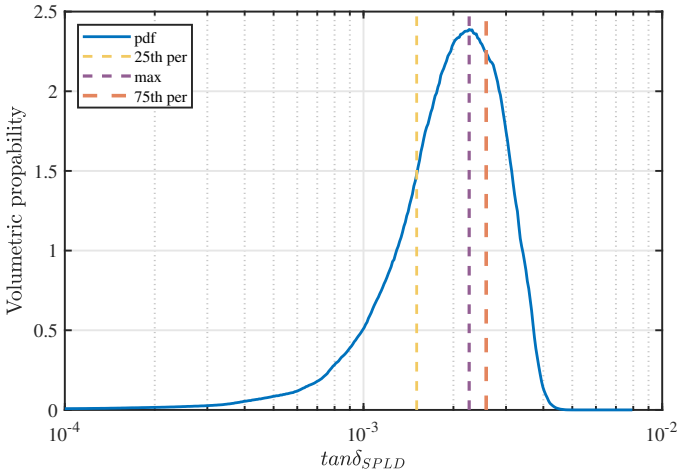

Figure 6.30: Volumetric probability of the estimated SPLD loss tangent obtained by analysis of MARSIS data collected outside the bright areas. The 25th percentile ($\tan\delta_{SPLD} = 1.5 \times 10^{-3}$) and 75th percentile ($\tan\delta_{SPLD} = 2.6 \times 10^{-3}$) is used to calculate loss tangent [65].

Moreover, we detected a very peculiar radar feature inside the main bright area [Figure (6.31) to (6.35)]: a strong multiple reflection visible in several MARSIS observations. In terrestrial radar data strong multiple reflections are caused by very large dielectric contrasts, such as those between ice and liquid water or brines [88]. These features cannot be produced by dielectric contrasts of smaller magnitude, for example at the interface between water ice and frozen soil or solid rocks. Such multiple reflections have been used to compute the loss tangent from the difference in echo power at two frequencies [Figure (6.34) and (6.35)]. The estimated values range between 1×10^{-3} and 4×10^{-3}, that are similar to those computed outside and inside the main bright area.

Assuming a possible range of dust loss tangent, $10^{-4} - 1$, and dust volumetric fraction $0.1 - 100\%$

the probability distribution is computed (Figure (6.36)). Dust volumetric fraction can be obtained from the median of probability distribution. For this purpose, assuming a dust loss tangent ranging between 7×10^{-3} and 4×10^{-2} which are typical values for terrestrial and lunar basalt and shergottite, we estimate that the amount of dust in the water ice is between 5% (25th percentile) and 12% (75th percentile) as displayed in Figure (6.37). In our calculations we did not consider any fraction of CO_2 ice in the SPLD which, even if present, would have no effect on our estimate of the dust content, owing to the fact that the CO_2 ice loss tangent is in the order of 10^{-3}, as shown in Figure (6.38).

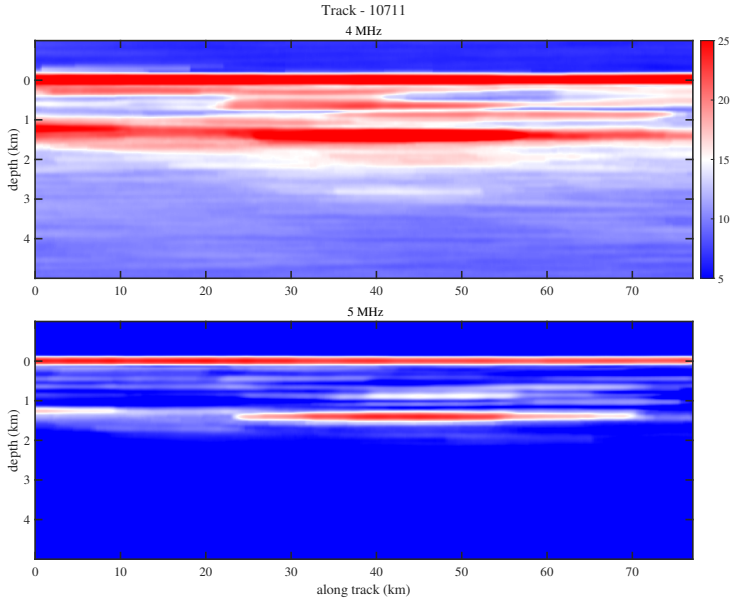

Figure 6.31: Radargram along track 10711. Multiple reflections are visible on the radar images at both frequencies.

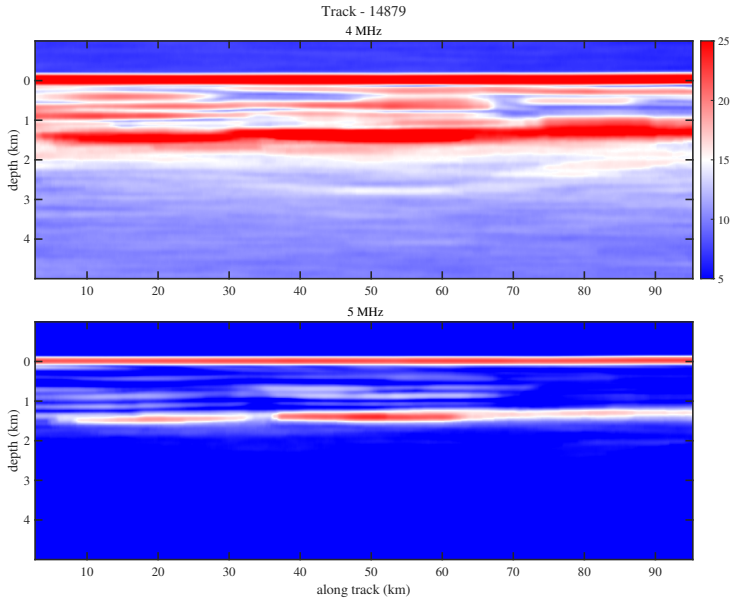

Figure 6.32: Radargram along track 14879. Multiple reflections are visible on the radar images at both frequencies.

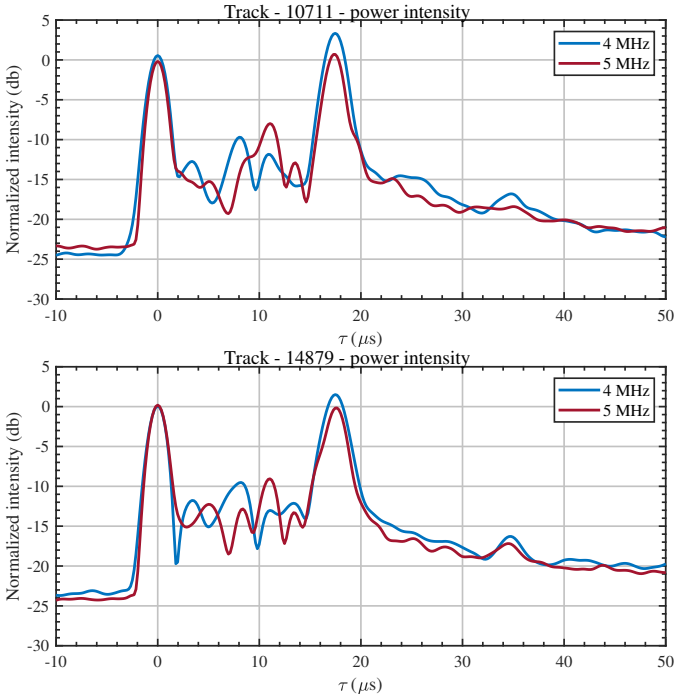

Figure 6.33: Plots of MARSIS traces collected inside the main bright area. The radar traces are extracted from two observations (10737 and 14879) collected at and 4 and 5 MHz. The multiple reflections are clearly visible at a time depth of about 35 μs, which is double the two-way travel time of the basal reflections (17.5 μs).

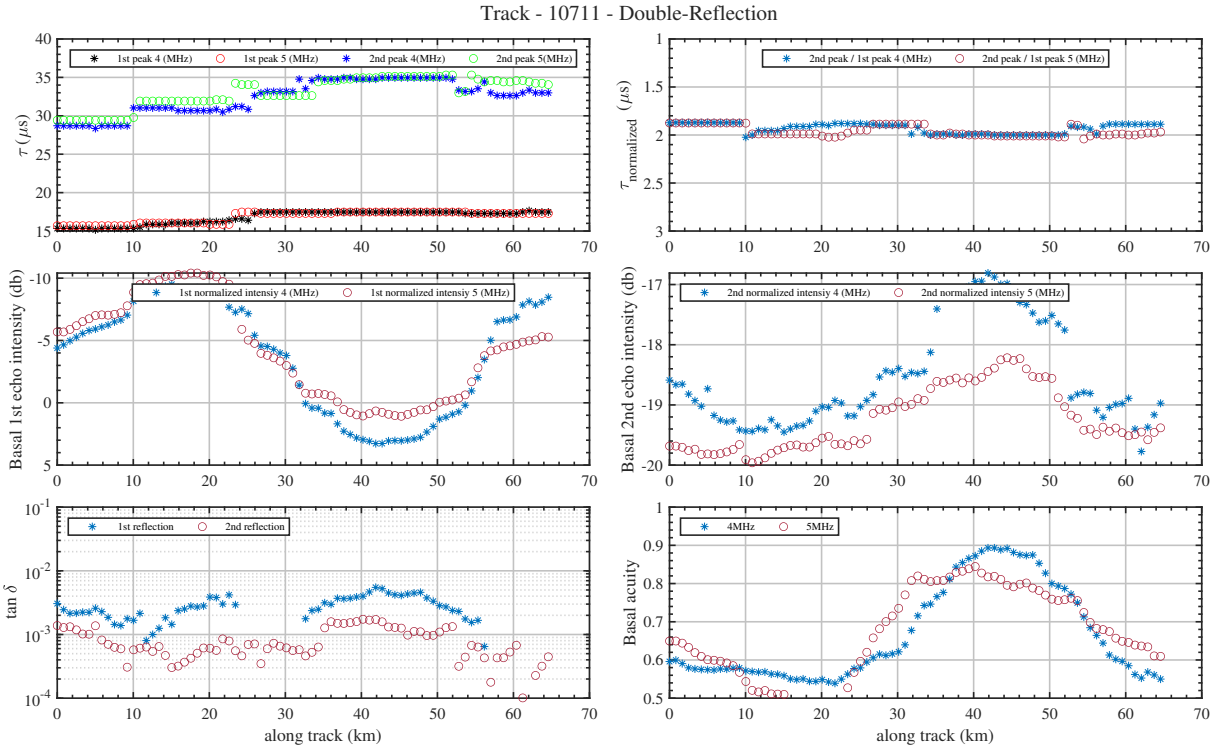

Figure 6.34: The loss tangent estimation from multiple reflections along track 10711. Such multiple reflections have been used to compute the loss tangent from the difference in echo power at two frequencies.

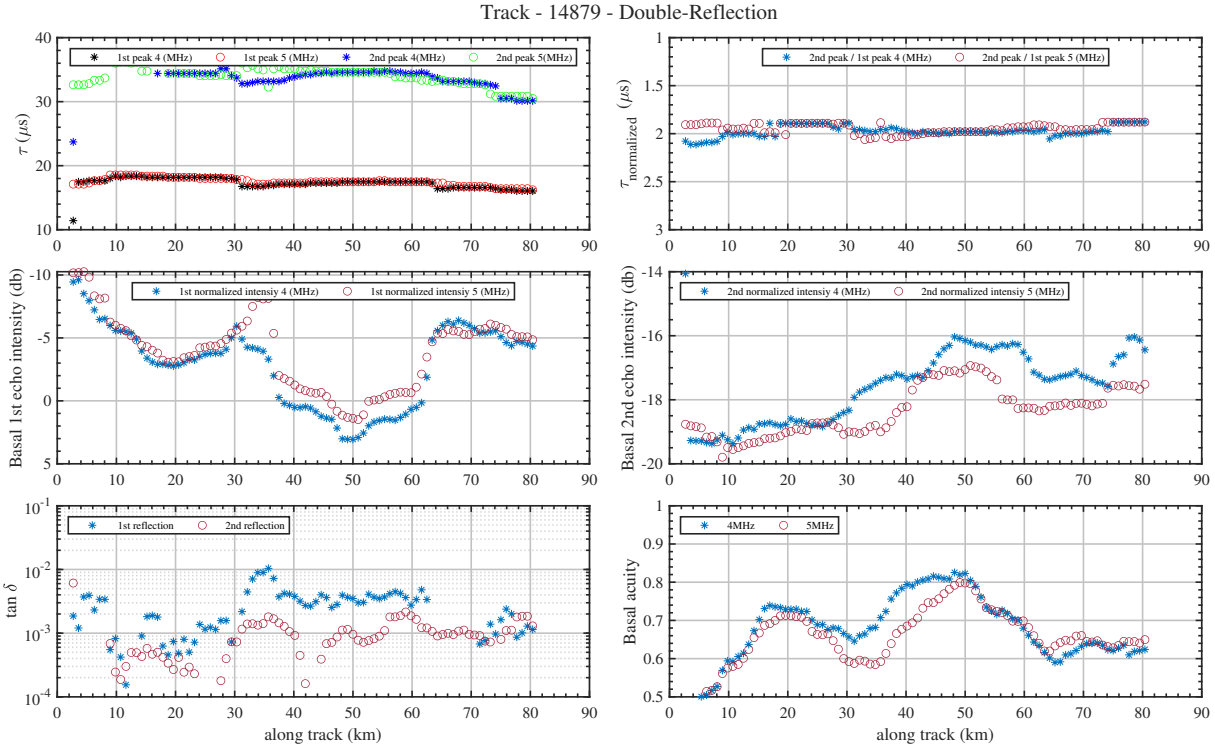

Figure 6.35: The loss tangent estimation from multiple reflections along track 14879. Such multiple reflections have been used to compute the loss tangent from the difference in echo power at two frequencies.

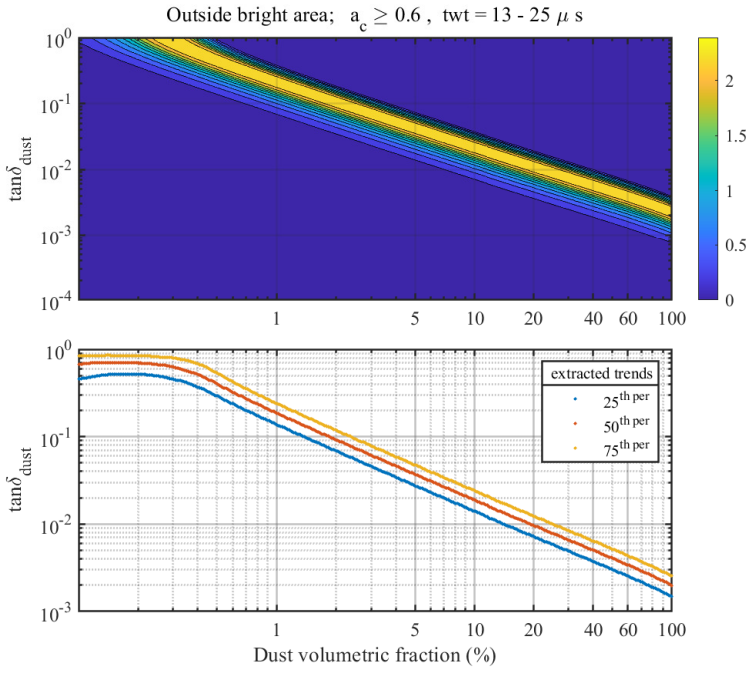

Figure 6.36: Probability distribution of dust loss tangent-dust volumetric fraction. The lower panel shows the extracted percentiles.

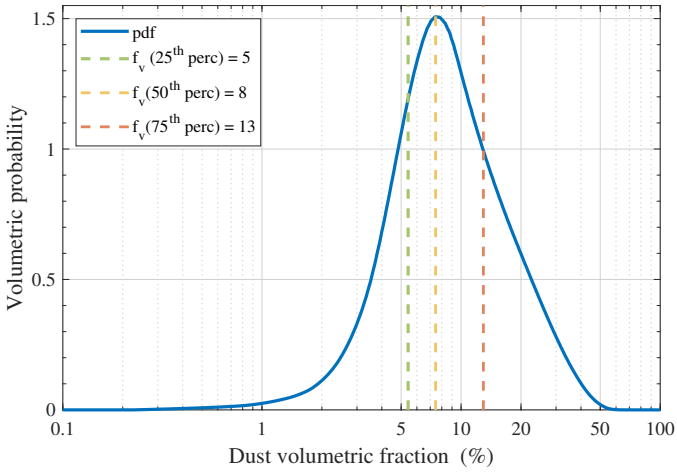

Figure 6.37: Dust volumetric probability obtained from analysis of MARSIS data collected outside the bright areas. The range $5-12\%$, corresponding to same percentiles which $\tan\delta_{SPLD}$ is estimated [see Figure (6.30)].

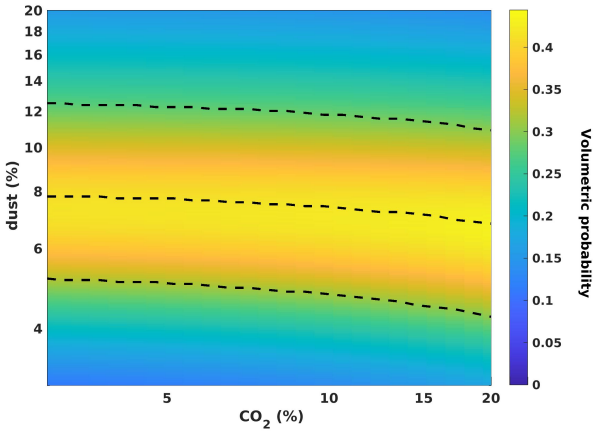

Figure 6.38: Effect of CO_2 ice on the estimation of the dust content in the SPLD. Estimation of dust content for a three-phase system (H_2O ice, $CO2$ ice, mineral dust) where $\varepsilon_{CO_2} = 2.2 \times (1 - j10^{-3})$. The image represents the volumetric probability where dashed black lines indicate the range of dust as a function of the CO_2 content, for $25th$, $50th$ and $75th$ percentiles. Note that the amount of dust only weakly depends on the CO_2 content.

6.2.5 Basal Permittivity Estimation

The loss tangent values estimated here are larger than that previously recognized [68], [97] implying a higher attenuation in the SPLD, which requires new calculations of the values of apparent basal permittivity. In [97], these were frequency dependent, with medians of 30, 33, 22 inside the bright area and 9.5, 7.5, 6.7 outside the bright area, at 3, 4 and 5 MHz respectively. To calculate the revised values of apparent basal permittivity, we applied the inversion procedure published by [69], filtering the data for an acuity value > 0.6 to mitigate the effect of the roughness of the base, consistently with what discussed in [68]. Here, we report the results obtained considering different thermal scenarios for the SPLD and the basal material, assuming a linear temperature increase inside the SPLD, from a fixed surface temperature ($160\ K$) to a variable value at the base of the ice ($160 - 270\ K$). Figure (6.39) presents the probability distribution of basal permittivity-basal temperature in a wide range of permittivity and temperature, inside and outside the bright area, with the marginal pdfs shown in Figure (6.40).

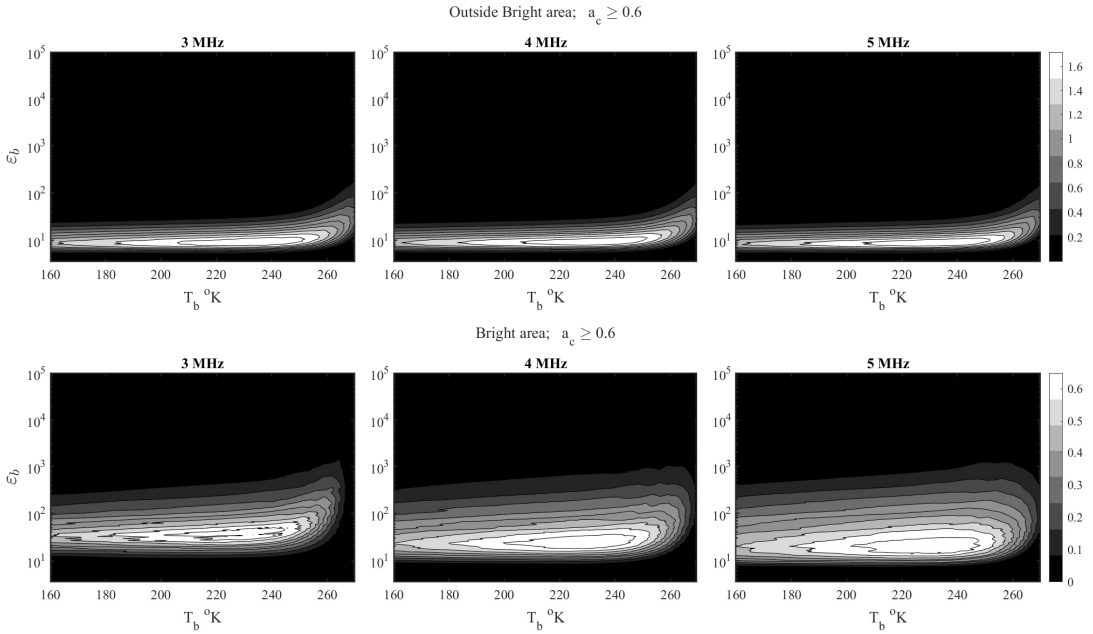

Figure 6.39: Basal permittivity-basal temperature probability distribution.

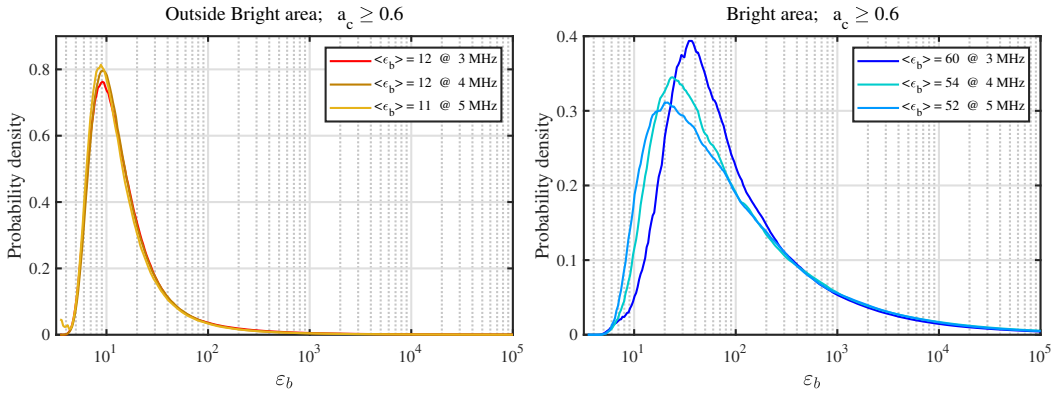

Figure 6.40: Basal permittivity marginal probability density function outside and inside bright area.

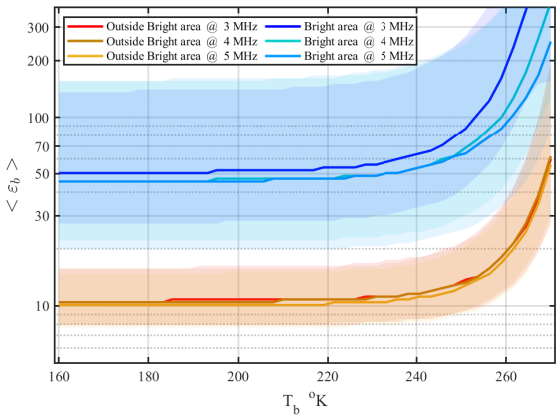

Figure 6.41: Apparent basal permittivity inside and outside the bright area as a function of basal temperature. Solid color lines are the median values at three frequencies, and the color bands indicate the $25th - 75th$ percentile range of apparent permittivity values. Above 230 K the median values estimated for both areas increase towards very high values.

Apparent basal permittivity inside and outside the bright area as a function of basal temperature is presented in Figure (6.41). The permittivity values are generally constant at temperatures between 160 and $\sim 210\ K$, step slightly upward beyond 210 K, and increase abruptly at a $T \geq 230\ K$. Outside the bright areas, the apparent permittivity values range from 7 ($25th$ percentile) to 12 ($75th$ percentile) with a median of 10, regardless of frequency. Inside the main bright area [blue region in Figure (6.26)], the median of the distribution is ~ 40 at all frequencies, with values ranging between 20 ($25th$ percentile) and 120 ($75th$ percentile). The attenuation computed here appears reliable because it corrects the apparent permittivity values computed at three frequencies and makes those values consistent, as they should be once the frequency effect is accounted for. This correction works well both inside and outside the bright areas, and it is evident that the SPLD are compositionally and thermally homogeneous in Ultimi Scopuli. We note that in both areas, the trend of the apparent permittivity with temperature, diverges at values larger than 230 K. Above such temperature the attenuation of the SPLD becomes progressively larger (Figure (6.28)) thus a higher basal apparent permittivity is required to produce the same intensity of the echo. Such high value, estimated outside the bright areas, appears to be unreliable when compared to those typical of dry and cold rocks. We thus conclude that the temperatures of the SPLD at Ultimi Scopuli cannot exceed 230 K, which can then be taken as the upper limit value of basal temperatures.

6.2.6 Discussion

The attenuation estimated in this work shifted upward the apparent permittivity values [see Figure (6.41)] retrieved by MARSIS data inversion with respect to previous calculations [97]. Inside the main bright area, the median of the apparent permittivity distribution is 40 and outside is 10, regardless the frequency. Moreover, in the range $160 - 210\ K$, these values are constant. To identify potential candidates as SPLD basal materials, we compared the apparent permittivity values retrieved at 200 K with those computed from literature data (Figure (6.42)) relevant to subglacial lithologies suggested in recent papers. Each material is represented by a range of values which reflects the variability of data present in the literature, aside from $300mM\ Ca(ClO_4)_2$ brines which are new data. Where possible, we reported values collected around 200 K however, terrestrial basalts were mostly measured at higher temperatures (around 300 K), often with poorly controlled moisture content, and must be considered an overestimation of the corresponding values for Martian temperatures. In fact, in agreement with dielectric behavior of rocks, if such values were measured at lower temperatures (200 K) the entire range would shift leftward towards smaller apparent permittivity values, <15. The comparison clearly highlights that 75% of the apparent permittivity distribution outside the bright areas is compatible with materials having apparent permittivity lower than 15, like terrestrial/lunar basaltic rocks or clay sediments, at Martian temperature. Conversely, 75% of the apparent permittivity distribution inside the main bright area is only compatible with the 300 mM $Ca(ClO_4)_2$ brines, which have reported values of apparent permittivity larger than 20.

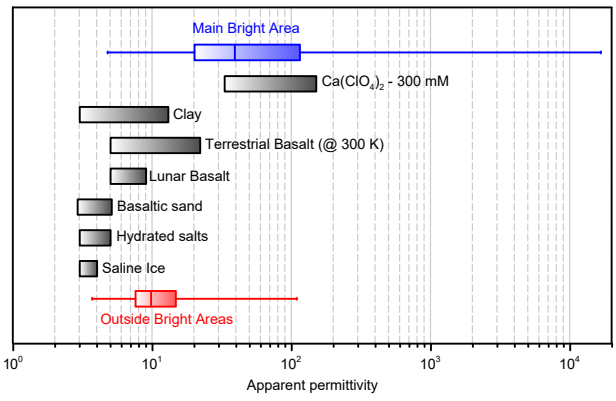

Figure 6.42: Apparent permittivity of various materials compared to those retrieved by MARSIS at Ultimi Scopuli. The box plots indicate the basal apparent permittivity retrieved inside the main bright area (blue) and outside the bright areas (red), where the whiskers represent the minimum and maximum values, the box extremes the lower and upper quartiles, and the center line the median of the data distributions. The grey bars indicate the range of apparent permittivity values for proposed basal materials measured at MARSIS operating frequencies 3,34,38-39,53-56,58-61: calcium perchlorate at $196 - 200\ K$; clays at 200 K; terrestrial basalts at 300 K; lunar basalts at 200 K; hydrated salts jarosite and meridianite at 200 K; saline ices at 200 K-; and basaltic sand at 200 K.

As an aside, our estimation of the attenuation in the SPLD suggests a plausible explanation as to the reason why SHARAD has thus far not been able to penetrate through the full depth of the deposits to detect the basement. Considering a loss tangent of the order of $1.5 - 2.6 \times 10^{-3}$, and neglecting the conductive term due to the low temperature at the base of the SPLD, equation (6.14) can be used to compute the attenuation at SHARAD frequency (20 MHz), which ranges between -14 and-25 dB. Given such values and the dynamic range of SHARAD, the presence of any additional scattering loss due to the structure of the SPLD may prevent the propagation of the signal at large depth, thus explaining why SHARAD cannot see the bright reflectors at Ultimi Scopuli and, more generally, the basal interface below the SPLD [see Appendix C].

Conclusion

In this thesis, a review of the fundamentals of electromagnetic wave propagation in materials, the physics of EM wave propagation, and basic approaches to evaluating electromagnetic wave attenuation from measured georadar data were presented, along with some novel approaches to estimate the attenuation of electromagnetic waves in lossy media. The problem of retrieving attenuation parameters from reflections was addressed by using synthetic GPR data, as well as real data obtained from Earth and planetary bodies (Moon and Mars). Following is a summary of the key conclusions:

1. The estimation of attenuation from reflection data is a challenging problem because scattering and variation of reflection coefficient due to heterogeneity adversely affect received pulse amplitudes. The introduced methodologies could mitigate the effects of scattering and interface heterogeneity by focusing on the frequency-dependent component of attenuation. A statistical inversion approach was used to determine the attenuation parameters from measured data. In addition, the uncertainties in data, which are required for the process of inversion, were evaluated mathematically, while the uncertainty estimates in analysis of geophysical data are often lacking.

2. To improve the reliability of georadar data interpretation, particularly in planetary crusts, it is necessary to know the electromagnetic properties of shallow deposits and analyze signal attenuation. Additionally, these studies are highly dependent on the optimal processing and interpretation of radar echoes, which in turn depend on the dielectric properties of planetary crust.

3. It is possible to map the stratigraphy of planets' subsurface by detecting dielectric discontinuities associated with compositional or structural discontinuities, which can be very relevant for understanding the dynamics and history of the first meters to kilometers.

4. The approaches and techniques presented in this thesis can be also relevant for the quantitative interpretation of radar-sounding data on the Mars, Venus, and satellites similar to the Earth system, such as the Moon, and icy moons. Since access to the site and radar acquisition geometries is limited, these studies are inherently challenging. The results, however, may provide some insights into the description and characterization of the lunar subsurface to better understand its stratigraphy. In general, obtaining the full set of dielectric parameters, such as permittivity, polarization, and conductivity, can greatly improve the interpretation of composition of the planetary subsurface.

5. In terms of comparative planetology, it is well established that Mars exploration is of great significance for a better understanding of the Earth. Present and future Mars missions will primarily use ground penetrating radars to examine the subsurface of the planet. Using such a technique, a number of fundamental questions about the history and evolution of Mars, including finding and locating water, mapping the stratigraphy of various regions on Mars (polar caps, sedimentary deposits, volcanic terrains, etc.), and finding evidence of past or present life may be answered.

6. It was shown that the probabilistic inversion approach is a robust strategy to retrieve the unknowns from GPR data and provides several statistical information.

7. The developed techniques were applied to Chang'E-4 Lunar Penetrating Radar (LPR) data. The results proposed that absorption attenuation (loss tangent) is almost constant along track while total loss presents a large variation that are caused by inhomogeneity and scatters. The average loss tangent and total loss of the investigated deposit were estimated $tan\delta = 0.0039 \pm 0.0023$, $Q^{-1} = 0.0049 \pm 0.0020$, respectively.

8. A different strategy based on the ratio between surface and subsurface power was presented to estimate SPLD loss tangent, using data acquired by MARSIS at 3, 4, and 5 MHz frequencies, resulting in the loss tangent in $tan\delta_{SPLD} = 1.5 \times 10^{-3} - 2.6 \times 10^{-3}$. This value shifted upward the previously reported values of the apparent permittivity. The median of apparent permeability distribution at Ultimi Scopuli is 40 and 10, respectively, inside and outside the main bright area. It was shown that these values are constant and independent of frequency in the temperature range 160-210 K. The SPLD at Ultimi Scopuli were found to be compositionally homogeneous, with dust contents between 5 and 12 per cent. Using these values as input and plausible estimates of surface temperature and heat flux, the basal temperatures were inferred around 200 K.

9. The use of radar experiments is being considered for future missions to asteroids, Mars, Moon, and the icy moons of giant planets, as well as Venus. Despite this, there is still relatively less knowledge associated with this technique than other remote sensing methods like spectroscopy. Our ability to retrieve quantitative information about the planetary subsurface's electrical nature still needs to be improved, and the problems associated with analyzing, interpreting, and inverting radar-sounding data have to be dealt with in deep.

Appendix A

Time-Frequency Distribution

In geophysical data analysis, the concept of a stationary time series is a mathematical idealization that never holds true in reality and is not particularly useful in the detection of signal arrivals. The standard Fourier transform provides the frequency information averaged over the entire signal time interval, however, for non-stationary signals in which frequency components of the signal vary over time and the signal has an obvious oscillatory manner, this information will not be adequate, and the dynamic spectrum or local spectral nature of the observations is required to analyze. Consequently, in our study that involve non-stationary signals, to compute the frequency variation versus time, the time-frequency distribution of data has to be analyzed. Several techniques of examining the time-varying nature of the spectrum have been proposed in the past (e.g., [15]); among them are the S-transform (ST) and short-time Fourier transform (STFT).

S-transform (ST): The $S-$transform is an extension of the continuous wavelet transform and is based on a moving and scalable localizing Gaussian window. The $S-$transform is obtained by convolving a signal with a scaled and shifted wavelet, which is a function that oscillates and decays rapidly in time and frequency. The resulting time-frequency distribution reveals the energy of the signal as a function of time and frequency. The $S-$transform provides frequency-dependent resolution while maintaining a direct relationship with the Fourier spectrum. The continues $S-$transform of a time series $h(t)$ is defined as [132]:

$$ST\left\{h[t]\right\}(\nu,\tau)=\frac{1}{\sqrt{2\pi}}\int_{-\infty}^{+\infty}h(t)|\nu|e^{-(\tau-t)^2\nu^2/2}e^{-j2\pi\nu t}dt \tag{A.1}$$

The $S-$transform has been used in various fields such as speech recognition, medical signal processing, and geophysical signal analysis. For example, in speech recognition, the $S-$transform can be used to analyze the frequency content of a speech signal over time, which can be useful for tasks such as phoneme recognition and speaker identification. In medical signal processing, the $S-$transform can be used to analyze the frequency content of a biological signal such as an electroencephalogram (EEG) or an electrocardiogram (ECG), which can be useful for diagnosing medical conditions.

Short-Time Fourier Transform (STFT): STFT provides the time-localized frequency information for a signal whose frequency components vary over time. The STFT is obtained by dividing a signal into overlapping segments of equal length, applying the Fourier transform to each segment, and then calculating the magnitude of the resulting frequency spectrum. By applying the Fourier transform to overlapping segments of the signal, we can observe how the frequency content changes over time. The $STFT$ of a time series $h(t)$ is given by (e.g., [113]):

$$STFT\left\{h[t]\right\}(\nu,\tau)=\int_{-\infty}^{+\infty}h(t)w\left(t-\tau\right)e^{-j2\pi\nu t}dt \tag{A.2}$$

where $w(t)$ is referred to time analysis window, $STFT\left\{h[t]\right\}(\nu,\tau)$ is a complex function representing the phase and magnitude of the signal over time-frequency and shows the local behavior of $h(t)$ as viewed

through the sliding window $w(t-\tau)$. The $STFT$ determines the time interval in which certain frequencies occur. There is a trade-off between time and frequency resolution. A wide-width time window leads to the better frequency resolution but poor time resolution, and conversely, narrow-width transform results in a better resolution in time in the expense of resolution in frequency. Therefore, increasing the frequency resolution results in a reduction in time resolution and vice versa. In addition, time-window needs to be narrow enough to make sure that the portion of the signal falling within the window is stationary, accordingly, the width of time window must be set appropriately. Window types of Gaussian and Hann perform well in our study.

The STFT has many applications in fields such as audio and speech processing, image processing, and vibration analysis. For example, in audio processing, the STFT can be used to analyze the frequency content of a sound signal over time, which can be useful for tasks such as speech recognition, music analysis, and noise reduction. In image processing, the STFT can be used to analyze the frequency content of an image over time or space, which can be useful for tasks such as image compression and feature extraction.

Appendix B

Chirp Radar and Pulse Compression

A chirped signal has an instantaneous frequency that changes linearly with time, and is reffered to as linear frequency modulation (FM). For a time harmonic pulse it is obtained by the substitution:

$$e^{j\omega_0 t} \longrightarrow e^{j\omega_0 t + \frac{1}{2} j\dot{\omega}_0 t^2} \tag{B.1}$$

hence, for an electric field

$$E(t) = e^{j\omega_0 t + \frac{1}{2} j\dot{\omega}_0 t^2} \tag{B.2}$$

where $\dot{\omega}_0$ is called chirping parameter and represents the rate of instantaneous frequency variation. The chirping parameter is constant and can be positive or negative values that results in an increasing or decreasing frequency, respectively. A chirped Gaussian pulse is obtained by modulating a chirped sinusoid (equation (B.1)) by a Gaussian envelope (e.g., [94]):

$$E\left(t\right) = e^{\left(j\omega_0 t + \frac{1}{2} j\dot{\omega}_0 t^2\right)} \exp\left[-\frac{t^2}{2\tau_0^2}\right] = e^{j\omega_0 t} \exp\left[-\frac{t^2}{2\tau_0^2}\left(1 - j\dot{\omega}_0 \tau_0^2\right)\right] \tag{B.3}$$

where τ_0 is the effective width of Gaussian input pulse. Equation (B.3) in time and frequency domain can be written in the forms:

$$E\left(t\right) = e^{j\omega_0 t} \exp\left[-\frac{t^2}{2\tau_{chirp}^2}\right] \Longleftrightarrow E\left(\omega\right) = \sqrt{2\pi\tau_{chirp}^2}\ \exp\left[\frac{-\tau_{chirp}^2}{2}\left(\omega - \omega_0\right)^2\right] \tag{B.4}$$

where τ_{chirp}^2 is an equivalent complex-valued width parameter.

In radar, the propagation medium is assumed to be non-dispersive (e.g., air), hence, it introduces only a propagation delay. Chirping is used to increase the bandwidth of the transmitted radar pulses, while keeping their time-duration long. The received pulses are processed by a dispersion compensation filter that cancels the frequency dispersion introduced by chirping and results in a time-compressed pulse. The basic system is shown in Figure (B.1). The technique effectively combines the benefits of a long-duration pulse (improved detectability and Doppler resolution) with those of a broadband pulse (improved range resolution).

A typical pulsed radar sends out sinusoidal pulses of some finite duration of T seconds. A pulse reflected from a stationary target at a distance R returns back at the radar attenuated and with an overall round-trip delay of $t_d = 2R/c$ sec. The range R is determined from the delay t_d. An uncertainty in measuring t_d from two nearby targets translates into an uncertainty in the range, $\Delta R = c\ \Delta t_d/2$. Because the pulse has duration T, the uncertainty in t_d will be $\Delta t_d = T$, and the uncertainty in the range, $\Delta R = cT/2$. Thus, to improve the range resolution, a short pulse duration T must be used. On the other hand, the detectability of the received pulse requires a certain minimum value of the signal-to-noise ratio (SNR), which in turn, requires a large value of T.

Linear FM Signals

It is possible, nevertheless, to have a waveform whose envelope has an arbitrary duration T while its spectrum has an arbitrary width B, at least in an approximate sense. The key idea in accomplishing

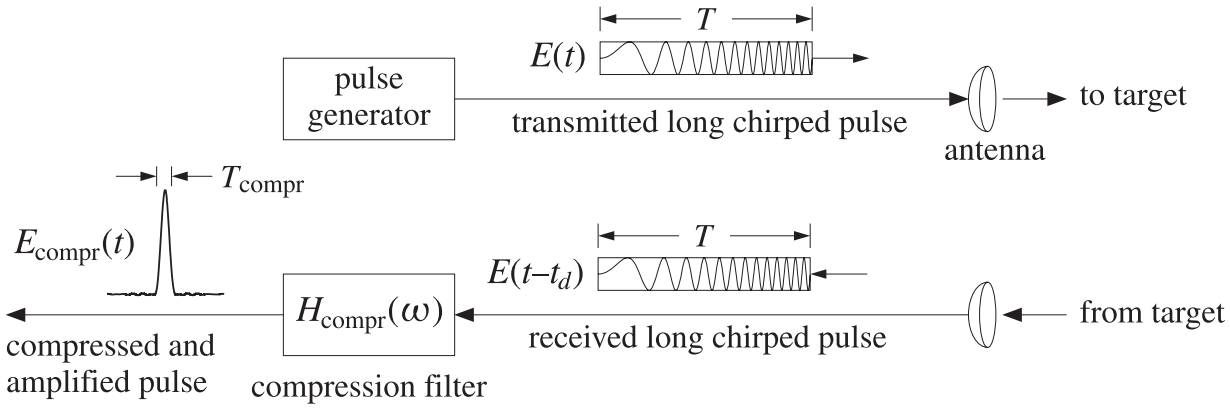

Figure B.1: Chirp radar system (Taken from [94]).

this is to have the instantaneous frequency of the signal vary-during the duration T of the envelope-over a set of values that span the desired bandwidth B. Such time variation of the instantaneous frequency translates in the frequency domain to a spectrum of effective width B. The simplest realization of this idea is through linear FM, or chirping, that corresponds to a linearly varying instantaneous frequency. More complicated schemes exist that use nonlinear time variations, or, using phase-coding in which the instantaneous phase of the signal changes by specified amounts during the duration T in such a way as to broaden the spectrum. A chirped pulse is given by:

$$E(t) = F(t)\ e^{j\omega_0 t + \frac{1}{2} j\dot{\omega}_0 t^2} \tag{B.5}$$

where $F(t)$ is an arbitrary envelope with an effective duration T, defined for example over the time interval $-T/2 \leq t \leq T/2$. The envelope $F(t)$ can be specified either in the time domain or in the frequency domain by means of its spectrum $\hat{F}(\omega)$:

$$\hat{F}(\omega) = \int_{-\infty}^{\infty} F(t)\ e^{-j\omega t} dt \Longleftrightarrow F(t) = \frac{1}{2\pi} \int_{-\infty}^{\infty} \hat{F}(\omega)\ e^{j\omega t} d\omega \tag{B.6}$$

Typically, $F(t)$ is real-valued and therefore, the instantaneous frequency of equation (B.5) is:

$$\omega(t) = \omega_0 + \dot{\omega}_0 t \tag{B.7}$$

During the time interval $-T/2 \leq t \leq T/2$ it varies over the band $\omega_0 - \dot{\omega}_0 T/2 \leq \omega(t) \leq \omega_0 + \dot{\omega}_0 T/2$, assuming that $\dot{\omega}_0 > 0$. Hence, the effective total bandwidth is:

$$B = \frac{\dot{\omega}_0 T}{2\pi} \tag{B.8}$$

Thus, given T and B, the chirping parameter can be chosen to be $\dot{\omega}_0 = 2\pi B/T$. It can be proved that the spectrum of chirped signal $E(t)$ is effectively confined in the band $|\nu - \nu_0| \leq B/2$. The received signal reflected from a target is an attenuated and delayed copy of the transmitted signal $E(t)$, that is,

$$E_{rec}(t) = aE(t - t_d) = aF(t - t_d)\ e^{j\omega_0 (t-t_d) + \frac{1}{2} j\dot{\omega}_0 (t-t_d)^2} \tag{B.9}$$

where a is an attenuation factor determined from the radar equation to be the ratio of the received to the transmitted powers $a = (P_{rec}/P_{tr})^{1/2}$, and t_d is time delay. This signal is then processed by a pulse compression filter that will compress the waveform to a shorter duration.

For an arbitrary envelope $F(t)$, one can derive the following fundamental result that relates the output of the compression filter to the Fourier transform, $\hat{F}(\omega)$, of the envelope, when the input is:

$$E(t) = F(t)\ e^{j\omega_0 t + \frac{1}{2} j\dot{\omega}_0 t^2} \tag{B.10}$$

$$E_{compr}(t) = \sqrt{\frac{j\dot{\omega}_0}{2\pi}}\ e^{j\omega_0 t - \frac{1}{2} j\dot{\omega}_0 t^2}\, \hat{F}(-\dot{\omega}_0 t) \tag{B.11}$$

For example, in the case of a rectangular envelope of duration T:

$$F(t) = rect\left(\frac{t}{T}\right) \Rightarrow E(t) = rect\left(\frac{t}{T}\right) e^{j\omega_0 t + \frac{1}{2} j\dot{\omega}_0 t^2} \tag{B.12}$$

Therefore, the output of the compression filter will be:

$$E_{compr}(t) = \sqrt{\frac{j\dot{\omega}_0}{2\pi}}\ e^{j\omega_0 t - \frac{1}{2} j\dot{\omega}_0 t^2} \left[T \frac{\sin\left(-\dot{\omega}_0 tT/2\right)}{-\dot{\omega}_0 tT/2}\right] \tag{B.13}$$

noting that $\dot{\omega}_0 T = 2\pi B$, we obtain:

$$E_{compr}(t) = \sqrt{jBT}\ \frac{\sin\left(\pi Bt\right)}{\pi Bt}\ e^{j\omega_0 t - \frac{1}{2} j\dot{\omega}_0 t^2} \tag{B.14}$$

In a plain language, a chirp signal, also known as a linear frequency modulated (LFM) signal, is a signal in which the frequency of the signal changes with time. The frequency of the signal increases or decreases linearly with time, resulting in a signal that appears to sweep through a range of frequencies. A chirp signal can be represented by the equation

$$s(t) = A\ sin[2\pi(\nu_0 t + \frac{k_c}{2\tau^2})] \tag{B.15}$$

where A is the amplitude, ν_0 is the initial frequency, k_c is the chirp rate, and τ is time. The chirp rate determines how quickly the frequency of the signal changes over time. If the chirp rate is positive, the frequency of the signal increases with time, while if the chirp rate is negative, the frequency of the signal decreases with time.

Chirp signals have many applications in fields such as radar, sonar, and communications. In radar and sonar, chirp signals are used to determine the distance and velocity of objects by analyzing the time delay and frequency shift of the reflected signal.

Appendix C

Alternative Hypothesis to Martian Subglacial Lake at SPLD

Detailed in Chapter 6, anomalously bright basal reflections have been detected in a 20 km wide area centered at 193 ^oE, 81 ^oS (Ultimi Scopuli) at the South Polar Layered Deposits (SPLD) of Mars by the Mars Advanced Radar for Subsurface and Ionosphere Sounding (MARSIS) onboard the Mars Express spacecraft [97], [68], (Figure C.1). Bright radar returns that are typically produced by materials of high permittivity, led to the initial interpretation that multiple subglacial water bodies are present at the base of the SPLD, whether in a water bearing material or through a coherent water body [97], [68].

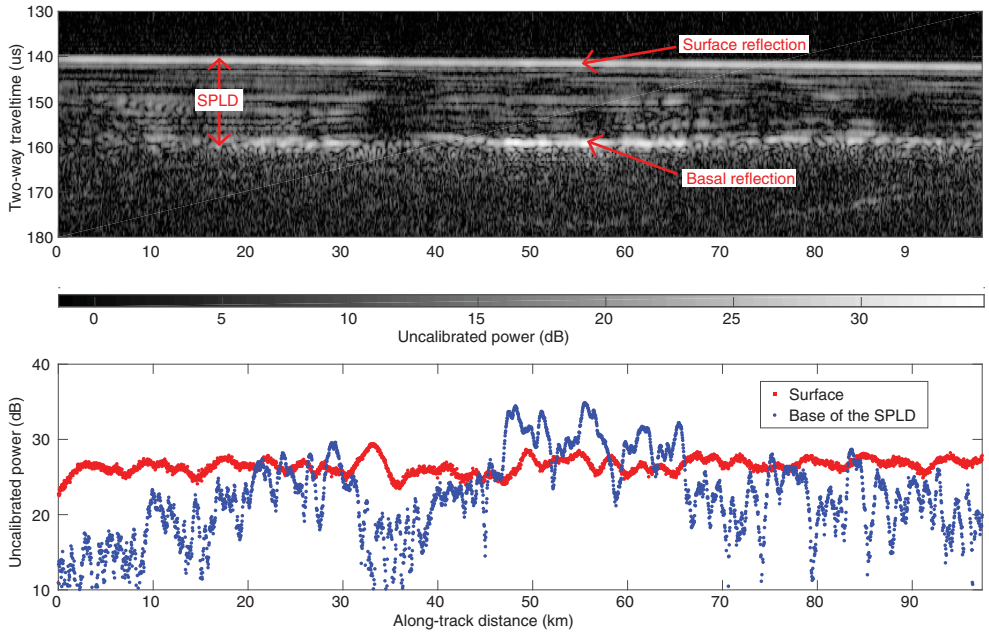

Figure C.1: (Upper panel) Radargram for MARSIS orbit 10737. The bottom reflector at about 160 μs corresponds to the interface between the SPLD and bedrock. (Lower panel) Surface and basal echo power for the radargram [97].

Recently, in several papers, different scenarios, other than presence of liquid water body, have been proposed to explain the source of anomalous bright radar reflection observed in Ultimi Scopuli, categorized as follows:
(1) Clay, metal-bearing minerals, hydrated salts, and saline ices having no negligible conductivity in base of SPLD. A main focus of this hypothesis is a too cold basal temperatures of the SPLD.
(2) The presence of CO_2 deposits within the ice.
Other hypotheses doubt the presence of subglacial lake in term of surface geology context:
(1) no geologic unit nor surface feature consistent with the water body hypothesis is evident Ultimi

Scopuli;
(2) bright reflections of SPLD are attributed to Martian terrain. Another criticism concerns the presence of stable liquid water at the base of the SPLD since the estimated heat flux and basal temperature on Mars are too low to explain the melting of ice.

The following sections summarize the alternative critiquing hypotheses and provide responses to them from recent publications.

C.1 Alternative Hypothesis to Liquid Water

C.1.1 Hypothesis by Smith et al., (2021) [130]

The findings of Sori and Bramson [131] and Ojha et al., [89] suggest that maintaining liquid water beneath the SPLD is unlikely due to the required amount of salt and heat (a localized heat source with the geothermal flux $\sim 72\ mW/m^2$). Accordingly, Smith et al. [130] propose an alternative hypothesis emphasizing the role of electrical conductivity (or the imaginary component of permittivity) of basal material in explaining bright reflections: *hydrated and cold clay-rich deposits at the base of SPLD can create the observed radar response.* Noting that, the smectite clays (a variety of hydrous clay) are known to be present on Mars. Further, Smith et al. [130] demonstrate that the loss tangent and hence imaginary permittivity of 0 for basal material ($tan\delta = 0;\ \varepsilon_b^{''} = 0$) is unrealistic. To take into account higher loss tangents consistent with smectite properties, they describe that lower basal real permittivity values $\varepsilon_b' = 13,\ 14,\ 18$ can be adequate to explain the MARSIS observations, and attribute these lower values ε_b' to the following factors:

I. **Lower basal temperature:** Assuming a basal temperature of 175 ^oK that is obtained from the thermal modeling with a geothermal flux of $10 - 30\ mW/m^2$ [131], the modeled overlying ice will have a lower attenuation, hence the real permittivity ε_b' of basal must be lower to match the modeling.

II. **High-loss nature of the smectite clay:** The reflectivity of a material depends on both the real and imaginary parts of the permittivity, even for a single-simple interface. Therefore, a contrast in either real or imaginary component of permittivity can result in the reflection. Materials with non-negligible conductivity (imaginary component of permittivity) and lower real permittivity values can produce the strong reflections. By including the loss tangent in modeling, Smith et al., concluded that the lossy materials with low ε_b' values can produce the bright reflections in SPLD.

As a conclusion, they suggest that thin layers of hydrated smectites at cryogenic temperatures [1] are sufficient to produce the bright reflections observed in MARSIS data, without the need for a heat source, salt, or melting hysteresis, as is the case with hypersaline liquid brines. Smith et al., further support this theory by pointing out that semectites are abundant on Mars, even at the margin of the SPLD.

C.1.2 Hypothesis by Bierson et al., (2021) [8]

For an ice layer of 1.3 km thickness and conductivity $10^{-6}\ S/m$, Bierson et al.,'s modeling with multiple frequency modes suggests that if bright reflections are caused by contrasts in dielectric permittivity, all frequency modes would have the same reflection power (left most region of Figure C.2). However, if it is due to a conductivity contrast, the 5 MHz return should be 1 dB weaker than the 4 MHz return (boxed region on Figure C.2), that matches the difference between the median reflection strengths measured by Orosei et al. [97].

Another proposed process that could produce a frequency-dependent return strength without a difference in the basal reflector, is attenuation within the SPLD itself. A decrease in the strength of higher frequencies is preferentially caused by attenuation, that is consistent with the trend in MARSIS observations. The main problem with this interpretation is that if the attenuation is strong enough to produce a 1 dB difference between the 4 and 5 MHz modes, it would be too strong for any basal reflection to be brighter than the surface reflection. In addition, the authors extend their modeling to the SHARAD frequency modes, 15-25 MHz, resulting in the reflection strength 8 dB weaker than that of 4 MHz. In

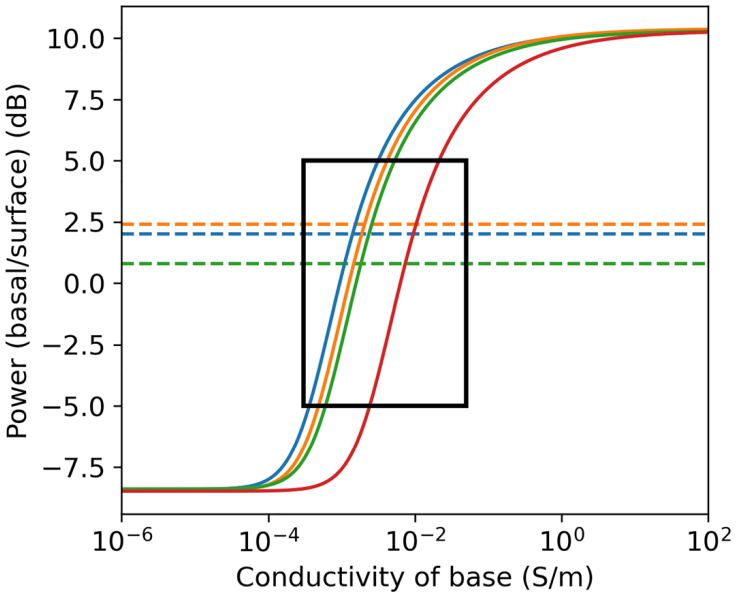

Figure C.2: Reflection power as a function of the conductivity of the basal layer [8].

this context, it is important to consider how significant is the lake of detection by SHARAD. Afterwards, Bierson et al., propose three candidate configurations for conductive basal interfaces; (1) hypersaline brines, (2) saline ice, and (3) conductive minerals. Then the candidate 1 and 2 are excluded by following reasoning: according to Sori and Bramson [131] even for a hypersaline brine to be present, under the most favorable compositional considerations, there must be a localized and recent heat source with a geothermal heat flux of $Q = 72\ mW/m^2$, while there are no evidences suggesting that this heat source is present. Rather, a global average of $Q = 19\ mW/m^2$ with regional variations between $Q = 14 - 25\ mW/m^2$ is calculated. This range of geothermal heat flux on Mars, estimates $\sim 171 - 176\ K$ for basal temperature of SPLD. According to them, at too cold temperatures saline ice may not be sufficiently conductive to explain the observed reflection power, hence the saline ice scenario is not plausible .

Finally, Bierson et al., conclude that conductive minerals with low real permittivity values can produce the bright radar reflections observed by MARSIS. The authors point out that if the reflection is solely due to a difference in permittivity, the difference in power between the MARSIS observing frequencies could still be explained by frequency-dependent attenuation in the SPLD.

C.1.3 Hypothesis by Lalich et al., (2022) [61]

A one-dimensional radar sounding model developed by Lalich et al., demonstrates how thin layer interferences can produce strong reflections similar to those observed by MARSIS without requiring liquid water, brines or any materials uncommon on Mars. Their layered model is composed of four materials: free space, water ice, CO_2 ice and basalt (Figure C.3). A laboratory-measured permittivity is assigned to each layer. The dusty water ice thickness in their simulation is 1.4 km with the 10 % of basaltic dust volume fraction in consistency with SPLD in the region including bright reflectors. The lowest layer is composed of basaltic rock that is semi-infinite half-space.

Since a large region of SPLD is composed of solid CO_2 ice up to a few meters thick, a 2 m thick layer of surfacial CO_2 ice is included in layered model as well. However, the simulation results propose that such a surficial CO_2 ice layer has little effect on reflections observed by MARSIS in the bright region. The simulation shows that a single CO_2 ice layer at the base of SPLD could produce a powerful reflection similar to those observed in bright region observed by MARSIS at 4 and 5 MHz frequencies. However, a single CO_2 ice layer at the base cannot explain the brightest observed reflections. The authors assume a basal temperature 175 ^{o}K in the simulation that is lower than that used by Orosei et al. [97] i.e., 205 ^oK. At lower temperature the overlying ice absorbs less energy resulting in more powerful reflections from

[1] Very low temperatures defined as from $-150\ ^oC$ to $-273\ ^oC$

the base.

Their three-basal layer model could create reflections with local maxima. This leads the authors to conclude that constructive interference between multiple subsurface layers with much lower permittivities than liquid water cause the strong reflection. Finally, it is suggested by Lalich et al. that this phenomenon can explain the bright reflections observed by MARSIS without requiring liquid water.

In any case, the authors acknowledge that their interpretation could be weak due to a requirement for specific layer thicknesses and relatively uncommon materials although still known to present in the polar cap.

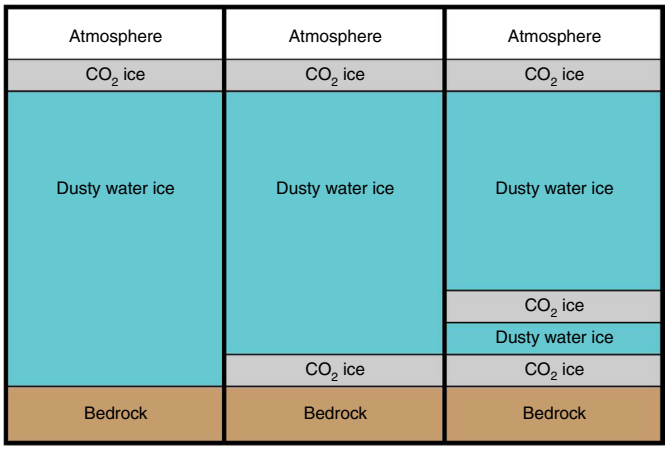

Figure C.3: Schematic diagrams of the three simulated scenarios by Lalich et al., [61].

C.1.4 Hypothesis by Khuller and Plaut, (2021) [57]

Khuller and Plaut generate detailed maps of elevation, topography, and reflected radar power of the basal interface by using around 44,000 points. These maps are used to determine the volume and thickness (ranging from 0 to 3.7 km) of the SPLD. In the produced maps, they indicate that areas with a basal echo power greater than surface power are not located only in Ultimi Scopuli but are distributed throughout the SPLD, and hence, attribute the anomalous bright basal reflections to the processes that are not limited only to Ultimi Scopuli. Additionally, some bright reflectors on the computed maps are near the surface where the average annual surface temperature is too low to permit even supercooled perchlorate brines to remain liquid. These findings lead Khuller and Plaut to debate the possibility of presence a stable subglacial water body in Ultimi Scopuli.

C.1.5 Hypothesis by Grima et al., (2022) [41]

Grima et al. [41] propose a forward approach with the aim to infer what would be the ratio of subsurface to surface power P_{ss}/P_s if the existing Martian terrains, as measured by MARSIS, were covered by an ice sheet with a thickness similar to the SLPD at the location of the bright basal reflector. Their results show $0.3\% - 2\%$ of the surface, some of them located in volcanic-related terrains, could produce basal reflections of magnitude similar to the SPLD measurements ($Pss/Ps > 5\ \ dB$), assuming 10% impure ice. They dispute the water-bearing material or subglacial lake as the polar basal material, suggesting that the bright reflection of SPLD results from Martian terrains. Most of these bright regions are subdivisions of larger volcanic structures, but they are not limited to a specific geologic period.

C.1.6 Hypothesis by Landis and Whitten, (2022) [62]

Landis and Whitten map the surface of the SPLD immediately above and surrounding the putative lakes in order to provide a geologic context for the interpretation of bright basal reflectors. The authors use Thermal Emission Imaging System daytime IR, Context Camera, and High Resolution Imaging Science Experiment data to characterize geologic units and typical surface roughness. They found evidence of

multiple geologic units containing features caused by CO2 and aeolian-related processes, but no geologic unit or surface feature appears to be uniquely associated with the mapped SPLD subglacial lake.

C.2 Disputing the Critiquing Hypotheses

C.2.1 Disputing the Hypothesis by Bierson et al. (2021), [8]

Mattei et al., [81] based on published data, simulations, and new laboratory measurements demonstrate that at MARSIS frequencies and Martian temperatures highly conductive material, clay, hydrated salts, and saline ices do not generate strong basal reflections, hence, suggesting perchlorates and chlorides brines as plausible candidates that exhibit a strong dielectric response at much lower temperatures than other materials. This study is summarized as follows:

Firstly, Figure(C.4) shows that in areas where hydrated minerals have been discovered and/or where they are particularly abundant, data collected by MARSIS and SHARAD, do not present any indication of bright reflections coming from the surface.

Next, temperature has a dominating effect on the dielectric properties of **clay and clay sediments**. This is confirmed by a set of measurements conducted on some good analogs for Martian clays, including clay sediments at different water content, clay content, and different mineralogy. Figure (C.5, left) reports the experimental results as apparent permittivity vs. temperature at 4 MHz, allowing a direct comparison with the basal apparent permittivity retrieved by MARSIS [97]. It is obvious that the MARSIS threshold value is only obtained at high temperatures ($\geq 250^o$ K). All clay samples show a similar trend at 200^o K and the apparent permittivity ranges between 4.0 and 6.4 and slightly increase up to 224^o K, at which point the values start to diverge. At about 230^o K, values of apparent permittivity range between 6 and 10. MARSIS threshold values are reached at temperatures from 252^o K to 268^o K for different samples. At a temperature of 290^o K the apparent permittivity reaches values ranging between $10^2 - 10^3$. It follows that very low temperatures, such as those commonly inferred at the base of the SPLD ($\leq 200^o$ K), are totally inconsistent with the hypothesis that clay sediments can generate a dielectric contrast with the SPLD large enough to obtain bright basal echoes. Thus, The hypothesis that clay sediments are capable of generating dielectric contrasts with the SPLD, large enough to produce bright basal echoes is totally inconsistent with extremely low temperatures, such as those commonly inferred at the base of the SPLD ($\leq 200^o$ K).

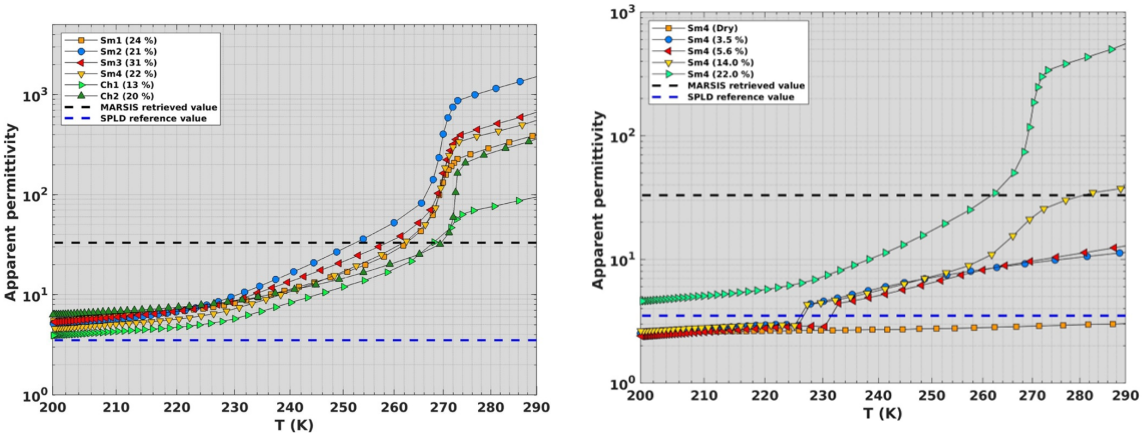

Figure C.5: (left) Apparent permittivity computed from real and imaginary parts measured at 4 MHz as a function of temperature on four smectite-rich (Sm) and two chlorite-rich (Ch) sediments having different water content. (right) Apparent permittivity of smectite sample Sm4 versus temperature for different water contents. Dry sample shows an apparent permittivity value around 3.0 which does not appreciably change with temperature. Black dashed line indicates the threshold retrieved by MARSIS, and blue dashed line shows the SPLD ice permittivity value ($\varepsilon_{ice} \approx 3.5$) used to compute the apparent permittivity.

The low water content ($2.3 - 3.1$ wt % H_2O) and cold temperatures on Mars have made clay minerals a concern for radar attenuation, but not as a strong surface reflector, capable to prevent radar signals

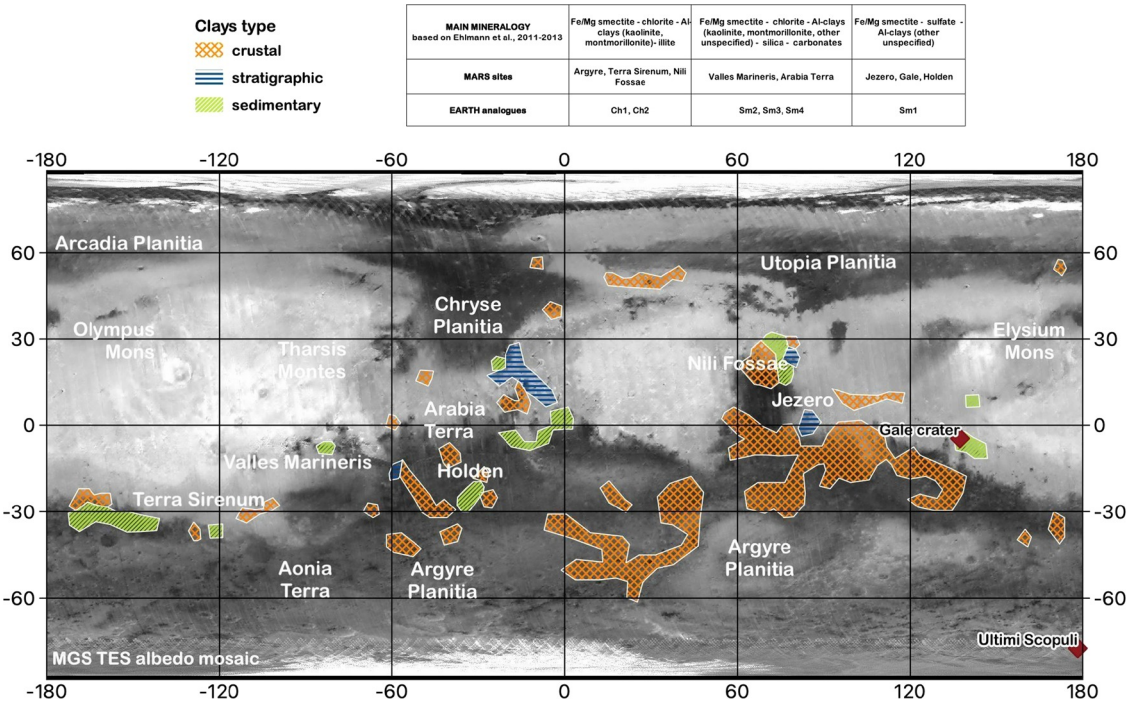

Figure C.4: Distribution of clays on Mars. Crustal clays mostly contain Fe-Mg smectite and chlorite as evidence of bedrock alteration (taken from [81], mapped based on data [28] and [27]).

penetrating through the surface. These observations are in good agreements with literature data and with the experimental results in Figure (C.5, right), which show that **hydrated salts and dry or low water content clay**, do not generate strong radar reflections on the Martian surface or at the base of SPLD (Table C.1). Consequently, even if large quantities of hydrated salts or dry clay are present in the basal sediments, the apparent permittivity will be similar to or even lower than that of the SPLD ice (Figure (C.5), right). Up to 230^o K, samples with 3.5, 5.6 and 14% water content exhibit the same value of apparent permittivity. Note that the discontinuity between 220^o K and 230^o K is due to the fact that in this temperature range the reflection coefficient approaches 0 since the permittivities are almost equal (Figure (C.5), right).

Table C.1: Real and imaginary parts of permittivity of some hydrous minerals of interest for Mars [81].

Hydrated salts	ε'_r	ε''_r	**Frequency MHz**	**Temperature K**
Meridianiite	4.7	~0	1	200
Jarosite	3.07	~0	1	180-296
Gypsum	6.4	0.01	1	298
Anhydrite	6.9	0.06	1	298
Dry clay				
Chlorite	7.4	1.5	1	298
Kaolinite	4.6	~0	30	298
Nontronite	3.7	0.08	10	220
Ca-montmorillonite (STx-1b)	3.6	0.08	10	220
Ca-bentonite	3.5	0.07	1	298

In addition, dielectric measurements of $Mg(ClO_4)_2$ and $CaCl_2$ brines at Martian subglacial conditions exclude salty ice as a source of MARSIS bright reflections. Totally, frozen brines having high concentration of salts exhibit very low apparent permittivity, because salt grain inclusions do not appreciably change

the dielectric properties of the ice at MARSIS frequencies (Figure C.6A). The apparent permittivity at low salt concentration (100 mM) does not exceed $10 - 15$ at the eutectic temperature. However, the results (Figure C.6, B) suggest that a few 100 s mM of salt would probably be enough to reach the MARSIS threshold value. Vice versa, given the very large apparent permittivity values measured for both $Mg(ClO_4)_2$ and $CaCl_2$ brines at high salt concentrations (Figure (C.6, A)), it is likely that a few tens percent of liquid brine volume fraction in the ice or in the soil would enhance the apparent permittivity well above the value obtained from MARSIS (Figure (C.6, A) and Figure (C.7)). MARSIS bright basal reflections observed in Ultimi Scopuli [97], [68] can therefore be explained by $Mg(ClO_4)_2$ and $CaCl_2$ brines alone, based on their dielectric behavior. It was argued that the eutectic temperatures of brines are too

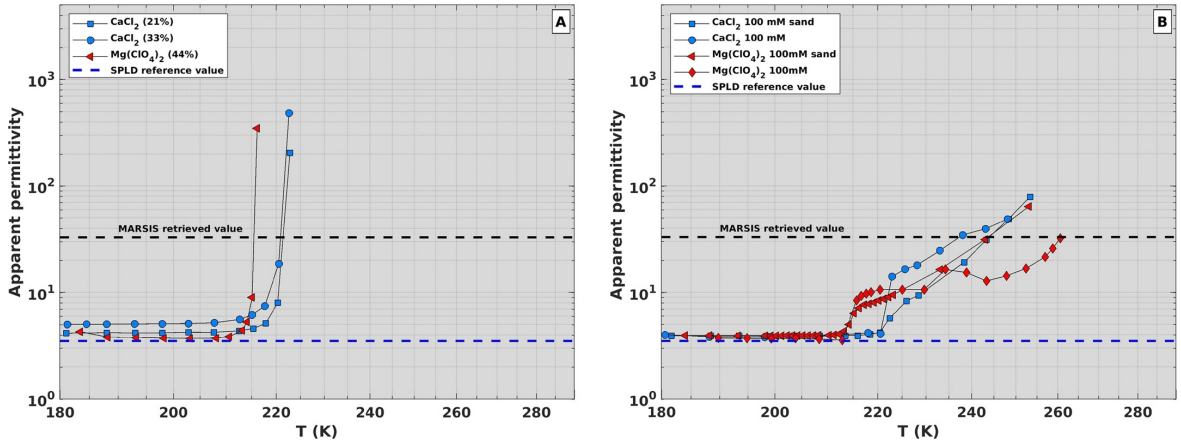

Figure C.6: Apparent permittivity of brines at 4 MHz as a function of temperature.

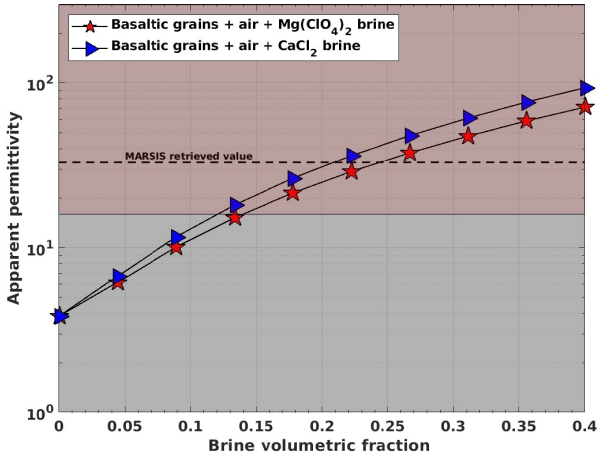

Figure C.7: Effect of brines contents on the apparent permittivity of a soil from CRIM simulations at 4 MHz.

high to explain the presence of liquid water at the base of the SPLD [131]. Previous studies have found that salts with large freezing point depressions also have large metastable eutectic temperatures that can be 10s of degrees lower than their eutectic temperature [115], [140]. Additionally, measurements have proven that a mixture of Ca and Mg perchlorate has eutectic temperature well below those of the single salts [87], and the brines can remain in a supercooled state at temperatures as low as 150 K [141]. Other than metastability, the thermal conductivity of SPLD deposits is another poorly constrained parameter that directly affects basal temperatures estimates: Sori and Bramson [131] argue that: under the current (and most likely) value of heat flux at the south polar region of Mars, the temperature at the base of the SPLD in Ultimi Scopuli is $\leq$180 K. Their model, however, relies on a highly conductive SPLD that has yet to be demonstrated, conclusively. In fact, small variations in estimated values of conductivity of the SPLD materials could dramatically increase basal temperatures to values equal to or even above those of perchlorate brine eutectics. It was subsequently suggested that a high geothermal gradient,

such as that produced by a magmatic chamber at depth, is required to reach the eutectic temperatures of concentrated salt solutions at the base of the deposits [131]. There is, however, no evidence of an anomalous geothermal gradient in the region, so this scenario is disputed [68].

Concept of Apparent Permittivity
MARSIS data lack the information on the signal polarity, and therefore, MARSIS reflectivity data cannot separately compute the real and imaginary parts of the complex permittivity. Assuming that the loss term of the first layer (here, SPLD) is negligible ($\varepsilon_1'' \approx 0,\ \varepsilon_1 \approx \varepsilon_1'$) it is possible to estimate the dielectric properties of the second layer introducing the concept of the apparent permittivity under the assumption that the permittivity of the second layer is larger than that of the first layer. The apparent permittivity that is a real quantity is expressed as [81]:

$$\varepsilon_a = \varepsilon_1 \left[\frac{1+ \mid \Gamma_{12} \mid}{1- \mid \Gamma_{12} \mid}\right]^2 = \varepsilon_1 \frac{\varepsilon_1 + \mid \varepsilon_2 \mid + \sqrt{\varepsilon_1^2 + \mid \varepsilon_2 \mid^2 - 2\varepsilon_1\varepsilon_2'}}{\varepsilon_1 + \mid \varepsilon_2 \mid - \sqrt{\varepsilon_1^2 + \mid \varepsilon_2 \mid^2 - 2\varepsilon_1\varepsilon_2'}} \tag{C.1}$$

where ε_1 is a real value presenting permittivity of first layer (SPLD), and ε_2' real part of second layer complex permittivity and $\mid \varepsilon_2 \mid$ is modulus of second layer complex permittivity. It is important to point out that the apparent permittivity is a real quantity that accounts for both polarization and conductive processes and fully describes the dielectric properties of a material.

C.2.2 Disputing the Hypotheses by Khuller A. R. and Plaut J. [57], Grima et al. (2022), [41]

The bright basal echoes could result from the presence of a CO_2 ice layer on the surface, as well [97]. The bright reflections exist several places beneath the SPLD, but they have never been investigated in detail. Most probably the largest cluster of bright echoes, in particular the bright area at top left of the pole in the residual cap area in [57] is not real and could result from the presence of a CO_2 ice layer on the surface. Indeed, there, surface CO_2 ice lowers reflectivity and enhances basal reflections by contrast. Further Grima et al. has suggested other location of high-surficial reflectivity. However, Lauro et al., [65] demonstrate that this is an artifact caused from interpreting on board processed MARSIS data.

In effect, these two interpretations rely on data processed on board the spacecraft contrary to [97] and [65] that use raw data in the specific area of interest. Processed data are averages of groups of 100–300 raw echoes after compensating for the vertical motion of the spacecraft. On board processed observations at Ultimi Scopuli are at least an order of magnitude more numerous than raw data and are less reliable than raw data to perform quantitative analysis [65].

C.2.3 Disputing the Hypothesis by Lalich et al. (2022), [61]

As previously mentioned, Lalich et al. [61] use a one-dimensional numerical model of electromagnetic propagation within a plane parallel stratigraphy and demonstrate that echoes from one or two CO_2 ice layers between bedrock and dusty water ice (SPLD) with varying thickness, could produce the strong radar echoes consistent with those observed by MARSIS. Additionally, a surficial CO_2 ice layer ranging from 0 to 2 m in thickness is considered.

Nevertheless, these phenomena either require very specific physical conditions or do not produce strong basal reflections. Based on the same mathematics employed by Lalich et al., Orosei et al. [95] comprehensively simulate electromagnetic wave propagation at three operating frequencies of MARSIS under a variety of different configurations of thin layers of solid CO_2, H_2O ice, and varying basal temperatures, dust content, and basal permittivity. The modeling indicates that no scenarios involving CO_2 ice layers can reproduce the strongest echoes detected by MARSIS over the bright areas in Ultimi Scopuli, and that the decrease of echo power with increasing frequency observed in measurements could not be produced by such modeling.

It is described that basal temperature, dust content and basal permittivity are three parameters that control the attenuation within the SPLD and the intensity of the reflection at the bottom of the SPLD. The results show that even for low amounts of dust and basal temperatures, the observed strong basal echos require a high basal reflectivity. Furthermore, the decrease in echo power with increasing frequency observed in the Ultimi Scopuli region both within and surrounding the high-reflectivity zone could not be

reproduced. The observed frequency dependence of reflections is associated with attenuation caused by dust within the overlaying SPLD. According to [65] the presence of a significant fraction of dust within the SPLD causes increasing attenuation, and thus a high basal permittivity is required to produce the observed echoes.

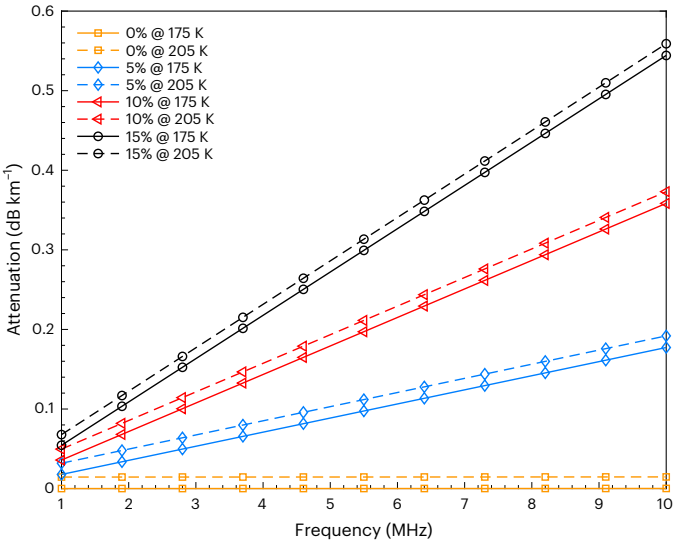

Figure C.8: Attenuation as a function of frequency in the SPLD. Attenuation is computed at 175 K and 205 K, in water ice with different content of of shergottite grains [67].

In addition, foundlings in Lalich et al. show that the local maxima at one MARSIS operating frequency do not match those at the other operating frequency. Any model aiming at reproducing MARSIS results should consider results concurrently obtained at all frequencies and be validated simultaneously at 3 MHz, 4 MHz, and 5 MHz. It means a layer stack producing constructive interference at one frequency does not produce the same effect at the other frequencies, which is inconsistent with MARSIS real data. Thus bright basal reflections at Ultimi Scopuli cannot be explained by constructive interference by basal layers.

More recently, [67] discard the hypothesis in term of three critical aspects in the Lalich et al. simulations: electromagnetic model, dielectric values, materials and geology.

Electromagnetic model: Lauro et al., [67] demonstrate that the normalized basal echo power (NBEP) value at each frequency is only obtained for a specific layer thickness, and there is no single layer-thickness that maximizes the NBEP values at all three MARSIS frequencies simultaneously. It is also shown that for the same layer thickness, the difference between NBEP values computed at different frequencies is variable and can be very large. These variations are typical of resonance phenomena but cannot explain the regular frequency trend exhibited by the three MARSIS median values. In particular, scenario 2 by Lalich et al. suggests that the assumption of basal temperature of, 175 K, lower than that considered in [97],[68] (205 K), explains the difference between their scenario 2 results and those published in [97],[68]. Lauro et al. describe that the difference in basal temperature is irrelevant, as presented in Figure (C.8). It is clear that temperature has a negligible effect on attenuation (~ 0.01 dB km), when compared with the effects of frequency and dust content.

Dielectric properties: Lalich et al. attribute a wrong value ($2.2 - j4.5 \times 10^{-7}$) to CO_2 complex permittivity while the correct value reported in literature is 2.1 ± 0.04 with no value for the imaginary part.

Materials and geology: Lauro et al. criticize the interpretations of the source of the bright basal reflections in terms of alternative materials, and by addressing several references, they demonstrate that such materials do not have dielectric properties consistent with the magnitude of the MARSIS reflections observed at Ultimi Scopuli.

Finally, they conclude that constructive interference model is not able to reproduce the real dataset collected by MARSIS at Ultimi Scopuli.

C.2.4 Basal Temperatures of Ultimi Scopuli

Heat flow and thermal conductivity of the SPLD heavily influence the estimated basal temperature at this location. Lauro et al. [65] demonstrate that basal temperatures of $\sim 171 - 176\ K$ calculated with heat flow ranges of $14 - 25\ mW/m^2$ [131] are probably underestimated. According to their results, a broader spectrum of dust and ice environmental conditions leads to higher basal temperatures ($\sim 193\ K$), which are much closer to perchlorate brines eutectic temperatures ($\sim 198\ K$). Using one-dimensional Fourier's law of heat conduction, $Q = k\nabla T$, Lauro et al. [65] calculate the temperature at the base of SPLD by assuming Q as the heat flux at the base of ice deposits, k the thermal conductivity of the deposits, and ∇T the temperature gradient.

The local surface temperatures are considered 160 K and 170 K where the latter is obtained averaging the summer and winter temperatures calculated from the thermophysical properties of water ice at these latitudes. The local heat flux at the Mars surface varies from $Q = 22\ mW/m^2$ to $Q = 28 \pm 5\ mW/m^2$ based on geochemical criteria while radar, gravity and topography data applied to a flexural loading model suggest values $Q < 23.5\ mW/m^2$. There is little constraint on the SPLD's thermal conductivity, since it is highly dependent on the nature and abundance of the materials forming the bulk of the deposits *i.e.*, water ice and dust.

Taking into account the effect of ice porosity, the estimated basal temperatures range from 176 K to 193 K for varying combinations of heat flux ($Q = 22, 30\ mW/m^2$), surface temperature ($160, 170\ K$), and dust fraction $5 - 12\%$. The maximum value is are only $\sim 5\ K$ below the eutectic temperature of calcium perchlorate. Note that, ice porosity leads to a decrease in thermal conductivity of the SPLD, and consequently, a higher temperature at the base of ice is expected. The temperatures could be even higher if a thermally insulating surficial layer of dust is included. In their computations of the content of dust the possible CO_2 ice in the SPLD is not accounted. By including CO_2 ice layers in calculations, the total proportion of water ice is reduced, leading to a further reduction in thermal conductivity, which results in an increase in estimated basal temperatures.

Finally, Lauro et al. concluded that the values of basal temperatures $\sim 171 - 176\ K$ published in some of the literature (e.g., [131]) are likely to underestimate the temperature at the base of the SPLD, and suggest that $\sim 200\ K$ is a reasonable representation of the actual base temperature.

C.2.5 Surface topography in Ultimi Scopuli

Landis M.E., and Whitten J.L., [62], used infrared data as well as high-resolution images to analyze the surface topography above the bright reflection area, but found no evidence of surface modification linked to postulated lakes. A Subglacial lakes is large water basins located beneath the ice sheet, whose origin is linked to a specific condition where the basal temperature is maintained at the pressure melting point of ice. Radio-echo sounding (RES) is the primary method for detecting terrestrial subglacial water on the earth. There are several alternative methods for detecting subglacial water: 1. Surface topography analysis, 2. Surface height changes, 3. Gravity survey, and 4. Seismic investigations.

Recently Arnold N. S. et al., [4] described an anomaly in the surface topography similar to those found above terrestrial subglacial lakes of comparable size. In addition, Sulcanese D. et al., [136] find the subglacial zone in Ultimi Scopuli using topographical analysis.

In surface topography analysis, it has been observed that surface areas directly above the subglacial water body can be remarkably flat and featureless. In general, this happens when ice is deposited in a hydrostatic equilibrium condition over subglacial lakes or saturated terrains that extend more than 4 km in length [125]. Despite this, the presence of an anomalous flat area on the surface of the icy deposits is not necessarily proof of subglacial liquid water. Furthermore, it is also possible that there is no flat area at the surface where subglacial liquid water is located. Therefore, on Earth, RES and altimetry data are combined to provide detailed information about Antarctic subglacial lakes.

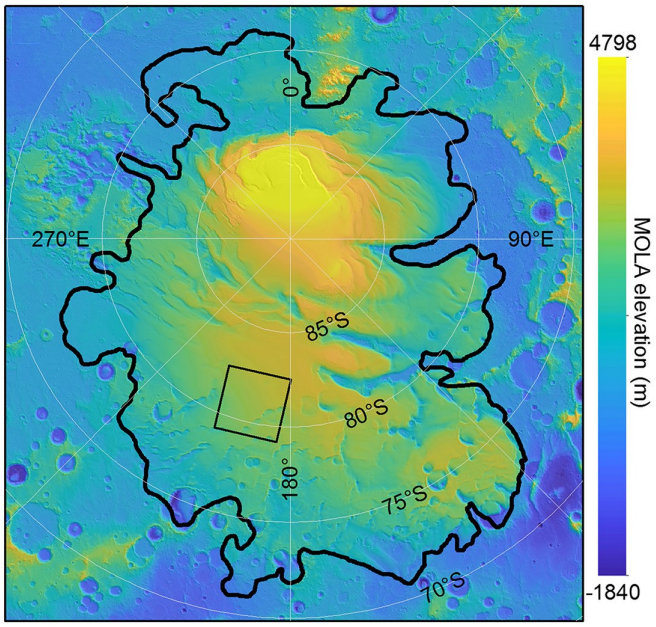

Figure C.9: Map of the south polar layered deposits, showing the region containing the high reflectance area argued to be subglacial liquid by Orosei et al. (2018). The surface topography is taken from the Mars Orbiter Laser Altimeter (MOLA) topographic dataset.

In this regard, Sulcanese D. et al. perform a topographical analysis of the surface right above Ultimi Scopuli (20 km wide) using three different Digital Elevations Models (DEMs) derived from: (1) MOLA (Mars Orbiter Laser Altimeter), (2) photogrammetric processing of the High-Resolution Stereo Camera (HRSC) images and (3) SHARAD radargrams. In each case, a flat and smooth area was found corresponding to a possible subglacial water zone. Similar to the observations above large terrestrial subglacial lakes, this indicates a condition of hydrostatic equilibrium of the ice. In conjunction with the high reflection observed by MARSIS radar data, the surface topography is consistent with the presence of subglacial bodies of liquid water at Ultimi Scopuli's base. based on the high radar reflectivity at the base and the flat topography at the surface, they conclude that an underglacial water body is likely to exist beneath the study area.

Glossary

Antarcitic ice sheet: One of the two polar ice caps of Earth that covers about 98 % of the Antarctic continent and is the largest single mass of ice on Earth, with an average thickness of over 2 kilometers.
Aquifer: A body of permeable rock or regolith saturated with water through which groundwater moves.
Asteroid: A sub-planetary object orbiting the Sun. The orbits of most asteroids lie between the orbits of Mars and Jupiter.
Attenuation: Energy reduction factor of electromagnetic waves propagating through a dissipative medium.
Basalt: A fine-grained igneous rock of mafic composition.
Brine: Salt water, particularly a highly concentrated water solution of common salt (sodium chloride). Natural brines occur underground, in salt lakes, or as seawater. Brine is formed naturally due to evaporation of ground saline water but it is also generated in the mining of sodium chloride.
Clay: The smallest clastic particles in sediment. The term is also used for a family of minerals.
Complex dielectric permittivity: Complex parameter, relating the electric field to current density, which considers both the storage and dissipation of energy associated to the polarization process.
Complex magnetic permeability: Complex parameter, relating the magnetic field to magnetic induction, which considers both the storage and dissipation of energy associated to the magnetization process.
Conductivity: A real coefficient relating electric field to current density in materials.
Crater: The depression at the summit of a volcano or a depression that is produced by a meteorite impact.
Crevasse: A deep, gaping crack in the upper surface of a glacier.
Dispersive behavior: Dependence of complex permittivity and permeability (and thus the wave velocity) on frequency.
Drainage basin: The land area that contributes water to stream.
Eutectic system: A homogeneous mixture that has a melting point lower than those of the constituents.
Eutectic temperature: The lowest possible melting point over all of the mixing ratios of the constituents.
Geometric spreading: Inverse square law reduction of power density which occurs along a transmitter-receiver radio path.
Glacier: A thick mass of ice originating on land from the compaction and recrystallization of snow that shows evidence of past or present flow.
Glacier: A permanent body of ice, consisting largely of recrystallized snow, that shows evidence of down-slope or outward movement, due to the stress of its own weight.
Hydrate: Any compound that contains water in the form of H_2O molecules, usually, but not always, with a definite content of water by weight. The best-known hydrates are crystalline solids that lose their fundamental structures upon removal of the bound water.
Ice cap: A mass of ice that covers mountain highlands, or low-lying lands in high latitudes.
Ice sheet: Continent-sized mass of ice that covers nearly all the land surface within its margins.
Igneous rock: Rock formed by the cooling and consolidation of magma.
Low-loss material: Material with a low value of the imaginary part of effective complex permittivity.
Meteorites: Naturally occurring objects that originate on a planetary body. There are three groups of Martian meteorite: shergottites, nakhlites and chassignites.
Moraine: A moraine is material left behind by a moving glacier which is usually soil and rock.
North and south polar layered deposits (NPLD and SPLD): Layered domes of dusty water ice on

Martian poles, several kilometers thick that consist predominantly of a mixture of water ice, dust, and seasonal CO_2 deposits and reach a maximum thickness at the highest latitudes.
Perchlorate: A chemical compound containing the perchlorate ion, ClO_4. Most perchlorates are colorless solids that are soluble in water. Perchlorate are present in Martian soil. Based on the temperature and pressure conditions on present-day Mars at the Phoenix lander site, conditions would allow a perchlorate salt solution to be stable in liquid form for a few hours each day during the summer.
Permafrost: Sediment, soil, or bedrock that remains continuously at a temperature below 0°C for an extended time.
Permeability: A measure of how easily a solid allows a fluid to pass through it.
Polarization: Displacement of bound charges in atoms and molecules (atomic or ionic polarization) or reorientation of existing dipoles under the effect of applied field.
Porosity: The proportion (in percent) of the total volume of a given body of bedrock or regolith that consists of pore spaces.
Reflection: The redirection of some waves back to the surface when waves hit a boundary between different Earth materials.
Regolith: The layer of rock and mineral fragments that nearly everywhere covers Earth's land surface. Regolith is a blanket of unconsolidated, loose, heterogeneous superficial deposits covering solid rock. It includes dust, broken rocks, and other related materials and is present on Earth, the Moon, Mars, some asteroids, and other terrestrial planet.
Relaxation process: Phenomenon associated with non instantaneous polarization response of a material to the applied electric field.
Remote sensing: Continuous or repetitive collection of information about a target from a distance.
Rock: A consolidated mixture of minerals.
Salinity: The proportion of dissolved salts to pure water, usually expressed in parts per thousand (g/kg).
Scattering: A reflection phenomenon that involves the dispersal of radiation in all directions by tiny particles, droplets, and gas molecule.
Sediment: Unconsolidated particles created by the weathering and erosion of rock by chemical precipitation from solution in water, or from the secretions of organisms, and transported by water, wind, or glaciers.
Shale: Soft finely stratified sedimentary rock that formed from consolidated mud or clay and can be split easily into fragile plates. Shale is the most abundant of the sedimentary rocks, accounting for roughly 70 percent of this rock type in the crust of the Earth.
Shergottite: The shergottites are the most abundant and the most diverse of the Martian meteorite subgroups. They are commonly divided into three types: basaltic, lherzolitic, and olivine–phyric shergottites.
Smectites: A class of lightly weathered hydrous phyllosilicate minerals with multiple hydration states and properties.
Soil: A combination of mineral and organic matter, water and air; The portion of the regolith that supports planet growth.
Static conductivity: Real coefficient relating electric field to current density in ice at frequencies lower than Debye relaxation.
Strata: Parallel layers of sedimentary rock.
Stratigraphy: The Study of strata.
Subglacial lakes: Large water basins located beneath the ice sheet, whose origin is linked to a specific condition where the basal temperature is maintained at the pressure melting point of ice.
Wave refraction: A change in direction of waves as they hit a boundary between two different materials.

Bibliography

[1] AP Annan. Ground penetrating radar principles. *Procedures & Applications*, 577, 2003.

[2] AP Annan. Ground-penetrating radar. In *Near-surface geophysics*, pages 357–438. Society of Exploration Geophysicists, 2005.

[3] AP Annan, JL Davis, et al. Radar range analysis for geological materials. *Geological Survey of Canada*, 77(1B):117–124, 1977.

[4] NS Arnold, FEG Butcher, SJ Conway, Colman Gallagher, and MR Balme. Surface topographic impact of subglacial water beneath the south polar ice cap of mars. *Nature Astronomy*, 6(11):1256–1262, 2022.

[5] Constantine A Balanis. *Advanced engineering electromagnetics*. John Wiley & Sons, 2012.

[6] Maksim Bano. Modelling of gpr waves for lossy media obeying a complex power law of frequency for dielectric permittivity. *Geophysical Prospecting*, 52(1):11–26, 2004.

[7] Rajiv R Bharti, Isaac B Smith, SK Mishra, N Srivastava, and Shital H Shukla. Sharad detection of sedimentary infilling within an unnamed crater near mangala fossa region, mars. *Icarus*, 371:114713, 2022.

[8] CJ Bierson, S Tulaczyk, SW Courville, and NE Putzig. Strong marsis radar reflections from the base of martian south polar cap may be due to conductive ice or minerals. *Geophysical Research Letters*, 48(13):e2021GL093880, 2021.

[9] Vitali Vasil evich Bogorodsky and Bogorodski. *Radioglaciology*, volume 1. Springer Science and Business Media, 1985.

[10] Joséphine Boisson, Essam Heggy, Stephen M Clifford, Alessandro Frigeri, Jeffrey J Plaut, William M Farrell, Nathaniel E Putzig, Giovanni Picardi, Roberto Orosei, Philippe Lognonné, et al. Sounding the subsurface of athabasca valles using marsis radar data: Exploring the volcanic and fluvial hypotheses for the origin of the rafted plate terrain. *Journal of Geophysical Research: Planets*, 114(E8), 2009.

[11] John H Bradford. Frequency-dependent attenuation analysis of ground-penetrating radar data. *Geophysics*, 72(3):J7–J16, 2007.

[12] John H Bradford. Estimating debye parameters from gpr reflection data using spectral ratios. In *Symposium on the Application of Geophysics to Engineering and Environmental Problems 2009*, pages 57–66. Society of Exploration Geophysicists, 2009.

[13] John H Bradford. Frequency dependent attenuation of gpr data as a tool for material property characterization: A review and new developments. In *2011 6th International Workshop on Advanced Ground Penetrating Radar (IWAGPR)*, pages 1–4. IEEE, 2011.

[14] John H Bradford, Joel T Harper, and Joel Brown. Complex dielectric permittivity measurements from ground-penetrating radar data to estimate snow liquid water content in the pendular regime. *Water resources research*, 45(8), 2009.

[15] John H Bradford and Yafei Wu. Instantaneous spectral analysis: Time-frequency mapping via wavelet matching with application to contaminated-site characterization by 3d gpr. *The Leading Edge*, 26(8):1018–1023, 2007.

[16] Lorenzo Bruzzone, Jeffrey J Plaut, Giovanni Alberti, Donald D Blankenship, Francesca Bovolo, Bruce A Campbell, Adamo Ferro, Yonggyu Gim, Wlodek Kofman, Goro Komatsu, et al. Rime: Radar for icy moon exploration. In *2013 IEEE international geoscience and remote sensing symposium-IGARSS*, pages 3907–3910. IEEE, 2013.

[17] Bruce Campbell, Lynn Carter, Roger Phillips, Jeffrey Plaut, Nathaniel Putzig, Ali Safaeinili, Roberto Seu, Daniela Biccari, Anthony Egan, and Roberto Orosei. Sharad radar sounding of the vastitas borealis formation in amazonis planitia. *Journal of Geophysical Research: Planets*, 113(E12), 2008.

[18] Bruce A Campbell and Gareth A Morgan. Fine-scale layering of mars polar deposits and signatures of ice content in nonpolar material from multiband sharad data processing. *Geophysical Research Letters*, 45(4):1759–1766, 2018.

[19] Dae H Chung. Laboratory studies on seismic and electrical properties of the moon. *The moon*, 4(3):356–372, 1972.

[20] Kenneth S Cole and Robert H Cole. Dispersion and absorption in dielectrics i. alternating current characteristics. *The Journal of chemical physics*, 9(4):341–351, 1941.

[21] J.L Davis and A.P ANNAN. Ground-penetrating radar for high-resolution mapping of soil and rock stratigraphy 1. *Geophysical prospecting*, 37(5):531–551, 1989.

[22] Michael Dentith and Stephen T Mudge. *Geophysics for the mineral exploration geoscientist*. Cambridge University Press, 2014.

[23] Chunyu Ding, Yan Su, Zhonghan Lei, Zongyu Zhang, Mi Song, Yuanzhou Liu, Ruigang Wang, Qingquan Li, Chunlai Li, and Shaopeng Huang. Electromagnetic signal attenuation characteristics in the lunar regolith observed by the lunar regolith penetrating radar (lrpr) onboard the chang'e-5 lander. *Remote Sensing*, 14(20):5189, 2022.

[24] Myron C Dobson, Fawwaz T Ulaby, Martti T Hallikainen, and Mohamed A El-Rayes. Microwave dielectric behavior of wet soil-part ii: Dielectric mixing models. *IEEE Transactions on geoscience and remote sensing*, (1):35–46, 1985.

[25] Julian A Dowdeswell and Stanley Evans. Investigations of the form and flow of ice sheets and glaciers using radio-echo sounding. *Reports on Progress in Physics*, 67(10):1821, 2004.

[26] Nikos Economou and George Kritikakis. Attenuation analysis of real gpr wavelets: The equivalent amplitude spectrum (eas). *Journal of Applied Geophysics*, 126:13–26, 2016.

[27] Bethany L Ehlmann, Gilles Berger, Nicolas Mangold, Joseph R Michalski, David C Catling, Steven W Ruff, Eric Chassefière, Paul B Niles, Vincent Chevrier, and Francois Poulet. Geochemical consequences of widespread clay mineral formation in mars' ancient crust. *Space Science Reviews*, 174(1):329–364, 2013.

[28] Bethany L Ehlmann, John F Mustard, Scott L Murchie, Jean-Pierre Bibring, Alain Meunier, Abigail A Fraeman, and Yves Langevin. Subsurface water and clay mineral formation during the early history of mars. *Nature*, 479(7371):53–60, 2011.

[29] Sigurd Eide, Titus M Casademont, Tor Berger, Henning Dypvik, Emileigh S Shoemaker, and Svein-Erik Hamran. Radar attenuation in the shallow martian subsurface: Rimfax time-frequency analysis and constant-q characterization over jezero crater floor. *Geophysical Research Letters*, page e2022GL101429, 2022.

[30] Atef Z Elsherbeni and Veysel Demir. *The finite-difference time-domain method for electromagnetics with MATLAB® simulations*, volume 2. IET, 2015.

[31] Wenzhe Fa, Meng-Hua Zhu, Tiantian Liu, and Jeffrey B Plescia. Regolith stratigraphy at the chang'e-3 landing site as seen by lunar penetrating radar. *Geophysical Research Letters*, 42(23):10–179, 2015.

[32] Kenneth A Farley, Kenneth H Williford, Kathryn M Stack, Rohit Bhartia, Al Chen, Manuel de la Torre, Kevin Hand, Yulia Goreva, Christopher DK Herd, Ricardo Hueso, et al. Mars 2020 mission overview. *Space Science Reviews*, 216(8):1–41, 2020.

[33] Jianqing Feng, Matthew A Siegler, and Mackenzie N White. Dielectric properties and stratigraphy of regolith in the lunar south pole-aitken basin: Observations from the lunar penetrating radar. *Astronomy & Astrophysics*, 661:A47, 2022.

[34] Jianqing Feng, Yan Su, Chunyu Ding, Shuguo Xing, Shun Dai, and Yongliao Zou. Dielectric properties estimation of the lunar regolith at ce-3 landing site using lunar penetrating radar data. *Icarus*, 284:424–430, 2017.

[35] Giorgio Franceschetti. *Campi elettromagnetici*. Bollati Boringhieri, 1992.

[36] Shuji Fujita, Takeshi Matsuoka, Toshihiro Ishida, Kenichi Matsuoka, and Shinji Mae. A summary of the complex dielectric permittivity of ice in the megahertz range and its applications for radar sounding of polar ice sheets. In *Physics of ice core records*, pages 185–212. Hokkaido University Press, 2000.

[37] Iraklis Giannakis, Antonios Giannopoulos, and Craig Warren. A realistic fdtd numerical modeling framework of ground penetrating radar for landmine detection. *IEEE journal of selected topics in applied earth observations and remote sensing*, 9(1):37–51, 2015.

[38] Antonis Giannopoulos. Modelling ground penetrating radar by gprmax. *Construction and building materials*, 19(10):755–762, 2005.

[39] P Glover. Geophysical properties of the near surface earth: Electrical properties: Treatise on geophysics, 11, 89–137, 2015.

[40] Olivier Grasset, MK Dougherty, A Coustenis, EJ Bunce, C Erd, D Titov, M Blanc, A Coates, P Drossart, LN Fletcher, et al. Jupiter icy moons explorer (juice): An esa mission to orbit ganymede and to characterise the jupiter system. *Planetary and Space Science*, 78:1–21, 2013.

[41] C Grima, J Mouginot, W Kofman, A Hérique, and P Beck. The basal detectability of an ice-covered mars by marsis. *Geophysical Research Letters*, 49(2):e2021GL096518, 2022.

[42] Cyril Grima, Wlodek Kofman, Jérémie Mouginot, Roger J Phillips, Alain Hérique, Daniela Biccari, Roberto Seu, and Marco Cutigni. North polar deposits of mars: Extreme purity of the water ice. *Geophysical Research Letters*, 36(3), 2009.

[43] Robert E Grimm, Essam Heggy, Stephen Clifford, Cynthia Dinwiddie, Ronald McGinnis, and David Farrell. Absorption and scattering in ground-penetrating radar: Analysis of the bishop tuff. *Journal of Geophysical Research: Planets*, 111(E6), 2006.

[44] Martti T Hallikainen, Fawwaz T Ulaby, Myron C Dobson, Mohamed A El-Rayes, and Lil-Kun Wu. Microwave dielectric behavior of wet soil-part 1: Empirical models and experimental observations. *IEEE Transactions on Geoscience and Remote Sensing*, (1):25–34, 1985.

[45] Svein-Erik Hamran, David A Paige, Hans EF Amundsen, Tor Berger, Sverre Brovoll, Lynn Carter, Leif Damsgård, Henning Dypvik, Jo Eide, Sigurd Eide, et al. Radar imager for mars' subsurface experiment—rimfax. *space science Reviews*, 216(8):1–39, 2020.

[46] Hussein Harbi and George A McMechan. Conductivity and scattering q in gpr data: Example from the ellenburger dolomite, central texas. *Geophysics*, 77(4):H63–H78, 2012.

[47] Mark S Haynes. Surface and subsurface radar equations for radar sounders. *Annals of Glaciology*, 61(81):135–142, 2020.

[48] Chunhua Hu, Ning Tu, and Wenkai Lu. Seismic attenuation estimation using an improved frequency shift method. *IEEE Geoscience and Remote Sensing Letters*, 10(5):1026–1030, 2013.

[49] George Hufford. A model for the complex permittivity of ice at frequencies below 1 thz. *International Journal of Infrared and Millimeter Waves*, 12(7):677–682, 1991.

[50] Wing-Huen Ip, Jun Yan, Chun-Lai Li, and Zi-Yuan Ouyang. Preface: The chang'e-3 lander and rover mission to the moon. *Research in Astronomy and Astrophysics*, 14(12):1511, 2014.

[51] James D Irving and Rosemary J Knight. Removal of wavelet dispersion from ground-penetrating radar data. *Geophysics*, 68(3):960–970, 2003.

[52] Akira Ishimaru. *Electromagnetic wave propagation, radiation, and scattering: from fundamentals to applications*. John Wiley & Sons, 2017.

[53] Harry M Jol. *Ground penetrating radar theory and applications*. elsevier, 2008.

[54] R Jordan, G Picardi, J Plaut, K Wheeler, D Kirchner, A Safaeinili, W Johnson, R Seu, D Calabrese, E Zampolini, et al. The mars express marsis sounder instrument. *Planetary and Space Science*, 57(14-15):1975–1986, 2009.

[55] Kwan Chi Kao. 2 - electric polarization and relaxation. In Kwan Chi Kao, editor, *Dielectric Phenomena in Solids*, pages 41–114. Academic Press, San Diego, 2004.

[56] George V Keller. Rock and mineral properties. *Electromagnetic methods in applied geophysics*, 1:13–52, 1988.

[57] Aditya R Khuller and Jeffrey J Plaut. Characteristics of the basal interface of the martian south polar layered deposits. *Geophysical Research Letters*, 48(13):e2021GL093631, 2021.

[58] Guido Kneib and Serge A Shapiro. Viscoacoustic wave propagation in 2-d random media and separation of absorption and scattering attenuation. *Geophysics*, 60(2):459–467, 1995.

[59] Jialong Lai, Yi Xu, Roberto Bugiolacchi, Xu Meng, Long Xiao, Minggang Xie, Bin Liu, Kaichang Di, Xiaoping Zhang, Bin Zhou, et al. First look by the yutu-2 rover at the deep subsurface structure at the lunar farside. *Nature communications*, 11(1):1–9, 2020.

[60] Jialong Lai, Yi Xu, Xiaoping Zhang, Long Xiao, Qi Yan, Xu Meng, Bin Zhou, Zehua Dong, and Di Zhao. Comparison of dielectric properties and structure of lunar regolith at chang'e-3 and chang'e-4 landing sites revealed by ground-penetrating radar. *Geophysical Research Letters*, 46(22):12783–12793, 2019.

[61] DE Lalich, AG Hayes, and V Poggiali. Explaining bright radar reflections below the south pole of mars without liquid water. *Nature Astronomy*, 6(10):1142–1146, 2022.

[62] ME Landis and JL Whitten. Geologic context of the bright marsis reflectors in ultimi scopuli, south polar layered deposits, mars. *Geophysical Research Letters*, page e2022GL098724, 2022.

[63] SE Lauro, E Mattei, B Cosciotti, F Di Paolo, SA Arcone, Marco Viccaro, and E Pettinelli. Electromagnetic signal penetration in a planetary soil simulant: Estimated attenuation rates using gpr and tdr in volcanic deposits on mount etna. *Journal of Geophysical Research: Planets*, 122(7):1392–1404, 2017.

[64] Sebastian E Lauro, Elisabetta Mattei, Francesco Soldovieri, Elena Pettinelli, Roberto Orosei, and Giuliano Vannaroni. Dielectric constant estimation of the uppermost basal unit layer in the martian boreales scopuli region. *Icarus*, 219(1):458–467, 2012.

[65] Sebastian E Lauro, Elena Pettinelli, Graziella Caprarelli, Jamaledin Baniamerian, Elisabetta Mattei, Barbara Cosciotti, David E Stillman, Katherine M Primm, Francesco Soldovieri, and Roberto Orosei. Using marsis signal attenuation to assess the presence of south polar layered deposit subglacial brines. *Nature communications*, 13(1):1–10, 2022.

[66] Sebastian Emanuel Lauro, Jamaledin Baniamerian, Barbara Cosciotti, Elisabetta Mattei, and Elena Pettinelli. Loss tangent estimation from ground-penetrating radar data using ricker wavelet centroid-frequency shift analysis. *Geophysics*, 87(3):H1–H12, 2022.

[67] Sebastian Emanuel Lauro, Elena Pettinelli, Graziella Caprarelli, Luca Guallini, Angelo Pio Rossi, Elisabetta Mattei, Barbara Cosciotti, Andrea Cicchetti, Francesco Soldovieri, M Cartacci, et al. Reply to: Explaining bright radar reflections below the south pole of mars without liquid water. *Nature Astronomy*, pages 1–3, 2023.

[68] Sebastian Emanuel Lauro, Elena Pettinelli, Graziella Caprarelli, Luca Guallini, Angelo Pio Rossi, Elisabetta Mattei, Barbara Cosciotti, Andrea Cicchetti, Francesco Soldovieri, Marco Cartacci, et al. Multiple subglacial water bodies below the south pole of mars unveiled by new marsis data. *Nature Astronomy*, 5(1):63–70, 2021.

[69] Sebastian Emanuel Lauro, Francesco Soldovieri, Roberto Orosei, Andrea Cicchetti, Marco Cartacci, Elisabetta Mattei, Barbara Cosciotti, Federico Di Paolo, Raffaella Noschese, and Elena Pettinelli. Liquid water detection under the south polar layered deposits of mars—a probabilistic inversion approach. *Remote Sensing*, 11(20):2445, 2019.

[70] Chuanhui Li and Xuewei Liu. A new method for interval q-factor inversion from seismic reflection data. *Geophysics*, 80(6):R361–R373, 2015.

[71] Chunlai Li, Dawei Liu, Bin Liu, Xin Ren, Jianjun Liu, Zhiping He, Wei Zuo, Xingguo Zeng, Rui Xu, Xu Tan, et al. Chang'e-4 initial spectroscopic identification of lunar far-side mantle-derived materials. *Nature*, 569(7756):378–382, 2019.

[72] Chunlai Li, Yan Su, Elena Pettinelli, Shuguo Xing, Chunyu Ding, Jianjun Liu, Xin Ren, Sebastian E Lauro, Francesco Soldovieri, Xingguo Zeng, et al. The moon's farside shallow subsurface structure unveiled by chang'e-4 lunar penetrating radar. *Science advances*, 6(9):eaay6898, 2020.

[73] Fangyu Li, Huailai Zhou, Nan Jiang, Jianxia Bi, and Kurt J Marfurt. Q estimation from reflection seismic data for hydrocarbon detection using a modified frequency shift method. *Journal of Geophysics and Engineering*, 12(4):577–586, 2015.

[74] Hans J Liebe, George A Hufford, and Takeshi Manabe. A model for the complex permittivity of water at frequencies below 1 thz. *International Journal of Infrared and Millimeter Waves*, 12(7):659–675, 1991.

[75] Lanbo Liu, John W Lane, and Youli Quan. Radar attenuation tomography using the centroid frequency downshift method. *Journal of Applied Geophysics*, 40(1-3):105–116, 1998.

[76] RG Loucks, PK Mescher, and GA McMechan. Architecture of a coalesced, collapsed-paleocave system in the lower ordovician ellenburger group, dean word quarry, marble falls, texas: Report prepared for gas research institute under contract no. Technical report, GRI-00/0122, CD-ROM, 2000.

[77] Joseph A MacGregor, Jilu Li, John D Paden, Ginny A Catania, Gary D Clow, Mark A Fahnestock, S Prasad Gogineni, Robert E Grimm, Mathieu Morlighem, Soumyaroop Nandi, et al. Radar attenuation and temperature within the greenland ice sheet. *Journal of Geophysical Research: Earth Surface*, 120(6):983–1008, 2015.

[78] Smriti Mallapaty. What china's mars rover will do next. *Nature*, 593:323–324, 2021.

[79] Kenichi Matsuoka, D Morse, and CF Raymond. Estimating englacial radar attenuation using depth profiles of the returned power, central west antarctica. *Journal of Geophysical Research: Earth Surface*, 115(F2), 2010.

[80] E Mattei, SE Lauro, G Vannaroni, B Cosciotti, F Bella, and E Pettinelli. Dielectric measurements and radar attenuation estimation of ice/basalt sand mixtures as martian polar caps analogues. *Icarus*, 229:428–433, 2014.

[81] Elisabetta Mattei, Elena Pettinelli, Sebastian Emanuel Lauro, David E Stillman, Barbara Cosciotti, Lucia Marinangeli, Anna Chiara Tangari, Francesco Soldovieri, Roberto Orosei, and Graziella Caprarelli. Assessing the role of clay and salts on the origin of marsis basal bright reflections. *Earth and Planetary Science Letters*, 579:117370, 2022.

[82] Christian Matzler. Microwave properties of ice and snow. In *Solar System Ices*, pages 241–257. Springer, 1998.

[83] Christian Matzler and Urs Wegmuller. Dielectric properties of freshwater ice at microwave frequencies. *Journal of Physics D: Applied Physics*, 20(12):1623, 1987.

[84] Ted A Maxwell and RJ Phillips. Stratigraphic correlation of the radar-detected subsurface interface in mare crisium. *Geophysical Research Letters*, 5(9):811–814, 1978.

[85] Thomas Meissner and Frank J Wentz. The complex dielectric constant of pure and sea water from microwave satellite observations. *IEEE Transactions on Geoscience and remote Sensing*, 42(9):1836–1849, 2004.

[86] Klaus Mosegaard, Albert Tarantola, et al. Probabilistic approach to inverse problems. *International Geophysics Series*, 81(A):237–268, 2002.

[87] CP Reghunadhan Nair and Vibhu Unnikrishnan. Stability of the liquid water phase on mars: a thermodynamic analysis considering martian atmospheric conditions and perchlorate brine solutions. *ACS omega*, 5(16):9391–9397, 2020.

[88] David C Nobes, Emma F Davis, and Steven A Arcone. "mirror-image" multiples in ground-penetrating radar. *Geophysics*, 70(1):K20–K22, 2005.

[89] Lujendra Ojha, Saman Karimi, Jacob Buffo, Stefano Nerozzi, John W Holt, Sue Smrekar, and Vincent Chevrier. Martian mantle heat flow estimate from the lack of lithospheric flexure in the south pole of mars: Implications for planetary evolution and basal melting. *Geophysical Research Letters*, 48(2):e2020GL091409, 2021.

[90] G R. Olhoeft and DW Strangway. Dielectric properties of the first 100 meters of the moon. *Earth and Planetary Science Letters*, 24(3):394–404, 1975.

[91] Gary R Olhoeft. Electromagnetic field and material properties in ground penetrating radar. In *Proceedings of the 2nd International Workshop onAdvanced Ground Penetrating Radar, 2003.*, pages 144–147. IEEE, 2003.

[92] Takayuki Ono, Atsushi Kumamoto, Hiromu Nakagawa, Yasushi Yamaguchi, Shoko Oshigami, Atsushi Yamaji, Takao Kobayashi, Yoshiya Kasahara, and Hiroshi Oya. Lunar radar sounder observations of subsurface layers under the nearside maria of the moon. *Science*, 323(5916):909–912, 2009.

[93] Alan V Oppenheim, John Buck, Michael Daniel, Alan S Willsky, Syed Hamid Nawab, and Andrew Singer. *Signals and systems*. Pearson Educactin, 1997.

[94] Sophocles J Orfanidis. Electromagnetic waves and antennas. 2002.

[95] Roberto Orosei, Graziella Caprarelli, Sebastian Lauro, Elena Pettinelli, Marco Cartacci, Andrea Cicchetti, Barbara Cosciotti, Alessandro De Lorenzis, Giorgio De Nunzio, Elisabetta Mattei, et al. Numerical simulations of radar echoes rule out basal co2 ice deposits at ultimi scopuli, mars. *Icarus*, 386:115163, 2022.

[96] Roberto Orosei, Chunyu Ding, Wenzhe Fa, Antonios Giannopoulos, Alain Hérique, Wlodek Kofman, Sebastian E Lauro, Chunlai Li, Elena Pettinelli, Yan Su, et al. The global search for liquid water on mars from orbit: Current and future perspectives. *Life*, 10(8):120, 2020.

[97] Roberto Orosei, SE Lauro, E Pettinelli, ANDREA Cicchetti, M Coradini, B Cosciotti, F Di Paolo, E Flamini, E Mattei, MAURIZIO Pajola, et al. Radar evidence of subglacial liquid water on mars. *Science*, 361(6401):490–493, 2018.

[98] Gordon KA Oswald, Soroush Rezvanbehbahani, and Leigh A Stearns. Radar evidence of ponded subglacial water in greenland. *Journal of Glaciology*, 64(247):711–729, 2018.

[99] E. I. Parkhomenko. *Dielectric Loss in Rocks*, pages 185–240. Springer US, 1967.

[100] Neil R Peplinski, Fawwaz T Ulaby, and Myron C Dobson. Dielectric properties of soils in the 0.3-1.3-ghz range. *IEEE transactions on Geoscience and Remote sensing*, 33(3):803–807, 1995.

[101] Neil R Peplinski, Fawwaz T Ulaby, and Myron Craig Dobson. Corrections to" dielectric properties of soils in the 0.3-1.3-ghz range". *IEEE Transactions on Geoscience and Remote Sensing*, 33(6):1340, 1995.

[102] Victor F Petrenko and Robert W Whitworth. *Physics of ice*. OUP Oxford, 1999.

[103] Elena Pettinelli, Paolo Burghignoli, Anna Rita Pisani, Francesca Ticconi, Alessandro Galli, Giuliano Vannaroni, and Francesco Bella. Electromagnetic propagation of gpr signals in martian subsurface scenarios including material losses and scattering. *IEEE Transactions on Geoscience and Remote Sensing*, 45(5):1271–1281, 2007.

[104] Elena Pettinelli, Barbara Cosciotti, Federico Di Paolo, Sebastian Emanuel Lauro, Elisabetta Mattei, Roberto Orosei, and Giuliano Vannaroni. Dielectric properties of jovian satellite ice analogs for subsurface radar exploration: A review. *Reviews of Geophysics*, 53(3):593–641, 2015.

[105] Elena Pettinelli, Barbara Cosciotti, Sebastian Emanuel Lauro, and Elisabetta Mattei. An overview of gpr subsurface exploration of planets and moons. *The Leading Edge*, 41(10):672–680, 2022.

[106] Elena Pettinelli, Sebastian E Lauro, Elisabetta Mattei, Barbara Cosciotti, and Francesco Soldovieri. Stratigraphy versus artefacts in the chang'e-4 low-frequency radar. *Nature Astronomy*, 5(9):890–893, 2021.

[107] G Picardi, D Biccari, M Cartacci, A Cicchetti, S Giuppi, A Marini, A Masdea, R Noschese, F Piccari, R Seu, et al. Marsis data inversion approach: Preliminary results. In *2008 IEEE Radar Conference*, pages 1–4. IEEE, 2008.

[108] G Picardi, D Biccari, R Seu, L Marinangeli, WTK Johnson, RL Jordan, J Plaut, A Safaenili, DA Gurnett, GG Ori, et al. Performance and surface scattering models for the mars advanced radar for subsurface and ionosphere sounding (marsis). *Planetary and Space Science*, 52(1-3):149–156, 2004.

[109] Giovanni Picardi, Jeffrey J Plaut, Daniela Biccari, Ornella Bombaci, Diego Calabrese, Marco Cartacci, Andrea Cicchetti, Stephen M Clifford, Peter Edenhofer, William M Farrell, et al. Radar soundings of the subsurface of mars. *science*, 310(5756):1925–1928, 2005.

[110] Jeffrey J. Plaut. *Radar Remote Sensing of Planetary Bodies*, page 604–623. Cambridge Planetary Science. Cambridge University Press, 2019.

[111] Jeffrey J Plaut, Giovanni Picardi, Ali Safaeinili, Anton B Ivanov, Sarah M Milkovich, Andrea Cicchetti, Wlodek Kofman, Jérémie Mouginot, William M Farrell, Roger J Phillips, et al. Subsurface radar sounding of the south polar layered deposits of mars. *science*, 316(5821):92–95, 2007.

[112] Leonard J Porcello, Roland L Jordan, JERRY S Zelenka, GF Adams, RJ Phillips, WE Brown, SH Ward, and PL Jackson. The apollo lunar sounder radar system. *Proceedings of the IEEE*, 62(6):769–783, 1974.

[113] Michael Portnoff. Time-frequency representation of digital signals and systems based on short-time fourier analysis. *IEEE Transactions on Acoustics, Speech, and Signal Processing*, 28(1):55–69, 1980.

[114] David M Pozar. *Microwave engineering*. John wiley & sons, 2011.

[115] KM Primm, DE Stillman, and TI Michaels. Investigating the hysteretic behavior of mars-relevant chlorides. *Icarus*, 342:113342, 2020.

[116] Youli Quan and Jerry M Harris. Seismic attenuation tomography using the frequency shift method. *Geophysics*, 62(3):895–905, 1997.

[117] John M Reynolds. *An introduction to applied and environmental geophysics*. John Wiley & Sons, 2011.

[118] James Rickett. Integrated estimation of interval-attenuation profiles. *Geophysics*, 71(4):A19–A23, 2006.

[119] KM Scanlan, DA Young, C Grima, G Steinbrugge, SD Kempf, and DD Blankenship. Englacial radar attenuation rates in the promethei lingula area of the martian south polar layered deposits. In *50th Annual Lunar and Planetary Science Conference*, number 2132, page 1994, 2019.

[120] Jack Schmitt. *Lunar sourcebook: A user's guide to the Moon*. Number 1259. CUP Archive, 1991.

[121] Jürgen H Schön. *Physical properties of rocks: Fundamentals and principles of petrophysics*. Elsevier, 2015.

[122] International Telecommunications Union Radiocommunication Sector. Effects of building materials and structures on radiowave propagation above about 100mhz. recommendation p.2040-1. itu-r, approved july 29, 2015. *ITU*, 2015.

[123] R Seu, D Biccari, R Orosei, LV Lorenzoni, RJ Phillips, L Marinangeli, G Picardi, A Masdea, and E Zampolini. Sharad: The mro 2005 shallow radar. *Planetary and Space Science*, 52(1-3):157–166, 2004.

[124] Roberto Seu, Roger J Phillips, Daniela Biccari, Roberto Orosei, Arturo Masdea, Giovanni Picardi, Ali Safaeinili, Bruce A Campbell, Jeffrey J Plaut, Lucia Marinangeli, et al. Sharad sounding radar on the mars reconnaissance orbiter. *Journal of Geophysical Research: Planets*, 112(E5), 2007.

[125] Martin J Siegert and Jeffrey K Ridley. An analysis of the ice-sheet surface and subsurface topography above the vostok station subglacial lake, central east antarctica. *Journal of Geophysical Research: Solid Earth*, 103(B5):10195–10207, 1998.

[126] Martin J Siegert, Justin Taylor, and Antony J Payne. Spectral roughness of subglacial topography and implications for former ice-sheet dynamics in east antarctica. *Global and Planetary Change*, 45(1-3):249–263, 2005.

[127] Ari Sihvola. Mixing rules with complex dielectric coefficients. *Subsurface sensing technologies and applications*, 1(4):393–415, 2000.

[128] Ari H Sihvola. *Electromagnetic mixing formulas and applications*. Number 47. Iet, 1999.

[129] Gene Simmons, Terry Todd, and Herbert Wang. The 25-km discontinuity: Implications for lunar history. *Science*, 182(4108):158–161, 1973.

[130] IB Smith, DE Lalich, C Rezza, BHN Horgan, JL Whitten, S Nerozzi, and JW Holt. A solid interpretation of bright radar reflectors under the mars south polar ice. *Geophysical Research Letters*, 48(15):e2021GL093618, 2021.

[131] Michael M Sori and Ali M Bramson. Water on mars, with a grain of salt: Local heat anomalies are required for basal melting of ice at the south pole today. *Geophysical Research Letters*, 46(3):1222–1231, 2019.

[132] Robert Glenn Stockwell, Lalu Mansinha, and RP Lowe. Localization of the complex spectrum: the s transform. *IEEE transactions on signal processing*, 44(4):998–1001, 1996.

[133] Julius Adams Stratton. *Electromagnetic theory*, volume 33. John Wiley & Sons, 2007.

[134] Yan Su, Guang-You Fang, Jian-Qing Feng, Shu-Guo Xing, Yi-Cai Ji, Bin Zhou, Yun-Ze Gao, Han Li, Shun Dai, Yuan Xiao, et al. Data processing and initial results of chang'e-3 lunar penetrating radar. *Research in astronomy and astrophysics*, 14(12):1623, 2014.

[135] Yan Su, Ruigang Wang, Xiangjin Deng, Zongyu Zhang, Jianfeng Zhou, Zhiyong Xiao, Chunyu Ding, Yuxi Li, Shun Dai, Xin Ren, et al. Hyperfine structure of regolith unveiled by chang'e-5 lunar regolith penetrating radar. *IEEE Transactions on Geoscience and Remote Sensing*, 60:1–14, 2022.

[136] Davide Sulcanese, Giuseppe Mitri, Antonio Genova, Flavio Petricca, Simone Andolfo, and Gianluca Chiarolanza. Topographical analysis of a candidate subglacial water region in ultimi scopuli, mars. *Icarus*, 392:115394, 2023.

[137] Iwao Takei and Norikazu Maeno. Dielectric low-frequency dispersion and crossover phenomena of hcl-doped ice. *The Journal of Physical Chemistry B*, 101(32):6234–6236, 1997.

[138] Albert Tarantola. *Inverse problem theory and methods for model parameter estimation*. SIAM, 2005.

[139] Sanchari Thakur, Elisa Sbalchiero, and Lorenzo Bruzzone. Exploring venus subsurface: Analysis of geological targets and their properties. *Planetary and Space Science*, 225:105620, 2023.

[140] JD Toner and DC Catling. Chlorate brines on mars: Implications for the occurrence of liquid water and deliquescence. *Earth and Planetary Science Letters*, 497:161–168, 2018.

[141] JD Toner, DC Catling, and B Light. The formation of supercooled brines, viscous liquids, and low-temperature perchlorate glasses in aqueous solutions relevant to mars. *Icarus*, 233:36–47, 2014.

[142] Rainer Tonn. The determination of the seismic quality factor q from vsp data: A comparison of different computational methods1. *Geophysical Prospecting*, 39(1):1–27, 1991.

[143] Slawek M Tulaczyk and Neil T Foley. The role of electrical conductivity in radar wave reflection from glacier beds. *The Cryosphere*, 14(12):4495–4506, 2020.

[144] Greg Turner and Anthony F Siggins. Constant q attenuation of subsurface radar pulses. *Geophysics*, 59(8):1192–1200, 1994.

[145] Fawwaz Tayssir Ulaby, David G Long, William J Blackwell, Charles Elachi, Adrian K Fung, Chris Ruf, Kamal Sarabandi, Howard A Zebker, and Jakob Van Zyl. *Microwave radar and radiometric remote sensing*, volume 4. University of Michigan Press Ann Arbor, MI, USA, 2014.

[146] Fawwaz Tayssir Ulaby, Eric Michielssen, and Umberto Ravaioli. *Fundamentals of applied electromagnetics*, volume 7. Pearson Upper Saddle River, NJ, 2015.

[147] Yanghua Wang. Frequencies of the ricker wavelet. *Geophysics*, 80(2):A31–A37, 2015.

[148] Stanley H Ward and Gerald W Hohmann. Electromagnetic theory for geophysical applications. In *Electromagnetic Methods in Applied Geophysics: Voume 1, Theory*, pages 130–311. Society of Exploration Geophysicists, 1988.

[149] Craig Warren, Antonios Giannopoulos, and Iraklis Giannakis. gprmax: Open source software to simulate electromagnetic wave propagation for ground penetrating radar. *Computer Physics Communications*, 209:163–170, 2016.

[150] Weiren Wu, Chunlai Li, Wei Zuo, Hongbo Zhang, Jianjun Liu, Weibin Wen, Yan Su, Xin Ren, Jun Yan, Dengyun Yu, et al. Lunar farside to be explored by chang'e-4. *Nature Geoscience*, 12(4):222–223, 2019.

[151] Ke Yan, Jinghuai Gao, Bing Zhang, Qian Wang, and Yang Yang. Seismic attenuation estimation using the centroid frequency shift and divergence. *IEEE Geoscience and Remote Sensing Letters*, 16(12):1924–1928, 2019.

[152] Changjun Zhang and Tadeusz J Ulrych. Estimation of quality factors from cmp records. *Geophysics*, 67(5):1542–1547, 2002.

[153] Hong-Bo Zhang, Lei Zheng, Yan Su, Guang-You Fang, Bin Zhou, Jian-Qing Feng, Shu-Guo Xing, Shun Dai, Jun-Duo Li, Yi-Cai Ji, et al. Performance evaluation of lunar penetrating radar onboard the rover of ce-3 probe based on results from ground experiments. *Research in Astronomy and Astrophysics*, 14(12):1633, 2014.

[154] Yongliao Zou, Yan Zhu, Yunfei Bai, Lianguo Wang, Yingzhuo Jia, Weihua Shen, Yu Fan, Yang Liu, Chi Wang, Aibing Zhang, et al. Scientific objectives and payloads of tianwen-1, china's first mars exploration mission. *Advances in Space Research*, 67(2):812–823, 2021.